STRUCTURAL STUDIES OF BECN1, A KEY AUTOPHAGY PROTEIN, AND INTRINSCIALLY DISORDERED REGIONS IN AUTOPHAGY PROTEINS

A Dissertation
Submitted to the Graduate Faculty
of the
North Dakota State University
of Agriculture and Applied Science

By

Yang Mei

In Partial Fulfillment of the Requirements
for the Degree of
DOCTOR OF PHILOSOPHY

Major Program:
Cellular and Molecular Biology

July 2016

Fargo, North Dakota

North Dakota State University
Graduate School

Title

Structural studies of BECN1, a key autophagy protein, and intrinsically disordered regions in autophagy proteins

By

Yang Mei

The Supervisory Committee certifies that this ***disquisition*** complies with North Dakota State University's regulations and meets the accepted standards for the degree of

DOCTOR OF PHILOSOPHY

SUPERVISORY COMMITTEE:

Sangita Sinha, Ph.D
Chair

Lawrence Reynolds, Ph.D

Christopher Colbert, Ph.D

John McEvoy, Ph.D

Approved:

07/07/2016
Date

Jane Schuh, Ph.D
Department Chair

ABSTRACT

Autophagy, a conserved catabolic process required for cellular homeostasis in eukaryotes, is regulated by many proteins. The central goal of my doctoral research is to investigate conformational flexibility of autophagy proteins, with a special focus on BECN1, a core component of the class III phosphatidylinositol-3 kinase autophagosome nucleation complex that may serve as an autophagy interaction hub.

Our rigorous bioinformatics analysis predicts that 57% of 59 key human autophagy proteins contain intrinsically disordered regions (IDRs), which lack stable secondary and tertiary structure. The prevalence of IDRs suggests that IDRs play an important, yet hitherto uninvestigated, role in autophagy. We confirm disorder of selected IDRs via biophysical methods, and use additional bioinformatics tools to predict protein-protein interaction and phosphorylation sites within IDRs, identifying potential biological functions.

We experimentally investigate four distinct BECN1 domains: (i) The IDR, which includes a functional BCL2 homology 3 domain (BH3D) that binds BCL2 proteins, undergoing a binding-associated disorder-to-helix transition and enabling BCL2s to inhibit autophagy. (ii) The flexible helical domain (FHD) which has an unstructured N-terminal half and structured C-terminal half forming a 2.5-turn helix in our 2.0 Å X-ray crystal structure. Our molecular dynamics simulations and circular dichroism spectroscopy analyses indicate the FHD transiently samples more helical conformations and likely undergoes a binding-associated disorder-to-helix transition. We also show that the FHD bears conserved residues critical for AMBRA1 interaction and for starvation-induced autophagy. (iii) A coiled-coil domain (CCD) which forms an anti-parallel homodimer in our 1.46 Å X-ray crystal structure. We have also built a atomistic model of an optimally packed, parallel BECN1:ATG14 CCD heterodimer that agrees with our

experimental SAXS data. Further, we show that BECN1:ATG14 heterodimer interface residues identified from this model are important for heterodimer formation and starvation-induced autophagy. (iv) A β-α repeated autophagy-specific domain which bears invariant residues that we show are important for starvation-induced autophagy. Thus, we demonstrate that conformational flexibility is a key BECN1 feature.

Lastly, we show that multi-domain BECN1 constructs have extended conformations with no intra-domain interactions that impact structure of other domains, suggesting that BECN1 structure and conformational flexibility enable its function as an autophagy interaction hub.

ACKNOWLEDGEMENTS

I would like to express my deepest appreciation to my advisor Dr. Sangita Sinha, who supports and encourages me all the time during my research. In the past 6 years, she has led me into the structural biology field, trained me to conduct research using various methods, guided me when I made mistakes, and mentored me to think critically in science. The research results in this thesis will not be achieved without her genius ideas. In particular, I appreciate her spending a lot of time to help me in my publications. Her devotion to the scientific research inspires me to pursue a career in science in my life.

I also want to thank my committee members Dr. Christopher Colbert, Dr. Larry Reynolds Dr. John McEvoy and Dr. Mark Sheridan for the supports and encouragement in all aspects over these years. Especially, I want to thank Dr. Colbert who teaches me a lot of the experimental techniques and gives me many useful advices on my research. Without his kindness help, the researches in this thesis will not be successfully finished.

In addition, I would like to show my appreciation to Dr. Saeed Salem for performing the bioinformatics work for me, Dr. John Wilkinson for teaching me doing CoIP assay, Dr. Pawel Borowicz for patiently teaching me to use the microscope and image analysis software in NDSU AIM lab, Dr Arvind Ramanathan and Dr. Christopher Stanley at Oak Ridge National Lab for performing the MD simulation for me, Dr. Ruslan Sanishvili and Dr. Srinivas Chakravarthy at Argonne National Lab for helping me with the X-ray diffraction and SAXS data collection, and Dr Zhongyu Yang at UCLA for performing the DEER-EPR experiments for me.

Last, but not least, I need to acknowledge all the lab members in Sinha Lab and Colbert Lab, especially Dr. Minfei Su, Ms. Karen Glover and Mr. Gaurav Soni. I would not be able to complete my research without their work.

DEDICATION

To,

Mom and Dad

for always loving and supporting me with no condition

TABLE OF CONTENTS

LIST OF TABLES

LIST OF FIGURES

LIST OF ABBREVIATIONS

AMBRA1 ..... activating molecule in BECN1-regulated autophagy protein 1

AMPK ..... 5’ AMP-activated protein kinase

ATG ..... autophagy-related protein

ATGD ..... autophagy related domain

ATM ..... ataxia-telangiectasiamutated

ATP ..... adenosine triphosphate

ATR ..... ATM and Rad 3-related

BARKOR ..... Beclin 1-Associated Autophagy-Related Key Regulator

BARAD ..... β-α repeats in autophagy domain

BATS ..... BARKOR/ATG14 autophagosome-targeting sequence

BCL2 ..... B-cell lymphoma-2

BECN1 ..... coiled-coil myosine-like BCL2-interacting protein

BH3D ..... BCL2 homolog 3 domain

BNIP3 ..... BCL2/adenovirus E1B 19 KD-interacting protein 3

BNIP3L ..... BCL2/ adenovirus E1B 19kDa interacting protein 3-like

CD ..... circular dichroism

CCD ..... coiled-coil domain

CCDs ..... charge-coupled devices

CMOS ..... complementary metal oxide semiconductor

CDK ..... cyclin-dependent kinase

CK2 ..... casein kinase 2

CLN3 ..... ceroid-lipofuscinosis, neuronal 3

Co-IP ..... coimmunoprecipitation

CRM1 ..... chromosomal maintenance protein 1

Cvt ..... cytosol-to-vacuole targeting

DAPK1 ..... phosphorylation of BECN1 at Thr119 by death-associated protein kinase 1

DDIT3 ..... DNA-damage-inducible transcript 3

DEER ..... double electron-electron resonance

DEPP ..... disorder-enhanced phosphorylation predictor

DLC1 ..... dynein light chain

DMEM ..... Dulbecco's Modified Eagle Medium

DNA ..... deoxyribonucleic acid

DTT ..... dithiothreitol

EBSS ..... Earle's balanced salt solution

ECD ..... evolutionary conserved domain

EDTA ..... ethylenediaminetetraacetic acid

EGFR ..... epidermal growth factor receptor

ELM ..... eukaryotic linear motifs

EPR ..... electron-paramagnetic resonance

ER ..... endoplasmic reticulum

ERK ..... extracellular signal-regulated kinase

EXOC8 ..... exocyst complex component 8

E.coli ..... *Escherichia coli*

FHD ..... flexible helical domain

FIP200 ..... FAK family kinase-interacting protein of 200KD

FR ..... flexible region

GABARAP ..... Gamma-aminobutyric acid receptor-associated protein

GAPR1 ..... Golgi-associated plant pathogenesis-related protein 1

GATE-16 ..... Golgi-associated ATPase enhancer of 16KD

GFP ..... green fluorescent protein

GOPC ..... Golgi associated PDZ and coiled-coil containing protein

GOSR1 ..... Golgi SNAP receptor complex member 1

HDAC6 ..... histone deacetylases 6

HIF-1α ..... hypoxia-inducible factor-1 alpha

HMGB1 ..... High mobility group box 1

IDR ..... intrinsically disordered region

IPTG ..... isopropyl β-D-1-thiogalactopyranoside

IRGM ..... immunity-related GTPase family, M

ITC ..... isothermal titration calorimetry

JNK ..... c-Jun N-terminal kinase

LAMP2 ..... lysosome-associated membrane protein 2

LC3 ..... microtubule-associated light chain 3

LKB1 ..... liver kinase B1

MAD ..... multiple-wavelength anomalous dispersion

MAP ..... microtubule-associated proteins

MAPK ..... mitogen-activated protein kinase

MBP ..... maltose binding protein

MCF7 ..... Michigan Cancer Foundation-7 (breast cancer cell line)

MCL1 ..... myeloid cell leukemia 1

MD ..... molecular dynamic

MIR ..... multiple isomorphous replacement

MoRF ..... molecular recognition feature

mTOR ..... mammalian target of rapamycin

MW ..... molecular weight

NBR ..... neighbor of BRCA1 gene

NES ..... nuclear export signal motif

NMR ..... nuclear magnetic resonance

NSF ..... N-ethylmaleimide-sensitive factor

PAS ..... pre-autophagosomal structure

PDPK2 ..... 3-phosphoinositide dependent protein kinase 1 pseudogene

PE ..... phosphatidylethanolamine

PKB/AKT ..... protein kinase B

PKC ..... protein kinase C

PKD ..... protein kinase D

PI ..... phosphatidylinositol

PI3KC3 ..... Class III phosphatidylinositol 3-kinase

PI3P ..... phosphatidylinositol 3-phosphate

PIK3R4 ..... phosphoinositide-3-kinase, regulatory subunit 4

PIKK ..... phosphatidylinositol kinase-related kinase

PINK1 ..... PTEN-induced putative kinase 1

PRAS40 ..... proline-rich AKT substrate of 40KD

PTEN ..... phosphatase and tensin homolog

PTM ..... post-translational modification

RALB ..... V-Ral simian leukemia viral oncogene homolog B

REDD1 ..... regulated in development and DNA damage responses 1

RB1CC1 ..... RB1-inducible coiled coil protein 1

RAB24 ..... member RAS oncogene family

RMSD ..... root-mean-square deviation

ROCK1 ..... Rho-associated protein kinase 1

ROS.....reactive oxygen species

RSK.....ribosomal s6 kinase

RUBICON.....Run domain protein as BECN1 interacting and cysteine-rich containing protein

SAD.....single-wavelength anomalous dispersion

SAXS .....small angle X-ray scattering

SEC .....size exclusion chromatography

SIR .....single isomorphous replacement

SLAMF1 .....signaling lymphocyte- molecule family

SLIM ..... short linear interaction motifs

SMURF1 ..... SMAD specific E3 ubiquitin protein ligase 1

SNARE ..... soluble N-ethylmaleimide-sensitive factor activating protein receptor

SNX18.....sorting nexin 18

SQSTM1 .....Sequestosome 1

TEV.....tobacco etch virus

TFE 2,2,2-trifluoroethanol

TGN .....*trans*-Golgi network

TLRs .....toll like receptors

TMEM74.....transmembrane protein 74

TNF .....tumor necrosis factor

TRAF6 ..... TNF receptor associated factor 6

TSC ..... tuberous sclerosis complex

ULK1/2 ..... Unc-51 Like Kinase 1/2

UVRAG .....UV radiation resistance-associated gene

VDAC1 ..... voltage dependent anion channel 1

VMP1 ..... vacuole membrane protein 1

VPS ..... vacuolar protein soring

WIPI ..... WD-repeat protein Interacting with phosphoInositides

WT ..... wild-type

Ala (A) ..... alanine

Asn (N) ..... asparagine

Arg (R) ..... arginine

Cys (C) ..... cysteine

Gln (Q) ..... glutamine

Glu (E) ..... glutamate

Gly (G) ..... glycine

His (H) ..... histidine

Ile (I) ..... isoleucine

Leu (L) ..... leucine

Lys (K) ..... lysine

Met (M) ..... methionine

Phe (F) ..... phenylalanine

Pro (P) ..... proline

Tyr (Y) ..... tyrosine

Ser (S) ..... serine

Thr (T) ..... threonine

Trp (W) ..... tryptophan

Tyr (Y) ..... tyrosine

Val (V) ..... valine

LIST OF SYMBOLS

d ..... distance between lays of atoms

f ..... scattering factor

q ..... momentum transfer

A ..... absorption factor

D_{max} ..... maximum dimension

F ..... structure factor

ΔG ..... Gibb's free energy

ΔH ..... enthalpy

I ..... intensity

K ..... scale factor

K_a ..... association constant

K_d ..... dissociation constant

L ..... Lorentz factor

R ..... gas constant

R_g ..... radius gyration

ΔS ..... entropy

T ..... temperature

θ ..... angle between incident rays and the surface of the crystals

λ ..... wavelength of X-ray

ρ ..... electron density

CHAPTER 1. AUTOPAGHY AND ITS IMPORTANT REGULATOR BECN1

1.1. General Introduction

Autophagy is an intracellular catabolic process conserved in all eukaryotes ranging from yeast to human beings. Under normal nutrient conditions, basal autophagy is responsible for cleaning intracellular contents, regulating cell size, and eliminating protein aggregates and toxic substances (Morselli, Galluzzi et al. 2011). Under nutrient deprivation or deoxyribonucleic acid (DNA) damage, induced autophagy serves as a survival mechanism to metabolic precursors such as amino acid and adenosine triphosphate (ATP) by recycling subcellular debris. However, extensive autophagy causes cell death (Nakamura, Asakawa et al. 2008, Longatti and Tooze 2009) (Figure 1.1). Autophagy is shown to play roles in a variety of diseases including cancers, neurodegenerative diseases, cardiovascular diseases, metabolic diseases and infective diseases (Klionsky 2010). Therefore, improving our understanding of the regulatory mechanism of autophagy has the potential to facilitate the development of therapeutic methods for all these diseases.

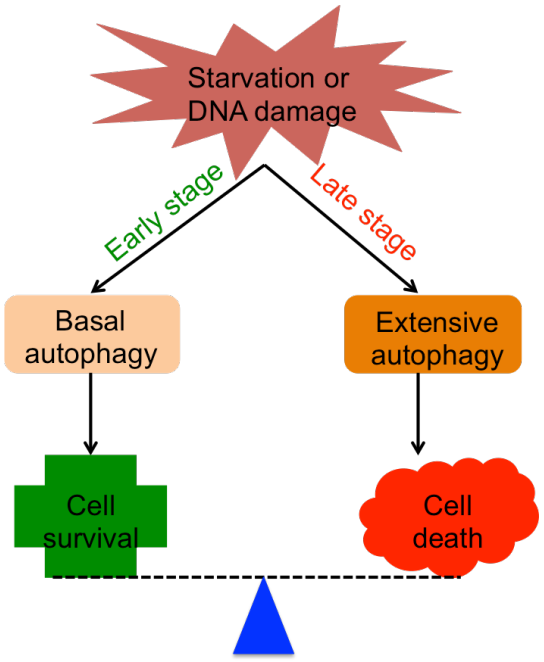

Figure 1.1. Schematic diagram representing the effects of low-level and extensive autophagy under cellular stresses.
The induced autophagy at early stage is important for cell survival while at late stage it causes cell death.

Stages in autophagy include initiation, vesicle nucleation, elongation, maturation and fusion with lysosome (Figure 1.2). Each stage requires multiple protein-protein interactions and formation of protein complex (Levine and Klionsky 2004, Mizushima 2007, Mizushima and Klionsky 2007).

The coiled-coil myosin-like B-cell lymphoma 2-interacting protein (BECN1) is a key component of the Class III phosphatidylinositol 3-kinase (PI3KC3) core complex responsible for vesicle nucleation (Figure 1.2) (He and Levine 2010). BECN1, a highly conserved eukaryotic protein, is a key autophagy regulator. It interacts with diverse protein partners, perhaps serving as an interaction hub for autophagy. The mutations or altered expression levels of BECN1 contribute to pathogenesis of various diseases (Levine and Kroemer 2008, Sinha and Levine 2008, He and Levine 2010, Kang, Zeh et al. 2011, Morris, Yip et al. 2015).

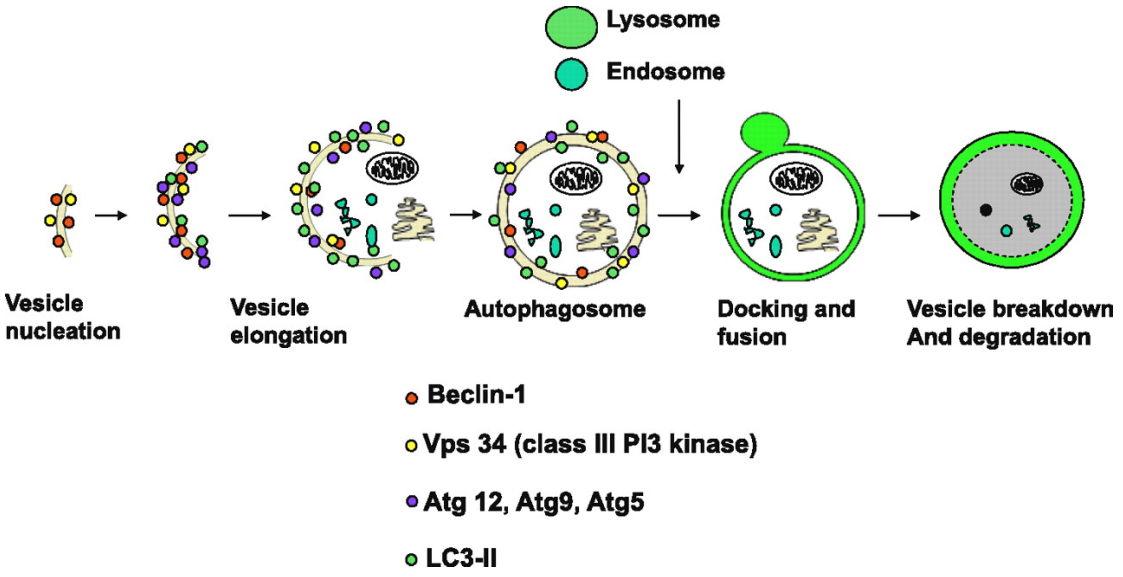

Figure 1.2. Schematic diagram depicting the process of autophagy.
The process of autophagy starts with the de novo formation of an isolation membrane or phagophore (vesicle nucleation), the cytosolic components are then captured by this isolation membrane with the presence of autophagy proteins such as BECN1, VPS34/PI3KC3, LC3, ATG12, etc. The phagophore then elongates and closes to form autophagosome, which further fuses with lysosome to form the autophagolysosome. The sequestered cytosolic contents are degraded by the hydrolase from lysosome to produce amino acids and released back into cells. (Yang, Kaushal et al. 2008).

Though much progress has been achieved in elucidating molecular mechanisms in different autophagy steps, a structure-based understanding of the protein-protein interaction and post-translational modifications in autophagy have not been determined. In particular, further investigation is needed concerning the structural information of BECN1 and its regulatory

mechanism in autophagy. The overall goal of my research is to delineate structural features important for protein interaction in autophagy using bioinformatics methods, with a special focus on elucidating the mechanism of proteins responsible for vesicle nucleation, especially BECN1 using a broad range of bioinformatics, molecular biology, biochemical, biophysical, structural biology and cellular biology methods. A detailed introduction to autophagy is provided in section 1.2, a comprehensive introduction to PI3KC3:BECN1 complex with a special focus on BECN1 is provided in section 1.3, and the methods used in this research are broadly described in section 1.4.

1.2. Introduction to Autophagy

1.2.1. Autophagy and Diseases

Both, deficient or extensive autophagy is associated with many human diseases. Many autophagy mediators such as BECN1 and p53 are integral components of cancer cell signaling networks (Shi, Li et al. 2013). Autophagy defects result in oxidative stress, accumulation of protein aggregates and misfolded proteins, damaged organelles, DNA and genome damage, all of which are associated with cancers. The production of oxidative stress causes toxicity to cells and induces tumorigenesis (Chen and Debnath 2010). The tumor suppressor p53 promotes autophagy and reduces oxidative stress, suggesting that autophagy may suppress tumorigenesis via reducing the reactive oxygen species (ROS) (Jin 2005). Moreover, extensive induced autophagy by stressors such as ROS may cause cancer cell death (Jin 2005). Therefore, autophagy provides an anti-carcinogenic function in a lot of cancer cells such as breast cancer, pancreatic cancer, and ovarian cancer.

In neuronal cells, autophagy is an initial adaptive response in neurodegeneration, subject to inhibition by the pathologic accumulation of substrates. Disruption of basal autophagy leads to

neurodegeneration due to the failure to clear protein aggregates by hydrolases or mitochondria dysfunction (Komatsu, Ueno et al. 2007). This deficiency in autophagy is often involved in aging related diseases such as Alzheimer's disease (Binder, Guillozet-Bongaarts et al. 2005), Huntington's disease (Li, Schilling et al. 1993) and Parkinson's disease (Narendra, Tanaka et al. 2008, Matsuda, Sato et al. 2010).

In the heart, basal autophagy is necessary for maintaining the correct size and function of cardiomyocytes (Nakai, Yamaguchi et al. 2007). For example, in Danon's disease, failure of autophagosome-lysosome fusion caused by mutations in the lysosome-associated membrane protein 2 (LAMP2) results in the increased accumulation of autophagic vacuoles and impaired autophagic flux (Saftig, Tanaka et al. 2001). Further, inhibition of autophagy results in the insufficient removal of damaged mitochondria, which in turn leads to the increased accumulation of ROS, and causes heart aging and other heart diseases (Terman 2001, Terman and Brunk 2005).

During infection, pattern recognition receptors such as Toll-like receptors (TLRs) recognize the pathogen associated molecular patterns and damage-associated molecular patterns, and trigger the ubiquitination of BECN1 by tumor necrosis factor (TNF) receptor-associated factor 6 (TRAF6) to induce autophagy to eliminate the invading microorganisms and suppress inflammation (Shelly, Lukinova et al. 2009, Levine, Mizushima et al. 2011, Tattoli, Sorbara et al. 2012). The pro-inflammatory cytokines such as interferon-γ induced by mycobacteria infection promote the phosphorylation of BECN1 at Thr119 by death-associated protein kinase 1 (DAPK1). The phosphorylated BECN1 then dissociates from autophagy inhibitor B-cell lymphoma-2 (BCL2) to up-regulate autophagy to defend against mycobacteria (Deretic, Saitoh

et al. 2013). Therefore, it is of great importance to better understand the regulation mechanisms of autophagy to improve human health.

1.2.2. Stages in Autophagy

With the presence of the AuTophaGy-related (ATG) proteins, autophagy, the 'self-eating' process, starts with the de novo formation of the phagophore or isolation membrane from multiple sources such as endoplasmic reticulum (ER) (Hayashi-Nishino, Fujita et al. 2010), mitochondria (Hailey, Rambold et al. 2010), or Golgi (Geng and Klionsky 2010) as a thin cisterna with clear lumen. This isolation membrane engulfs targeted cytoplasmic components, and the autophagosome forms following the elongation and closure of the isolation membrane. Autophagosomes fuse with lysosomes to degrade the captured cargo to recycle nutrients and energy to maintain the cell survival. In this process, autophagosome is a transient organelle for the sequestration of cytoplasmic components (Figure 1.2) (Nakamura, Asakawa et al. 2008, Longatti and Tooze 2009) to maintain cellular homeostasis.

To date, about 60 proteins have been discovered in the autophagy pathway and discoveries of new autophagy proteins keep emerging. The execution of each stage of autophagy involves several protein-protein interactions, often forming multi-protein complexes (Figure 1.3): the Unc-51-like kinase 1 (ULK1) complex in autophagy initiation; the PI3KC3 complex in vesicle nucleation; two ubiquitin-like conjugation pathways: ATG12:ATG5:ATG16 and microtubule-associated light chain 3 (LC3/ATG8) conjugation complexes in vesicle elongation; the ATG9 trafficking complex providing membrane sources for autophagosome elongation and formation; and soluble N-ethylmaleimide-sensitive factor (NSF) attachment protein receptors (SNAREs) in lysosome fusion.

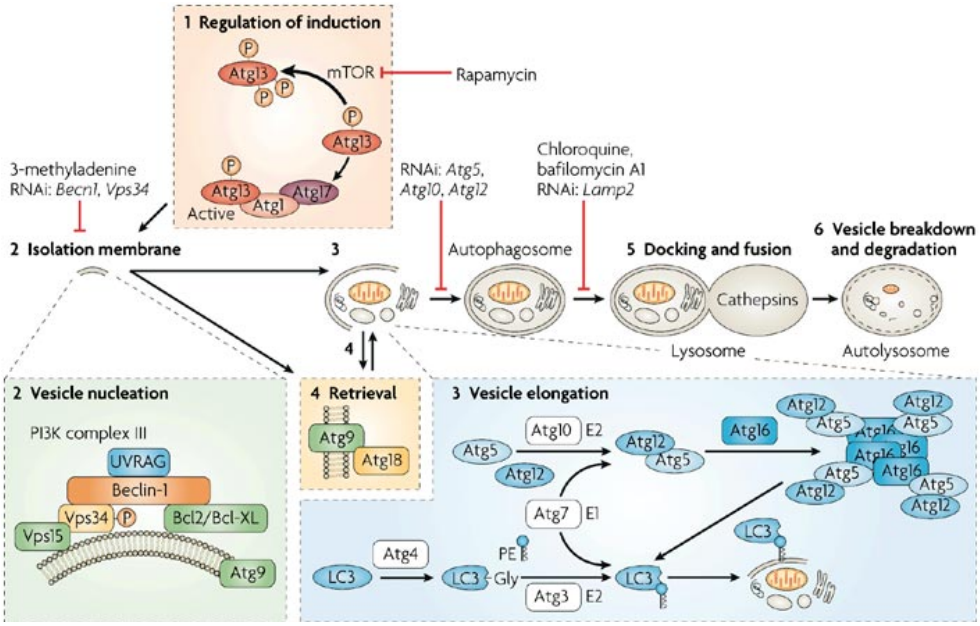

Figure 1.3. Protein complexes in autophagy.
Each autophagy step requires protein interactions (Behrends, Sowa et al. 2010): The activation of ULK1/ATG1 complex in induction step starts the formation of isolation membrane; The formation and activation of PI3KC3 complex in vesicle nucleation step triggers the autophagosome elongation; ATG12:ATG5:ATG16 and LC3/ATG8 complex in vesicle elongation step is required for the autophagosome formation; ATG9 retrieval from pre-autophagosomal structure (PAS) in complex with ATG18 and ATG2 is required for autophagy.

1.2.3. Proteins Responsible for Each Stage of Autophagy

Under conditions of autophagy stimulation such as nutrient depletion, different autophagy proteins interact with each other and form different protein complexes to accomplish autophagy.

1.2.3.1. Initiation: ULK1/ATG1 Protein Complex

ATG1 is the only kinase among the recognized yeast ATG genes (Wong, Puente et al. 2013). ULK1, the human counterpart of ATG1, is a 112KD protein consisting of an N-terminal kinase domain, a serine-proline rich region and a C-terminal domain (Kim, Kundu et al. 2011). Human ULK2 is another functional homolog of ATG1, but has a much lower expression level than ULK1 (Dunlop, Hunt et al. 2011). It is thought to provide an additional mechanism for autophagy regulation in mammals. The ULK1/2 protein kinase complex consists of ULK1/2,

ATG13, FAK family kinase-interacting protein (FIP200)/RB1-inducible coiled coil protein 1 (RB1CC1) and ATG101, in which ATG13 and FIP200 are required to activate ULK1/2 kinase activity in autophagy (Ganley, Lam et al. 2009) (Figure 1.4). The loss of ULK1/2 leads to the failure of autophagy induction.

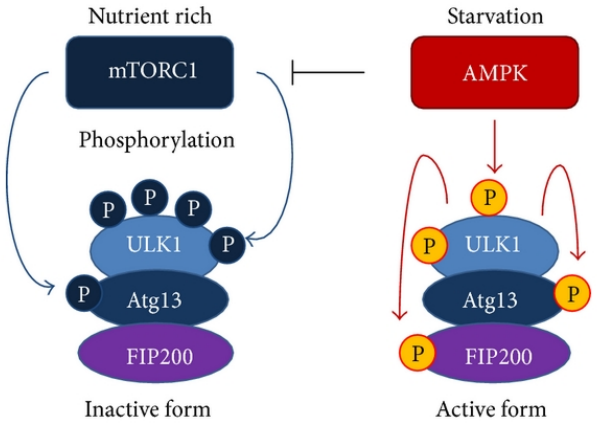

Figure 1.4. ULK1 complex activation under starvation condition.
The ULK1 complex components are shown. In nutrient rich conditions, mTORC1 phosphorylates ULK1 and ATG13 on multiple sites to inactivate the ULK1 activity. The starvation induces the activation of AMPK (AMP-activated protein kinase) to dephosphorylation ULK1, which further dephosphorylates the inactive form of the phosphorylated ATG13 and phosphorylates ATG13 and FIP200 at different sites to activate the kinase activity (Yamahara, Yasuda et al. 2013)

1.2.3.2. Vesicle Nucleation: PI3KC3 Complex

There are two PI3KC3 complexes: Complex I: BECN1:ATG14 (Beclin 1-Associated Autophagy-Related Key Regulator, BARKOR) :PI3KC3:p150 and complex II: BECN1:UVRAG (UV radiation resistance associated gene):PI3KC3:p150 (Itakura, Kishi et al. 2008, Itakura and Mizushima 2009, Baskaran, Carlson et al. 2014, Rostislavleva, Soler et al. 2015). The kinase activity of PI3KC3 is activated to produce phosphatidylinositol 3-phosphate (PI3P) from phosphatidylinositol (PI), which is vital for the autophagosome formation (Axe, Walker et al. 2008, Obara, Noda et al. 2008, Obara and Ohsumi 2008). Immunoprecipitation results reveal that PI3KC3, BECN1 and p150 form a core complex to interact with either ATG14/BARKOR or

UVRAG via BECN1 (Sun, Fan et al. 2008). The interaction of PI3KC3 with BECN1 and other components is required and vital for the induction of kinase activity (Figure 1.5) (He and Levine 2010).

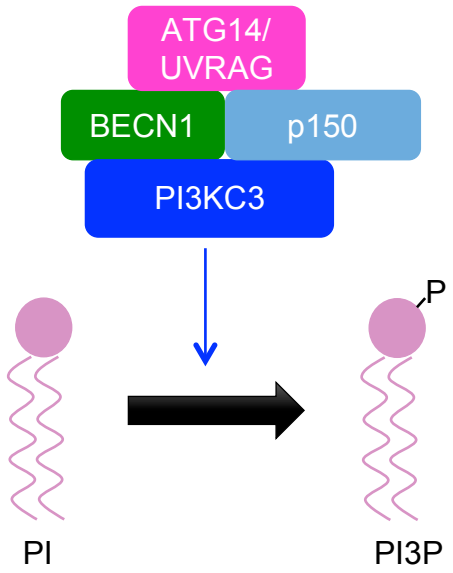

Figure 1.5. PI3KC3 complex produces PI3K from PI.
With the formation of the PI3KC3 complex containing PI3KC3, BECN1, p150, ATG14 or UVRAG, etc., the lipid kinase is activated to produce PI3P on the membrane. Each PI3KC3 component is colored differently and shown in figure.

1.2.3.3. Two Ubiquitin-like Conjugation Systems

ATG12 and LC3/ATG8 are two ubiquitin-like modifiers that are activated and conjugated to target proteins through two ubiquitin-like conjugation systems (Figure 1.6) in a manner similar to the process of protein ubiquitination (Geng and Klionsky 2008).

In the ATG12 ubiquitin-like system, the cysteine of E1-like ATG7 (Tanida, Mizushima et al. 1999) and E2-like ATG10 (Shintani, Mizushima et al. 1999) sequentially form thioester bonds with ATG12 via their C-terminal Glycine. Then, ATG12 is conjugated to the lysine 149 in ATG5 to form the isopeptide-bonded complex, which further recruits ATG16, a coiled-coil protein (Mizushima, Sugita et al. 1998, Mizushima, Noda et al. 1999). The ATG12:ATG5:ATG16 complex preferentially associates with the convex surface of the

membrane and dissociates from it upon autophagosome completion (Mizushima, Kuma et al. 2003), indicating its important role in autophagosome formation.

In the LC3/ATG8 system (Figure 1.6), the cysteine protease ATG4 recognizes LC3 and cleaves the peptide bond between Gly and Arg of LC3 to expose Gly at its C-terminus (Kabeya, Mizushima et al. 2004). Similar to ATG12 conjugation system, the E1-like ATG7 and E2-like ATG3 sequentially conjugate LC3-I (a non-lipidated form)(Tanida, Tanida-Miyake et al. 2001, Tanida, Tanida-Miyake et al. 2002) to form the ATG3-LC3-thioster (Kabeya, Mizushima et al. 2004). Lastly, the ATG12:ATG5 conjugate acts as an E3-like ligase to facilitate the formation of a lipidated LC3-II-PE (phosphatidylethanolamine) similar to ATG8-PE (Hanada, Noda et al. 2007, Fujioka, Noda et al. 2008, Fujita, Itoh et al. 2008), which crosslinks the two conjugation systems. ATG16 is not required for the E3-like activity, but important for the localization of the complex at autophagy membranes. Meanwhile, the ATG12-dependent membrane recruitment of ATG3 is more efficient upon formation of the ATG12:ATG5:ATG16 complex (Mizushima, Yamamoto et al. 2001, Suzuki, Kirisako et al. 2001). In the presence of ATG3 thioester-linked LC3/ATG8, the ATG3-binding surface of ATG12 is released from ATG5 in ATG12:ATG5:ATG16 complex to enable the interaction between ATG12 and ATG3, targeting the LC3/ATG8-linked ATG3 to the membrane surface and facilitating the transfer of LC3/ATG8 from ATG3 to the PE on the membrane surface (Noda, Fujioka et al. 2013). In this process, the appearance of the ATG12:ATG5 complex on membrane surface reorients the cysteine toward the threonine of E2-like ATG3 and enhances the activity of ATG3. In humans, the LC3-II-PE complex is evenly distributed on the surface of the autophagosome membrane. Thus the green fluorescent protein (GFP) tagged LC3-II is usually used as a marker of autophagosome formation in mammalian cells (Ueno, Sato et al. 2008).

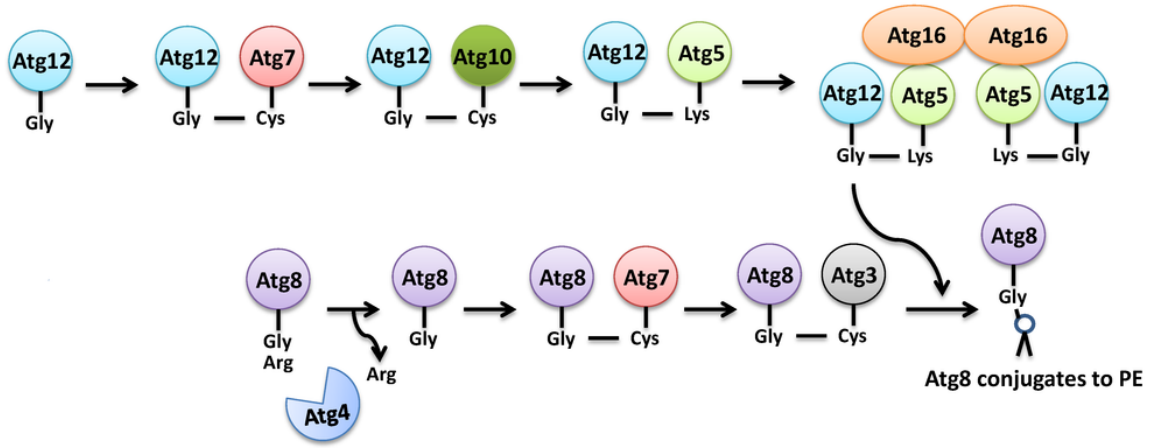

Figure 1.6. Two ubiquitin-like conjugation systems in autophagy.
ATG4 first cleaves ATG8 at its C-terminal glycine and activates it. Then ATG7 acts as an E1-like enzyme to form thioester bond with either ATG12 or ATG8 and transfer them to E2-like enzyme ATG10 or ATG3 respectively. ATG12 finally conjugates with ATG5 forming an isopeptide bond. ATG5 then binds to ATG16 forming ATG12:ATG5:ATG16 complex. Two ATG16 molecules homodimerize via the coiled-coil domain, forming a dimer of ATG12:ATG5:ATG16 tertiary complex. ATG12:ATG5 complex also functions as an E3-like ligase in ATG8 system to facilitate the formation of ATG8-PE on membrane (Yang and Rosenwald 2014).

1.2.3.4. ATG9 Trafficking Complex

ATG9 is the only transmembrane protein required for vesicle formation of autophagy (Lang, Reiche et al. 2000, Noda, Kim et al. 2000, Young, Chan et al. 2006). ATG9 is found to localize on pre-autophagosomal structure (PAS) in yeast mitochondria, mammalian endosomes and *trans*-Golgi network (TGN) (Reggiori, Shintani et al. 2005), indicating that these organelles may provide the membrane source for autophagy. In yeast, ATG9 vesicles derived from Golgi are dependent on ATG23 and ATG27. During starvation, a few of these vesicles fuse with the outer membrane of autophagosome (Yamamoto, Kakuta et al. 2012). Yeast ATG9 is shown to traffic between PAS and non-PAS compartments, which is dependent on the ATG1:ATG13 complex. ATG1 together with the PI3P produced by PI3KC3 helps to recruit ATG2 and ATG18 to ATG9 on PAS for the proper function of ATG9 retrieval from PAS (Reggiori, Tucker et al. 2004). ATG9 itself is also required for ATG2-ATG18 localization to the PAS, indicating ATG9

also plays a role in recruiting the proteins necessary for its recycling (Suzuki, Kubota et al. 2007). In mammals, inhibition of mammalian target of rapamycin (mTOR) by rapamycin or nutrient deprivation triggers the redistribution of ATG9 from TGN to peripheral structures to activate autophagy (Webber and Tooze 2010, Tang, Wang et al. 2011). However, the structure of proteins in ATG9 trafficking complex and mechanism by which it regulates autophagy is poorly understood and needs to be further investigated.

1.2.4. Signaling Regulation of Autophagy

Post-translational modifications (PTMs), especially phosphorylation, play important roles in regulating autophagy proteins interactions and function. Kinases play important roles in autophagy regulation by adding a phosphoryl group to a residue such as serine, threonine and tyrosine (Table 1.1). The phosphorylation of autophagy proteins, in turn, mediates protein-protein interaction during autophagy.

Target of rapamycin (TOR), a S/T protein kinase, regulates autophagy in both yeast and mammals. mTOR is a large protein with a molecular size of 289KD (Janus, Robak et al. 2005) belonging to the phosphatidylinositol kinase-related kinase (PIKK) (Hynes and Lane 2005) family. It forms mTOR complex I (mTORC1) with Raptor, GβL, and DEPTOR. The mTORC1 then integrates autophagy regulation with various signaling pathways such as protein kinase B (PKB/AKT), AMP-activated protein kinase (AMPK), mitogen-activated protein kinases (MAPK)/extracellular signal-regulated kinases (ERK) and ribosomal s6 kinase (RSK).

In the presence of growth factors, tuberous sclerosis complex 2 (TSC2) is inactivated when it is phosphorylated by MAPK/ERK at Ser540 and Ser664 (Ma, Chen et al. 2005), by AKT at Ser939 and Thr1462 (Potter, Pedraza et al. 2002), or by RSK1 at Ser1798 (Roux, Ballif et al. 2004). TSC2 suppresses mTOR by blocking the phosphorylation of mTORC1 at Ser2448 (Inoki,

Li et al. 2002). Therefore, mTORC1 is activated when TSC2 is inactivated. AKT can also promote the phosphorylation at Thr246 of Proline-Rich AKT Substrate of 40KD (PRAS40), an mTORC1 inhibitor (Sancak, Thoreen et al. 2007). This promotes the further phosphorylation of PRAS40 by mTORC1 at Ser183 and Ser221 (Nascimento, Snel et al. 2010). PRAS40 then dissociates from mTORC1 to activate mTOR.

Contrary to AKT, the activation of AMPK down-regulates the activity of mTORC1. Under conditions of hypoxia, AMPK is up-regulated in a TSC1:TSC2 complex-dependent manner to down-regulate the mTOR activity (Feng, Zhang et al. 2005). In addition, under metabolic stresses such as the glucose starvation, the ratio of AMP/ATP increases and the energy-sensing kinase AMPK is activated to inhibit mTOR in mTORC1 (Towler and Hardie 2007). In response to DNA damage, liver kinase B1 (LKB1) phosphorylates and activates AMPK to inhibit mTOR signaling (Alexander and Walker 2011).

p53, an important tumor suppressor, is activated via phosphorylation at Ser15 by Ataxia-Telangiectasia Mutated (ATM)/ATM and Rad 3-related (ATR) in cytoplasm to inhibit mTOR via activation of AMPK under genotoxic stresses (Siliciano, Canman et al. 1997, Feng, Zhang et al. 2005). Another protein, Regulated in Development and DNA damage responses 1 (REDD1) is also an inhibitor of mTOR signaling in response to hypoxia or DNA damages (Brugarolas, Lei et al. 2004, Sofer, Lei et al. 2005).

mTOR kinase negatively regulates autophagy by phosphorylating ULK1 at Ser757 and ATG13 at Ser258 (Puente, Hendrickson et al. 2016), to disrupt the interaction between ULK1 and AMPK to block the autophagy. On the other hand, the X-ray crystal structure of ULK1 indicated that its activation loop contains a self-phosphorylation site, Thr180, whose phosphorylation is required for the ULK1 autophosphorylation activity to activate autophagy

(Bach, Larance et al. 2011). Therefore, phosphorylation is critical for regulating the activity of ULK1. Recently, ULK1 was found to directly phosphorylate ATG13 at Ser318 within its intrinsically disordered region (IDR), leading to the selective translocation of ATG13 to mitochondria and activation of mitophagy (Joo, Dorsey et al. 2011).

MAPK8/c-Jun N-terminal kinase 1 (JNK1) phosphorylates BCL2 at Thr69, Ser70 and Ser87 within its IDR upon starvation or ceramide treatment, thereby releasing BECN1 from BCL2 (Wei, Pattingre et al. 2008).

The lipid kinase activity of PI3KC3, the core component of PI3KC3 complex during vesicle nucleation of autophagy, also needs to be activated through phosphorylation at different sites. Cyclin-dependent kinases (CDKs) control PI3P production by regulating the PI3KC3 activity. Thr159 of vacuolar protein sorting 34 (VPS34), the yeast homolog of PI3KC3, is phosphorylated by cyclin-dependent kinase 1 (CDK1) and inhibits its interaction with BECN1/ATG6, whereas CDK5 eliminates the activity of VPS34 by phosphorylation at Thr668 (Furuya, Kim et al. 2010). In glucose starvation conditions, AMPK phosphorylates VPS34 at Thr163 and Ser165, thus activating PI3KC3 kinase activity to protect cells from starvation (Kim, Kim et al. 2013). Src, a Tyrosine family kinase, phosphorylates VPS34 at Tyr231 located at the linker between VPS34 C2 domain and helical domain to activate lipid kinase activity of VPS34 (Hirsch, Shen et al. 2010). The Ser/Thr protein kinase D (PKD) stimulates autophagy via the phosphorylation of VPS34 at Thr677 (Eisenberg-Lerner and Kimchi 2012).

In the ubiquitin-like conjugates, the N-terminal LC3 is phosphorylated by protein kinase A (PKA) at Ser12 (Cherra, Kulich et al. 2010), and by protein kinase C (PKC) at Thr6 and Thr29 (Jiang, Cheng et al. 2010). PKA inhibits LC3 lipidation and leads to the failure of incorporation LC3 into autophagosome (Cherra, Kulich et al. 2010). Under starvation conditions,

MAPK15/ERK8, a microtubule-associated proteins kinase involved in cell proliferation and transformation, is activated to localize to autophagosomes, inducing LC3 lipidation and preventing the inhibitory phosphorylation of LC3 by PKA (Colecchia, Strambi et al. 2012).

ATG5 is phosphorylated by p38 at Thr75, a conserved residue ranging from yeast to human, to inhibit the lipidation of LC3-I to LC3-II and thus inhibit autophagy (Keil, Hocker et al. 2013). Casein kinase 2 (CK2) phosphorylates p62 at Ser403 to increase its affinity for its ubiquitinated substrates to induce their degradation by autophagy (Matsumoto, Wada et al. 2011).

Phosphorylation also plays important regulatory role in the ATG9 trafficking complex. Under starvation conditions, ATG9 interacts with WD-repeat protein Interacting with PhosphoInositides 1 (WIPI-1) /ATG18 and travels from the TGN and late endosomes toward the PAS, enabling the transport of phospholipids or membranes (Young, Chan et al. 2006). This relocalization has been shown to depend on phosphorylation of ULK1 by AMPK (Young, Chan et al. 2006, Mack, Zheng et al. 2012). ATG1/ULK1 is also shown to phosphorylate multiple sites in ATG9 (Table 1.1), which is required for the recruiting ATG8 and ATG18 to the PAS to expand the isolation membrane during autophagosome formation (Papinski, Schuschnig et al. 2014). However, the mechanism by which ATG9 travels through the cell during autophagy is still unclear.

Table 1.1. Phosphorylation sites in autophagy proteins.

Protein Name	Phosphorylation Site	Kinase	Effect on Autophagy	Reference
ULK1	S317, S555, S777	AMPK	Activation	(Kim, Kundu et al. 2011), (Bach, Larance et al. 2011)
	S757	mTOR	Disrupt ULK1-AMPK interaction and inhibition autophagy	(Puente, Hendrickson et al. 2016)
	S774	AKT	Inhibition	(Bach, Larance et al. 2011)
	T180	autophosphorylation	Activation	(Bach, Larance et al. 2011)
ATG13	S258	mTOR	Disrupt ULK1-AMPK interaction and inhibition autophagy	(Puente, Hendrickson et al. 2016)
	S318	ULK1	Translocate ATG13 in mitochondria and activate mitophagy	(Joo, Dorsey et al. 2011)
BCL2	T69, S70, S87	MAPK8/JNK1	Release BECN1 and activate autophagy	(Wei, Pattingre et al. 2008)
VPS34	T159	CDK1	Disrupt BECN1 interaction to inhibit autophagy	(Furuya, Kim et al. 2010)
	T163, S165	AMPK	Activate kinase activity to induce autophagy	(Kim, Kim et al. 2013)
	Y231	Src	Activate lipid kinase activity of VPS34 to induce autophagy	(Hirsch, Shen et al. 2010)
	T668	CDK5	Eliminate VPS34 activity	(Furuya, Kim et al. 2010)
	T677	PKD	Activation	(Eisenberg-Lerner and Kimchi 2012)
LC3	T6, T29	PKC	Inhibition	(Jiang, Cheng et al. 2010)
	S12	PKA	Inhibition	(Cherra, Kulich et al. 2010)
ATG5	T75	p38/MAPK	Inhibit LC3-I to LC3-II lipidation and inhibit autophagy	(Keil, Hocker et al. 2013)

Table 1.1. Phosphorylation sites in autophagy proteins (continued).

Protein Name	Phosphorylation Site	Kinase	Effect on Autophagy	Reference
p62	S403	CK2	Increase degradation in autophagy	(Matsumoto, Wada et al. 2011)
ATG9	S19, S657, S802, S831, S948, S969	ATG1/ULK1	Required for Cvt and autophagy	(Papinski, Schuschnig et al. 2014)

1.3. PI3KC3:BECN1 Core Complex in Vesicle Nucleation

PI3KC3 plays important roles in autophagosome formation and protein sorting by forming different PI3KC3 complexes whose core consists of with PI3KC3/VPS34, p150/VPS15, BECN1/ATG6/VPS30 and either BARKOR/ATG14 or UVRAG/VPS38.

1.3.1. PI3KC3/VPS34

PI3KC3 contains 3 domains: N-terminal C2 domain, helical domain and catalytic domain (Walker, Perisic et al. 1999). The coimmunoprecipitation (Co-IP) results indicate that C2 domain is required for the BECN1 interaction (Furuya, Kim et al. 2010). The X-ray crystal structure of human (Dowdle, Nyfeler et al. 2014, Ronan, Flamand et al. 2014, Pasquier, El-Ahmad et al. 2015), fly (Miller, Tavshanjian et al. 2010) and yeast (Rostislavleva, Soler et al. 2015) class III PI3K has been solved in complex with different inhibitors or activators. The X-ray crystal of VPS34, the yeast homolog of human PI3KC3 helical and catalytic domains, show that the helical domain is a solenoid with two lobes (N-lobe and C-lobe) that packs against a catalytic kinase domain, forming a compact unit with extensive inter-domain contacts. It has a completely ordered phosphoinositide-binding loop (activation loop), which is disordered in other classes of PI3 kinases. Bulky residues in the phosphate-binding loop (P-loop) cause the increased rigidity of VPS34 ATP binding pocket, which is critical for the catalytic domain to selectively bind its substrate or the ATP adenine mimic, 3-MA (Miller, Tavshanjian et al. 2010). VPS34 has another

conserved catalytic loop within the DRH motif, in which His745 acts as the catalytic base to abstract a proton from 3-OH to facilitate nucleophilic attack on the γ-phosphate of ATP, whereas the Asp743 and Asp761 act as metal ligands to neutralize the negative charge in the transition state (Miller, Tavshanjian et al. 2010). The C-terminal helix (Kα12) has critical roles in membrane binding and catalytic function. In the closed form, this helix folds over the catalytic loop and locks the catalytic His745 in its inactive conformation. Conversely, the activation loop could help to remove it from the catalytic loop to activate the kinase function. In addition, the yeast two-hybrid results show that the yeast VPS34 C terminus residues 837-864 are necessary and sufficient for binding to yeast VPS15, which, in turn, activates the kinase activity of VPS34 (Stack, Herman et al. 1993, Budovskaya, Hama et al. 2002).

1.3.2. P150/VPS15

VPS15, the yeast homolog of Ser/Thr kinase p150, is required for the activity of VPS34, the yeast homolog of PI3KC3 (Lindmo, Brech et al. 2008). VPS15 contains three domains: an N-terminal kinase domain with two lobes (N-lobe and C-lobe), a HEAT domain and a C-terminal WD40 domain. The N-lobe of the VPS15 kinase domain interacts with the C-lobe of VPS34 kinase domain. The helical VPS15 HEAT domain nestles the VPS34 C2 domain (Lindmo, Brech et al. 2008). VPS15 is required for VPS34 kinase activity and disrupts vesicular trafficking (Backer 2008). The WD40 domain interacts with BECN1 (Lindmo, Brech et al. 2008). A recent 28Å cryo-EM structure of the yeast PI3KC3 complex I showed that VPS15 WD40 domain is located next to the BECN1 β-α-repeated autophagy-specific domain (BARAD), suggesting an interaction between these two domains (Baskaran, Carlson et al. 2014). Further, in the nutrient starvation conditions, the up-regulation of autophagy by PI3KC3/VPS34 complex requires the presence of p150/VPS15 (Kihara, Noda et al. 2001, Obara, Noda et al. 2008). GTPase RAB5 and

RAB7 bind to p150 to activate the PI3KC3/p150 heterodimer complex at membrane, which links autophagy to endocytosis (Murray, Panaretou et al. 2002, Stein, Feng et al. 2003).

1.3.3. BECN1: An Interaction Hub

BECN1 is a tumor suppressor and an autophagy regulator in many diseases. It is the mammalian ortholog of yeast ATG6/VPS30 and *C. elegans* BEC-1. As the important component of PI3KC3 core complex, BECN1 interacts with a variety of proteins such as autophagy/Beclin-1 regulator 1 (AMBRA1), ATG14, UVARG, etc., and localizes them to PAS to trigger autophagy (Figure 1.3) (He and Levine 2010).

1.3.3.1. Pathologies Associated with the BECN1 Gene

The BECN1 gene is mapped on human chromosome 17q21 locus, about 150kb centromeric to a cancer-associated gene of BRCA1, and encodes a 60KD, 450-amino acid coiled-coil protein, called BECN1. BECN1 was the first mammalian gene shown to be required for autophagy under starvation condition in mammalian cells (Liang, Jackson et al. 1999). For example, in BECN1-absent MCF7 human breast cancer cells, autophagy is not up-regulated under the starvation conditions (Liang, Jackson et al. 1999). Reduced level of BECN1 expression or monoallelic deletion of BECN1 promotes tumorigenesis in breast, ovarian and prostate cancer (Qu, Yu et al. 2003). BECN1 mRNA levels are low in cells of colon cancer (Koneri, Goi et al. 2007), breast tumor (Li, Chen et al. 2010) and brain tumor (Miracco, Cosci et al. 2007) *et al*. This evidence indicates that BECN1 may act as a tumor suppressor by promoting autophagy. The mouse embryo study shows that loss of BECN1 also results in the failure of embryonic development (Yue, Jin et al. 2003). The deletion of BECN1 also results in the increase of tumor cell proliferation, growth, invasion and metastasis (Wang, Fan et al. 2013, Weng, Wang et al. 2014, Wang, Wu et al. 2015). Therefore, understanding the molecular mechanism of BECN1 in autophagy is important for understanding the physiological and pathological impacts of this protein.

1.3.3.2. BECN1 Domains Architecture Established before this Project

Structural, sequence predictions, cellular and molecular biology studies revealed that BECN1 is a 450-amino acid protein with an unstructured N-terminal domain, a BCL2 homolog 3 domain (BH3D, residues 105-130, Figure 1.7, cyan box) interacting with anti-apoptotic BCL2 family protein to adopt the α-helical conformation (Feng, Huang et al. 2007, Oberstein, Jeffrey et al. 2007, Ku, Woo et al. 2008, Sinha, Colbert et al. 2008), a central coiled-coil domain (CCD)

(residues 144-269, Figure 1.7, magenta box) to interact with CCDs of ATG14 or UVRAG, and an evolutionary conserved domain (ECD, residues 244-337, Figure 1.7, green box) (Furuya, Yu et al. 2005) that is involved in the membrane association.

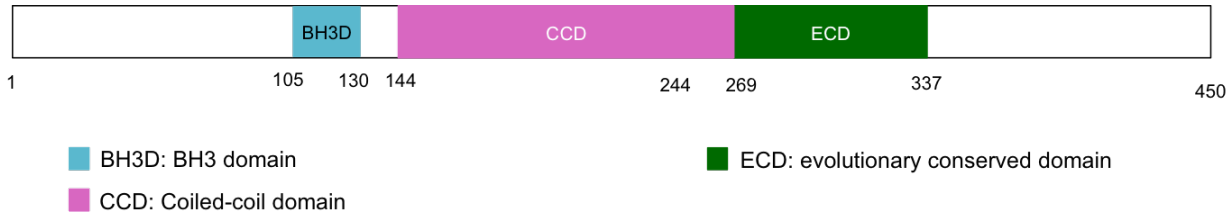

Figure 1.7. BECN1 domain architecture before 2010.
Each BECN1 domain with the labeled residue boundary is colored differently as shown in figure.

1.3.3.2.1. BH3D (Residues 105-130)

BECN1 contains a single BH3D (residues 105-130) (Figure 1.7, cyan box), which is required and sufficient for binding to the anti-apoptotic BCL2s (Feng, Huang et al. 2007, Oberstein, Jeffrey et al. 2007, Ku, Woo et al. 2008, Ku, Woo et al. 2008, Sinha, Colbert et al. 2008, Sinha and Levine 2009). Structural studies show that the BECN1 BH3D acts like a BH3-only pro-apoptotic protein to bind in the hydrophobic groove of anti-apoptotic BCL2 family proteins such as M11, the viral BCL2 homolog (Ku, Woo et al. 2008, Sinha, Colbert et al. 2008) and BCLXL, the cellular BCL2 homolog (Feng, Huang et al. 2007, Oberstein, Jeffrey et al. 2007). The results show that the BH3D forms a 4-turn helix in complex and M11 α2 adopts an extra turn in the BH3D-bound state (Figure 1.8) (Maiuri, Le Toumelin et al. 2007, Ku, Woo et al. 2008, Sinha, Colbert et al. 2008). This interaction prevents BECN1 from forming the PI3KC3 complex, inhibits the lipid-kinase activity of the PI3KC3 and prevents autophagosome nucleation. Although the BH3D has no invariant residue, it has some conserved residue equivalent to BECN1 L112, L116, G120, D121 and F123. Comparison of the complex structures reveals these residues have the most extensive interaction. Further cellular autophagy assays

show the disruption of the interaction between BECN1 BH3D and BCL2 proteins rescues autophagy induced by nutrient starvation (Sinha, Colbert et al. 2008). Additionally, some BH3D mimetic drugs are designed to interrupt the interaction between BECN1 and cellular BCL2 to stimulate autophagy (Maiuri, Criollo et al. 2007).

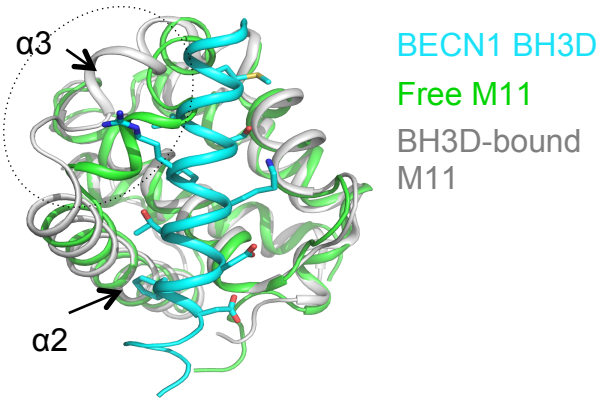

Figure 1.8. Superposition of the structures of the BECN1 BH3D: γ herpesvirus 68 BCL-2 homolog (M11) complex and Free M11.
M11 and the BECN1 BH3D are rendered as cartoon, with the free M11 (2ABO) colored green, BECN1 BH3D colored cyan and BH3D-bound M11 (3DVU) colored grey. The residues in the BH3D involved in binding M11 are shown in stick. α2-α3 loop and α2 that undergo conformational change upon BH3D binding are circled.

1.3.3.2.2. CCD (Residues 144-269)

BECN1 CCD (Figure 1.7, magenta box) was defined as ranging from residue 144 to 269 (Liang, Feng et al. 2006) and is sufficient for self-interaction in cells (Noble, Dong et al. 2008, Adi-Harel, Erlich et al. 2010). BECN1 homo-oligomers were detected in mammalian cells via Co-IP and immuno-blotting, even during starvation and rapamycin-induced autophagy (Adi-Harel, Erlich et al. 2010). Further, while *in vitro* isothermal titration calorimetry (ITC) studies indicate that UVRAG, which heterodimerizes via the BECN1 CCD, disrupts the BECN1 homodimer (Noble, Dong et al. 2008); overexpression of the UVRAG CCD in cell culture diminishes, but does not abolish homo-oligomerization (Noble, Dong et al. 2008, Adi-Harel,

Erlich et al. 2010). These studies suggest that the BECN1 CCD also functions as a homodimer; beyond forming heterodimers within PI3KC3 complexes.

Lastly, the CCD bears a leucine-rich nuclear export signal motif (NES, residues 180-190). Mutation of the Leu184 and Leu187 block the chromosomal maintenance protein 1 (CRM1)-dependent nuclear export of BECN1 as well as the autophagy and tumor suppressor functions in MCF7 cells (Liang, Yu et al. 2001).

1.3.3.2.3. ECD (Residues 244-337)

ECD contains most of the conserved residues in BECN1, including the C-terminal region of BECN1 CCD (Figure 1.7) and is required for autophagy regulation. Cellular autophagy and Co-IP assays show that knocking out ECD of the ectopically expressed BECN1 in MCF7 cells results in the failure of binding to PI3KC3/VPS34 and the low autophagy levels under starvation-induced condition (Furuya, Yu et al. 2005).

1.3.3.3. Current BECN1 Domain Architecture

During the course of my Ph.D. research, structural, biophysical and bioinformatics studies from our and other groups have provided a lot of information regarding BECN1 domain architecture. Based on these results, we delineate four structurally-distinct domains/regions in human BECN1 (Figure 1.9): (i) an IDR (residues 1-140) (Mei, Su et al. 2014, Lee, Perugini et al. 2016) including the functional BH3D (residues 105-130), (ii) a flexible helical domain (FHD, residues 141-171) (Mei, Ramanathan et al. 2016), also called coiled-coil 1 (CC1) (Rostislavleva, Soler et al. 2015), (iii) a CCD (residues 175-265) (Li, He et al. 2012, Mei, Su et al. 2016), and (iv) a BARAD (residues 266-450) (Huang, Choi et al. 2012, Noda, Kobayashi et al. 2012).

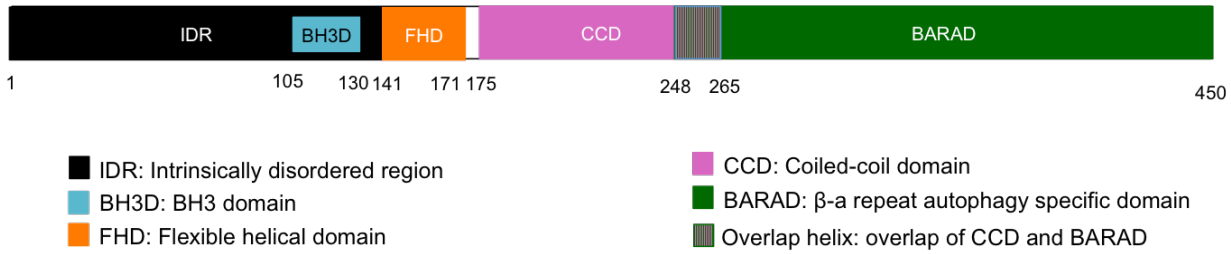

Figure 1.9. Current domain architecture of BECN1.
Each BECN1 domain with the labeled residue boundary is colored differently as shown in figure.

1.3.3.4. PTMs of BECN1

PTMs play important roles in regulating BECN1 interactions and function. PTMs of BECN1 and its interaction partners include phosphorylation to regulate catalytic activity and protein-protein interactions, ubiquitination to control signal degradation, and acetylation to impact gene expression and metabolism.

1.3.3.4.1. Phosphorylation

Phosphorylation is the most common BECN1 PTM (Table 2). The BECN1 IDR contains several phosphorylation sites required for starvation-induced activation of the PI3KC3 complex. BECN1 IDR phosphorylation affects binding and may result in conformational changes that impact autophagy or other cellular functions.

In *C. elegans*, BECN1 Ser14 (Ser15 in human) is phosphorylated by the Ser/Thr-protein kinase ULK1 involved in autophagy initiation. This phosphorylation is crucial for VPS34 activation during amino acid starvation-induced autophagy (Russell, Tian et al. 2013). Upon starvation, AMBRA1 also promotes association of AMPK and ULK1 to facilitate phosphorylation of AMPK at Thr172, and ULK1 at Ser317; which can then phosphorylate BECN1 at Ser14/Ser15, increasing PI3KC3 Complex I formation, PI3KC3 activation and autophagy (Russell, Tian et al. 2013, Shi, Wu et al. 2014). ATG14 and UVRAG also stimulate this phosphorylation by promoting BECN1 association with ULK1 (Russell, Tian et al. 2013).

This phosphorylation site is conserved from human to worm BECN1, highlighting its importance in PI3KC3 activation and autophagy induction.

Phosphorylation of BECN1 Ser90 by the MAPK p38 is required for starvation-induced autophagy and tumor suppression in MCF7 cells (Wei, An et al. 2015). BCL2 binding to the BECN1 BH3D prevents MAPK-mediated phosphorylation at Ser90, likely because steric conflicts prevent MAPK binding.

ATG14L-dependent phosphorylation of BECN1 at Ser93/Ser96 by AMPK enables BECN1 interaction with PI3KC3 and formation of pro-autophagic PI3KC3 complexes (Kim, Kim et al. 2013). Phosphorylation at these two sites, as well as at Ser15, is dependent on heterodimerization with either ATG14 or UVRAG. Drug-induced BECN1 phosphorylation at Ser93/Ser96 by AMPK causes AMPK:BECN1:caspase 8 complex formation, resulting in caspase-8 cleavage of BECN1 to down-regulate autophagy and up-regulate apoptosis (Song, Kim et al. 2014). Therefore, Ser93/Ser96 phosphorylation also cross-regulates autophagy and apoptosis.

MST1 phosphorylates BECN1 BH3D Thr108, enhancing BECN1 and BCL2/BCL2XL interaction, which stabilizes the BECN1 homodimer and significantly impairs BECN1 and ATG14/VPS34 interaction (Maejima, Kyoi et al. 2013). Thr119 within the BECN1 BH3D Anchor region is phosphorylated by Rho-associated protein kinase 1 (ROCK1) or DAPK upon starvation. However, this phosphorylation promotes BECN1:BCL2 complex dissociation. Inhibition of ROCK1 activity increases interaction between BECN1 and BCL2, down-regulating starvation-induced autophagy (Gurkar, Chu et al. 2013).

Within the BECN1 CCD, Ser234 and Ser295 are phosphorylated by AKT, enhancing BECN1 interaction with 14-3-3 and intermediate filament proteins, whose depletion increases

autophagy (Wang, Wei et al. 2012). Since intermediate filament proteins are markers of tumor initiation and progression, their interaction with 14-3-3 and BECN1 emphasizes the important regulatory role of autophagy in tumorigenesis inhibition (Altomare and Testa 2005).

Cellular assays demonstrate that the epidermal growth factor receptor (EGFR) tyrosine kinase binds and phosphorylates BECN1 at the CCD Tyr229, Tyr233 and BARAD Tyr352 to promote homodimer formation, while diminishing CoIP with PI3KC3, presumably due to decreased interaction with the VPS15 WD40 within PI3KC3 complexes (Wei, An et al. 2015). This inactivates the PI3KC3 kinase and suppresses autophagy.

Lastly, BECN1 phosphorylation also relates to other PTMs. BARAD Ser409 phosphorylation by CK1 is required for BECN1 acetylation at Lys430 and Lys437 by p300 (Sun, Li et al. 2015). BECN1 phosphorylation at Tyr352 is important for neural precursor cell expressed developmentally down-regulated protein 4 (NEDD4) binding, which ubiquitinates BECN1 (Xu, Duong et al. 2009, Platta, Abrahamsen et al. 2012).

1.3.3.4.2. Acetylation

Acetylation involves the attachment of an acetyl group, normally at the N-terminus of a protein. BECN1 is acetylated by p300, a lysine acetyltransferase, at Lys430 and Lys437 and is deacetylated by sirtuin 1 (Sun, Li et al. 2015). Lys430 and Lys437 acetylation promotes the recruitment of Run domain Beclin 1-interacting and cysteine-rich domain-containing protein (RUBICON) to the UVRAG:BECN1 complex to inhibit autophagosome maturation and endocytic trafficking.

1.3.3.4.3. Ubiquitination

BECN1 undergoes K11-, K63- and K48-linked ubiquitination. K63-linked ubiquitination of BECN1 BH3D K117 by TRAF6 E3 ligase promotes binding to the PI3KC3 complex rather than to BCL2 proteins, to induce autophagy; and is crucial for TLR4-triggered autophagy in

macrophages (Shi and Kehrl 2010). Similarly, K63-linked ubiquitination of BARAD Lys437 by the AMBRA1-DDB1-Cul4-Rbx1 E3 ligase augments PI3KC3 activity to induce autophagy (Xia, Wang et al. 2013). NEDD4 ubiquitinates BECN1 with K11-linked polyubiquitin chains to increase proteasomal degradation of BECN1 (Xu, Duong et al. 2009, Platta, Abrahamsen et al. 2012). This degradation is greatly enhanced upon PI3KC3 knock-down in cells, suggesting that association within the PI3KC3 complex protects BECN1 from degradation (Platta, Abrahamsen et al. 2012). BECN1 is the first tumor suppressor shown to be regulated by K11-linked polyubiquitination, although the BECN1 ubiquitination site is unidentified. In addition to binding BECN1 within the PI3KC3 complex, AMBRA1 also triggers polyubiquitination and BECN1 stabilization during autophagy(Xia, Wang et al. 2013).

Table 1.2. Post-translational modification of BECN1.

Modification type	Site	Enzyme	Effect on autophagy	Reference
Phosphorylation	S14	ULK1	Activate PI3KC3/VPS34	(Russell, Tian et al. 2013)
	S90	p38	Activate PI3KC3/VPS34 in starvation condition	(Wei, An et al. 2015)
	S93, S96	AMPK	Activate PI3KC3/VPS34 in starvation condition, play role crosstalk between apoptosis and autophagy	(Kim, Kim et al. 2013),
	T108	MST1	Enhance BCL2 and BH3D interaction, stabilize BECN1 homodimer and impair PI3KC3/VPS34 activity	(Maejima, Kyoi et al. 2013)
	T119	DAPK	Dissociate from BCL-XL to activate autophagy	(Zalckvar, Berissi et al. 2009, Zalckvar, Berissi et al. 2009)
	Y229, Y233, Y352	EGFR	Promote BECN1 homodimer formation to inhibit autophagy	(Wei, An et al. 2015), (Wei, Zou et al. 2013)
	S234, S295	AKT	Increase interaction between BECN and 14-3-3 to inhibit autophagy	(Wang, Wei et al. 2012)

Table 1.2. Post-translational modification of BECN1 (continued).

Modification type	Site	Enzyme	Effect on autophagy	Reference
Phosphorylation	S409	CK1	Important for p300 binding to acetylate BECN1	(Sun, Li et al. 2015)
Acetylation	K430, K437	p300	Decrease autophagosome maturation	(Xia, Wang et al. 2013)
Ubiquitination	K117	TRAF6 E3 ligase	TRL4 triggered autophagy	(Shi and Kehrl 2010)
	K437	K63-linked ubiquitination	Increase activity of PI3KC3	(Sun, Li et al. 2015)

1.4. Methods to Investigate Protein Structures and Interactions

1.4.1. Structural Biology Methods

Different biophysics methods can be used to investigate protein folding and characterize the three-dimentional molecular structure of proteins.

1.4.1.1. Circular Dichroism (CD) Spectroscopy

CD spectroscopy is an excellent method to evaluate secondary structure content (Figure 1.10), folding and binding properties of proteins (Johnson 1990). It measures the difference in absorption between left- and right-handed circularly polarized light. Different secondary structure elements show different CD spectrum characteristics due to the optical transitions of their backbone chromophores shifting or splitting differently upon 'exciton' interaction. The secondary structure content of the protein is determined from the CD spectra curves recorded between 195 nm and 250 nm: α-helices have a positive transition at 193nm and two negative bands at 208nm and 222nm; β-strands normally show a positive peak at 195 nm and a negative

transition at 218 nm; and the disordered random coil has a negative band near 195 nm and ellipticity around 0 above 210 nm (Greenfield 2006). The development of data analysis programs such as the CDpro suite (Sreerama and Woody 1993, Sreerama, Venyaminov et al. 1999) or K2D2 program (Perez-Iratxeta and Andrade-Navarro 2008) makes analysis of the secondary structure content quite easy and fast.

The near UV (250-350nm) spectral region provides information about certain tertiary structure characteristics such as disulfide bonds. It is also sensitive to the conformational changes upon protein-protein interactions (Greenfield 2006). CD spectroscopy can also be used to measure the thermal stability of the protein by assessing the changes in spectrum with the increasing temperature. One advantage to CD spectroscopy is the small amounts of protein necessary for this method. However, a disadvantage is a buffer without optical activity is needed for obtaining clear CD spectra.

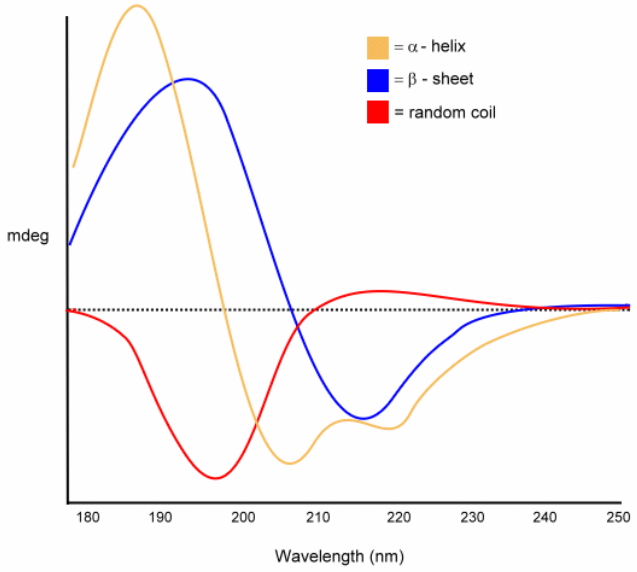

Figure 1.10. CD spectra curves presenting three secondary structural elements. An α-helical protein (yellow curve) have negative bands at 222 nm and 208 nm and a positive band at 193 nm. Proteins with well-defined antiparallel β-pleated sheets (blue curve) have negative bands at 218 nm and positive bands at 195 nm, while disordered proteins (red curve) have very low ellipticity above 210 nm and negative bands near 195 nm (Greenfield 2006). This image is adapted from http://www.proteinchemist.com/cd/cdspec.html.

1.4.1.2. X-ray Crystallography

The function of a protein can often be deduced from its 3 dimensional structure. X-ray crystallography is one of the most powerful biophysical methods to determine three-dimensional structures of proteins in atomic detail, which, in turn, facilitates the better understanding of their functions.

The birth of X-ray crystallography was marked by the discoveries of Marx von Laue, William Henry and William Lawrence Bragg, who were awarded Nobel prizes in 1914 and 1915. Max von Laue showed an X-ray diffraction pattern from crystals in 1912 and William Lawrence Bragg derived a general equation, known as the Bragg's Law (Equation 1) to describe the founding principle of images formed by X-ray diffraction.

$$n\lambda = 2dsin\theta \quad (1)$$

where λ is the wavelength, θ is the angle between incident rays and the surface of the crystals, and d is the distance between lays of atoms.

The Ewald construction is used to describe the reciprocal lattice of the diffraction spots with the crystal placing the in the sphere ($r=1/\lambda$) center. The origin of the reciprocal lattice is on the sphere, when the reciprocal lattice points (identified by their Miller indices) intersect the surface of Ewald sphere, the Bragg's law is satisfied and lead to a reflection. For any particular orientation, not all reflections will show on the Ewald sphere surface. The number depends on the unit-cell dimensions of the crystal. Only crystals with larger unit-cell dimensions than the wavelength of the radiation have reflections on the surface of Ewald sphere. The resulting reciprocal lattice spots of each crystal plane are recorded in the lunes formed from intersecting ellipses when the crystal is rotated. Crystals with large unit-cell dimensions will produce more lunes. The width of the lune is proportional to the rotation range per exposure. The diffraction

spots within each lune represent the regularity of the reciprocal lattice. And due to the rotation, the circles of the Ewald sphere would be distorted as a consequence on a flat detector surface. The degree of distortion depends on the diffraction angle.

Nowadays, the standard process of X-ray crystallographic structure determination consists of growing diffraction-quality crystals, recording diffraction data, processing data including indexing, integration and scaling, solving phases, and model building and refinement (Smyth and Martin 2000) (Figure 1.11).

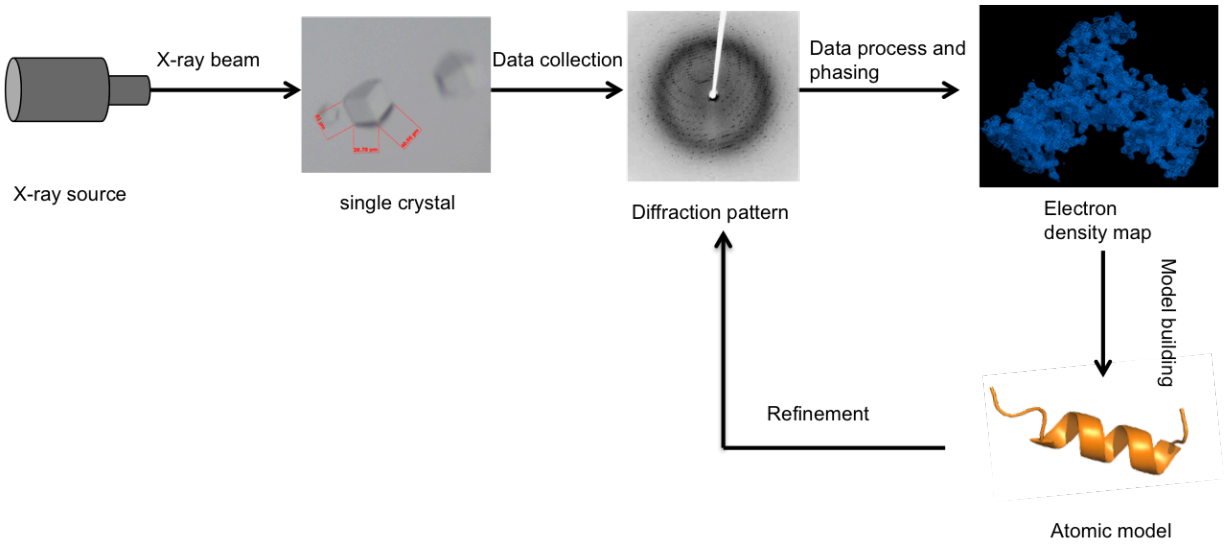

Figure 1.11. Schematic representation of X-ray crystallography in determining the atomic structure of a protein crystal.
A crystal is exposed in an intense X-ray beam of a single wavelength, producing a series of diffraction images containing structural information of the protein. The space group and unit cell are indexed and the electron density map is obtained after the phase is solved. The atomic model is built based on the electron density map and further refined to fit to the observed diffraction data.

The most important thing before growing a crystal is to get the pure and homogeneous protein. To obtain a crystal with good diffraction properties is a vital step to successfully determine the final atomic structure. Crystal growing is a complicated and time-consuming process. Under different solution conditions, all molecules have a solubility curve that can be divided into three regions: under saturated or soluble region, where the molecules are soluble in

solution; precipitation region, where the molecules form nonspecific interactions and are no longer soluble; and the supersaturation region, where the molecules are soluble, but may form ordered interactions (crystals) and come out of solution. The crystallization process has three stages: nucleation, crystal growth and cessation of growth. These stages take place within the supersaturation region of the solubility curve. In the supersaturated region, there is a nucleation zone and a metastable zone. Crystals form when the molecules are within the nucleation zone and continue to grow as they pass through the metastable zone. Since the physical and chemical properties of every protein are different, one protein crystallization solution does not apply to others. Important variables often needed to identify crystallization conditions include some common reagents such as precipitants, buffer and salts. Temperature is also an important parameter to modify (Dessau and Modis 2011).

The next step is data collection, the last experimental step in X-ray crystallography. X-rays of a suitable wavelength (0.5-2.5Å) for protein crystallography are normally generated by X-ray tubes, rotating anodes and synchrotrons. One of the important advantages of synchrotron radiation is its tunable wavelength, where a narrow wavelength distribution can be selected. This allows the experimenter to take advantage of anomalous scattering from certain atoms, making it possible for the single- or multiple-wavelength anomalous dispersion (SAD or MAD) experiments.

When the crystal is properly mounted, which is normally performed by robots in synchrotron nowadays, and exposed to the intense and monochromated X-ray beam, the diffraction pattern can be recorded on a detector as electric charges. These detectors include charge-coupled devices (CCDs) and complementary metal oxide semiconductor (CMOS) sensors. The collected X-ray diffraction data contain the information of position and intensity of

the reflection. The most important aim in X-ray data collection strategy is to collect a dataset with high completeness and a high signal to noise ratio. The completeness of the indices relies on the geometry of crystal lattice and the detector setup. To get as many diffraction points as possible, the most commonly used approach is to rotate the crystal. The rotation angle range is also related to the symmetry of the crystal, with high symmetry, a small rotation angle range may be recorded. To avoid the 'blind spot' in reciprocal lattice, the rotation axis should not align with a symmetry axis. A good data collection strategy should also consider the sample-to-detector distance. The detector should be placed at the maximum distance without reducing the capacity to capture high-resolution data, because increasing the distance can decrease the background scatter. The best way to increase the diffraction signal is to grow a large crystal. Additionally, increasing the exposure time without causing serious radiation damages by using cryopreservation can also be used to improve signal.

After the data has been collected, the data processing procedures including: indexing, integration, merging if multiple datasets used, and scaling will be conducted. Indexing is the process of determining the space group and unit cell dimensions from the reflection positions. Integration determines and saves the reflection intensity value and its error. Scaling combines the integrated intensities from different images recorded into one set of structure factor intensities, normalizes them and calculates the symmetry-related R-factor. A lot of software such as HKL2000/3000 (Otwinowski and Minor 1997), Mosflm (Battye, Kontogiannis et al. 2011), and XDS (Kabsch 1988) have been developed to perform this process and to transfer the collected diffraction data from spots to numbers, providing information of the collected data quality as well as the space group and unit cell parameters.

The structure factor amplitudes ($|F_{hkl}|$), determined from the intensities, and phases (α_{hkl}), which are unknown from the diffraction pattern, are used to calculate an electron density map that allows building a starting model of the protein. The equation for electron density at position (xyz) (Equation 2) is therefore defined as:

$$\rho_{(xyz)} = \frac{1}{V}\sum_{hkl}\left|F_{(hkl)}\right| cos2\pi[hx + ky + lz - \alpha_{(hkl)}] \quad (2)$$

The intensity (I_{hkl}) of each diffraction spot is recorded and proportional to square of structure factor amplitude ($|F_{hkl}|$) (Equation 3):

$$I_{(hkl)} = |F_{(hkl)}|^2 KALp \quad (3)$$

in which, K is a scale factor, A is the absorption factor, L is the Lorentz factor, and p is the polarization factor; The structure factor F function (Equation 4) defines the ordered atomic contents of the unit cell

$$F_{(hkl)} = \sum_{j=1}^{atoms} f_{(j)} \exp\left[2\pi \cdot i\left(hx_{(j)} + ky_{(j)} + lz_{(j)}\right)\right]$$

$$= \sum_{j=1}^{atoms} f_{(j)} \exp\left[i(\alpha_{(hkl)})\right] \quad (4)$$

in which, $f_{(j)}$ is the scattering factor of atom j.

Phasing is the next important but most difficult problem. For macromolecules like protein, several phasing methods have been developed: molecular replacement (MR), single- or multiple-isomorphous replacement (SIR/MIR), SAD/MAD, or combination of different methods.

MR (Taylor 2010) is a phasing method that uses a search model with the known structure to solve the unknown crystal structure of a related or homologous molecule. The main restriction on the use of MR is the requirement for a suitable search model. In most cases of the successful MR, a good search model shares at least 35% sequence identity with the target, which corresponds to a C_α RMSD of about 1.5Å (Abergel 2013). In this method, Patterson function

(Equation 5) is used to calculate an interatomic vector map that can be directly calculated from the experimental diffraction intensities by Fourier transformation of squared structure factor amplitude (|F|2) with phases set to zero. Then another map of the known homolog model can be calculated using Patterson function. After comparing the Patterson map of the unknown structure to the Patterson map of the homolog structure, the Patterson map of the known homolog model is reoriented to obtain a similar orientation as the Patterson map of the unknown structure. Then the translation will be applied to obtain the correct co-ordinates within the asymmetric unit. This will result in a new Patterson map of orientation and translation within the unit cell, correlated to the Patterson map of unknown structure. Therefore, the aim of MR method is to find operators of orientation and translation to determine phase information of the electron density map.

$$P_{(xyz)} = \frac{1}{V}\sum_{hkl} |F_{(hkl)}|^2 \exp\left[-2\pi \cdot i(hx + ky + lz)\right] \quad (5)$$

in which, *(xyz)* is the coordinates of the atom in crystal, *V* is the volume of the unit cell.

SIR/MIR is an experimental phasing method, in which one (SIR) or at least two (MIR) heavy atom is reacted with the protein, usually by soaking crystals in a dilute solution, the diffraction pattern of this modified crystal is then compared to difference of to diffraction of the native crystal. The heavy atoms in the crystal cause changes in the diffraction pattern related to their positions with the crystal. These changes in the diffraction pattern are then used to obtain the locations of the heavy atoms and initial phases for all atoms in the crystal (Taylor 2010). The structure factors of heavy-atom derivative (F_{PH}), native protein (F_P) and heavy atom (F_H) have the following relationship:

$$F_{PH} = F_P + F_H = |F_P|\exp(i\alpha_P) + |F_H|\exp(i\alpha_H) \quad (6)$$

in which, α_P and α_H are the phases for native protein and heavy-atom model, respectively.

If the structure factor amplitudes ($|F_{PH}|$) and ($|F_P|$) are measured experimentally, ($|F_H|$) and phase angle are obtained from heavy-atom model, only one heavy-atom derivative (SIR) gives two possible solutions for phase of (F_P). One of these is the true solution. When a second heavy-atom is used (MIR), another derivative (F_{PH2}) with a different position is obtained, then a unique solution can be obtained. However, non-isomorphism is normally inevitable in reality. The 'phase probability' concept (Blow and Crick 1959) was introduced to assume all the errors only exist in the reflection amplitude of heavy-atom derivative ($|F_{PH}|$) and follow a Gaussian distribution, then the phase-probability distribution could be determined (Taylor 2010).

SAD/MAD (Taylor 2010) is another experimental phasing method, in which anomalous diffraction is recorded at single (SAD) or multiple (MAD) X-ray wavelengths to obtain the information about the atomic position of specific atoms. Two factors affect the atomic scattering (Equation 7): Bragg angle that determines the normal scattering term (f^0) and wavelength that determines the dispersive term (f') and absorption term (f''), representing the anomalous scattering that occurs at the absorption edge when the X-ray photon energy is sufficient to promote an electron from an inner shell.

$$f(\lambda) = f^0 + f'(\lambda) + if''(\lambda) \tag{7}$$

The dispersive term (f') modifies the normal scattering factor, whereas the absorption term (f'') is 90° advanced in phase. The presence of an anomalous scatterer gives rise to differences in the diffraction intensities that can be used to locate the anomalous scatterers. Some heavy or special atoms such as sulfur can be used in this method to provide anomalous scattering for phase determination. Once the heavy-atom sub-structure is known, the calculated structure factor amplitude and phase of this contribution can be calculated. In MAD, data are usually collected at three wavelengths to maximize the absorption and dispersive effects. Typically, wavelengths are

chosen at the absorption (f'') peak (λ1); at the point of inflection on the absorption curve (λ2), where the dispersive term (f') (which is the derivative of the (f'') curve has its minimum; and at a remote wavelength (λ3) to maximize the dispersive difference to (λ2). Whereas, in the SAD, data is only collected at (λ1) to estimate the contribution to the anomalous scattering of the heavy or special atom and to enable the determination positions of the anomalous scattering atoms (Taylor 2010).

In SAD/MAD, the anomalous scattering atoms can be treated like the heavy atoms in SIR/MIR. Similar to the SIR/MIR, the total scattering structure factor (F_{PA}) is contributed by the structure factor of normal scattering atoms (F_P) and of anomalous scattering atoms (F_A). Therefore, (F_{PA}) can be calculated using the equation similar to Equation 6.

$$F_{PA} = F_P + F_A = |F_P|\exp(i\alpha_P) + |F_A|\exp(i\alpha_A) \quad (8)$$

Then combining Equation 7 with Equation 8, it becomes Equation 9 and 10 for the Friedel-related pair of reflections:

$$|F_{PA}(+)|^2 = |F_{PA}|^2 + a|F_A^{''}|^2 + b|F_{PA}||F_A^{''}|\cos(\Delta\alpha) + c|F_{PA}||F_A^{''}|\sin(\Delta\alpha) \quad (9)$$

$$|F_{PA}(-)|^2 = |F_{PA}|^2 + a|F_A^{''}|^2 + b|F_{PA}||F_A^{''}|\cos(\Delta\alpha) - c|F_{PA}||F_A^{''}|\sin(\Delta\alpha) \quad (10)$$

in which, $a=(f'^2+f''^2)/f^{02}$, $b=2f'/f^0$, $c=2f''/f^0$, and ($\Delta\alpha$) is the difference in phase between native and anomalous scattering components. If the data is collected at more than two wavelengths (MAD), the (F_{PA}), (F_A), and ($\Delta\alpha$) can be determined.

During anomalous scattering, Friedel's law is broken: $|F(hkl)| \neq |F(-h-k-l)|$, therefore the difference caused by anomalous scattering is given in Equation 11:

$$|F_{PA}(+)|^2 - |F_{PA}(-)|^2 = 2c|F_{PA}||F_A^{''}|\sin(\Delta\alpha) \quad (11)$$

If we assume that structure factor amplitude $|F_{PA}|$ is:

$$|F_{PA}| = 1/2[|F_{PA}(+)| + |F_{PA}(-)|] \quad (12)$$

Then Equation 11 changes to Equation 13:

$$|F_{PA}(+)| - |F_{PA}(-)| = c|F_A^{"}|\sin(\Delta\alpha) \quad (13)$$

So the data collected using one wavelength (SAD) is sufficient to find the heavy atom and solve the phase.

Sulfur (S)-SAD allows using the S atom from native proteins to determine the protein structure without growing the selenomethionine substitutes. As the widely presence of the Met and Cys with S atom in protein, this method is commonly used. Since the absorption edge of sulfur is about 5Å, shorter wavelength ranging from 1.5-2.5Å is needed to collect the data. Also sulfur is a weak scatter, highly redundant data are needed for a high signal to noise data. This problem could be overcome by recording multiple isomorphorous crystals (Liu, Liu et al. 2013).

The phasing programs such as SHELXC/D/E (Nanao, Sheldrick et al. 2005) and Phaser (McCoy, Grosse-Kunstleve et al. 2007) are commonly used in determining initial electron density maps (Hauptman 1991, Taylor 2010). A well-defined electron density map reveals the atoms in the structured portion of the protein while the unstructured or disordered regions always produce poor or no electron density. A model is then constructed in a process called 'model building' or 'map interpretation' by placing atoms into the electron density map. In the MR case, it is quite straightforward since a coordinates for backbone atoms are already there to work with. During experimental phasing, the heavy atoms present in the electron density are located first, there are no peptide backbone atoms defined. Some automated model-building software such as AutoSol (Adams, Afonine et al. 2010), Buccaneer (Cowtan 2006), etc. are easily accessible and very powerful. However, using an automated program tends to have some misinterpretation, the researcher will then need to manually make the changes to the model in Coot (Emsley, Lohkamp et al. 2010), a commonly used program for manual building. Based on the map resolution, the

backbone register needs to then be set if possible. Then the sidechain details and other unit cell contents are fixed later, during several runs of refinement, which improves phases and maps.

Refinement adjusts the model coordinates to fit the diffraction data better. In this process, an R-factor (Equation 14), typically referred to as R-work, is used to indicate how well the model agrees with the diffraction data:

$$R = \frac{\sum ||F_{obs}| - |F_{cal}||}{\sum |F_{obs}|} \tag{14}$$

in which, ($|F_{obs}|$) is structure factor amplitude observed from the experimental data, ($|F_{cal}|$) is the structure factor amplitude calculated from model.

A subset of the diffraction data (normally 5%) serves as a validation set and is excluded from the refinement to avoid the false impression of having a good model in 'R-work' from over fitting the model. This is called the free R factor (R-free) (Brunger 1992). Both R-work and R-free are calculated in refinement and a decent gap between them is about 5%. During refinement, the bond distance, angles and torsions and B-factor (temperature factor) are also restrained to a proper value. A few different programs are available for the refinement step, such as Refmac (Murshudov, Vagin et al. 1997), Phenix.refine (Adams, Afonine et al. 2010), to name two.

Currently, some program suites package programs dealing with all aspects of computational crystallography, including data processing, phasing, model building, refinement and model validation, are available. Collaborative Computing Project 4 (CCP4) (Winn, Ballard et al. 2011) was created in 1979. The CCP4 software suite is a collection of programs created by structural biology researchers for various stages of the X-ray structure determination process. Now, CCP4 has incorporated more than 250 programs. Phenix (Adams, Afonine et al. 2010) is another software suite. Phenix utilizes consistent programming languages and conventions to establish the standard structural workflows. These programs save the effects and shorten the time

for users to process, validate X-ray diffraction data and solve the atomic structures of proteins. With the increase of X-ray crystallography structure data, several databases have been developed: Cambridge Structural Data Base (CSD, http://www.ccdc.cam.ac.uk), Protein Data Bank (PDB, http://www.rcsb.org/pdb/home/hoe.do), Biological Macromolecule Crystallization Database (BMCD, http://xpdb.nist.gov:8060/BMCD4/index.faces), etc.

The advantage of X-ray crystallography is that it can provide high-resolution atomic information with no size restriction on proteins. Once sufficient quality diffraction data are obtained, the structure determination process by computational methods is quite straightforward. But X-ray crystallography requires large quantities of pure and homogenous protein, which is often difficult to generate. In addition, it is tricky, tedious and time-consuming work to grow crystals that yield good X-ray diffraction data.

1.4.1.3. Small-angle X-ray scattering (SAXS)

In addition to X-ray crystallography, SAXS is also a powerful tool to study biological macromolecules. In X-ray crystallography, the electrons from the regularly positioned and oriented atoms in the crystal diffract X-rays to yield diffraction peaks being used in 3D reconstruction. Whereas in SAXS, diffraction peaks are not observed since the molecules in solution are randomly positioned and oriented. The basic principle of SAXS is to scatter X-ray photons elastically off molecules in solution and record the scattering intensity as a function of the scattering angle (2θ) (Putnam, Hammel et al. 2007). It is a complement to X-ray crystallography. In the absence of crystals, SAXS may provide low-resolution structural information on the overall shape, conformation and assembly state of proteins from the 1D solution X-ray scattering profiles. Therefore, SAXS allows the study of the structure of native particles in solution environments. SAXS also has the ability to analyze changes in these

parameters in response to variations in external conditions, such as perturbations in pH, temperature, salt concentration, ligands etc.

Like X-ray crystallography, the first and most important step of SAXS is to get the pure and homogeneous protein. The protein concentration required for SAXS experiment is proportional to the protein size. For proteins of a size comparable to lysozyme (14.3 kDa), a concentration of 2 mg/ml can give reasonably good data quality. SAXS can be used to examine proteins with molecular weight (MW) from 5KD to 100MD. Higher concentrations with no aggregation will give better data quality. Sample is loaded either directly into the quartz capillary in static SAXS or onto a size exclusion chromatography (SEC) column in SEC-SAXS. In a SAXS experiment (Figure 1.12), a monochromatic X-ray beam illuminates the protein solution in the quatz capillary, and the intensity of the scattered X-rays at a very small angle is recorded by an X-ray detector. The scattering pattern of the buffer is also recorded and subtracted from the sample solution scattering. The subtracted intensity is the signal from the macromolecules of interest. Due to the random orientations of the molecules in protein solution, the scattering pattern is isotropic, and thus, the scattering pattern recorded can be radially averaged. The scattering intensity I is represented as a function of momentum transfer $(q)($Equation 15):

$$q = 4\pi \sin\theta/\lambda \tag{15}$$

in which λ is the beam wavelength and 2θ is the scattering angle and plotted as radially averaged one-dimensional curves $I(q)$ (Figure 1.12) (Kikhney and Svergun 2015). From this scattering pattern, a modest resolution envelope of 1-10 nm resolution can be obtained to provide the shape and size of the protein.

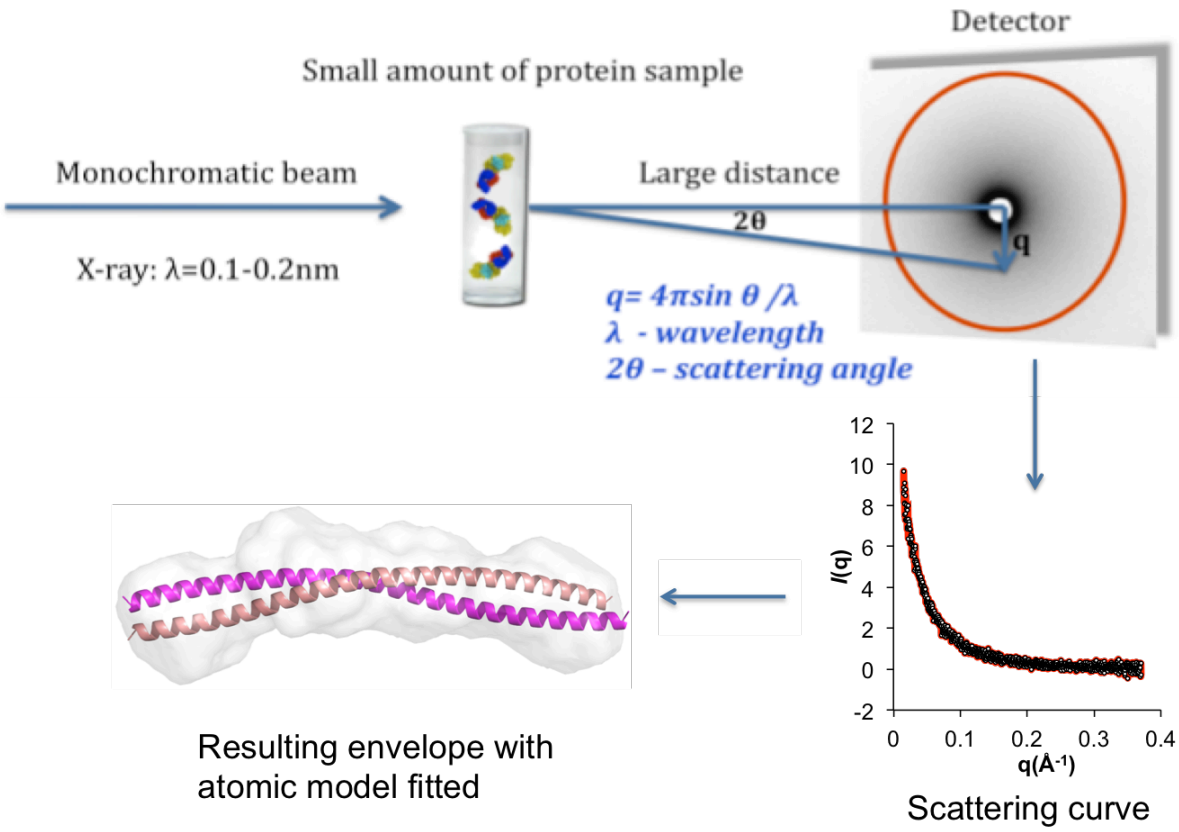

Figure 1.12. Schematic represntation of small angle X-ray scattering experiment. In small angle X-ray scattering (SAXS) experiments, a sample with inhomogeneities is illuminated by X-rays and the scattered radiation is registered by a detector. The SAXS measurement is done at a very small angle. The scattering pattern of the pure solvent is collected as well and subtracted from the sample solution scattering leaving only the signal from the particles of interest. Due to the random orientations of the particles in solution the scattering pattern is isotropic, and thus, the scattering pattern recorded usually by a two-dimensional detector can be radially averaged. The resulting scattering pattern is related to the overall shape and size of the particles under investigation. Then the high resolution atomic structure of the molecule can be fitted to the resulting envelope. Part of the images adapted from https://www.rbvi.ucsf.edu/Research/projects/sali/.

For monodisperse systems with non-interacting identical particles, the background-corrected intensity is proportional to the scattering from a single particle averaged over all orientations. The radius of gyration (R_g) and the forward scattering I(0) are determined by the Guinier formula (Svergun 1992, Konarev, Volkov et al. 2003) . The plot should be linear with q $\times$Rg < 1.3 for pure monodisperse sample, whereby the slope of the line gives R_g, and its intersection with the ordinate provides the forward scattering intensity. R_g is a model-free

characterization of the molecular size and I(0) is proportional to the molecular weight. GNOM (Svergun 1992) programmed by Svergun can be used to obtain max intramolecular distance (D_{max}) from the pairwise distribution function P(r) based on an indirect Fourier transform of the scattering profile. In addition, molecular weight can be calculated directly from the particle volume derived from the experimental scattering pattern. The folding state of the proteins can be derived from the SAXS profile using a Kratky plot. In this plot, the well-folded proteins show a peak at low angles whereas the unfolded proteins display no peak but a slightly increase at high q region instead. In the case of the flexible proteins, the Kratky plot also shows a peak as folded globular proteins.

Due to the angular orientation and lack of phase information, it is not possible to get a unique 3D model from 1D scattering profile. However, a bead-model representing the average shape of the macromolecules can be calculated. The introduction of automatic beads modeling makes the more detailed *ab* initio modeling possible. The most popular *ab* initio program based on this approach is DAMMIN (Svergun 1999). In this program, each bead can be assigned either to solvent or to a protein, and the configuration of the ensemble is represented as a binary string of length M (the total number of beads). At each step, one bead of the model is changed, the theoretical scattering pattern is computed using spherical harmonics, and the discrepancy between the scattering from the bead model and the experimental pattern is calculated. MONSA (Svergun 1999) applied a multiphase version of this bead-modeling algorithm. The beads can also be assigned to different phases such as different proteins in a protein complex. DAMMIF (Franke and Svergun 2009) is a faster version of DAMMIN (Svergun 1999). Another *ab* initio program GASBOR (Svergun, Petoukhov et al. 2001) uses dummy residues having the scattering density of an average amino acid residue in water, instead of densely packed beads. The

assumption of homogeneous density is not required in this method and the scattering data can be fitted up to higher scattering angles ($10nm^{-1}$). After this DAMAVER (Volkov and Svergun 2003) can be applied to construct an averaged shape, keeping the most persistent features, reducing the ambiguity of the reconstruction. CRYSOL (Svergun, Barberato et al. 1995) is a fast and efficient program to calculate scattering patterns from atomic models. The rigid body modeling program SASREF (Petoukhov and Svergun 2005) allows construction of complex or multi-domain structures using simulated annealing for simultaneous fitting of multiple SAXS curves. If the atomic model is known, SUPCOMB (Kozin and Svergun 2001) can be used to align the SAXS shape with the high resolution atomic structures. Svergun and coworkers have created tools to model molecular complexes from SAXS data if the structures of the individual components are (partially) known from higher resolution experiments (Blanchet and Svergun 2013).

In flexible systems or polydisperse systems, the solution contains different types of particles (Svergun 1992, Konarev, Volkov et al. 2003). Contrary to monodisperse systems, the measured intensity is no longer related to the scattering from a single particle. Instead, each individual protein structure presented in the investigated sample adds to the scattering pattern, resulting in an averaged intensity. The worst case of a polydisperse system in practical application is unspecific aggregation. Such samples are not appropriate for SAXS analysis.

1.4.2. Methods to Investigate Protein-Protein Interaction

Many biochemical and biophysical methods have been developed to investigate the protein-protein interaction *in vivo* or *in vitro*. Here, I mainly discuss the methods used in my projects.

1.4.2.1. Co-IP

Co-IP is a commonly used method to detect protein-protein interactions *in vitro*. In Co-IP, protein interactions are detected under non-denaturing conditions. It is similar in principle to the immunoprecipitation technique, in which the antigen is precipitated by an antibody that recognizes it specifically. The protein with no epitope identified by the antibody only precipitates together with the antigen if there is a native interaction between the antigen and the protein. Co-IP consists of five major steps: preparing the cell lysate containing the protein mixture, coupling antibodies to Sepharose beads, incubating the protein mixture with antibody-coupled beads, washing off unbound proteins and eluting the bounded protein complex, and analyzing by SDS-PAGE followed by western blot detection using the specific antibody to target protein (Figure 1.13) (Lee 2007, Lee, Ryu et al. 2013).

The lysis buffer is a key factor in maintaining complex formation throughout all the steps. The lysis buffer used for Co-IP is relatively mild to avoid interfering with antibody-antigen binding. Low ionic strength (<150mM NaCl) and some non-ionic detergents, such as NP-40 and Triton X-100 that do not disrupt protein-protein interaction in cell lysate, are normally used in the lysis buffer. Samples should be handled gently and sonication or vortexing of the sample should be avoided. Protease inhibitors are often used to prevent proteolysis.

Another issue in Co-IP is contamination from the antibody heavy (50KD) and light (25KD) chain in SDS -PAGE gel. These polypeptides can obscure target proteins of similar molecular weights. This problem can be circumvented by using the HRP-conjugated primary antibody or a secondary antibody that specifically recognizes native primary antibody in Western blotting.

However, Co−IP does not eliminate the possibility that a third intermediary protein might be involved in the protein-protein interaction.

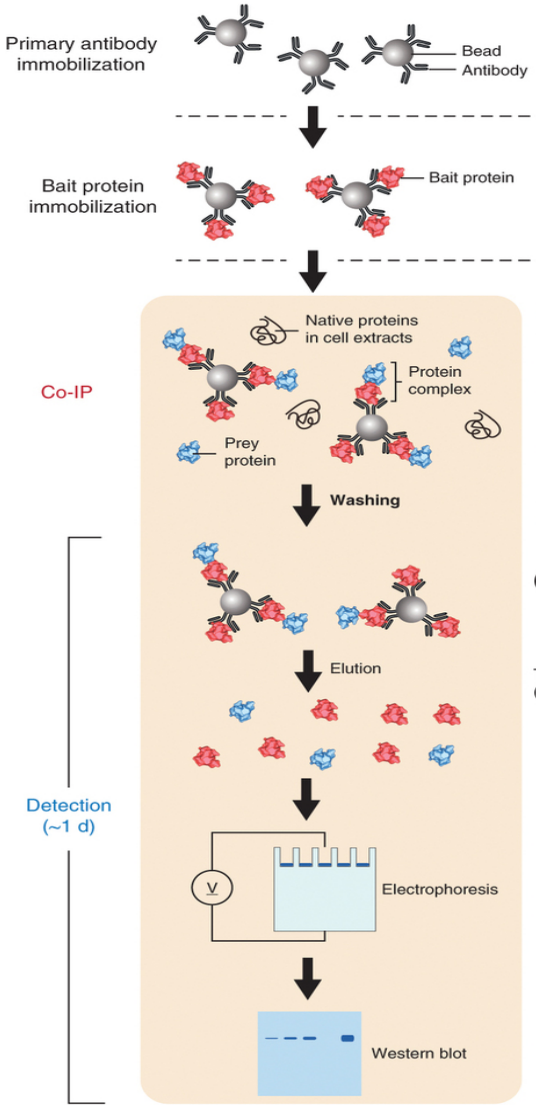

Figure 1.13. Schematic graph showing the co-immunoprecipitation procedures.
Five major steps of Co-IP consisting of cell lysate harvesting, beads incubation, antibody binding, eluting and SDS-PAGE analysis combined with western blotting (Lee, Ryu et al. 2013).

1.4.2.2. Pull-down Assay

Pull-down assay is another important method to determine the physical interaction between two or more proteins *in vitro*. It is similar to immunoprecipitation, but a 'bait' protein is

used instead of antibody. It is a form of affinity chromatography in which the 'bait' protein is tagged and captured by the immobilized affinity resin specific for the tag. Then the 'prey' protein in cell lysate will bind this 'bait' protein and then be eluted with the 'bait' protein if a protein-protein complex is formed. Pull-down assays can confirm suspected interactions by directly detect the interaction between two proteins using purified proteins. However, a disadvantage is that some proteins are not easily expressed and purified.

1.4.2.3. ITC

ITC is considered to be one of the most quantitative techniques available for measuring the thermodynamic properties of protein-protein interactions. In a microcalorimeter, there are two cells (Figure 1.14A): one reference cell filled with water or buffer and one sample cell filled with protein sample. The potential binding partner is titrated into the sample cell from a syringe to produce heat changes that are compensated by heaters to maintain the two cells at the same temperature during the binding process. The molar concentration of sample in the syringe is normally 10 times higher than the protein in cell. Ideally, injection of the syringe sample into the cell sample continually increases the molar ratio of the syringe protein to the cell protein until the protein in the sample cell is saturated and no heat change detected (Figure 1.14B). In this process, the heat produced in the titration process is measured by the calorimeter to determine the thermodynamic parameters of the molecular interaction, including binding constants (K_d), reaction stoichiometry (n), and enthalpy (ΔH) (Figure 1.14C) (Pierce, Raman et al. 1999, Velazquez-Campoy, Leavitt et al. 2004). Gibb's free energy (ΔG) and entropy (ΔS) are also calculated (Equation 16 and 17):

$$\Delta G = RTlnK_d \tag{16}$$

$$\Delta G = \Delta H - T\Delta S \tag{17}$$

R: gas constant, 8.314 J•mol^{-1}•K^{-1}, T: temperature in Kelvin (K)

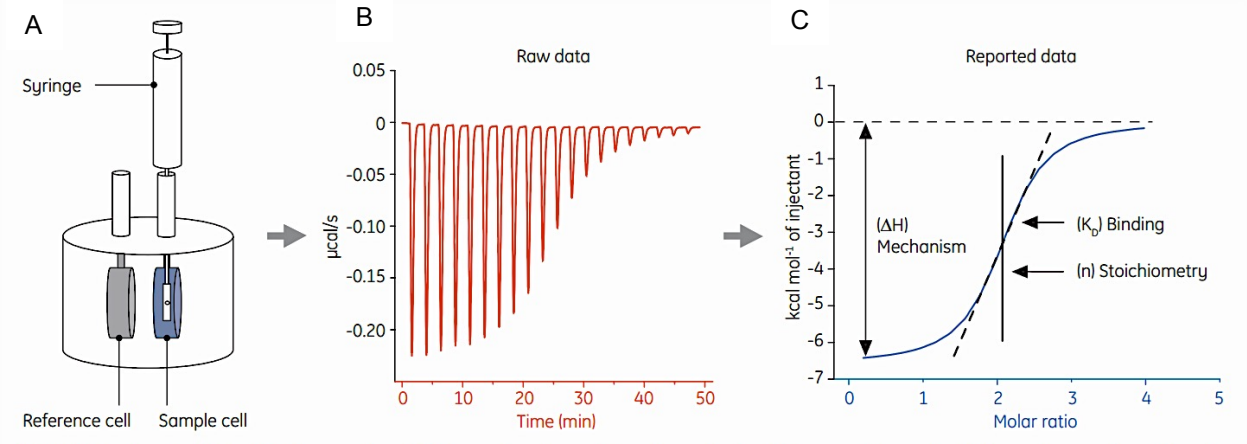

Figure 1.14. Schematic diagram representing the ITC experiment.
(A) The ITC instrument consists of two identical-shaped cells: one reference cell and one sample cell. A heater is linked to each cell and the power is delivered to each cell to maintain thermal equilibrium between cells. The macromolecule of interest is normally loaded into the sample cell while water or buffer is loaded into the reference cell. The binding partner of interest is loaded in the syringe to titrate the macromolecule in to the sample cell. (B) Example of raw ITC data: when a small volume of titrant (~2 µL) is injected into the sample cell, the ITC instrument detects the heat that is released or absorbed as a result of the interaction. If the reaction is exothermic, negative peaks will be produced. (C) The peaks in (B) are integrated and presented in a Wiseman plot. An appropriate binding model is chosen to fit the raw data and yield the parameters of ΔH, K_d and n for the interaction process. Images adapted from (http://www.malvern.com/en/products/technology/isothermal-titration-calorimetry/).

A good C value, the dimensionless number obtained by multiplying the association constant (K_a), the molar concentration of protein ([M]) in sample cell and the stoichiometry parameter (n), is between 10 and 100 to give a good titration curve. If the C-value is too high, the curve will be too steep to obtain an accurate K_d, whereas if the C-value is too low, the titration curve is too shallow to resolve all parameters. Therefore, the binding affinity and solubility of the proteins involved limit the accurate measurement of protein-protein interaction by ITC.

Several additional parameters must be considered for successful ITC measurements. Buffer choice is a very important factor. A buffer with a low or negligible enthalpy of ionization is normally used if protons will be taken up or released during complex formation. Additionally if a reducing agent is required, the reducing agent dithiothreitol (DTT) could cause erratic baseline drift, so <1 mM TCEP or BME is recommended. Lastly, to ensure proper mixing of the two proteins, the variables of injection length and stirring speed may need to be altered in order for the baseline to sufficiently stabilize between injections.

1.5. Conclusion and Outstanding Questions

As described above, protein interactions, especially interactions with BECN1 play an important role in autophagy regulation. In autophagy, there is a complicated protein-protein interaction network whose structural and functional features are barely known. Though some protein interactions have been studied, many questions regarding the structural features of the proteins involved in protein interactions and how autophagy is regulated by these interactions, remain.

BECN1, an interaction hub in autophagy, is an autophagy regulator related to many diseases especially cancers. At the start of this research, the structure-based molecular mechanism of BECN1 in autophagy regulation, including the mechanism of various protein interactions, was unknown. Initial structural research focused on determining how BCL2s bind BECN1 to inhibit autophagy (Maiuri, Le Toumelin et al. 2007, Ku, Woo et al. 2008, Sinha, Colbert et al. 2008, Mei, Su et al. 2014), and most information about other BECN1 interactions was based on cellular assays. Therefore, the structure of other domains and their role in protein interaction still needed to be investigated. Such molecular level information about BECN1 interactions will help improve our understanding of autophagy regulation.

1.6. Specific Aims of this Research

The overall goal of this thesis is to obtain a better structure-based mechanistic understanding of the biological function of autophagy proteins, with a special focus on BECN1. The following aims contribute to this overall goal:

1. **To delineate IDRs in human autophagy proteins and outline their potential biological roles**: About 60 proteins have been shown to be involved in autophagy. We hypothesize that most autophagy proteins have IDRs that are poorly conserved and serve as interaction sites because of their structural flexibility (Chapter 2). Detailed bioinformatics analyses of autophagy protein sequences will be used to identify potential IDRs in all autophagy proteins, and selected IDRs will be confirmed using biophysical methods. Further, we will use bioinformatics analysis to predict the potential biological function of the identified IDRs. Available protein structures will be analyzed to provide experimental support for the presence of IDRs in some human autophagy proteins. Bioinformatics tools will also be used to identify protein-protein interactions and post-translational sites located in the protein IDRs. However, the biological roles and mechanism of IDRs wil need to be further clarified by future studies.
2. **To experimentally investigate the structure of the IDR, with a special focus on the BH3D and its interactions:** The BECN1 BH3D is shown to adopt a 4-turn α helix upon binding to BCL2 homologs. Based on bioinformatics analysis described in Chapter 2, we hypothesize that the BH3D is disordered in the absence or interactions with other proteins and contains a region that facilitates structure stabilization upon binding to BCL2 homologs. We will use CD to examine these

binding-associated structural transitions, and CD and ITC to examine the role of critical BH3D residues in this transition and in regulation of autophagy by BCL2 proteins. The results of these biophysical studies will be verified by cellular autophagy assays. Further, the vacuole membrane protein 1 (VMP1) autophagy domain (ATGD) has also been reported to interact with the BECN1 BH3D to up-regulate autophagy. Therefore, we will use CD and ITC to also examine this interaction and associated structural transitions (Chapter 3).

3. **To probe the structure of BECN1 residues 141-171, and their role in protein interaction and autophagy regulation:** Though BECN1 residues 141-171 were considered part of the CCD, available crystal structures of the BECN1 BH3D and CCD indicate that this region comprises an independent domain. Various biophysical, biochemical and cellular biology methods will be used to investigate the structure of this domain. We hypothesize that (1) this domain forms a helix; and (2) the conserved residues are important for protein interactions and for autophagy (Chapter 4).
4. **To investigate the structure of the BECN1:ATG14 CCD heterodimer complex and identify CCD interface residues important for autophagy:** The BECN1 CCD crystal structure was solved by a competitor in 2012, who showed that the BECN1 CCD forms a metastable homodimer. However there is minimal structure information about the interaction of the ATG14 CCD and the BECN1 CCD. BECN1:ATG14 CCD heterodimer formation is required for the autophagosome formation. We hypothesize that BECN1 residues involved in metastable BECN1 CCD homodimer formation are also responsible for the heterodimer interaction with

ATG14 CCD. Further, a combination of diverse structural methods should allow us to identify ATG14 CCD interface residues and investigate their importance in autophagy (Chapter 5).

5. **Invariant residues in the BECN1 BARAD are important for starvation-induced autophagy:** The BECN1 CCD crystal structure was solved by a competitor in 2012, and shown to have a novel protein fold. Though BARAD contains many of the conversed residues in BECN1, the impact of these residues on autophagy regulation has not been investigated. We hypothesize that these conserved residues are important for the starvation-induced up-regulation of autophagy. We teat this hypothesis using cellular autophagy assays.
6. **To investigate structures of and interactions within BECN1 multi-domain constructs:** The structures of individual domains of BECN1 provide valuable information, however, structural studies of BECN1 multi-domain constructs should help elucidate the structure of BECN1 in the absence of any interactions and enable a better understanding of how BECN1, as an interaction hub, arranges and uses its individual domains to regulate autophagy via different protein interactions. We hypothesize here that the BECN1 multi-domain fragments adopts an extended conformation, which may play an important role in protein interaction (Chapter 6) and use a diverse array of biophysical methods such as CD and SAXS to examine the structure of these BECN1 fragments.

CHAPTER 2. TO DELINEATE IDRS IN HUMAN AUTOPHAGY PROTEINS AND OUTLINE THEIR POTENTIAL BIOLOGICAL ROLES

2.1. Introduction

Autophagy is a catabolic cellular pathway responsible for sequestering intracellular macromolecular assemblies, such as obsolete, damaged or harmful proteins, organelles and pathogens, into multi-layered vesicles called autophagosomes. Following that, the lysosome fuses with the autophagosome to degrade the sequestered molecules and recycle nutrients (Klionsky and Emr 2000, Levine and Klionsky 2004). Hence, autophagy is essential for cellular homeostasis as well as survival during cellular and organismal stress. The disruption or dysfunction of autophagy is implicated in numerous diseases such as neurodegenerative disorders, muscular diseases, cardiomyopathy, cancer and infectious diseases (Shintani and Klionsky 2004, Levine and Kroemer 2008, Mizushima, Levine et al. 2008).

Proteins that execute the process of autophagy are conserved in all eukaryotes (Levine and Klionsky 2004, Legakis and Klionski 2006). Known autophagy-related effectors (Table 2.1) may be grouped according to their function and association with other autophagy-related effectors, and at least three of these four groups function via formation of multi-protein complexes (Klionsky and Emr 2000, Levine and Klionsky 2004, Mizushima, Yoshimori et al. 2011). Four groups implicated in different functional stages of autophagy are: (i) the ULK1/ATG1 kinase signaling complex that initiates autophagy; (ii) the PI3KC3:BECN1 complex implicated in autophagosome nucleation; (iii) the ubiquitin-like ATG12 and LC3/ATG8 conjugation complexes implicated in autophagosome expansion; and (iv) proteins involved in phagophore formation. In addition to these autophagy-related effectors, two other groups of proteins are important for autophagy: (i) proteins that select and target cytoplasmic

macromolecular assemblies to the autophagosome and (ii) numerous autophagy regulators that modulate levels of autophagy within a cell via direct interactions with different autophagy-related effectors included in the previous groups. The biological role of many of these proteins is known and preliminary sequence analyses have helped to delineate their domain architecture; but a detailed, mechanistic understanding of the function of these proteins in autophagy is only now beginning to emerge.

Intrinsically disordered regions (IDRs), also called natively unstructured regions, are protein regions that have negligible folded tertiary structure or stable secondary structural elements like α-helices and β-sheets (Dyson and Wright 2005). It is thought that the sequence of IDRs has low complexity compared to the ordered protein regions (Romero, Obradovic et al. 2001). The amino acid composition of these domains dictates an inherent structural flexibility, preventing the formation of a well-ordered, central hydrophobic core for packing. More and more evidence shows that the disordered protein regions have important biological function such as protein-protein interactions (Mark, Liao et al. 2005, Hsu, Oldfield et al. 2012, Amartely, David et al. 2014) and post-translational modifications (Sakaguchi, Sakamoto et al. 1997, Luo, Li et al. 2004, Hashimoto, Kodera et al. 2013, Huang, Chadee et al. 2013). Thus, these regions appear to be exceptions to canonical paradigms that postulate that the three-dimensional structure of a protein dictates its function; and that three-dimensional structure is conserved more strongly than primary sequence. Because of the difficulty in characterizing IDRs of autophagy proteins due to their flexibility, the importance of IDRs in autophagy processes is often overlooked.

IDRs are present in many autophagy proteins that are involved in protein-protein interaction. For example, IDRs are found in ULK1/ATG1 complex proteins and involved in their

interactions (Mao, Chew et al. 2013, Feng, Wu et al. 2015, Noda and Fujioka 2015). Structures of ULK1 in complex with inhibitors revealed that the important phosphorylation site, Thr180, is on the disordered kinase activation loop (Bach, Larance et al. 2011, Lazarus, Novotny et al. 2015). Under autophagy inducing condition such as starvation, mTOR complex is inhibited by AMPK, leading to the dephosphorylation of ATG13 and ULK1/2. The dephosphorylated ULK1/2 then interacts with dephosphorylated ATG13 via the C-terminal IDRs. Biochemical, biophysical and structural biology experiemnts (Fujioka, Suzuki et al. 2014) show that a short region in ATG13 C-terminal IDR, called the flexible region might interact with ATG17, thus forming the ATG1:ATG13:ATG17 complex to induce PAS assembly with dimerization of ATG17 (Ragusa, Stanley et al. 2012) and initiate autophagy.

Other proteins such as ATG31 and ATG29 in yeast (Ragusa, Stanley et al. 2012, Fujioka, Suzuki et al. 2014), ATG101 in mammals (Suzuki, Kaizuka et al. 2015) also bind to this initiation complex to the autophagy. ATG101 has only been found in humans, and appears to regulate autophagy through interacting with ATG13 in the ULK1 complex (Hosokawa, Sasaki et al. 2009, Mercer, Kaliappan et al. 2009). ATG101 is the HORMA (residues 1-198) domain-only protein (Hegedus, Nagy et al. 2014). The X-ray structure of ATG101 (Suzuki, Kaizuka et al. 2015) shows that it is locked in the open conformation of HORMA domain whereas ATG13 N-terminal HORMA (residues 12-190) domain is locked in the closed conformation (Michel, Schwarten et al. 2015). ATG13 and ATG101 dimerize with these two HORMA domains, forming a Closed (C)-Mad2-Open (O)-Mad2 conformational dimer (Mapelli, Massimiliano et al. 2007) to function as an interaction hub for IDRs of other autophagy proteins such as ULK1 and PI3KC3 to regulate autophagy (Michel, Schwarten et al. 2015, Qi, Kim et al. 2015).

The crystal structure of VPS34, the yeast homolog of PI3KC3, shows that it has a completely ordered phosphoinositide-binding loop (activation loop/P loop), which is disordered in other classes of PI3 kinases. The bulk residues in the P-loop cause the increased rigidity of VPS34 pocket loop, which is critical for the catalytic domain to selectively bind its substrate such as 3-MA mimicking adenine of ATP to inhibit autophagy (Miller, Tavshanjian et al. 2010).

In the ubiquitin conjugation system, the disordered flexible region (FR) of E2-like ATG3 is essential for the ATG7 interaction: the FR interacts with a distal groove in the 'shoulder' region on the ATG7 N-terminal domain 'wing' (Kaiser, Qiu et al. 2013). Although, the IDR in ATG3 mostly remains, the conformational change of α-helix is still observed upon binding ATG7, indicating the structural flexibility of ATG3 and its role in protein interaction (Popelka, Uversky et al. 2014).

Some post-translational sites, especially phosphorylation sites are located in IDRs in autophagy proteins. ULK1, the kinase in the autophagy initiation step, is phosphorylated by various kinases at its IDRs (Khan and Kumar 2012). PKB, also known as AKT, phosphorylates ULK1 at Ser774 to inhibit autophagy in the nutrient rich condition (Bach, Larance et al. 2011). On the other hand, AMPK can activate autophagy by phosphorylating ULK1 at Ser317, Ser555 and Ser777 under starvation condition (Bach, Larance et al. 2011, Kim, Kundu et al. 2011).

Therefore, the systematic investigation of the IDRs in autophagy and their function is of great importance to further understand the autophagy regulation mechanism. Here we perform a rigorous primary structure analysis using multiple prediction programs to identify minimal consensus IDRs in key human autophagy-related effectors and regulators, and find that the majority of proteins with established roles in autophagy contain IDRs. We experimentally verify the lack of secondary structure in a selected subset of these IDRs. Further, we find that while

IDRs are often present at equivalent positions in the primary structure of autophagy-related effector homologs from diverse eukaryotes, IDR sequences are poorly conserved. An investigation of the potential functions of these IDRs demonstrates that many of the larger IDRs may serve as interaction sites for other proteins and may adopt more ordered conformations upon binding to other proteins. For each IDR-containing protein, we also mine available biological databases to identify potential proteins that might interact via the IDRs. Finally, we show that many of these IDRs are potential sites of post-translational modification, such as phosphorylation, which may be an important mechanism for regulating the autophagy function of these proteins.

The results reported here provide important information needed to direct future cell biology, biochemistry and structural research to better understand the function and mechanism of IDRs in autophagy. It is likely that a better understanding of the role and mechanism of these IDRs will not only improve our understanding of autophagy and other related cellular pathways, but also help identify new and unique therapeutic targets to manipulate cellular levels of autophagy for health benefits.

Table 2.1. Names and aliases of human autophagy protein.

Acronym	Expansion; Aliases
Autophagy Initiation	
ULK1	Unc-51-like kinase 1
ULK2	Unc-51-like kinase 2
FIP200	Focal adhesion kinase family interacting protein of 200 kDa
Vesicle Nucleation	
PIK3C3	Phosphatidylinositol-3-kinase, class III
PIK3R4	phosphoinositide-3-kinase, regulatory subunit 4
BECN1	Beclin 1; Coiled-coil, myosin-like BCL2-interacting protein; Atg6
AMBRA1	Autophagy/ Beclin-1 regulator 1
UVRAG	UV radiation resistance associated gene
VMP1	Vacuole membrane protein 1; TMEME49
Autophagosome Expansion	
ATG16L1	ATG16 autophagy related 16-like 1
MAP1LC3A	ATG8E or LC3A
MAP1LC3B	ATG8F or LC3B
MAP1LC3C	ATG8J or LC3C
GABARAP	ATG8A
GABARAPL2	ATG8C
GABARAPL1	ATG8L
MAP1LC3A	ATG8E or LC3A
Autophagosome Maturation	
WIPI1	WD repeat domain, phosphoinositide interacting; Atg18 homologs
SNX18	Sorting nexin 18
GOSR1	Golgi SNAP receptor complex member 1; GOS28
RAB24	Member RAS oncogene family
Autophagy Targeting	
NBR1	Neighbor of BRCA1 gene 1
NBR2	Neighbor of BRCA1 gene 2
SQSTM1	Sequestosome 1
SMURF1	SMAD specific E3 ubiquitin protein ligase 1
Autophagy Regulation	
BNIP3L	BCL2/ adenovirus E1B 19kDa interacting protein 3-like; NIX
BNIP3	BCL2/ adenovirus E1B 19kDa interacting protein 3; NIP3

Table 2.1. Names and aliases of human autophagy protein (continued).

Acronym	Expansion; Aliases
Autophagy Regulation	
BCL2	B-cell lymphoma factor 2
BCL2L1	Bcl2-like protein1
KIAA0226	Beclin-1 associated RUN domain containing protein
CLN3	Ceroid-lipofuscinosis, neuronal 3 / BTS / JNCL
GOPC	Golgi associated PDZ and coiled-coil containing protein; FIG / PIST / CAL
TMEM74	Transmembrane protein 74; NET36
PINK1	PTEN induced kinase 1; BRPK /PARK6
HMGB1	High mobility group box 1,SBP-1
EXOC8	Exocyst complex component 8
HDAC6	Histone deacetylase 6
HIF1A	Hypoxia inducible factor 1a
TRAF2	TNF receptor-associated factor 2
DDIT3	DNA-damage-inducible transcript 3
PDPK2	3-phosphoinositide dependent protein kinase 1 pseudogene
IRGM	Immunity-related GTPase family, M or IFI1
RALB	v-ral simian leukemia viral oncogene homolog B (ras related; GTP binding protein)

2.2. Materials and Methods

2.2.1. Identifying IDRs in Autophagy Proteins

The amino acid sequences of 59 important autophagy effectors and regulators were downloaded from the NCBI human genome RefSeq Protein database, cross-checked with the autophagy database (http://autophagy.info/autophagy/); and analyzed using the four programs below to predict IDRs based on several properties. The disorder predictor, PSIPRED (http://bioinf.cs.ucl.ac.uk/psipred/) calculates the probability of a residue being disordered based on similarity to regions with missing electron density in known crystal structures (Jones 1999, Ward, McGuffin et al. 2004). The protein disorder prediction system, PrDOS

(http://prdos.hgc.jp), provides a disorder probability for each residue based on a combination of the conservation of intrinsic disorder in protein families and on local amino acid sequence information, such as a higher frequency of hydrophilic or charged residues, or low sequence complexity (Ishida and Kinoshita 2007). The various short and long 2B algorithm, VSL2B algorithm, in the Predictors of Natural Disordered Regions, PONDR program suite, (http://www.dabi.temple.edu/disprot/predictor.php) (Obradovic, Peng et al. 2005, Peng, Radivojac et al. 2006), optimized for short (<=30 residues) and long (>30 residues) disordered regions, assesses amino acid frequencies, sequence complexity, ratio of net charge/hydrophobicity from averaged PSI-BLAST (Altschul, Madden et al. 1997) profiles based on a training data set comprising 1,335 non-redundant protein sequences, and calculates a disorder probability. The intrinsically unstructured protein predictor, IUPred (http://iupred.enzim.hu/), calculates a disorder probability by estimating pairwise energy content from amino acid composition to assess formation of favorable interactions and identify regions that do not adopt a stable structure because of the lack of such interactions (Dosztányi, Csizmok et al. 2005). In each of these programs, residues with a disorder probability greater than 0.5 are marked as disordered. Further, contiguous stretches of at least 25 disordered residues in PSIPRED and 30 disordered residues in IUPred, were predicted as IDRs (Table 2.2). For the PrDOS and PONDR analysis (Table 2.2), we listed contiguous stretches of at least 25 disordered residues as IDRs Gaurav Soni contributed to this analysis.

2.2.2. Identification of IDR-containing Autophagy Protein Orthologs

Sequences of the closest identifiable homologs from *Drosophila melanogaster*, *Arabidopsis thaliana* and *Saccharomyces cerevisiae* were identified by a combination of ways: from the autophagy database (http://autophagy.info/autophagy/); GeneCards

(http://www.genecards.org/); by BLASTP searches of Genomic RefSeq Protein databases (http://blast.ncbi.nlm.nih.gov/) for each organism; and in selected cases, by the examination of relevant literature.

2.2.3. Sequence Alignment of IDR-containing Autophagy Protein Orthologs

Multiple-sequence alignment of each set of orthologs was done using CLUSTALW (Thompson, Higgins et al. 1994) (http://www.ebi.ac.uk/Tools/msa/clustalw2/). IDRs in each ortholog were delineated from this multiple sequence alignment, based on the location of consensus IDRs in the human autophagy effector. The overall percentage identity and similarity for each set of orthologs was calculated from each alignment, simply as the ratio of the total number of invariant residues, or conservative substitutions, to the length of the shortest homolog. The percentage identity or similarity between regions equivalent to each IDR was calculated as the ratio of the number of invariant or conserved residues to the length of the human IDR regions. Gaps and insertions, if any, were not penalized for either calculation. This analysis was performed by my colleague, Minfei Su.

2.2.4. Predicting Autophagy Protein IDR Regions that Bind to Other Proteins

ELM (http://elm.eu.org) (Dinkel, Michael et al. 2012), a searchable database of experimentally validated interaction motifs that can be used to predict linear interaction motifs in protein sequences was used to identify eukaryotic linear motifs (ELMs) in IDR-containing proteins. ANCHOR (http://anchor.enzim.hu) (Dosztányi, Mészáros et al. 2009) was used to predict parts of IDRs, or regions flanking IDRs, likely to gain stabilizing energy upon interaction with a globular protein partner. Each residue is assigned a "binding probability" based on energetic gain upon interaction; and contiguous stretches of at least five residues with a binding

probability higher than 0.5, which are also predicted to be disordered by IUPred, are identified as potential “Anchors”.

2.2.5. Interactome of IDR-containing Autophagy Proteins

The Biological General Repository for Interaction Datasets (Stark, Breitkreutz et al. 2006), BioGRID$^{3.1}$ (http://thebiogrid.org/) online database - version 3.1.89, was data-mined to identify known interactions involving IDR-containing autophagy proteins, as well as the original research publications reporting each interaction. Prior to data mining, aliases for each protein, as well as the alias used in BioGRID were verified using GeneCards (http://www.genecards.org/). Duplicate interactions were removed from the output. This work was performed by Dr. Christopher Colbert and Dr. Saeed Salem. The published research reporting each interaction was then manually examined to determine whether the techniques used unambiguously demonstrate direct protein-protein interactions rather than just participation in the same complex.

2.2.6. Predicting Phosphorylation Sites

Phosphorylation sites were predicted using the NetPhos 2.0 Server (http://www.cbs.dtu.dk/services/NetPhos/), which predicts novel sites using artificial neural network techniques trained on large sets of experimentally verified phosphorylation sites to recognize fuzzy sequence patterns (Blom, Gammeltoft et al. 1999). (**Part of this work was performed by Gaurav Soni)**

2.2.7. Production of Potential IDR Constructs

Peptides corresponding to the following human consensus IDRs:

ATG13 (^{334}SDRTHCAATPSSSEDTETVSNSSEGRASPH^{363});

BECN1 BH3D (^{105}DGGTMENLSRRLKVTGDLFDIMSGQT^{130});

ATG16L1 (^{59}EKHDVPNRHEISPGHDGTWNDNQLQE^{84});

ATG2A (^{1244}HPPPRPPSPTEIAGQKLSESPASLPSCPPV^{1273});

SMURF1 (^{343}MNHQCQLKEPSQPLPLPSEGSLEDEELP^{370});

GOPC (^{255}HPPPRPPSPTEIAGQKLSESPASLPSCPPV^{279});

were chemically synthesized, and then HPLC purified to > 95% purity with purity confirmed by electrospray mass spectrometry (Protein Chem. Tech. Core, UTSW or EZBioLabs).

2.2.8. CD Spectroscopy

The IDR constructs were diluted to 50-200 μM in a buffer comprising 10mM potassium phosphate (pH7.6), 100mM $(NH_4)_2SO_4$. 300μL samples were added into the 1 mm rectangular quartz cuvette and the spectra were measured with a Jasco J-815 spectrometer equipped with a PFD-425S peltier cell holder at 4°C between 195-250 nm. Each spectrum was smoothened and buffer-subtracted, and secondary structure content of various constructs calculated using K2D2 (Perez-Iratxeta and Andrade-Navarro 2008) (http://www.ogic.ca/projects/k2d2/) and SELCON3 (Sreerama and Woody 1993, Sreerama, Venyaminov et al. 1999) in CDpro program (Sreerama and Woody 2000).

2.2.9. Nuclear Magnetic Resonance (NMR) Spectroscopy

1D-^{1}H NMR spectra were recorded at 25°C using a Varian Inova 500-MHz spectrometer equipped with a swpfg 2 channel probe, after the addition of 10% v/v D_2O to 500 mL of a 1 mM solution for each construct prepared in 10 mM potassium phosphate buffer, pH 6.0, with 50mM NaCl. NMR data were analyzed with the program MestreNova 5.3.1 and the chemical peak dispersion in the amide and methyl regions qualitatively assessed for the presence of secondary structure and folded tertiary structure content (Rehm, Huber et al. 2002, Hill 2008). The region between 4.5 ppm – 7 ppm was removed from the spectra due to poor water peak suppression (Figure 2.3). Additionally, since there were no signals less than -1.0 ppm and beyond 10.5 ppm, these regions were also removed from the displayed spectra. **(This work was performed with the help of Dr. Christopher Colbert.)**

Table 2.2. IDR predictions in human autophagy proteins by different programs.

Protein	**IDRs predicted by different programs**			
	PrDOS	**PSIPRED**	**VSL2B**	**IUPred**
ULK1	291-355, 365-428, 446-506, 520-552, 574-610, 709-832	292-557, 563-833	262-839. 865-877,	283-813, 822-839
ULK2	285-349, 364-398, 408-481, 493-523, 447-587, 626-672, 682-804	277-819	270-379, 386-828, 904-915.	307-354, 393-712, 720-730, 736-748, 772-783, 813-824
ATG13	319-363, 405-441	201-444, 455-493	219-276,302-363, 400-451.	252-271, 298-365, 401-441
RB1CC1	221-302, 621-679, 859-895,936-1052, 1069-1100, 1142-1256, 1265-1330, 1350-1404, 1414-1495	236-272, 544-578, 641-756, 1392-1434.	215-296, 526-583, 622-776, 856-1121, 1140-1495.	224-294, 630-682, 696-759, 1271-1290, 1302-1324, 1346-1373, 1408-1449.
PIK3C3	412-468	none	149-184, 251-290, 411-470, 555-587	147-171, 273-288, 414-433, 446-468, 506-516
PIK3R4	502-526, 744-766, 798-816, 836-935, 949-977	746-782, 834-936, 952-978	506-530, 745-984, 1298-1326	510-524, 752-762, 830-902, 951-985, 1302-1326
BECN1	42-116	37-116	1-16, 27-115, 141-254	1-13, 44-112
ATG14	1-21, 212-236, 448-472	1-22, 212-235, 442-474	1-32, 68-181, 212-242, 384-492	134-169, 215-234, 288-296, 406-438, 446-472
AMBRA1	249-284, 319-444, 453-497, 514-564, 585-651, 661-692, 739-802, 1093-1148, 1187-1264	250-282, 313-500, 515-564, 584-646, 742-805, 1111-1145, 1190-1224	205-805, 1060-1298	200-217, 254-290, 320-495, 515-565, 582-692, 700-722, 739-797, 1058-1298
UVRAG	1-30, 254-303, 468-696	1-39, 267-299, 466-619	1-43, 216-303, 392-413, 471-621	1-23, 468-480, 488-614,

Table 2.2. IDR predictions in human autophagy proteins by different programs (continued).

Protein	IDRs predicted by different programs			
	PrDOS	**PSIPRED**	**VSL2B**	**IUPred**
VMP1	1-36	1-40	1-41, 214-241	6-33
ATG16L1	217-262	58-89, 212-261	1-30, 53-165, 176-285, 289-307, 570-590	59-84, 117-129, 184-266, 290-306
ATG12	1-49	1-52	1-60	1-14, 18-47
ATG3	114-192	114-146	129-191	139-169
ATG4D	1-60, 170-204	8-68	1-64, 172-214, 412-474	1-61
ATG9A	585-701, 715-800, 805-839	573-706	1-24, 606-839	631-686, 709-839
WIPI1	268-298, 361-410	362-410	1-16, 360-409,	362-410
ATG2A	108-153, 369-419, 743-779, 881-924, 1241-1276, 1317-1355, 1438-1477, 1606-1658, 1816-1885.	337-364, 338-425, 741-788, 838-876, 1238-1273, 1317-1362, 1431-1479, 1605-1663.	105-155, 203-279, 288-475, 541-726, 748-800, 849-935, 1013-1049, 1240-1368, 1432-1518, 1609-1659, 1783-1798, 1818-1853.	105-123, 135-155, 206-217, 237-251, 333-354, 395-424, 550-578, 614-634, 663-703, 748-795, 902-922, 1028-1042, 1243-1276, 1318-1362, 1377-1411, 1441-1477, 1497-1511, 1543-1564, 1612-1655.
SNX18	63-151, 168-228	95-122, 176-270, 550-579	58-235, 385－401.	53-224
NBR1	80-109, 119-148, 274-365, 485-543, 598-643, 663-729, 748-806, 818-883.	118-148, 483-542, 598-644, 661-733, 748-802, 817-881.	52-204, 267-366, 481-531, 581-884.	79-102, 132-145, 300-313, 487-499, 579-621, 627-641, 660-734, 745-878.
SQSTM1	253-388	249-390	15-59, 101-120, 173-397	196-401
SMURF1	135-234, 268-307, 340-370	115-234, 267-311.	1-12, 158-250, 343-426, 571-585	167-250, 259-275, 293-310, 334-370.
BNIP3L	80-129	1-32, 77-122	1-178	1-132, 151-163
BNIP3	51-101	48-97	1-18, 23-148	1-105
BCL2	30-88	30-91	37-115	32-83
BCL2L1	27-78	25-83	15-77	27-58

Table 2.2. IDR predictions in human autophagy proteins by different programs (continued).

Protein	**IDRs predicted by different programs**			
	PrDOS	**PSIPRED**	**VSL2B**	**IUPred**
KIAA0226	214-322, 328-458, 515-586, 943-972	198-474, 505-623, 555-692	1-32, 193-621, 652-675, 913-972	1-17, 232-446.
CLN3	237-268	1-32, 233-269.	1-24, 63-92, 230-371	6-27, 67-82, 240-254
GOPC	429-462	132-188, 254-283, 370-462.	1-24, 86-190, 255-305, 374-414, 422-462.	157-177, 255-279, 420-450.
TMEM74	1-46, 50-96, 117-170	6-37, 45-98,121-173	1-97, 116-173, 264-305.	52-88, 122-167,
PINK1	179-210	175－219	1-66, 133-145, 179-234, 459-500	134-145, 182-210
HMGB1	165-215	163-215	1-117,135-215	1-11, 71-94, 116-150, 157-215
EXOC8	102-158, 284-332	282-331	1-61, 90-163, 264-336, 366-412	33-54, 116-128, 135-163, 284-328.
HDAC6	1-72, 841-1099	1-80, 840-874, 966-1001, 1022-1092	1-83, 425-483, 568-581, 849-1111	1-56, 442-464, 842-1092

2.3. Results

2.3.1. Identification of Consensus IDRs

IDRs can be reliably identified solely from protein sequence (Obradovic, Peng et al. 2005) based on distinctive features of amino acid composition such as: (i) low propensity to form well-packed hydrophobic cores; (ii) low propensity to form secondary structure; (iii) high charge fraction; (iv) low complexity sequences and; (v) similarity to disordered loops in crystal structures. Here we have identified consensus IDRs predicted using four programs that use subsets of these criteria: (Jones 1999) (Ward, McGuffin et al. 2004); PrDOS (Ishida and Kinoshita 2007); IUPred (Dosztányi, Csizmok et al. 2005); and the VSL2B algorithm in PONDR

(Obradovic, Peng et al. 2005, Peng, Radivojac et al. 2006). Each program was used to analyze and identify IDRs within fifty-nine human autophagy-related effectors, regulators and targeting proteins (Table 2.2). Perhaps not surprisingly, we found that there are significant overlaps in disordered regions predicted by the programs (Table 2.2).

The combined predictions from these four programs were used to define consensus IDRs (Table 2.3) as regions comprising at least 25 contiguous residues that were predicted to be disordered by at least three of the four programs. Further, disordered regions separated by short stretches of fifteen or fewer residues that were predicted to be ordered by only one or two programs, were defined as a single, contiguous IDR. In summary, a consensus IDR was defined as an unbroken stretch of at least 25 residues within which every residue was predicted to be disordered, by at least three of the four programs. There is disagreement regarding the sequence length that should be used to define IDRs, with the programs we used defining stretches of either 25 (Ward, McGuffin et al. 2004) or 30 (Dosztányi, Csizmok et al. 2005) predicted disordered residues as an IDR. We selected the 25-residue length criteria, as this is comparable to the sizes of the smallest structured domains, yet allows us to distinguish IDRs from smaller disordered sequences that may be classified as loops.

Table 2.3. Consensus human IDRs and their conservation in orthologs.

Protein	Homolog length (residues)				Full protein (%)		Human protein IDRs	IDR (%)	
	Human	Insect	Plant	Yeast	Identity	Similarity		Identity	Similarity
Autophagy Signaling Network									
ULK1	1050	835	691	897	9.6	29.2	291-833	0.7	9.0
ULK2	1036	835	626	897	13.1	35.0	285-354; 386-819	0^{nPY}; 0.9	0^{nPY}; 6.2
ATG13	517	523	603	529	0.8	15.1	302-363; 401-441	0; 0	19.4; 17.1
FIP200	1594	1357	1085	944	0.6	19.8	224-294; 630-756; 1271-1324; 1350-1449	0; 0; 0^{nIPY}; 0	9.9; 8.7; 0^{nIPY}; 10.0
Autophagosome Nucleation									
PI3KC3	887	949	499	875	32.9	64.1	414-468	1.8	7.3
PI3KR4	1358	1342	1494	1454	12.6	39.5	834-978	0	12.4
BECN1	450	422	517	557	12.1	42.2	42-115	0	20.3
ATG14	492	503	1730	344	1.7	20.4	442-472	3.2	6.5
AMBRA1	1298	361	726	1201	3.9	21.3	249-282; 319-497; 515-564; 584-692; 739-805; 1093-1148; 1187-1264	0; 0; 0^{nI}; 0^{nI}; 0^{nI}; 0^{nIP}; 0^{nIP}	11.8; 6.2; 0^{nI}; 0^{nI}; 0^{nI}; 0^{nIP}; 0^{nIP}
UVRAG	699	696	276	412	0.7	14.5	1-30; 267-299; 468-619	0^{nPY}; 0; 0.7	0^{nPY}; 9.1; 2.0
VMP1	406	541	416	--	26.9	54.7	1-36	2.8	16.7

Superscript text denotes human protein IDRs missing in orthologs from Insect, nI; Plant, nP; Yeast, nY; Insect and Plant, nIP; Plant and Yeast, nPY;

Table 2.3. Consensus human IDRs and their conservation in orthologs (continued).

Protein	Homolog length (residues)				Full protein (%)		Human protein IDRs	IDR (%)	
	Human	Insect	Plant	Yeast	Identity	Similarity		Identity	Similarity
Autophagosome Expansion									
ATG16L1	607	604	509	150*	5.3	30.7	59-84; 212-262	0; 0^{nY}	11.5; 0^{nY}
ATG12	140	111	96	186	16.7	56.3	1-49	0	6.1
ATG3	314	330	313	310	21.9	49.0	129-169	2.4	36.6
ATG4D	474	653	467	494	10.5	29.1	1-61	3.3	13.1
Autophagosome Maturation									
ATG9A	839	845	866	997	7.5	31.2	606-700; 715-839	1.0; 0	7.3; 9.6
WIPI1	446	377	425	500	11.9	43.8	362-410	0	2.0
ATG2A	1938	1906	1892	1592	3.3	23.7	108-153; 337-424; 748-788; 1241-1276; 1318-1362; 1438-1477; 1606-1658	0; 0; 0; 0; 0; 0; 0^{nY}	10.9; 14.8; 7.3; 8.3; 15.6; 17.5; 0^{nY}
SNX18	628	565	--	--	31.3	67.4	63-224	12.4	41.4
Autophagy Targeting									
NBR1	966	--	--	--	--	--	80-145; 485-531; 598-643; 661-881	--	--
SQSTM1	440	--	--	--	--	--	249-390	--	--
SMURF1	757	1087	1139	809	17.0	44.5	158-234; 268-307; 343-370	3.9; 0 0	13.0; 10.0 10.7

Superscript text denotes human protein IDRs missing in orthologs from Insect, nI; Plant, nP; Yeast, nY; Insect and Plant, nIP; Plant and Yeast, nPY;

* = Identified from the autophagy database;

Table 2.3. Consensus human IDRs and their conservation in orthologs (continued).

Protein	Homolog length (residues)				Full protein (%)		Human protein IDRs	IDR (%)	
	Human	Insect	Plant	Yeast	Identity	Similarity		Identity	Similarity
Autophagy Regulation									
BNIP3L	219	--	--	--	--	--	1-32; 77-129	--	--
BNIP3	194	--	--	--	--	--	48-101	--	--
BCL 2	239	--	--	--	--	--	32-88	--	--
BCLXL	233	--	--	--	--	--	27-77	--	--
RUBICON	972	--	--	--	--	--	214-458; 515-586	--	--
CLN3	438	422	--	408	23.5	49.8	237-268	0	12.5
GOPC	462	--	--	--	--	--	255-279; 422-462	--	--
TMEM74	305	--	--	--	--	--	6-96; 121-170	--	--
PINK1	581	706	1202	497	1.4	17.1	179-210	0	18.8
HMGB1	215	402	446	99	10.1	36.4	163-215	0^{nY}	0^{nY}
EXO84	725	671	752	683	1.2	17.0	116-158 284-332	0; 0	2.3; 10.2
HDAC6	1215	883	471	706	9.3	32.9	1-72; 842-1092	0; 0^{nPY}	4.2; 0^{nPY}

Superscript text denotes human protein IDRs missing in orthologs from Insect, nI; Plant, nP; Yeast, nY; Insect and Plant, nIP; Plant and Yeast, nPY;

Based on these criteria, 34 of 59 proteins analyzed were found to contain consensus IDRs, and these are listed and grouped according to function in Table 2.3. It is likely that these consensus IDRs represent a conservative minimal boundary for each IDR, and that actual IDR boundaries extend beyond the residues listed. For four additional proteins, IDRs were predicted by only one or two programs, or the consensus length was a little shorter than our 25-residue definition, and consequently, while these fail our definition of consensus IDRs, it is possible that these proteins do contain IDRs. Thus, some of the consensus IDR-containing proteins listed may also have additional IDRs that did not meet our stringent criteria for a consensus IDR, compared

to that for individual programs. Lastly, we noticed that of the consensus IDRs identified in Table 2.3, only three were shorter than 30 residues, but each of these three proteins also had additional larger IDRs.

2.3.2. Human Autophagy Proteins that Contain IDRs

The signaling network that triggers autophagy comprises of at least four proteins: either one of the ATG1 S/T kinase homologs, ULK1 or ULK2; the ATG1-activating protein, ATG13; the protein interaction hub, FIP200; and the ATG13-interacting protein ATG101. Of these, only ATG101 does not appear to contain an IDR. The other four proteins each contain a consensus IDR larger than sixty residues (Table 2.3). Thus, four out of five proteins important in signaling autophagy initiation contain IDRs.

All key autophagy-related effectors that participate in the PI3KC3:BECN1 complex contain large consensus IDRs (Table 2.3). The core components of this complex are the VPS34 homolog, PI3KC3, responsible for formation of phosphatidylinositol-phosphate; PI3KR4/p150, a S/T kinase VPS15 homolog; and the ATG6 homolog, BECN1, which is a protein interaction hub. Other important effectors such as ATG14, AMBRA1, VMP1 and UVRAG, differentially associate with BECN1, modulating the function of the core complex, although the mechanism of these autophagy-related effectors is unclear. Thus, IDRs play an important role in autophagy nucleation and other trafficking functions involving the PI3KC3:BECN1 complex.

Autophagosome expansion is carried out by two ubiquitin-like conjugation complexes: the ATG12:ATG5:ATG16 complex and the LC3/ATG8-phosphatidylethanolamine complex. Both ATG12 and ATG8 have ubiquitin-like folds and share the same E1-activating enzyme, ATG7. The ATG12 ubiquitin-like fold is preceded by a consensus IDR at the N-terminus. In contrast, none of the ATG8 paralogs, ATG8E, ATG8F, ATG8J, ATG8A, ATG8C or ATG8L,

contain IDRs. Humans have four ATG4 paralogs, a protease that cleaves ATG8 homologs to release the C-terminal glycine required for conjugation. Of these paralogs, only ATG4D bears a consensus IDR, located at its N-terminus (Table 2.3); while ATG4B and ATG4C do not contain IDRs. An 11-residue consensus disordered region in ATG4A, which we do not classify as a consensus IDR, is predicted to be longer by a subset of the programs, and so this might also constitute an IDR (Table 2.2). ATG7, the E1 activating enzyme shared by both conjugation systems; and ATG10, the E2 conjugating enzyme for the ATG12 system; do not contain IDRs. However, ATG3, the E2 enzyme for the ATG8 system, has a 41-residue consensus IDR (Table 2.3). ATG12 is conjugated to ATG5, which does not contain an IDR, but the ATG12:ATG5 conjugate forms a complex with another effector, ATG16L1, which contains two IDRs. Thus, although IDRs are not a common feature of proteins involved in autophagosome expansion, four key effectors contain IDRs.

Autophagosome maturation and lysosomal fusion involves some ATG8 paralogs listed above, and other proteins with membrane-associating domains. These include four WD40 domain-containing ATG18 paralogs. Of these, WIPI1 contains a large consensus IDR (Table 2.3); WIPI3 and WIPI4 do not contain IDRs; and WIPI2 contains a 17-residue, consensus disordered region identified by all programs that is shorter than our consensus IDR length definition (Table 2.2). In contrast, eight consensus IDRs were identified in ATG2A, which binds to ATG18. Lastly, the first transmembrane protein implicated in autophagy, ATG9, also contains two IDRs, each over 90 residues long; and the PX-BAR domain-containing SNX18, shown to play a critical role in autophagosome tubulation, also contains a very large, 162-residue IDR (Table 2.3). Thus, although a couple of proteins like GOSR1 and RAB24 do not contain IDRs, most of the key proteins responsible for autophagosome maturation bear IDRs.

Amongst proteins involved in selective targeting of macromolecular assemblies to the autophagosome, NBR1, SQSTM1 and SMURF1 contain consensus IDRs. SQSTM1 contains one large, 142-residue consensus IDR, while NBR1 and SMURF1 contain multiple IDRs, including a very large 221-residue consensus IDR in NBR1 (Table 2.3). NBR2 is the only targeting protein lacking a consensus IDR, although it bears an 18-residue, consensus disordered region predicted to be longer by a subset of programs (Table 2.2). Thus, IDRs are common in proteins important for targeting macromolecular assemblies for autophagy.

Several proteins modulate cellular autophagy levels via direct interactions with autophagy-related effectors. Some regulators such as HIF1α, TRAF2, DDIT3, PDPK2, IRGM and RALB, do not contain consensus IDRs. However, many others, especially those that regulate the PI3KC3:BECN1 complex, such as BCL2, BCLXL, BNIP3, BNIP3L1, AMBRA1, RUBICON, CLN3, GOPC, ITPR1, PINK1, HMGB1, EXO84 and TMEM74 all contain consensus IDRs (Table 2.3). HDAC6, shown to selectively regulate autophagy maturation in response to the presence of defective macromolecular assemblies, also contains a large consensus IDR.

2.3.3. Autophagy-related Effector Homologs Have Analogous, but Poorly Conserved IDRs

We identified the closest orthologs of each IDR-containing human autophagy protein from *Drosophila melanogaster* (insect), *Arabidopsis thaliana* (plant) and *Saccharomyces cerevisiae* (yeast), ensuring a wide diversity of eukaryotes (Table 2.3). Each species had orthologs of all IDR-containing autophagy-related effectors, emphasizing the conservation of the autophagy pathway in eukaryotes. Interestingly however, although the autophagy-related effectors are conserved, not all these species had orthologs of the autophagy targeting proteins,

NBR1 and SQSTM1, or of many human autophagy regulators, including BNIP3, BNIP3L, BCL2, BCLXL, RUBICON, CLN3, GOPC, TMEM74 and PINK1.

We find that most orthologs contain IDRs at positions in their primary structure analogous to the human proteins (alignments of ATG13, PI3KC3 and ATG16L1 are shown as examples in Figure 2.1): the available structures of all orthologs do not show any determined structure of these regions. But strikingly, they consistently share low sequence similarity, regardless of the overall conservation of the autophagy-related effector (Table 2.3). For instance, although PI3KC3 orthologs are highly conserved, sharing ~33% identity and ~64% similarity (Table 2.3); the PI3KC3 IDR shares less than 2% sequence identity and 8% sequence similarity. Other effectors such as Atg16L1 are not as well conserved, sharing less than 6% identity and 32% similarity respectively; yet, Atg16L1 IDRs share ~ 4% identity and 8-14% similarity, which is comparable to the conservation of the PI3KC3 IDRs. This low level of sequence conservation, and lack of correlation with the conservation of the rest of the protein, is a feature of all IDRs in the autophagy proteins analyzed (Table 2.3).

A. ATG13

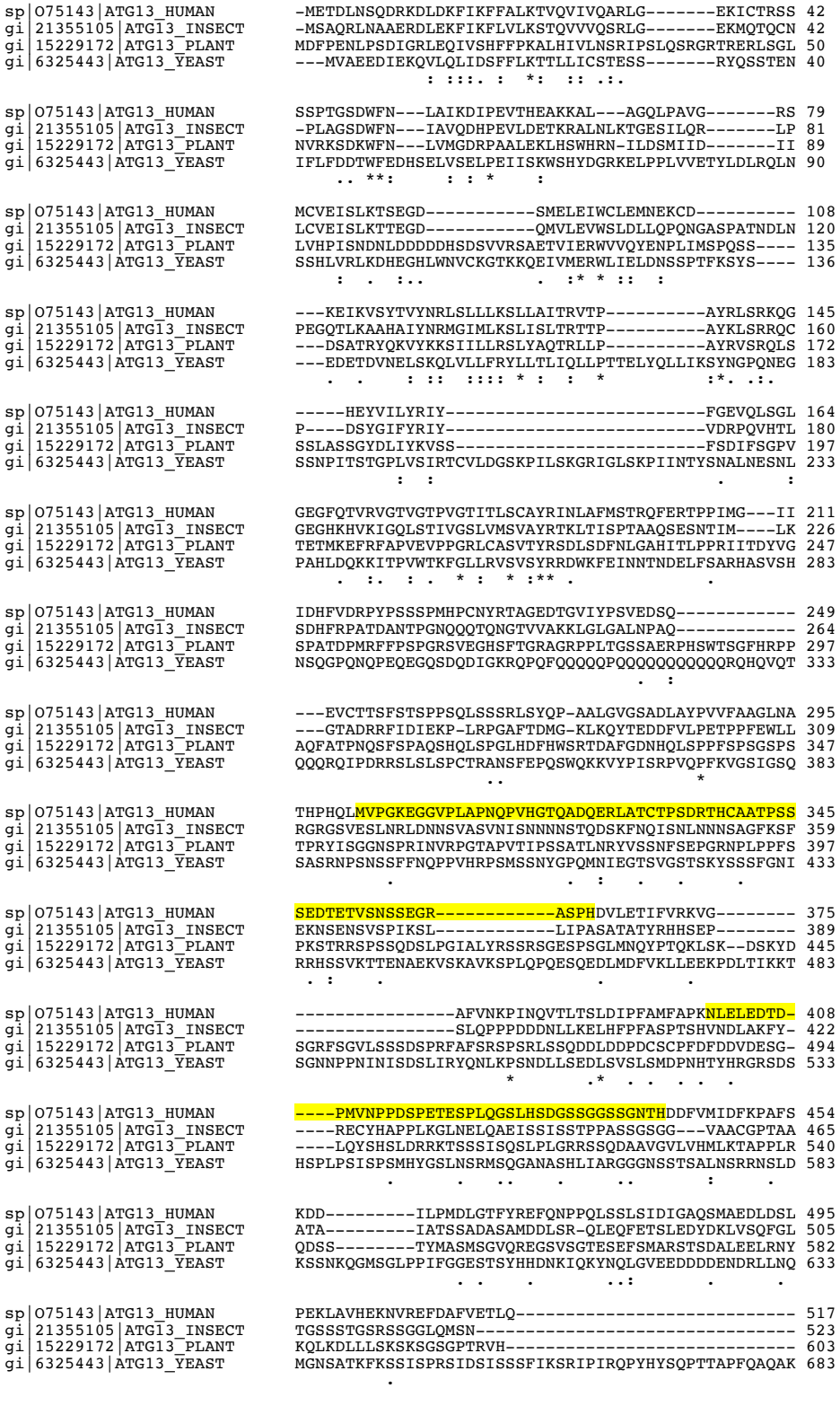

Figure 2.1. Sequence alignments of orthologs for three proteins.
Consensus IDRs within human orthologs are highlighted in yellow within (A) ATG13, (B) PIK3C3 and (C) ATG16L1.

```
sp|O75143|ATG13_HUMAN       --------------------------------------------------
gi|21355105|ATG13_INSECT    --------------------------------------------------
gi|15229172|ATG13_PLANT     --------------------------------------------------
gi|6325443|ATG13_YEAST      FHKPANKLIDNGNRSNSNNNNHNGNDAVGVMHNDEDDQDDDLVFFMSDMN 733


sp|O75143|ATG13_HUMAN       -----
gi|21355105|ATG13_INSECT    -----
gi|15229172|ATG13_PLANT     -----
gi|6325443|ATG13_YEAST      LSKEG 738
```

B. PIK3C3

```
sp|Q8NEB9|PIK3C3_HUMAN      MG-EAEKFHYIYSCDLDINVQLKIGSLEGKREQKSYKAVLEDPMLKFSGL 49
gi|17137150|PIK3C3_INSECT   MDQPDDHFRYIHSSSLHERVQIKVGTLEGKKRQPDYEKLLEDPILRFSGL 50
gi|15219743|PIK3C3_PLANT    MG--ANEFRFFLSCDINSPVTFRIEKLDGN---LPVKKSSDSGVVSIA-- 43
gi|6323269|PIK3C3_YEAST     MS--LNNITFCVSQDLDVPLKVKIKSLEGHKPLLKPSQKILNPELMLIGS 48
                            *.   :.: :  * .:.  : .:: .*:*:      .    .  : :

sp|Q8NEB9|PIK3C3_HUMAN      YQETCSDLYVTCQVFAE--GKPLALPVRTSYKAFSTRWNWNEWLKLPVKY 97
gi|17137150|PIK3C3_INSECT   YSEEHPSFQVRLQVFNQ--GRPYCLPVTSSYKAFGKRWSWNEWVTLPLQF 98
gi|15219743|PIK3C3_PLANT    -EEKKPELYIECALYID--GAPFGLPMRTRLKTTGPPYCWNELITLSSKY 90
gi|6323269|PIK3C3_YEAST     NVFPSSDLIVSLQVFDKERNRNLTLPIYTPYIPFRNSRTWDYWLTLPIRI 98
                                 ..: :   :: .  .    **: :   .      *:  :.*. :

sp|Q8NEB9|PIK3C3_HUMAN      PDLPRNAQVALTIWDVYGPGKAVPVGGTTVSLFGKYGMFRQGMHDLKVWP 147
gi|17137150|PIK3C3_INSECT   SDLPRSAMLVLTILDCSGAGQTTVIGGTSISMFGKDGMFRQGMYDLRVWL 148
gi|15219743|PIK3C3_PLANT    RDLTAHSQLAITVWDVSCGKTEGLIGGATVLLFNSKMQMKSGKQKLRLWQ 140
gi|6323269|PIK3C3_YEAST     KQLTFSSHLRIILWEYNGSKQIPFFNLETSIFNLKDCTLKRGFESLKFRY 148
                             :*.  : : : : :          ..  :  :  .   :: *  .*:.

sp|Q8NEB9|PIK3C3_HUMAN      NVEADGSEPTKTPGRT-SSTLSEDQMSR---LAKLTKAHRQGHMVKVDWL 193
gi|17137150|PIK3C3_INSECT   GVEGDGNFPSRTPGK--GKESSKSQMQR---LGKLAKKHRNGQVQKVDWL 193
gi|15219743|PIK3C3_PLANT    GKEADGSFPTSTPGK--VPRHERGELER---LEKLMNKYERGQIQSIDWL 185
gi|6323269|PIK3C3_YEAST     DVIDHCEVVTDNKDQENLNKYFQGEFTRLPWLDEITISKLRKQRENRTWP 198
                            .   . .  : . .:       ..:: *   * ::     . :  .  *

sp|Q8NEB9|PIK3C3_HUMAN      DRLTFREIEM-INESE--KRSSNFMYLMVEFRCVKCDDKE-YGIVYYEKD 239
gi|17137150|PIK3C3_INSECT   DRLTFREIEV-INERE--KRMSDYMFLMIEFPAIVVDDMYNYAVVYFEPE 240
gi|15219743|PIK3C3_PLANT    DRLMLKSLDT-IKEQESTKHGSSHLFVVIDFCS------FEHRVVFQESG 228
gi|6323269|PIK3C3_YEAST     QGTFVLNLEFPMLELPVVFIEREIMNTQMNIPTLKNNPGLSTDLREPNRN 248
                            :   . .::  : *        . :   :::            :   :

sp|Q8NEB9|PIK3C3_HUMAN      GD--ESSPILTSFELVKVPDPQMSMENLVESKHHKLARSLRSGPSDHDLK 287
gi|17137150|PIK3C3_INSECT   GD--VKYKLPAKPKLVSVPDSEIQMENLVERKHHRLARSERSGISDRDAK 288
gi|15219743|PIK3C3_PLANT    ANLFITAPIGSTNEFVTVWDTELGKTNPSENKQLKLARSLDRGIIDRDLK 278
gi|6323269|PIK3C3_YEAST     DPQIKISLGDKYHSTLKFYDPDQPNNDPIEEKYRRLERASKNANLDKQVK 298
                                      . :.. *.:    :  * *  :* *:   .  *:: *

sp|Q8NEB9|PIK3C3_HUMAN      PNAATRDQLNIIVS-YPPTKQLTYEEQDLVWKFRYYLTNQEKALTKFLKC 336
gi|17137150|PIK3C3_INSECT   PTASIRDQLHTIVYRYPPTYVLSSEEQDLVWKFRFYLSSHKKALTKFLKC 338
gi|15219743|PIK3C3_PLANT    PSNIERKSIQRVLK-YPPTRTLSGDERQLLWKFRFSLMSEKRALTKFLRC 327
gi|6323269|PIK3C3_YEAST     PDIKKRDYLNKIIN-YPPGTKLTAHEKGSIWKYRYYLMNNKKALTKLLQS 347
                            *    *. :: ::  ***   *: .*:  :**:*: * ..::****:*:.

sp|Q8NEB9|PIK3C3_HUMAN      VNWDLPQEAKQALELLGKWKPMDVEDSLELLSSHYTNPTVRRYAVARLRQ 386
gi|17137150|PIK3C3_INSECT   INWKLEDEVTQALWMLANWAPMDVEDALELLSPTFTHPQVRKYAVSRLAQ 388
gi|15219743|PIK3C3_PLANT    VEWSDVQEAKQAIQLMYKWEMIDVCDALELLSPLFESEEVRAYAVSVLER 377
gi|6323269|PIK3C3_YEAST     TNLREESERVEVLELMDSWAEIDIDDALELLGSTFKNLSVRSYAVNRLKK 397
                             :    .*  :.: :: .*  :*: *:****.. :    ** ***  * :

sp|Q8NEB9|PIK3C3_HUMAN      ADDEDLLMYLLQLVQALKYEN----------------------FDDIKNGL 415
gi|17137150|PIK3C3_INSECT   APDEDLLLYLLQLVQALKYEDPRHIVHLHGCIFPERDVVRSILDDNGSLL 438
gi|15219743|PIK3C3_PLANT    ADDEELQCYLLQLVQALRFER---------------------------- 398
gi|6323269|PIK3C3_YEAST     ASDKELELYLLQLVEAVCFEN---------------------------- 418
                            * *::*  ******:*: :*

sp|Q8NEB9|PIK3C3_HUMAN      EPTKKDSQSSVSENVSNSGINS--------AEIDSSQIITS--------- 448
gi|17137150|PIK3C3_INSECT   DQSSLSDLSATSSGLHGSVIPANQRAASVLAAIKSDKSVSPGSAGGSGSG 488
gi|15219743|PIK3C3_PLANT    -----SDRSCLSQ------------------------------------ 406
gi|6323269|PIK3C3_YEAST     -LSTFSDKSNSEFTIVDAVSSQ---------KLSGDSMLLS--------- 449
                                 .. *  .

sp|Q8NEB9|PIK3C3_HUMAN      -----PLPSVSSPPPASKTKEVPDGEN-------------LEQDLCTFLI 480
gi|17137150|PIK3C3_INSECT   GQGSVALPNPSAPATPGSSSLPCDSNSNALMLAEGISFGSVPANLCTFLI 538
gi|15219743|PIK3C3_PLANT    ----------------------------------------------FLV 409
gi|6323269|PIK3C3_YEAST     ----TSHANQKLLKSISSESETSGTES----------LPIVISPLAEFLI 485
                                                                      **:
```

Figure 2.1. Sequence alignments of orthologs for three proteins (continued). Consensus IDRs within human orthologs are highlighted in yellow within (A) ATG13, (B) PIK3C3 and (C) ATG16L1.

C. ATG16L1

```
sp|Q676U5|ATG16L1_HUMAN     MSSGLRAADFPRWKRHISEQLR-----RRDRLQRQAFEEIILQYNKLLEKSDLHSVLAQ- 54
gi|28572018|ATG16L1_INSECT  -----MSTEEHVWRAHVVRRLR-----ERNRKECDNFKEIIEQNNRLIDHVAQLKADNL- 49
gi|675383437|ATG16L1_PLANT  -------MEDYSYKTNVIASLK-----KRNAR-EHSFRDVIIYSNKLLESLDYLQRSVIL 47
gi|2497167|ATG16L1_YEAST    -------------MGNFIITERKKAKEERSNPQTDSMDDLLI------------------ 29
                                         ..    :     .*.    . : :::

sp|Q676U5|ATG16L1_HUMAN     -KLQAEKHDVPNRHEISPGHDGTWNDNQLQEMAQLRIKHQEELTELHK-KRGELAQLVID 112
gi|28572018|ATG16L1_INSECT  -KISVEN--EQLRNAVSTGGTG--SNVAIATLEKKLLSQQEELTELHK-RKGENSQMIVD 103
gi|675383437|ATG16L1_PLANT  RNIQTTKA-----EQTSPAILAHDLSAEERTMLMKCCDLQNDLAECHK-KISDYAQQVIE 101
gi|2497167|ATG16L1_YEAST    RRLTDRN-----------------------------DKEAHLNELFQDNSGAIGGNIVS  59
                             .:   :                              . : .* * .: . .  .  ::.

sp|Q676U5|ATG16L1_HUMAN     LNNQMQRKDREMQMNEAKIAECLQTISDLETECLDLRTKLCDLERANQTLKDEYDALQIT 172
gi|28572018|ATG16L1_INSECT  LNQKVEQQRIIISEKEHSLVEQQTNNNRLRAEVQLLHSSLEELKKLNNTMLDEHTALQLA 163
gi|675383437|ATG16L1_PLANT  FRNALDQKNQIISNQKREMEEMKNTLSNYQELCKKHCKELADIKIAFQNKVDECDALNIT 161
gi|2497167|ATG16L1_YEAST    HDDALLNTLAILQ---KELKSKEQEIRRLKE-------VIALKNKNTERLNDELISGTIE 109
                              : : .    :.    .: .        .         :   :   :   **  :  :

sp|Q676U5|ATG16L1_HUMAN     FTALEGKLRKTTEENQELVTRWMAEKAQEANRLNAENEKDSRRRQARLQKELAEAAKEPL 232
gi|28572018|ATG16L1_INSECT  FSSLEEKLRGVQDENRRLLERLMQYKSKDADKLNEENESIIRKRSAKLKRDLEDAVREPS 223
gi|675383437|ATG16L1_PLANT  YSSLECKKNNLEIENQNLKAQLAEVKKAEIA------------------R----SLSESL 199
gi|2497167|ATG16L1_YEAST    NNVLQQKLSDLKKEHSQLVARWLKKTEKETEAMNSEIDGTK-------------------- 150
                             . *: *      *. .*  :    .  :

sp|Q676U5|ATG16L1_HUMAN     PVEQDDDIEVIVDETSDHTEETSPVRAISRAATKRLSQPAGGLLDSIT----------NI 282
gi|28572018|ATG16L1_INSECT  SSSNAASSPGAA----SLQRNSSP------------AQFVGGLIGDEDFDEAAINGAMEA 267
gi|675383437|ATG16L1_PLANT  PKVAQDSSDKNV-------------------------KKFSSGTQVREE------------ 223
gi|2497167|ATG16L1_YEAST    ------------------------------------------------------------ 150

sp|Q676U5|ATG16L1_HUMAN     FGRRS----VSSFP------VPQDNVDTHPGSG-KEVRVPATALCVFDAHDGEVNAVQFS 331
gi|28572018|ATG16L1_INSECT  IGLDDNEYISARFTAGEIAENSRASIDTLKATGYLGQANPTKILMKFEAHENESHAVRWS 327
gi|675383437|ATG16L1_PLANT  ----------------RASLKITSVD--VNAANLNSIVPEKIKYEFNAHDSDVNAVLWL 264
gi|2497167|ATG16L1_YEAST    ------------------------------------------------------------ 150

sp|Q676U5|ATG16L1_HUMAN     PGSRLLATGGMDRRVKLWEVFGEKC-EFKGSLSGSNAGITSIEFDSAGSYLLAASNDFAS 390
gi|28572018|ATG16L1_INSECT  PVERMVATGGADRKVKLWDIGKNST-EPRAVLSGSSAGINSVDFDSTGAYILGTSNDYGA 386
gi|675383437|ATG16L1_PLANT  PTFSHLITAGADRKVKLWELLKDGSIVLKKSVRDCNSSIMSVDLDADSSLLLCTSCDFAS 324
gi|2497167|ATG16L1_YEAST    ------------------------------------------------------------ 150

sp|Q676U5|ATG16L1_HUMAN     RIWTVDDYRLRHTLTGHSGKVLSAKFLLDNARIVSGSHDRTLKLWDLRSKVCIKTVFAGS 450
gi|28572018|ATG16L1_INSECT  RVWTVMDNRLRHTLTGHSGKVMAAKYVQEPIKVVTGSHDRTLKIWDLRSIACIETKFAGS 446
gi|675383437|ATG16L1_PLANT  RIWTLNDFTLRHTLTGHSGKVMSAKFMYEINKIVSGSLDQTLKVWDLRRRACIQTSFSNS 384
gi|2497167|ATG16L1_YEAST    ------------------------------------------------------------ 150

sp|Q676U5|ATG16L1_HUMAN     SCNDIVCTE---QCVMSGHFDKKIRFWDIRSESIVREMELLGKITALDLNPERTELLSCS 507
gi|28572018|ATG16L1_INSECT  SCNDLVTTDSLGSTIISGHYDKKIRFWDIRTEKQADDVLMPAKITSLDLSKDCNYLICSV 506
gi|675383437|ATG16L1_PLANT  QVHDVICKS--GHVIISGHADKKVRLWDMRSNKETSQIASTGVVTSLDLSKNGYLLLVSQ 442
gi|2497167|ATG16L1_YEAST    ------------------------------------------------------------ 150

sp|Q676U5|ATG16L1_HUMAN     RDDLLKVIDLRTNAIKQTFSAPGFKCGSDWTRVVFSPDGSYVAAGSAEGSLYIWSVLTGK 567
gi|28572018|ATG16L1_INSECT  RDDTIKLLDLRKNQVISTFTNEHFKISCDFARASFNSSGLKIACGSADGAIYIWNVNG-F 565
gi|675383437|ATG16L1_PLANT  RDNVLKVFDLRTNFALNSLKADNFEVAYDWTRAKFSPDDQYCVCGSKNGSVFIWNINKET 502
gi|2497167|ATG16L1_YEAST    ------------------------------------------------------------150

sp|Q676U5|ATG16L1_HUMAN     VEKVLSKQHSSSINAVAWSPSGSHVVSVDKGCKAVLWAQY  607
gi|28572018|ATG16L1_INSECT  L-EATLKGHSTAVNAVSWSPNNNMLASVGKNKRCTIYSES  604
gi|675383437|ATG16L1_PLANT  VEKELKG-----------------------------------  509
gi|2497167|ATG16L1_YEAST    ------------------------------------------  150
```

Figure 2.1. Sequence alignments of orthologs for three proteins (continued). Consensus IDRs within human orthologs are highlighted in yellow within (A) ATG13, (B) PIK3C3 and (C) ATG16L1.

2.3.4. Experimental Verification of Consensus IDRs

While experimental verification of the lack of structure in each of the predicted consensus IDRs is not possible within the scope of this work, we used CD spectroscopy to demonstrate the absence of secondary structure in IDRs selected from each functional group of proteins: residues 334-363 of ATG13, which is part of the autophagy initiation signaling complex; residues 105-128 of BECN1, which is part of the autophagosome nucleation complex; residues 59-84 of ATG16L1 which is part of the autophagosome expansion complex; residues 1443-1472 of ATG2A which is involved in autophagosome maturation; residues 343-370 of SMURF1 which is involved in targeting substrates such as viruses to the autophagosome, and residues 255-279 from GOPC which regulates autophagy. The residues selected for analysis from ATG16L1, ATG2A, SMURF1 and GOPC constitute an entire consensus IDR (Table 2.3). For ATG13, the last 30 residues from the large IDR comprising residues 302-363 were selected for experimental analysis. Of the selected BECN1 residues 105-128, only residues 105-115 were predicted to be part of the larger consensus IDR. The reason we chose this entire region for analysis is that it was previously shown to constitute a BCL2 homology 3 domain (BH3D) bearing a conserved sequence motif: -ϕ-xxx-ϕ-K-xx-G-D-x-ϕ- (with ϕ representing hydrophobic residues), which is required and sufficient for binding to BCL2s (Sinha and Levine 2009), and therefore constitutes a real functional domain.

CD spectra of polypeptides that are α-helical display a positive band at ~192 nm and a large negative split transition at 208 nm and 222 nm; those that are β-strand show a positive band at 195 nm and a negative band at 218 nm; while those in coil conformation show a large single negative transition at ~195 nm and a small positive transition at ~220 nm (Greenfield 2006).Without exception, all six potential IDRs tested showed a large single negative transition

at ~195 nm, indicative of a coil conformation (Figure 2.2). Secondary structure content within each IDR was quantified by analyzing these CD spectra using two different programs: K2D2 (Perez-Iratxeta and Andrade-Navarro 2008) and SELCON3 (Sreerama and Woody 1993) (Table 2.4). Secondary structure content, as estimated by an analysis of the CD spectra recorded for each of the six potential IDRs using both programs, indicated that most of these residues had a coil conformation. K2D2 tends to provide a more accurate estimation of structured proteins with helix and strand (Perez-Iratxeta and Andrade-Navarro 2008). While the programs in CDpro show some discrepancy in different secondary structural elements (Greenfield 2006). Here we pick SELCON3 since it is trained on a reference data set that included denatured proteins and likely to provide the most accurate estimation of unordered structure (Sreerama and Woody 2000). Both K2D2 and SELCON3 showed the high amount of random coil in all these picked IDRs, especially all peptides are estimated to contain more than 70% random coil by SELCON3. Moreover, the secondary structure content estimated using SELCON3 indicates that the fraction of residues estimated to have either α-helix or β-strand content are insufficient to form stable secondary structures. Not surprisingly, BECN1 BH3D containing the residues following the consensus IDR also shows disordered, indicating our definition of IDRs in autophagy proteins is too strict and the autophagy-related effectors may actually contain more and longer IDRs than we have identified here.

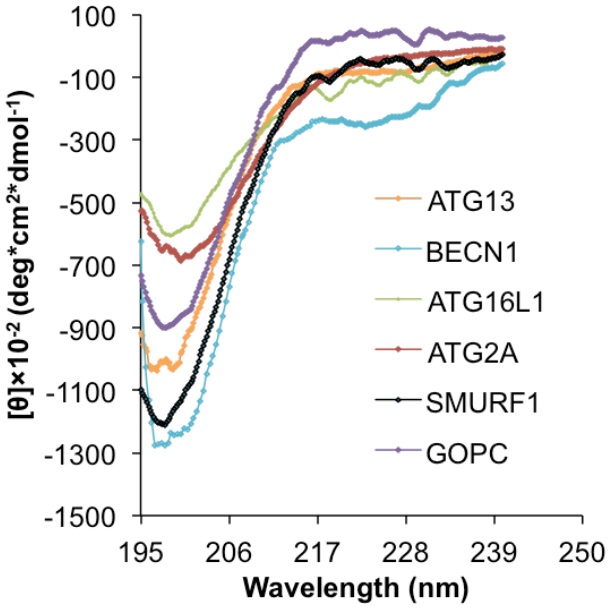

Figure 2.2. CD spectra of IDRs selected from each group of autophagy proteins.
Each IDR is different colored as shown in figure. All the picked IDRs are shown as random coil.

Table 2.4. Secondary structure estimation from CD spectra using K2D2 and SELCON3 in CDpro.

	Percentage of secondary structural elements estimated from K2D2		**Percentage of secondary structural elements estimated from SELCON3**		
Peptide Name	Helix	Strand	Helix	Strand	Coil
BECN1	8.2	24.0	9	10.4	83.1
ATG13	8.0	22.1	3.9	3.8	92.2
ATG2A	7.1	29.8	18.2	10	73.4
ATG16L1	6.7	29.7	4.8	7.2	91.5
GOPC	7.9	29.1	5.4	2.2	90.2
SMURF1	8.1	28.7	4.5	4.5	92.5

1D-^{1}H NMR spectroscopy is now routinely used to assess the folded state of proteins (Rehm, Huber et al. 2002, Yee, Chang et al. 2002, Page, Peti et al. 2004, Hill 2008). Therefore, the lack of structure in these IDRs can be further verified by the acquisition of 1D-^{1}H NMR

spectra (Figure 2.3). Importantly, these data reflect peptide backbone flexibility, but not backbone conformations or secondary structure content. For each of the six potential IDRs tested, the 1D-^{1}H NMR spectra (Figure 2.3) lacked peaks upfield of the strong methyl peaks at 0.8 ppm; contained broad peaks at about 8.3 ppm, the region characteristic for amide groups in random-coil conformation; and had little signal dispersion visible downfield of ~8.5 ppm, with the few peaks visible below 8.5 ppm being attributable to Trp sidechain shifts, which are indicative of unordered regions (Rehm, Huber et al. 2002, Hill 2008).

Thus, for each of six potential IDRs (from ATG13, BECN1, ATG16L1, ATG2A, SMURF1 and GOPC) representing different functional groups of autophagy-related proteins that were analyzed, the information obtained from the CD and 1D-^{1}H NMR spectra is consistent, and experimentally demonstrates that these regions are real IDR. Significantly, this data demonstrates that in the absence of BCL2 binding, the BECN1 BH3D is disordered, which indicates that the BECN1 IDR extends beyond the consensus IDR we identified (Table 1), suggesting that our stringent predictions identify conservative or minimal IDR boundaries, and that actual IDRs may well extend beyond the boundaries predicted.

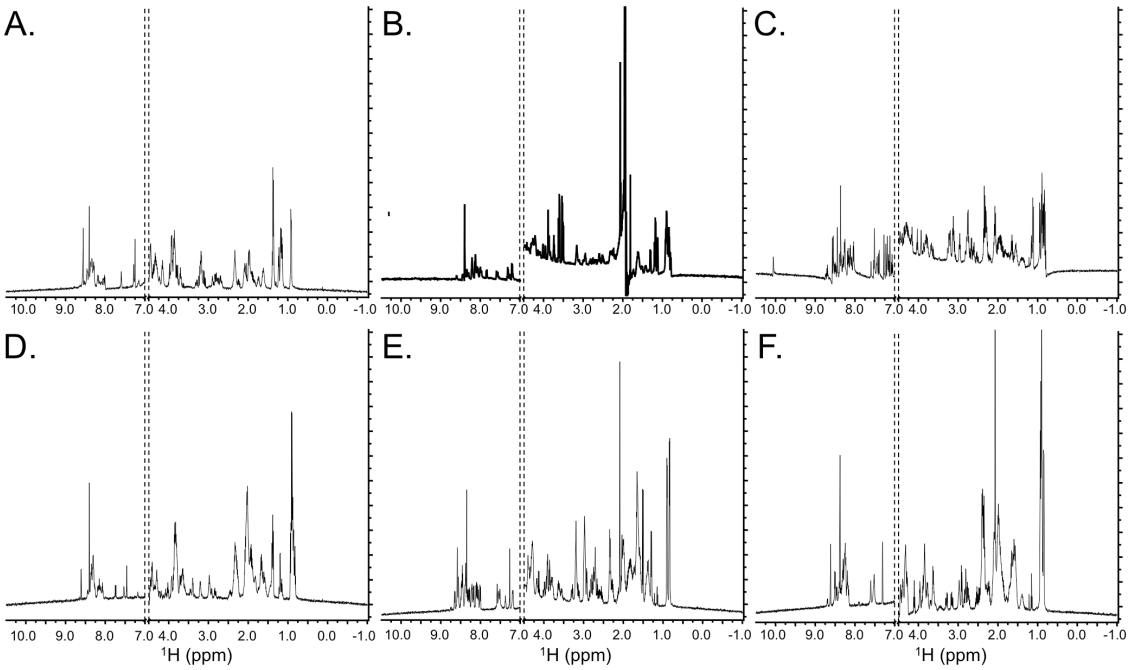

Figure 2.3. 1D-^{1}H NMR spectra of consensus IDRs.
(A) ATG13 (334-363); (B) BECN1 (105-128); (C) ATG16L1 (59-84); (D) ATG2A (1443-1472); (E) SMURF1 (343-370) and (F) GOPC (255-279). Only ^{1}H chemical shifts between -1.0 ppm to 4.5 ppm (methyl region) and 7.0 ppm to 10.5 ppm (amide) are shown.

2.3.5. Autophagy Protein IDRs may be Responsible for Protein Interactions

A potential IDR function is to facilitate protein-protein interaction (Hsu, Oldfield et al. 2012), therefore we investigated whether these were likely functions of IDRs within autophagy proteins. We first searched the sequences of consensus IDR-containing effector for ELMs, using the ELM server (Dinkel, Michael et al. 2012). ELMs are short, evolutionarily-plastic linear sequence motifs experimentally shown to be key for various protein-protein interactions. We then intend to use ELM server to identify the short linear interaction motifs (SLIMs) present in autophagy proteins. ELMs are found in each effector, but have a variable distribution between IDRs and ordered regions, with 5-70% of the ELMs found in each effector mapping to IDRs (Table 2.5). The distribution of ELMs correlated somewhat imperfectly with the fraction of total protein residues comprising the IDR (Tables 2.3 and 2.5).

Table 2.5. Binding motifs associated with consensus IDRs in human autophagy proteins.

Protein name	**Total No. of interaction features**		**Residues predicted by ELM in IDR**	**Residues predicted to be stabilized by binding to other proteins (Anchor regions)**	**No. associated with consensus IDRs**	
	ELMs	**Anchors**			**ELMs**	**Anchors**
ULK1	60	16	285-291,285-292,307-313, 311-316, 315-319, 400-405, 425-431, 464-469, 466-472, 475-481,502-505, 508-514, 545-551,553-558, 553-559, 566-571, 570-574, 573-579, 603-609, 613-621, 623-629, 629-633, 631-634, 635-640, 641-647, 654-658, 657-662, 658-664 659-662, 691-696, 693-699, 697-703, 697-704,715-721, 719-722, 729-733, 786-793, 787-791,814-820	252-260, **270-279, 312-342, 351-372, 381-397, 419-479, 482-519, 522-532, 545-572, 574-586, 594-654, 661-678, 688-711, 720-759, 770-796, 806-825**	40	15
ULK2	44	18	300-304, 328-331, 331-334, 395-400, 396-402, 438-442, 438-443, 466-471, 475-481,481-487, 525-529, 525-530, 529-535, 536-539, 561-564, 585-589, 574-580, 578-583, 628-631, 628-634, 637-645,642-661, 668-674, 687-693, 719-726, 745-750,746-752, 792-795, 805-809, 815-821,822-828	246-251, **350-361, 376-388, 404-418, 432-455, 457-468, 477-495, 516-543, 553-561, 584-599, 608-626, 641-651, 660-671, 699-712, 718-728, 739-746, 760-768, 803-808**	31	17
ATG13	37	5	310-314, 319-325, 323-326, 327-332, 330-336, 347-353, 400-404, 438-444	270-296, **301-307, 325-341, 363-404, 443-468**	8	4

Anchor regions related to IDR are shown bold black.

Table 2.5. Binding motifs associated with consensus IDRs in human autophagy proteins (continued).

Protein name	**Total No. of interaction features**		**Residues predicted by ELM in IDR**	**Residues predicted to be stabilized by binding to other proteins (Anchor regions)**	**No. associated with consensus IDRs**	
	ELMs	**Anchors**			**ELMs**	**Anchors**
RB1CC1	58	9	219-224, 235-242, 236-242,247-253, 290-296, 629-635, 673-679, 686-689, 1278-1284, 1281-1283, 1402-1405, 1403-1409, 1426-1432, 1444-1447	**254-260**, 301-311, **676-705, 714-725, 731-742**, 761-770, **1346-1353, 1394-1417, 1441-1446**	14	7
PIK3C3	18	0	156-163, 162-168, 164-170, 180-190	None	4	0
PIK3R4	53	7	752-757, 834-840, 836-839, 836-842, 879-882, 888-892	787-800, 816-833, **857-870, 895-904, 921-941,** 983-989, 1265-1271	6	3
BECN1	40	5	9-15, 41-47, 38-41, 52-60, 55-61, 57-60, 64-67, 78-82, 114-118, 117-123, 128-134	**13-49, 79-103, 116-128, 137-145**, 162-169	11	4
ATG14	37	4	1-4, 1-5, 425-428, 431-437, 439-443	110-119, 197-208, **436-451, 467-490**	5	2

Anchor regions related to IDR are shown bold black.

Table 2.5. Binding motifs associated with consensus IDRs in human autophagy proteins (continued).

Protein name	**Total No. of interaction features**		**Residues predicted by ELM in IDR**	**Residues predicted to be stabilized by binding to other proteins (Anchor regions)**	**No. associated with consensus IDRs**	
	ELMs	**Anchors**			**ELMs**	**Anchors**
AMBRA1	76	20	259-265, 335-340, 339-343, 356-362, 384-388, 407-414, 413-419, 418-424, 421-427, 436-440, 463-466,477-483, 549-554, 616-624, 639-642, 640-643, 643-649, 661-664, 666-671, 678-686, 683-686, 710-716, 752-757,754-759, 770-776, 1060-1065, 1076-1082, 1102-1108, 1104-1110, 1114-1120,1116-1122, 1152-1159, 1159-1165, 1192-1198, 1202-1207, 1212-1216, 1224-1228, 1229-1234, 1236-1241, 1236-1242	223-229, 238-254, **285-296, 338-347, 363-428, 442-455, 458-479, 495-520, 530-538, 562-582, 598-612, 645-664, 691-706, 719-741, 1045-1057, 1080-1092, 1101-1115, 1138-1193, 1208-1235, 1247-1290**	40	18
UVRAG	53	8	1-5, 11-15, 29-33, 468-481, 470-475, 481-485, 520-523, 542-548, 551-557, 553-557, 553-559, 558-562, 581-584	**1-6, 424-430, 457-466, 482-496, 520-534, 543-559, 566-576,** 623-628	13	7
VMP1	19	0	1-5	None	1	0
ATG16L1	17	11	183-186, 231-239, 252-258, 262-267, 263-269, 286-291	34-44, **48-54,** 106-113, 131-137, 146-152, 167-176, **223-228, 239-245, 259-264, 271-288,** 312-319	6	5
ATG12	15	2	1-5, 28-34	**1-24, 55-62**	2	2

Anchor regions related to IDR are shown bold black.

Table 2.5. Binding motifs associated with consensus IDRs in human autophagy proteins (continued).

Protein name	**Total No. of interaction features**		**Residues predicted by ELM in IDR**	**Residues predicted to be stabilized by binding to other proteins (Anchor regions)**	**No. associated with consensus IDRs**	
	ELMs	**Anchors**			**ELMs**	**Anchors**
ATG3	1	1	---	**136-143**	0	1
ATG4D	36	2	12-17, 54-62	1-15, 43-49	2	2
ATG9A	48	5	633-636, 667-673, 712-715, 741-749, 751-757,758-762,758-763, 772-778, 796-801, 822-830	**618-629, 648-658, 686-720, 750-816, 831-839**	10	5
WIPI1	34	3	362-368, 364-367, 368-372, 373-378	351-359, **380-385**, 414-436	4	1
ATG2A	131	22	240-243, 241-244, 351-357, 356-360, 370-376, 414-430, 506-515, 508-514, 508-515, 509-514, 529-534, 535-541, 555-573, 536-539, 559-565, 571-577, 690-696,695-701, 696-700, 745-751, 764-772, 780-786, 1236-1239, 1238-1244, 1245-1249, 1273-1279, 1395-1398, 1401-1407, 1507-1510, 1542-1545, 1561-1565, 1614-1620, 1625-1631, 1652-1657	122-136, **153-175,** 222-234, 255-261, 283-288, **326-331**, **357-390**, **424-439**, 454-460, 582-609, 642-649, 695-704, **730-741**, **760-766**, 930-936, 982-989, **1275-1321**, **1358-1378**, **1391-1410**, **1421-1436**, **1480-1495**, 1575-1584	35	11
SNX18	19	6	72-77, 77-81, 78-81, 82-86, 89-93, 93-97, 100-104, 115-119, 161-167, 194-199, 195-201, 198-204, 206-211	26-37, 49-59, **78-114, 118-203, 229-237, 257-262**	13	4

Anchor regions related to IDR are shown bold black.

Next, we used the program ANCHOR (Dosztányi, Mészáros et al. 2009) to identify sequences flanking or overlapping IDRs that would be stabilized as secondary structures upon binding to a globular protein partner (Dyson and Wright 2002). Here we call such sequences "Anchors". We find that IDRs of most autophagy proteins contain or are adjacent to Anchors (Table 2.5). Perhaps not surprisingly, the number of Anchors associated with each protein IDR is somewhat correlated to the length of the consensus IDR. Interestingly, in ATG13, AMBRA1 and ATG9A, short Anchors bridge two consensus IDRs, suggesting that in the absence of an appropriate binding partner, the Anchor sequence is part of the IDR. In ULK1 and AMBRA1, ELMs are predicted within Anchors, suggesting that these ELMs might nucleate interactions to stabilize secondary structure.

Lastly, Dr. Christopher Colbert and Dr. Saeed Salem helped to mine BioGRID$^{3.1}$(Stark, Breitkreutz et al. 2006) to identify proteins that bind to each consensus IDR. Most IDR-containing effectors appear to be involved in multiple protein-protein interactions (Figure 2.4). We supplemented and overlaid this data with published information regarding the nature of these interactions. Many interactions included in BioGRID$^{3.1}$ were identified based on cellular pull-down experiments followed by protein identification, rather than by experiments showing direct interactions between proteins (Figure 2.4, dashed lines). Hence, some of these interactions likely represent participation in the same cellular protein complex inside cells, rather than direct interactions between proteins. For established direct interactions between proteins, we further distinguish between interactions involving coiled-coil, ubiquitin-like, WD40 or other structured domains (Figure 2.2, black lines); those suspected to involve IDRs (Figure 2.4, red lines) and those that involve only IDRs (Figure 2.4, sinusoidal red lines). Notably, proteins with IDRs not

predicted to be involved in binding, also have fewer interaction partners, suggesting that these IDRs may have roles other than in binding.

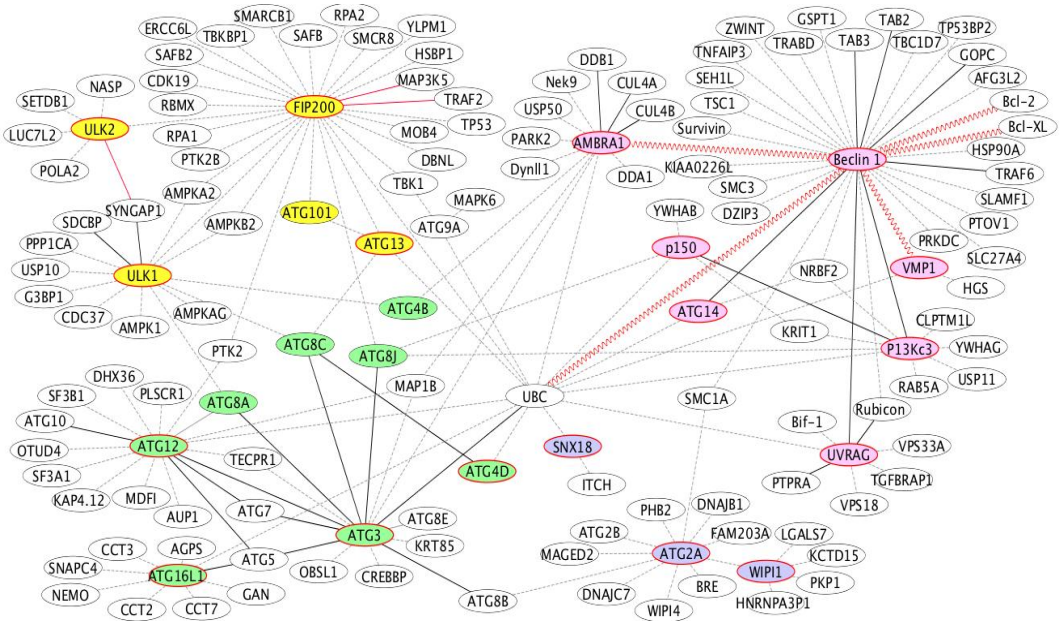

Figure 2.4. Interaction network of autophagy proteins.
IDRs of Ovals represent proteins, with autophagy-related effectors color-coded according to function: autophagy signaling (yellow), autophagosome nucleation (pink), enlargement (green), and maturation (blue). Effectors that neither contain IDRs themselves nor are implicated in interactions with other IDR-containing effectors are not shown. Effectors that contain consensus IDRs are outlined in red. Dotted lines indicate protein interactions not yet shown to be direct. Solid lines indicate demonstrated direct interactions; with black lines denoting interactions involving structured domains; red lines denoting interactions involving IDRs; and sinusoidal lines denoting interactions involving only the IDR.

2.3.6. Autophagy Proteins are Probable Sites for Phosphorylation

Phosphorylation sites are often located on hinges and loops as these are usually located at the protein surface, and consequently are accessible to kinases (Gnad, Ren et al. 2007, Gnad, Gunawardena et al. 2011) Hinges and loops have intrinsically flexible structures, which may also be an important requirement for phosphorylation. Therefore, we decided to investigate whether IDRs may bear more potential phosphorylation sites than other regions of IDR-containing proteins. We identified potential phosphorylation sites in all consensus IDR-containing proteins

(Table 2.2) using a general phosphorylation site predictor, NetPhos (Blom, Gammeltoft et al. 1999).

We find that in all IDR-containing autophagy proteins except ATG3, a higher proportion of the predicted S/T phosphorylation sites, but not Y phosphorylation sites, map to the consensus IDRs than to regions predicted to be structured (Table 2.6). Also about half of the proteins in ULK1 complex of the autophagy initiation step and PI3KC3 complex of the vesicle nucleation steps contain more than 50% of the phosphorylation sites in IDRs. Further, proteins with consensus IDRs predicted to bear a higher number of phosphorylation sites, such as ULK1, ULK2, FIP200 and AMBRA1, are also predicted to have a high likelihood of being involved in protein-protein interactions (Figure 2.2). Therefore, IDR may play important role in and protein phosphorylation in addition to protein-protein interaction.

Table 2.6. Distribution of phosphorylation sites in IDR-containing proteins.

	Protein	Total no. of potential phosphorylation sites			% of phosphorylation sites predicted within IDRs		
		S	T	Y	S	T	Y
1	ULK1	67	15	1	83.6	53.3	100
2	ULK2	65	16	3	72.3	56.2	66.7
3	ATG13	28	11	1	37.0	54.5	0
4	FIP200	76	20	7	47.4	40	14.3
5	PI3KC3	26	12	12	26.9	16.7	0
6	PIK3R4	38	15	9	13.9	26.7	0
7	BECN1	11	3	3	31.1	66.7	0
8	ATG14	24	7	3	13.1	0	0
9	AMBRA1	91	22	6	74.7	56.0	33.3
10	UVRAG	27	11	7	55.5	27.3	28.6
11	VMP1	6	1	2	16.7	0	0
12	ATG16L1	26	8	4	15.4	25.0	0
13	ATG12	3	7	1	66.7	42.9	0
14	ATG3	1	6	7	0	0	14.3
15	ATG4D	24	5	4	20.8	0	0
16	ATG9A	29	7	7	70.0	14.3	0
17	WIPI1	16	4	6	31.3	25.0	16.7
18	ATG2A	68	23	6	39.7	30.4	0
19	SNX18	21	7	6	42.9	14.3	33.3
20	NBR1	32	13	6	59.4	23.1	16.7
21	SQSTM1	30	1	0	60.0	100	0
22	SMURF1	16	8	12	25.0	12.5	16.7
23	BNIP3L	19	2	1	52.6	50	0
24	BNIP3	17	6	0	76.5	33.3	0
25	BCL2	4	4	2	50	50	0
26	BCLXL	9	2	2	55.6	50	0
27	RUBICON	62	12	10	64.5	41.7	50
28	CLN3	17	4	1	23.5	0	0
29	GOPC	12	3	2	16.7	33.3	0
30	TMEM74	21	6	4	66.7	66.7	0
31	PINK1	12	10	2	0	10	0
32	HMGB1	8	2	5	12.5	0	0

Table 2.6. Distribution of phosphorylation sites in IDR-containing proteins (continued).

	Protein	Total no. of potential phosphorylation sites			% of phosphorylation sites predicted within IDRs		
		S	T	Y	S	T	Y
33	EXO84	22	10	4	18.2	40	0
34	HDAC6	34	31	11	52.9	67.7	0

2.4. Discussion

Although the *de novo* prediction of a globular tertiary fold based only on its primary sequence is challenging and often not successful, the unique features of amino acid composition and sequence make it possible to identify IDRs with relative accuracy. Further, the application of multiple criteria makes these predictions much more robust. Despite the ease of prediction of these domains, and their common occurrence in proteins, comparatively little research has been focused on understanding the biological roles of these proteins. Our unusual approach of delineating and investigating IDRs in all the proteins involved in a single, yet essential, cellular process provides a unique perspective on the role of IDRs in this process. It is very important to note that, while our objective was to unambiguously identify IDRs, it is likely that the criteria we have used are overly stringent and that disordered regions predicted by each individual program that lie outside the consensus IDR may also constitute IDRs. Our CD spectra show that beyond the consensus IDR of BECN1 (residues 42-115), the functional domain BH3D (residues 105-130) is also disordered. In addition to our results, experimental verification of one of the consensus IDRs identified was provided in the recently determined X-ray crystal structure of Drosophila VPS34, which demonstrated that residues analogous to human PI3KC3 407-472 were missing ordered electron density (Miller, Tavshanjian et al. 2010), providing conclusive

proof that this region was an IDR. These experimentally determined boundaries agree very well with the consensus IDR identified between residues 414-468.

IDRs have been predicted in ~30% of prokaryotic proteins (Ward, Sodhi et al. 2004) and an even larger proportion, 45-50%, of eukaryotic proteins (Tompa 2002). Here we show that IDRs are present in more than 50% of human autophagy proteins identified to date, and constitute at least 6-60% of each of these proteins, indicating that these unstructured regions play a very important role in almost every stage of autophagy. In fact, as many of the proteins that do not contain IDRs are paralogs (for instance, six ATG8 paralogs and three WIPI paralogs), the proportion of unique autophagy proteins that contain IDRs is even higher. IDRs are present in almost all the key proteins of the: the ATG1 kinase signaling complex responsible for autophagy initiation; the class III PI3K –BECN1 complex implicated in autophagosome nucleation; and in the selection and targeting of macromolecular assemblies to the autophagosome. Further, IDRs are also present in many of the proteins involved in the two ubiquitin-like conjugation complexes implicated in autophagosome enlargement; in autophagosome maturation, lysosomal fusion and subsequent recycling of autophagy proteins; and in many regulatory proteins that interact directly with autophagy effectors.

Our investigation into the conservation of IDRs has highlighted a general feature of autophagy – i.e. while the basic autophagy machinery is conserved in all eukaryotes, the proteins involved in selecting and targeting macromolecular assemblies for autophagy as well as those that regulate autophagy via direct interactions with the autophagy machinery are not conserved amongst diverse eukaryotes. This suggests that equivalent functions in these other organisms are either performed by proteins that share very low, undetectable sequence identity to the human proteins or by alternate, completely different, proteins. More relevant to IDRs in autophagy

effectors, we found that compared to higher eukaryotes, the lower eukaryotes have fewer, and often shorter, IDRs. This suggests that IDRs constitute protein features that evolved relative late and represent an advanced feature of autophagy proteins. Further, we found that, even when homologs contain IDRs in equivalent positions, the IDR sequences are the most variable regions of the protein. An important corollary of this observation is that autophagy effectors with very large IDRs show lower conservation across species. Consequently, these homologs are difficult to identify based solely on primary structure, and many of these autophagy effector homologs have been identified based on their interaction with other autophagy effectors. This may reveal the involvement of IDRs in different, species-specific, protein-protein interactions and/or signaling features. The low sequence conservation of IDRs also suggests that the freedom from sequence constraints implicit in maintaining a defined 3D structure enables increased mutability of these regions. Thus, IDRs serve as an important feature that facilitates protein plasticity during evolution, making IDRs a powerful mechanism for evolution.

The reason for this preponderance of IDR-containing proteins in autophagy is not yet understood, but these domains must play a role in the biological function of these proteins. One common biological feature of many autophagy proteins is the requirement to interact with multiple partners, which is facilitated by the presence of promiscuous interaction domains like the coiled-coil domains, ubiquitin-like domains, WD40 domains and probably IDRs. IDRs are unstructured because internal inter-residue interactions do not provide sufficient enthalpic compensation for the loss of entropy upon folding. However, this energy may be provided by interactions with protein binding partners, which then facilitate a more ordered structure in subsets of IDRs that are called molecular recognition features (MoRFs) (Mohan, Oldfield et al. 2006). Moreover, MoRFs may be further classified as α-, β- or σ-MoRFs, depending on whether

they fold into α-helices, β-strands or stay in an ordered coil conformation, upon binding to interaction partners (Hsu, Oldfield et al. 2012). IDRs may serve as a powerful mechanism to allow interactions of multiple partners to the same sequence, as the flexible structure of these IDRs may enable them to form surfaces that are complementary to their interaction partners. Therefore, we computationally predicted potential Anchor regions within IDR-containing proteins that may facilitate binding to interaction partners. These predictions demonstrated that the IDRs of only three proteins did not appear to be associated with Anchor regions. Such IDRs have previously been called entropic chains or non-folders, and the function of such IDRs is unclear. However, most IDRs in autophagy proteins are associated with Anchor regions. For example, BECN1 BH3D could be defined as an α-MoRF because it forms a 4-turn helix upon binding to BCL2s (Feng, Huang et al. 2007, Oberstein, Jeffrey et al. 2007, Ku, Woo et al. 2008, Sinha, Colbert et al. 2008). It also contains an Anchor following the consensus IDR, indicating Anchor probably constitutes MoRF involved in binding to other proteins. The entropic cost of converting from a disordered or flexible state to a restrained or even ordered state enforces specificity, even if the actual affinity of binding is not very high. This allows an interaction to be specific, yet reversible, which is an invaluable asset in physiological interactions.

Potential interaction partners were identified from a biological interaction database, BioGRID. As expected, most IDR-containing proteins are found to have multiple interaction partners. The role of IDRs may be two-fold: 1) their flexibility enhances their ability to undergo dramatic conformational changes to form diverse interaction surfaces complementary to different proteins and 2) different regions of an IDR may simultaneously bind to different interaction partners. This would be a valuable asset in signaling processes. The role of IDRs in most of these interactions is not yet known. Therefore, future research focused on identifying interaction

partners of each MoRF-associated IDR, will be important for understanding the mechanism of these proteins and their role in autophagy.

Strikingly but not surprisingly, BECN1 depends a lot on IDRs in its interaction with other proteins such as BCL2s. Further research focusing on BECN1 regarding the exact roles of IDRs in protein-protein interaction might provide a detailed understanding of the structure, function and mechanism of IDRs in autophagy and other cellular pathways.

Another important function of IDRs may be to serve as sites of post-translational modification, such as phosphorylation. We found that potential phosphorylation sites, even when predicted based on criteria that did not involve any assessment of disorder, often clustered within IDRs. Two reasons might count for this. It is possible that disordered regions are better substrates for protein kinases as they are more accessible to kinase active sites, and/or that phosphorylation is an important mechanism for regulating IDR functions such as interaction with other proteins. Although only a few residues, typically S, T and Y, are targets for the vast majority of protein phosphorylation events in eukaryotes, identification of phosphorylation sites is complicated by the high variability of amino acid residues flanking these residues, as well as the short sequence length (typically under ten residues) that serve as recognition motifs for kinases. Therefore, it is possible that, using position-specific amino acid frequencies as well as disorder information to improve the discrimination between phosphorylation and non-phosphorylation sites will facilitate more reliable prediction of phosphorylation sites such as by the program DEPP (Disorder-enhanced phosphorylation predictor) (Iakoucheva, Radivojac et al. 2004). Future experimental verification of potential phosphorylation sites and identification of the kinases responsible for phosphorylation will improve our understanding of phosphorylation-mediated regulation of autophagy.

CHAPTER 3. TO EXPERIMENTALLY INVESTIGATE THE STRUCTURE OF THE IDR, WITH A SPECIAL FOCUS ON THE BH3D AND ITS INTERACTION

3.1. Introduction

BCL2 protein and its homologs form the most prominent family of apoptosis regulators, named the BCL2 family. These proteins can be classified into two sub-classes: pro-apoptotic and anti-apoptotic proteins based on the presence or absence of the four unique and evolutionary conserved BCL2 homology (BH) domains (or more accurately termed BH motifs) (Reed, Miyashita et al. 1996, Kelekar and Thompson 1998). These BH domains are numbered 1-4 in the order of discovery (Reed, Miyashita et al. 1996) and fold into α helical segments (Reed, Miyashita et al. 1996, Adams and Cory 1998, Kelekar and Thompson 1998). The anti-apoptotic members: BCL2, BCLXL, BCLw, MCL1 and BFL-1 contain four BH domains and protect cells from apoptosis. Some pro-apoptotic proteins such as BAX and BAK contain BH domains BH1, BH2 and BH3, while others such as BAD, BID, and BIM, contain only the BH3D. The BH3D was first identified in pro-apoptotic proteins functioning in cell death (Chittenden, Flemington et al. 1995). The BH3D of pro-apoptotic proteins binds to a hydrophobic groove of the anti-apoptotic proteins to inhibit the anti-apoptotic proteins and accelerate the cell death process (Zha, Aime-Sempe et al. 1996). Although sequence conservation in orthologs is low, a BH3D is defined by the presence of a Hy-X-X-X-Hy-K/R-X-X-Sm-D/E-X-Hy sequence motif (Hy: hydrophobic residues; Sm: residues with small side-chains, typically glycine (Sinha and Levine 2008).

Co-IP and autophagy assays show that anti-apoptotic BCL2-family proteins interact with the BECN1 residues 88-150 to block the phosphotidylinositol-3-kinase (PI3KC3) complex

formation, decrease the BECN1-associated lipid-kinase activity of PI3KC3 and inhibit BECN1-dependent autophagy in MCF7 cells (Liang, Kleeman et al. 1998, Pattingre, Tassa et al. 2005).

Sequence analysis shows that BECN1 is also a BH3-only protein, with its BH3D comprising residues 108-127 (Sinha and Levine 2008). The structure of the BECN1 BH3D when bound to various BCL2 proteins, has been solved by X-ray crystallography and NMR spectroscopy (Feng, Huang et al. 2007, Oberstein, Jeffrey et al. 2007, Ku, Woo et al. 2008, Sinha, Colbert et al. 2008). The structures of these complexes reveal that the BECN1 BH3D forms a 4-turn, amphipathic helix when bound to BCL2 proteins, with hydrophobic residues buried in the interaction interface (Feng, Huang et al. 2007, Oberstein, Jeffrey et al. 2007, Sinha, Colbert et al. 2008). Moreover, BECN1 BH3D binding induces a coil-to-helix transition in a loop at the end of α2 of the viral BCL2 homolog, M11, resulting in the addition of another helical turn to α2 (Sinha, Colbert et al. 2008).

In the previous chapter (Chapter 2), we used bioinformatics analyses to show that the human BECN1 contains a consensus IDR (residues 42-115) at its N-terminus (Mei, Su et al. 2014). Moreover, our CD spectroscopy and 1D-NMR analyses in Chapter 2 show that BECN1 BH3D is disordered. Taken together, these analyses indicate the BH3D is part of the BECN1 IDR and disordered in the absence of binding interactions.

Although it is now clear that the disordered BECN1 BH3D undergoes a disorder-to-helix transition upon binding BCL2 proteins, the mechanism of this binding-induced conformational change has not been fully understood. IDRs experimentally confirmed to undergo a disorder to secondary structure transition have been called molecular recognition features (MoRFs), which are further classified as α-, β- or σ-MoRFs, depending on whether they fold into α-helices, β-strands or restrained coils, respectively (Mohan, Oldfield et al. 2006). Thus, the BECN1 BH3D

appears to be a α-MoRF that undergoes a disorder to α-helix transition upon binding to BCL2s. As shown in the previous chapter, the BECN1 BH3D contains an Anchor region that is predicted to be involved in interaction with globular proteins. We hypothesized that the Anchor region in the BECN1 BH3D might be essential to nucleate binding and the conformational changes.

In addition, it was recently found that Vacuole membrane protein 1 (VMP1), a 406-residue, trans-membrane protein highly expressed in the pancreas during acute pancreatitis, promotes intracellular vacuolization and cell death (Dusetti, Jiang et al. 2002, Jiang, Motoo et al. 2004), is also required for autophagosome development under both nutrient rich and starvation conditions through its interaction with BECN1 (Vaccaro, Ropolo et al. 2008). Loss of VMP1 completely blocks autophagy (Ropolo, Grasso et al. 2007). Co-IP and pull-down assays show that the VMP1 autophagy domain (ATGD, residues 386-406) and the BECN1 BCL2 binding region (residues 88-150), which contains the BH3D, are sufficient for the interaction between these two proteins (Ropolo, Grasso et al. 2007, Molejon, Ropolo et al. 2013). Additional Co-IP assays show that the BECN1 BH3D F123 is required for the BECN1:VMP1 interaction. This interaction causes the release of BCL2 from BECN1 and helps recruit other proteins such as VPS34 and ATG16L to the BECN1-PI3KC3 complex, to promote the generation of PI3P on the autophagosomal membrane to trigger autophagy (Molejon, Ropolo et al. 2013). However, the BECN1:VMP1 interaction has not yet been structurally characterized, nor have the binding-associated conformational changes been investigated. We hypothesized that residues in the BECN1 BH3D might be important for the BECN1:VMP1 ATGD interaction.

In the research reported in this chapter, we have successfully purified two IDR-containing constructs of BECN1, BECN1 1-104 and 1-135, and used CD spectroscopy to show that these BECN1 fragments are structurally disordered. We also demonstrate that binding of the BH3D to

BCL2, is largely dependent on the residues in the Anchor region that nucleate concomitant binding and folding. We mutated residues in BH3D involved in BCL2 binding in order to determine the mediation effects of these residues on autophagy down-regulated by BCL2 homologs. This allowed us identify a BECN1 G120E+D121A double mutant that selectively rescues autophagy inhibited by M11, a viral BCL2. In addition, we also tried to investigate binding of BECN1 BH3D (residue 105-130) to the VMP1 ATGD (residues 386-406) using ITC. CD spectra show that both the BECN1 BH3D and VMP1 ATGD are disordered and that mixing these two peptides induces no significant conformational change in either peptide. Therefore, the disorder-to-helix change of BECN1 BH3D is probably binding partner dependent.

3.2. Materials and Methods

3.2.1. Over-expression and Purification of the BECN1 IDR

Human BECN1 residues 1-135 comprising the IDR through the end of the BH3D, were cloned between BamHI and NotI restriction enzyme sites of pParallel1 vectors (Sheffield, Garrard et al. 1999) containing a maltose binding protein (MBP) tag to enable amylose affinity purification. These constructs were made by Dr. Sangita Sinha. MBP•BECN1 residues 1-104 comprising the IDR preceding the BH3D was prepared by adding a stop codon after residue 104 using site-directed mutagenesis (Agilent Technology). Competent BL21 (DE3) pLysS *Escherichia coli* (*E.coli*) cells were transformed with MBP•BECN1 (1-104) or MBP•BECN1 (1-135). Luria broth media was inoculated with the transformed cells, cultured at 37°C while shaking at 220 rpm until $OD_{600} \approx 0.8$, and then induced with 0.5 mM isopropyl β-D-1-thiogalactopyranoside (IPTG) at 20°C for 16 hours. The cell lysate was centrifuged at 15,000g for 30 minutes and the supernatant was collected. MBP•BECN1 (1-104) and MBP•BECN1 (1-135) were purified from the supernatant by amylose affinity chromatography. The supernatant

was loaded on the amylose affinity resin (New England BioLabs Inc.) and unbound protein was washed off with buffer containing 25 mH HEPES (pH 7.5), 150 mM NaCl, 1 mM ethylenediaminetetraacetic acid (EDTA) and 0.05% β-mercaptoethanol). Then MBP•BECN1 (1-104) and MBP•BECN1 (1-135) were eluted with elution buffer containing 25 mM HEPES (pH 7.5), 150 mM NaCl, 1 mM EDTA, 0.05% β-mercaptoethanol and 20 mM maltose. Both proteins were ultimately purified to homogeneity using gel filtration chromatography with tandem 10/300 Superdex 200 and Superdex 75 analytical columns (GE Healthcare). An Amicon Ultra concentrator (Millipore) was used to concentrate the purified proteins to 1.0 mM in 25 mM HEPES, pH 7.5, 150 mM NaCl, l and 2 mM BME.

3.2.2. Peptide Synthesis

Peptides corresponding to the human wild-type (WT) BECN1 BH3D (^{105}DGGTMENLSRRLKVTGDLFDIMSGQT^{130}) (Protein Chemistry Technology Core, UTSW; RS synthesis, Louisville, KY; or EZbiolab, Carmel, IN), various BH3D-derived peptides with single substitutions of M109A, L112A, L116A, K117Q, and F123 A, and a double substitutions of G120E+D121A (Protein Chemistry Technology Core, UTSW), WT VMP1 ATGD (^{386} SMAQSYAKRIQQRLNSEEKTK^{406}) (EZBiolab, Carmel, IN), and GWG-ATGD (GWG-^{386} SMAQSYAKRIQQRLNSEEKTK^{406}) (EZBiolab, Carmel, IN) were chemically synthesized, and then HPLC purified to > 95% purity with purity confirmed by electrospray mass spectrometry.

3.2.3. BCL2 Production

Soluble human BCL2 (residues 1-207), lacking the C-terminal transmembrane helix, was expressed and purified as previously described (Petros, Medek et al. 2001, Sinha, Colbert et al. 2008).

3.2.4. CD Spectroscopy

BCL2 protein and WT or G120E+D121A doubly-substituted (DS) BH3D (Protein Chemistry Technology Core, UTSW) were mixed in 1:1, 1:10 and 2:1 ratios and incubated at 4°C for 30 minutes before dialysis. BCL2, WT BECN1 BH3D, DS BECN1 BH3D, and all BH3D:BCL2 mixtures were loaded into Slide-A-Lyzer G2 dialysis cassettes (Thermofisher) and dialyzed against 2 L CD buffer of 10 mM potassium phosphate (pH 7.6), 100 mM ammonium sulfate overnight prior to CD spectroscopy analysis.

VMP1 ATGD (^{386} SMAQSYAKRIQQRLNSEEKTK^{406}) (EZBiolab, Carmel, IN) and BECN1 BH3D (^{105}DGGTMENLSRRLKVTGDLFDIMSGQT^{130}) (RS synthesis, Louisville, KY) were mixed in a 1:1 molar ratio with different resulting concentrations of 7.65 μM, 30 μM, 100 μM and 300 μM. The same dialysis method against the same CD buffer as mentioned above was also applied to VMP1 ATGD, WT BH3D and all BECN1 BH3D:VMP1 ATGD mixtures. MBP•BECN1 (1-104), MBP•BECN1 (1-135), and MBP were dialyzed using the same dialysis procedure as above. Continuous scanning CD spectra were recorded from 195-250 nm at 4 °C in a 300 μL, 1mm quartz cell on a Jasco J-815 spectrometer equipped with a PFD-425S Peltier thermoelectric temperature control to determine the secondary structure content. The secondary structural content was analyzed using SELCON3 (Sreerama and Woody 1993, Sreerama, Venyaminov et al. 1999) of the CDpro program suite (Sreerama and Woody 2000).

3.2.5. ITC

BCL2 protein and the various BH3D-derived peptides (Protein Chemistry Technology Core, UTSW) were loaded into separate Slide-A-Lyzer G2 dialysis cassettes (Thermofisher), and simultaneously dialyzed against 2 L of 50 mM HEPES, pH 7.5, 150 mM NaCl, and 2 mM BME buffer to ensure buffer match. The BECN1 BH3D (RS synthesis, Louisville, KY) and VMP1

ATGD (EZBiolab, Carmel, IN) were also dialyzed into the same buffer in the same manner. ITC experiments were performed at 25°C with a stirring rate of 250 rpm on a TA Instruments Low Volume Gold Nano ITC (TA Instruments). 400 μL of 200 μM BCL2 was placed in the ITC cell and 50 μL of 2 mM various BECN1 BH3D-derived peptide was titrated into the cell at 300-second intervals using 25 injections of 2 μL each. Similarly, 400 μL of 40 μM VMP1 ATGD was added into the ITC cell, and 50 μL of 400 μM WT BECN1 BH3D peptide was titrated into the cell using 25 injections of 2 μL each with 300-second intervals at 25°C with a stirring rate of 250 rpm. Data were plotted and analyzed using NanoAnalyze software with an independent binding model to calculate binding affinities.

Yue Li in the lab also repeated the ITC experiments to investigate the interaction between VMP1 and BECN1. The BECN1 BH3D, VMP1 ATGD and GWG-ATGD peptides (EZBiolab, Carmel, IN) were dialyzed against 1 L of 25 mM HEPES pH 8.0, 150 mM NaCl, and 2 mM BME buffer for 24 h to ensure buffer match. ITC was performed at 20 °C with a stirring rate of 250 rpm. 350 μL of 100μM VMP1 ATGD was placed in the ITC cell, and 50 μL of 1 mM WT BECN1 BH3D peptide was titrated into the cell at 300-second intervals using 20 injections of 2.5 μL. Likewise, 350 μL of 100μM MBP•BECN1 1-135 was placed in the ITC cell, and 50 μL of 1 mM VMP1 ATGD peptide was titrated into the cell at 300-second intervals using 20 injections of 2.5 μL. For VMP1 GWG-ATGD, 50 μL of 1 mM WT BECN1 BH3D peptide was titrated into the calorimeter cell loaded with 350 μL of 100μM VMP1 GWG-ATGD, using 25 injections of 2μL at 300-second intervals. Data were plotted and analyzed using NanoAnalyze software with an independent binding model to calculate binding affinities.

3.2.6. Autophagy Assay

Mammalian cell expression plasmids of BECN1 mutants: L112A, L116A, K117A, G120E, G120E+D121A, and F123A were made using site-directed mutagenesis (Agilent Technology). These plasmids except for G120E+D121A mutant were given by Dr. Sangita Sinha and constructed at UTSW. The G120E+D121A mutant was made by James Moulton, our summer undergraduate student. 3×10^5 MCF7 cells were seeded into four-well Millicell EZ SLIDE (EMD MILLIPORE) slides and cultured in DMEM (GIBCO) with 10% fetal bovine serum (growth medium). At confluence, Lipofectamine 2000 (Invitrogen) was used to co-transfect cells with a total of 4 μg of plasmids including GFP-LC3 (1.6 μg), Flag-tagged BECN1 (1.2 μg), and either Flag-tagged BCLXL (1.2 μg) or M11 (1.2 μg) mammalian expression plasmids. Around 24 hours after transfection, cells were either starved for 4 hours in starvation media of Earle's balanced salt solution (GIBCO), or grown in nutrient-rich media (growth medium enriched with 2×essential amino acids and 2×nonessential amino acids). Cells were then fixed to the slides by incubation with 4% fresh formaldehyde in PBS for 20 minutes at 4°C and then mounted with Fluoromout Aqueous mounting medium (Sigma). Quantification of fluorescent autophagosomes in MCF7 cells was performed using an inverted Axio Observer (Zeiss). The number of GFP-LC3 puncta per GFP-LC3 positive cells was assessed by counting a minimum of 50 cells via Image ProPlus for duplicate samples per condition in three independent experiments. The significance of alterations in autophagy levels were determined by a two-tailed, heteroscedastic student's t-test, wherein $p \leq 0.05$ is considered significant.

3.2.7. Western Blotting

1×10^6 MCF7 cells were seeded into each well of a 6-well plate (Corning Costar) and grown to confluence in DMEM plus 10% fetal bovine serum. Cells were co-transfected with WT

or mutant BECN1 and either BCL-X_L or M11 using Lipofectamine 2000 (Invitrogen) according to the manufacturer's method. Cells were then lysed with 50 mM Tris-HCl (pH 7.5), 150 mM NaCl, 1mM DTT, 1mM EDTA, 1% Triton X-100 and cOmplete-EDTA-free protease inhibitor tablet (Roche). Cells were rocked at 4 °C for 30 minutes to complete lysis and then centrifuged at 14000 x g for 10 minutes at 4 °C. The supernatant of the cell lysate was collected for SDS-PAGE. Expression levels of Flag-tagged BECN1, BCLXL and M11 in MCF7 cells were verified by western blot analysis using commercial mouse monoclonal anti-Flag M2-peroxidase antibody (Sigma). As a loading control, the levels of Actin in MCF7 cell lysates were detected with mouse anti-Actin (Chemicon).

3.3. Results

3.3.1. Expression and Purification of the BECN1 IDR

The two MBP-tagged constructs, BECN1 1-104 and BECN1 1-135, were purified to facilitate biophysical studies of the BECN1 IDR. The size-exclusion chromatogram profile for MBP•BECN1 1-104 (Figure 3.1A) has a predominant peak with a MW of 152 KD (p2: Peak 2) calculated based on the SEC WT standards. The theoretical MW of MBP•BECN1 1-104, is 55 KD, which indicates this peak contains a dimer or trimer. Two smaller peaks, one in the void volume (p1: Peak 1) and another with a MW lower than 44 KD (p3: Peak 3) are present on the chromatogram. SDS-PAGE analysis (Figure 3.1A) indicates that only fractions from Peak 2 contain a pure single band with a MW at around 55 KD. The concentration of fractions from Peak1 is too low to visualize by SDS-PAGE and Peak 3 fractions contain bands smaller than 50 KD, which likely represent degradation products.

For MBP•BECN1 1-135, the size-exclusion chromatogram (Figure 3.1B) indicates that the predominant peak (P1: Peak1) appears in the void volume, indicating that this construct is

more aggregated than MBP•BECN1 1-104. This suggests that MBP•BECN1 1-135 is more unfolded than MBP•BECN1 1-104. Following the void volume peak are two comparable peaks showing MWs of 344 KD (P2) and 122 KD (P3), respectively (Figure 3.1B). However, in SDS-PAGE they present at the similar positions corresponding to a MW of 60 KD (Figure 3.1B), consistent with the theoretical MW of 59 KD, indicating that MBP•BECN1 1-135 might form different oligomers in these two peaks. The final yield of MBP•BECN1 1-104 and MBP•BECN1 1-135 was 9 mg/L and 4 mg/L, respectively. However, cleavage of the MBP tag resulted in significant aggregation (precipitation) or degradation (data not shown here) of both BECN1 IDR fragments, consistent with its disorder.

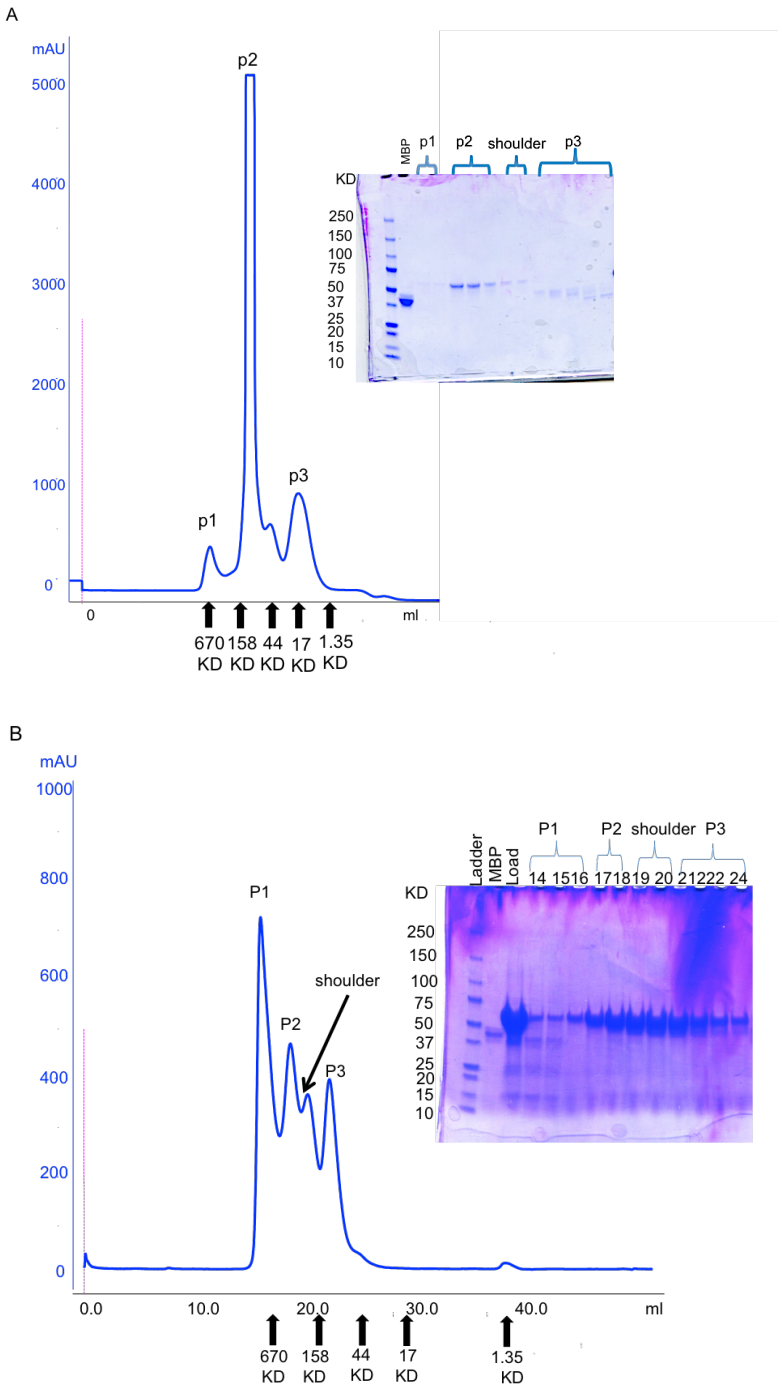

Figure 3.1. Size exclusion chromatograms of two BECN1 IDR constructs and the corresponding SDS-PAGE images.

SEC chromatograms corresponding to (A) MBP•BECN1 (1-104) and (B) MBP•BECN1 (1-135) are shown in blue. Elution positions for different molecular weight markers are indicated with arrows. The peaks presented in each chromatogram are labeled and the corresponding fractions analyzed by SDS-PAGE and the molecular weight marker are also labeled on the gel image.

3.3.2. BECN1 1-135 is More Disordered than BECN1 1-104

The presence of MBP, a largely helical protein, causes the CD spectra for both MBP•BECN1 1-104 and MBP•BECN1 1-135 to show helical features (i.e. a positive transition at ~195 nm and two negative transitions at 208 nm and 222 nm (Figure 3.2). Therefore, we also measured the CD spectra of MBP to permit comparison of MBP•BECN1 1-104 and MBP•BECN1 1-135. The secondary structure content of these constructs was analyzed with SELCON3, a program that provides the most accurate estimation for random coil (Sreerama and Woody 2000).

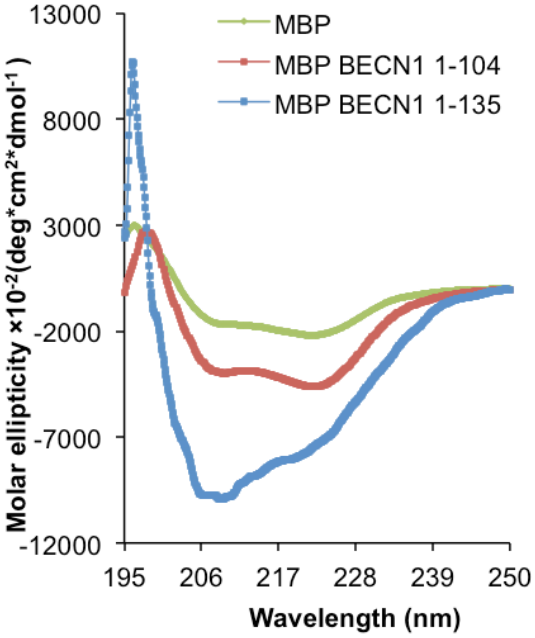

Figure 3.2. CD spectra of BECN1 IDR-containing constructs.
The MBP, MBP•BECN1 1-104 and MBP•BECN1 1-135 are colored as shown in figure.

Table 3.1. Secondary structure content of different BECN1 constructs estimated from CD spectra.

Constructs	**Residue number**	**Percentage of the secondary contents (%)**		
		Helix	**Strand**	**Coil**
MBP	371	57.6	14.1	28.3
MBP•BECN1 1-104	500	56.8	10.8	32.4
MBP•BECN1 1-135	531	43.9	9.4	47.1
BH3D	26	4.0	3.8	91.9

Since there is a 25-residue linker region between MBP and BECN1, the total number of residues in the expressed MBP•BECN1 1-104 and•BECN1 1-135 is 500 (371 residues from MBP, 25 residues in the linker and 104 residues from BECN1) and 531 (371 residues from MBP, 25 residues in the linker and 135 residues from BECN1), respectively (Table 3.1). Analysis of a CD spectrum recorded from MBP alone indicates that of the 371 total residues, 214 residues are in helical conformation, 52 in β-conformation and 105 in random coil-conformation (Table 3.1). Estiamtion of the secondary structure content in MBP•BECN1 1-104 indicates that it contains 284 residues in α-helix, 54 residues in β-strand and 162 residues in coil (Table 3.1). Comparing to the secondary contents of MBP, it has 70 more residues in α-helix and 57 more residues in coil. There is no increase in the β-strand content (Table 3.1). For the MBP •BECN1 1-135, the secondary structure estimations show that it has 233 residues in α-helix, 50 residues in β-strand and 250 residues in coil. Again, compared to MBP, there is almost no change in β-strand. However, it has 19 more residues in α-helix and 145 more residues in coil than those of MBP. Since there is almost no changes in β-strand content in both BECN1 constructs, we will just consider the changes in α-helix and coil here.

Assuming the secondary structure of MBP does not change between the isolated MBP and the fusion protein, and the 25-residue linker is still disordered, BECN1 1-135 is highly disordered with only 19 helical residues, while BECN1 1-104 has 70 residues in α-helix. On the other hand, if BECN1 accounts for the entire increase in coil content, BECN1 1-104 still has 47 residues in α-helix, while BECN1 1-135 is totally disordered. It is also possible that in MBP•BECN1 1-104, BECN1 contributes 57 additional residues in random coil and in MBP•BECN1 1-135, BECN1 contributes the additional 19 helical residues. In this case, BECN1 1-135 is still more disordered than BECN1 1-104. Therefore, inclusion of BH3D increases the random coil content in either case.

3.3.3. Residues in BH3D Anchor Region are Important for Binding to BCL2

BECN1 BH3D residues 116-128 (Figure 3.3, colored green), which flank the BECN1 consensus IDR at the C-terminus, are predicted to be an Anchor region. Although this Anchor region comprises only half the BH3D, it bears most of the residues involved in binding (Figure 3.3). In order to further investigate the effect of these residues on BCL2 binding, we chemically synthesized BECN1 BH3D-derived peptides with substitutions of M109, L112, L116, K117, G120+D121, and F123 (Figure 3.3).

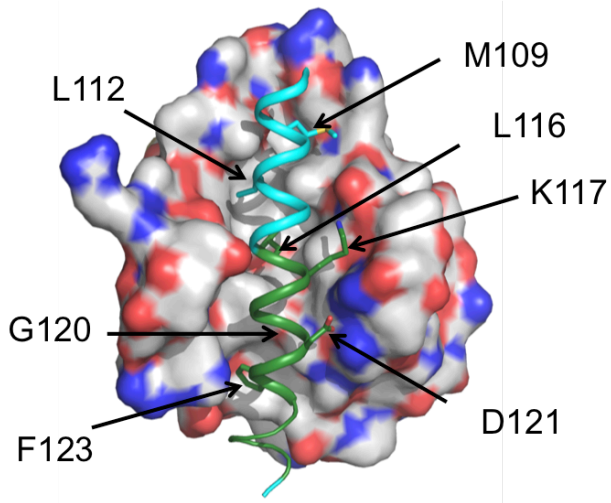

Figure 3.3. X-ray crystal structure of the BECN1 BH3D bound to M11 (PDB: 3DVU). The γ-herpesvirus 68 BCL2 homolog M11 is rendered as molecular surface with C colored white, N colored blue, O colored red and S colored yellow. The BH3D is rendered as cartoon and colored cyan (residues 105-115, 129-130) or green (Anchor region, residues 116-128). The side-chains of residues involved in protein interaction are shown stick with C in Anchor region colored green and C outside Anchor region colored cyan, N colored blue, O colored red and S colored yellow.

ITC experiments (Figure 3.4, Table 3.3) show that the WT BECN1 BH3D binds to BCL2 with a K_d of 10.4 μM (Figure 3.4A, Table 3.3), but this binding is abolished by mutagenesis of residues L112, L116, G120+D121 or F123 (Table 3.2). Four of these five residues are located in the Anchor region, and only L112 lies outside the BH3D Anchor region. It is likely that for binding of these BH3D-derived peptides, the decreased ΔH due to diminished interactions is not compensated by increased ΔS arising from improved BH3D helicity from increased Ala content (Pace and Scholtz 1998). The effect of the BH3D Anchor region on binding is further emphasized by the observation that K_d, ΔH and ΔS are minimally affected for the M109A substitution (Figure 3.4B), which lies outside the BH3D Anchor region, whereas the dissociation constant doubles for a K117Q (Figure 3.4 C) Anchor region substitution as the decreased enthalpy is offset by the decrease in entropy (Table 3.2). Thus the BH3D Anchor region likely nucleates α-MoRF structure by triggering concomitant binding and folding.

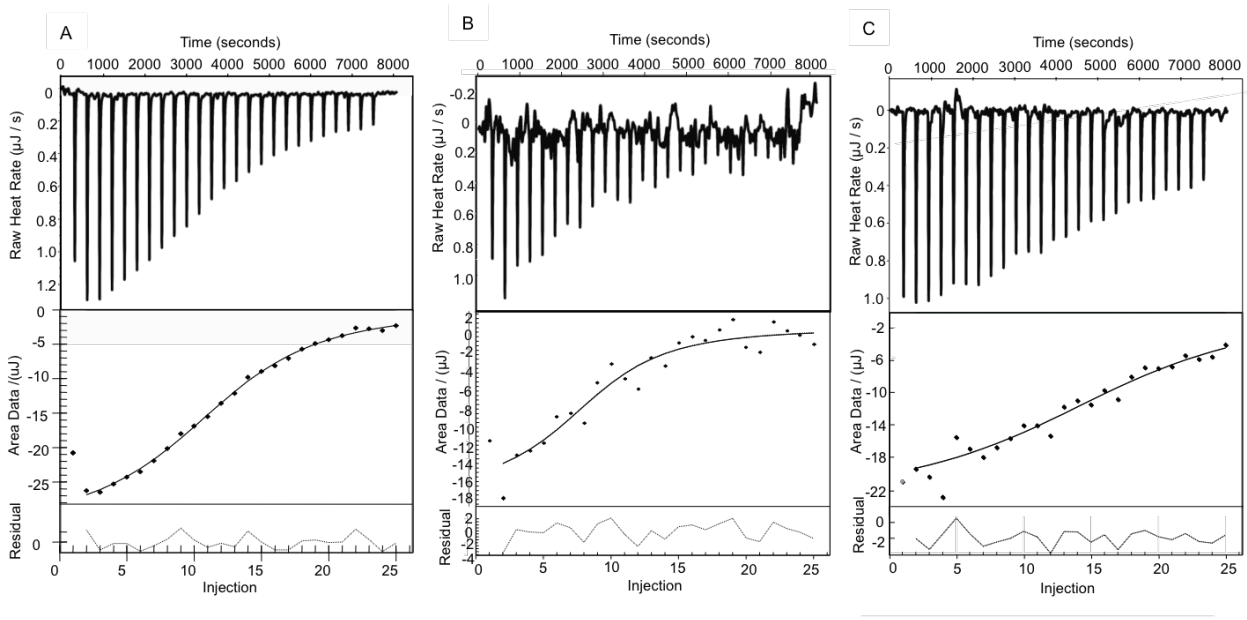

Figure 3.4. ITC data of BECN1 BH3D peptides titrated into BCL2.
(A) BECN1 BH3D WT (B) BECN1 BH3D M109A (C) BECN1 BH3D K117Q with upper panel showing the raw data and lower panel showing the fitting curve.

Table 3.2. Summary of the thermodynamic parameters for binding of various BECN1 BH3D-derived peptides to BCL2.

BH3D	**K_d (µM)**	**ΔH (kJ/mol)**	**ΔG (kJ/mol)**	**ΔS (J/K•mol)**
WT	10.4 ± 3.5	-17.8 ± 6.5	-28.2 ± 0.7	35.2 ± 24.1
M109A	14.5 ± 2.3	-15.8 ± 2.9	-27.6 ± 0.4	39.6 ± 11.2
L112A	No binding	--	--	--
L116A	No binding	--	--	--
K117Q	24.5 ± 6.0	-21.4 ± 4.6	-26.4 ± 0.6	16.7 ± 13.5
G120E+D121A	No binding	--	--	--
F123A	No binding	--	--	--

3.3.4. BH3D Undergoes Binding-associated Disorder-to-helix Change, Which is Nucleated by an Anchor Region

In order to further investigate how folding of the BECN1 BH3D is associated with its binding BCL2 to modulate autophagy, we used CD spectroscopy methods similar to those

described previously where coupled folding and binding of calmodulin binding targets (CaMBTs) to calmodulin (CaM), a largely helical protein (Yuan, Gomes et al. 2004, Rumi-Masante, Rusinga et al. 2012, Dunlap, Kirk et al. 2013). Here, we applied a similar method to determine that the BECN1 BH3D undergoes coupled folding based upon binding the largely helical BCL2.

We directly confirmed the disorder-to-helix structural transition of the BH3D by estimating and comparing the secondary structure content (Figure 3.5 and Table 3.3) of different molar mixtures of BCL2 and the BECN 1 BH3D, as well as of BCL2 and G120E+E121A DS BH3D, which does not bind to BCL2 (Table 3.3) and is disordered in solution with 83.1% random coil content (Figure 3.5 and Table 3.3). Our CD spectra (Figure 3.5 and Table 3.3) indicate that BCL2 is 81% helical in solution, which agrees with crystal and NMR structures of BCL2 (Petros, Medek et al. 2001, Porter, Payne et al. 2009, Perez, Banfi et al. 2012, Souers, Leverson et al. 2013), showing BCL2 comprises of 8 helices and a disordered region of about 53 residues (25% of 207 residues).

Secondary structure content (Table 3.3) remains unchanged upon addition of equimolar or 0.5-fold molar BECN1 BH3D as compared to BCL2 alone, suggesting that the BH3D folds into a helix upon binding. However, addition of a 10-fold molar excess of the BH3D reduces the helical content of the sample to 76%, consistent with a significant population of unbound BH3D molecules remaining in random coil conformation. In contrast to the BH3D, addition of equimolar or 10-fold excess molar DS BH3D peptide dramatically reduces the helical content of the sample to ~67 % and ~45 % respectively, indicating that there is no change in the secondary structure of the DS BH3D peptide (Table 3.3). The inability of the DS BH3D peptide to undergo a disorder-to-helical transition upon loss of BCL2 binding, confirms that folding is coupled to

binding. Therefore, concomitant folding of the BECN1 BH3D upon BCL2 binding is triggered by the Anchor region.

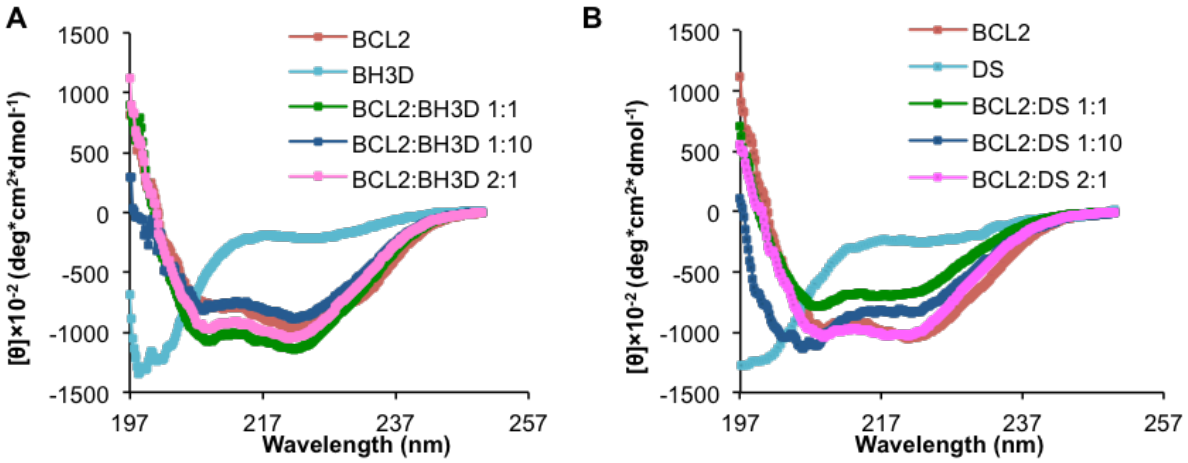

Figure 3.5. CD spectra of BCL2 complex with WT BH3D and its double substitution (DS). (A) The CD spectra of BCL2, BH3D and BCL2:BH3D complex with molar ratios of 1:1, 1:10 and 2:1. (B) The CD spectra of BCL2, BH3D DS and BCL2:DS complex with molar ratios as in (A).

Table 3.3. Secondary structural contents in BCL2:BH3D and BCL2:DS complexes estimated from CD spectra.

Protein	**Length (residues)**	**Percentage of the secondary contents (%)**		
		Helix	**Strand**	**Coil**
BCL2	207	81.0	0	19.9
BH3D	26	4.0	3.8	91.9
BCL2:BH3D 1:1	233	80.9	0	19.8
BCL2:BH3D 1:10	467	76.3	0.1	24.9
BCL2:BH3D 2:1	440	80.9	0	20.2
DS	26	0.9	10.4	83.1
BCL2:DS 1:1	233	66.6	0	34.7
BCL2:DS 1:10	267	44.6	11.4	45.1
BCL2:DS 2:1	440	80.9	0	19.3

3.3.5. BECN1 G120E+D121A Abrogates Autophagy Down-regulation by BCLXL but not M11

A comparison of complex structures of the BECN1 BH3D bound to γHV68 M11, a viral BCL2 homolog (Ku, Woo et al. 2008, Sinha, Colbert et al. 2008) or BCLXL (Feng, Huang et al. 2007, Oberstein, Jeffrey et al. 2007), a cellular BCL2 homolog, demonstrates that each interaction involves the same twelve BECN1 residues. Of these twelve residues, the six residues (L112, L116, K117, G120, D121 and F123) that have the most extensive interactions are also important for BCL2 interaction based on the ITC results above (Figure 3.4, Table 3.2). Therefore, we created the following mutant BECN1 expression plasmids: L112A, L116A, K117A, G120E, F123A and G120E+D121A to investigate their roles in BCL2 homolog (BCLXL and M11) mediated autophagy inhibition in MCF7 cells. Expression of all BECN1 mutants was comparable to that of WT BECN1 in both starvation and nutrient-rich conditions (Figure 3.6A). BCLXL and M11 also expressed comparably in both starvation and nutrient-rich conditions.

MCF7 cells were used to measure the autophagy levels because this cell line expresses low levels of endogenous BECN1 and does not initiate starvation-induced autophagy unless BECN1 is ectopically expressed (Liang, Jackson et al. 1999, Liang, Yu et al. 2001, Furuya, Yu et al. 2005, Pattingre, Tassa et al. 2005) (Figure 3.6). Due to the deficiency of the endogenous BECN1 expression in MCF7, we can use it to assay the effects of BECN1 mutants on autophagy. Earlier studies have utilized multiple diverse methods to conclusively demonstrate that in starvation conditions, cellular and viral BCL2 homologs, including BCLXL and M11, reduce autophagic flux by binding BECN1 (Pattingre, Tassa et al. 2005, Erlich, Mizrachy et al. 2007, Maiuri, Le Toumelin et al. 2007, Ku, Woo et al. 2008, Ku, Woo et al. 2008, Sinha, Colbert et al.

2008, Wei, Pattingre et al. 2008, Pattingre, Bauvy et al. 2009). Therefore, here we monitored autophagy levels simply by quantifying the change in cellular localization of a GFP-tagged, transiently expressed mammalian autophagy-specific marker, LC3 (GFP-LC3) from a diffuse cytoplasmic distribution to membrane-localized punctae corresponding to autophagosomal structures (Figure 3.6)

Transient expression of WT BECN1 in MCF7 cells led to a marked increase in autophagy upon starvation ($p = 6.0\times10^{-4}$ for starved versus nutrient-rich cells; Figure 3.6B-D). Basel autophagy (Figure 3.6E) levels in nutrient-rich media are typically much lower and less consistent than in starvation conditions. Therefore, here we focus on the autophagy levels observed in starvation conditions. The levels of autophagy mediated by each BECN1 mutant tested was comparable to that mediated by WT BECN1 (ranging between $p = 0.11$ to 0.93 for mutants versus WT BECN1; Figure 3.6B).

The transient co-expression of either BCLXL or M11 with BECN1 was used to assay the ability of these two homologs to down-regulate autophagy upon expression of each BECN1 mutant (Figure 3.6). Starvation-induced, BECN1-dependent autophagy is significantly down-regulated by ectopic expression of either BCLXL ($p = 3.3\times10^{-4}$ for BCLXL versus no BCLXL transfection; Figure 3.6C) or M11 ($p = 4.3\times10^{-3}$ for M11 versus no M11 transfection; Figure 3.6D), as has been previously shown (Pattingre, Tassa et al. 2005, Ku, Woo et al. 2008, Sinha, Colbert et al. 2008). When co-transfected with WT BECN1, both M11 and BCLXL significantly down-regulate starvation-induced autophagy (Figure 3.6 C-D), but in general, BECN1 BH3D mutations are less deleterious for the M11-mediated down-regulation of BECN1-dependent autophagy.

Under starvation conditions, BCLXL down-regulates autophagy mediated by BECN1 K117A as effectively as that mediated by WT BECN1 ($p = 0.50$ for K117A versus WT BECN 1; Figure 3.6C). However, BCLXL–mediated down-regulation of autophagy is less pronounced upon expression of BECN1 L112A ($p = 0.062$ for L112A versus WT BECN1) or G120E ($p = 0.012$ for G120E versus WT BECN1) (Figure 3.6C). Amongst the BECN1 single mutants, the most significant abrogation of BCLXL–mediated down-regulation of autophagy was observed upon expression of the BECN1 F123A ($p = 2.4\times10^{-3}$ for F123A versus WT BECN1) and BECN1 L116A ($p = 2.1\times10^{-3}$ for L116A versus WT BECN1; Figure 3.6C).

Similar to BCLXL, expression of the BECN1 K117A ($p = 0.16$ for K117A versus WT BECN1) did not affect M11-mediated down-regulation of autophagy (Figure 3.6D). M11–mediated autophagy down-regulation is significantly weaker upon expression of the BECN1 F123A ($p = 0.011$ for F123A versus WT BECN1) and BECN1 L112A ($p = 6.5\times10^{-4}$ for L112A versus WT BECN1). The most significant abrogation of M11–mediated autophagy down-regulation is observed when BECN1 L116A was expressed ($p = 0.043$ for L116A versus WT BECN1).

Surprisingly however, and contrary to expectations from structural analysis, M11 effectively down-regulates autophagy upon expression of the G120E single mutant ($p = 0.031$ for G120E versus WT BECN1). Due to the previous cellular co-immunoprecipitation assays showing that BECN1 G120A+D121A binds to M11 (Sinha, Colbert et al. 2008), we expected that mutation of G120 to a large and negatively-charged Glu residue would disrupt binding to both BCLXL and M11, consequently abrogating the down-regulation of autophagy by these BCL2 homologs. However, our data indicate that unlike BCLXL (Figure 3.6 C), the M11

binding site appears to accommodate the Glu side chain (Su, Mei et al. 2014), allowing M11 to effectively down-regulate autophagy mediated by G120E BECN1 (Figure 3.6D).

Our ITC data (Figure 3.4 and Table 3.2) show that DS BH3D disrupts the interaction between BECN1 BH3D and BCL2. We then further examined the role of D121 in the context of the G120E mutation, by assaying the ability of BCLXL and M11 to down-regulate autophagy mediated by a BECN1 G120E+D121A double mutant. As expected, expression of the BECN1 G120E+D121A abrogates BCLXL-mediated autophagy down-regulation ($p = 7.9\times10^{-4}$ for double mutant versus WT BECN1), which is comparable to the effect observed upon expression of the BECN1 L116A (Figure 3.6C). However, in complete contrast to BCLXL, M11 effectively down-regulates autophagy mediated by the BECN1 double mutant ($p = 0.23$ for double mutant versus WT BECN1; Figure 3D). Thus, the G120E+D121A BECN1 enables selective inhibition of autophagy by M11.

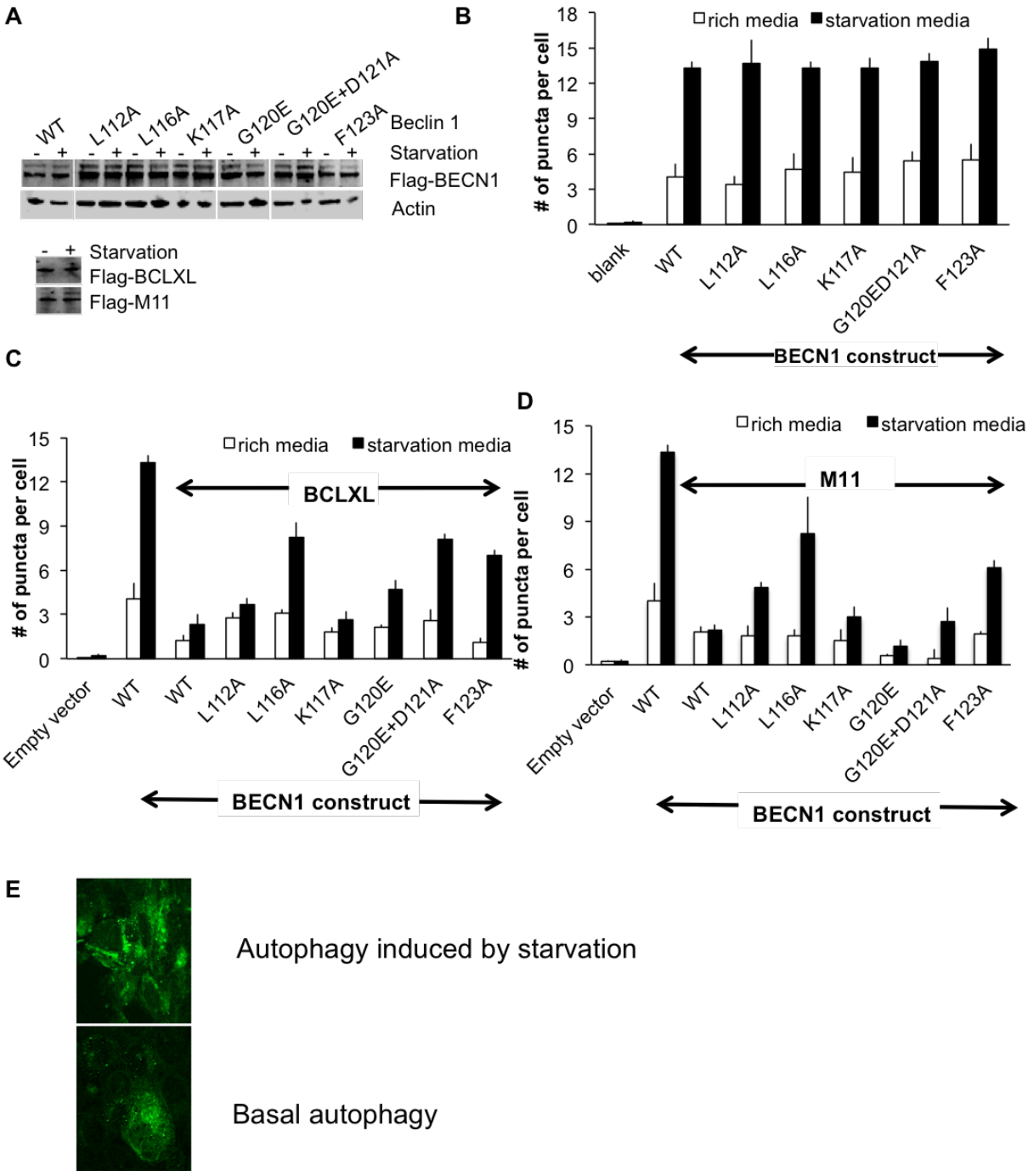

Figure 3.6. The effect of BECN1 BH3D mutants on starvation-induced autophagy.
(A) Western blot of Flag-BECN1, Flag-BCLXL and Flag-M11 expression in MCF7 cells under both nutrient rich and starvation-induced conditions; Quantification of the number of fluorescent GFP-LC3 puncta per cell in both rich media (white bar) and starvation media (black bar) cotransfected with (B) GFP-LC3, WT and mutant BECN1; (C) GFP-LC3, WT and mutant BECN1, and BCLXL; (D) GFP-LC3, WT and mutant BECN1, and M11. (E) Representative images of GLP-LC3 labeled puntae in MCF7 cells of basal and starvation-induced autophagy.

3.3.6. The BECN1 BH3D Interacts with the VMP1 ATGD with a Moderate Affinity without Conclusive Conformational Changes in Either Peptide

Since the interaction between BCL2 and BECN1 BH3D (residues 105-130) is disrupted when the VMP1 ATGD binds to BECN1 residues 88-150 (Ropolo, Grasso et al. 2007, Molejon, Ropolo et al. 2013), we proceeded to investigate the interaction between the VMP1 ATGD and BECN1 BH3D using ITC (Figure 3.7A). The VMP1 ATGD (EZBiolab, Carmel, IN) and BECN1 BH3D (RS synthesis, Louisville, KY) interacts with a moderate affinity of K_d=11.4 μM (Table 3.5), similar to the binding affinity of K_d=10.4 μM between BCL2 and BECN1 BH3D (Figure 3.3A and Table 3.2).

Subsequently, Yue Li repeated this work. She measured a high binding affinity of K_d =1.3 μM between VMP1 ATD (EZBiolab, Carmel, IN) and BECN1 BH3D (RS synthesis, Louisville, KY) (Figure 3.7B and Table 3.4 and 3.5). However, this dissociation constant may be inaccurate because the titration started to saturate after the first injection, indicating that the concentration of the ATGD in calorimeter cell was too low (Figure 3.7B upper panel). This result is probably due to the inaccurate measurement of the VMP1 ATGD concentration. Since the VMP1 ATGD has only one Phe, it has a low extinction coefficient, which may have led to an inaccurate measurement of the VMP1 ATGD concentration.

Table 3.4. Differences in ITC experiments performed to assess BH3D:ATGD interaction.

	By Yang	By Yue
Method of estimating ATGD concentration	VMP1 ATGD peptide powder was weighed, and then dissolved in a fixed volume of buffer. Concentration was calculated by dividing the peptide mass dissolved by buffer volume.	VMP1 ATGD peptide powder dissolved into the buffer, then concentration of solution assessed by measuring the OD_{280}.
Method of estimating BECN1 BH3D concentration	BH3D powder was weighed, and then dissolved in a fixed volume of buffer. Concentration was calculated by dividing the peptide mass dissolved by buffer volume.	BH3D powder was weighed, and then dissolved in a fixed volume of buffer. Concentration was calculated by dividing the peptide mass dissolved by buffer volume.
BECN1 BH3D concentration	400 μM	1 mM
VMP1 ATGD concentration	40 μM	100 μM
Buffer used	50 mM HEPES, pH 7.5, 150 mM NaCl, and 2 mM BME	25 mM HEPES, pH 8.0, 150 mM NaCl, and 2 mM BME
Temperature (°C)	25	20
Stir speed	250 rpm	250 rom

Lastly, when Yue repeated the experiment using newly purchased BECN1 BH3D from another supplier (EZbiolab), no binding was detected. Meanwhile, in order to enable quantification of absorbance of the peptide solution at A_{280}, we designed a VMP1 ATGD peptide with three extra residues 'GWG' at the N terminus to increase the extinction coefficient. However, GWG-VMP1-ATGD also does not bind the newly ordered BECN1 BH3D (Figure 3.7C and Table 3.5). Since Co-IP experiments show that BECN1 residues 88-150 interact with the VMP1 ATGD (Molejon, Ropolo et al. 2013), we also measured the interaction between MBP•BECN1 1-135 and the VMP1 ATGD by ITC. Contrary to our expectation, no interaction was detected between the VMP1 ATGD and the larger BECN1 construct (Table 3.5). These inconclusive binding results might result from the inconsistent peptide quality.

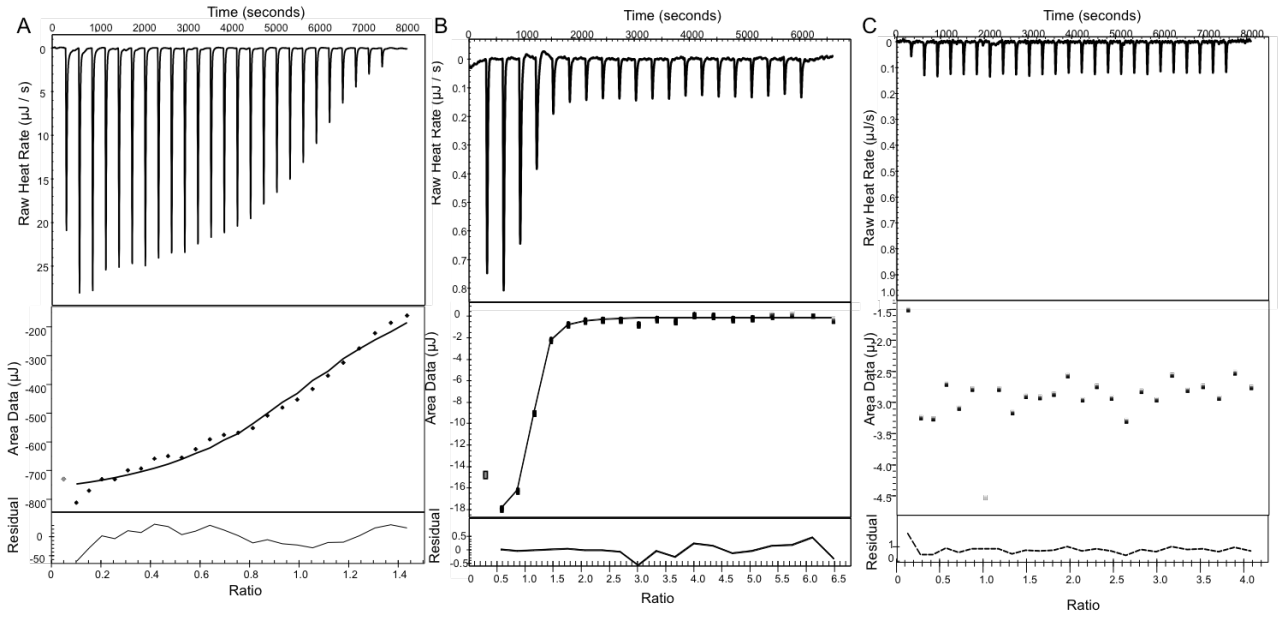

Figure 3.7. ITC data of BECN1 BH3D peptide titrated into VMP1 ATGD peptide.
The upper panel shows the raw data and lower panel shows the fitting curve using NanoAnalyze software for (A) WT VMP1 ATGD with BECN1 BH3D, (B) WT VMP1 ATGD with BECN1 BH3D repeated by Yue Li, and (C) GWG-ATGD with BECN1 BH3D.

Table 3.5. Summary of the thermodynamic parameters for binding of VMP1 ATGD to BECN1 BH3D or MBP•BECN1 1-135.

	BECN1 BH3D					MBP•BECN1 1-135				
	K_d (µM)	ΔH (kJ/mol)	ΔG (kJ/mol)	ΔS (J/K•mol)	n	K_d (µM)	ΔH (kJ/mol)	ΔG (kJ/mol)	ΔS (J/K•mol)	N
WT ATGD	11.4± 3.2	-181± 49.8	-28.4± 0.66	511±170	1.00± 0.01					
WT ATGD (Yue Li's work)	1.3	-3.8	-18.9	99.8	1	No binding	--	--	--	--
GWG-ATGD (Yue Li's work)	No binding	--	--	--	--					

The impact of potential interaction between the BECN1 BH3D and VMP1 ATGD on the secondary structure content of each domain was assessed by CD spectroscopy. Analysis of the CD spectrum recorded from VMP1 ATGD indicates that it contains 4 residues α-helical

conformation, 1 residue in β-strand and 16 residues in coil (Table 3.6). As described before, the BH3D has 1 residue in α-helix and β-strand, and 24 residues in coil (Table 3.6). Since it requires at least 6 residues to form a stable α-helix or β-strand (Kabsch and Sander 1983, Frishman and Argos 1995), neither peptide contains enough residues to form those secondary structures. So both BECN1 BH3D and VMP1 ATGD remain highly disordered in solution (Figure 3.8 and Table 3.6).

Next, we mixed the BH3D and ATGD in a 1:1 molar ratio at one concentration lower than the K_d and three concentrations higher than the K_d (Table 3.5 and 3.6). The concentrations of BH3D and ATGD mixture used were 7.65 μM, 30μM, 100μM and 300μM respectively (Figure 3.8). However, none of these concentrations induced an obvious conformational change (Figure 3.8). A negative peak at ~197 nm was observed in all CD spectra, indicating significant random coil content (Figure 3.8). When calculating the secondary structure content by SELCON3 (Sreerama and Woody 1993, Sreerama, Venyaminov et al. 1999), we found that the 100 μM mixture has the highest helical content (14 residues) and the lowest random coil content (29 residues), while the β-strand content fluctuates, but lacks sufficient residues to form a stable β-strand, under different concentrations, (Table 3.6). These results suggest that the interaction between two IDRs may slightly increase the helical content (from 3 residues to 14 residues) at the expense of coil content. However, under all concentrations the mixture is highly disordered, with more than 61% of the residues being random coil.

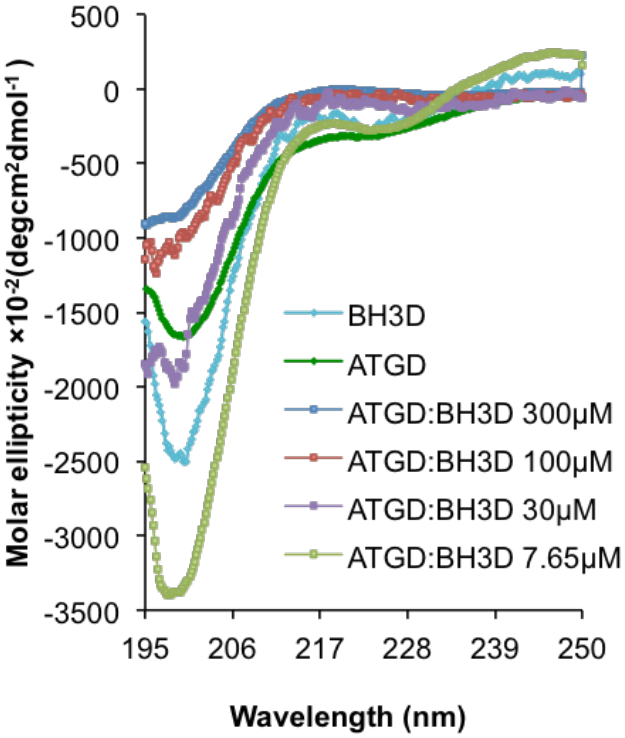

Figure 3.8. CD spectra of VMP1 ATGD complex with BECN1 BH3D.
ATGD and BH3D were mixed in a molar ration of 1:1 with different concentrations of 300μM, 100μM, 30μM and 7.65μM.

Table 3.6. Secondary structure contents analysis of CD spectra for VMP1 ATGD and BECN1 BH3D complexes.

Constructs	Residue number	**Percentage of the secondary content (%)**		
		Helix	Strand	Coil
BECN1 BH3D	26	4.0	3.8	91.9
VMP1 ATGD	21	20.1	4.8	79.1
BH3D:ATGD (7.65μM)	47	6.7	12	81.4
BH3D:ATGD (30 μM)	47	17.1	7.7	77.6
BH3D:ATGD (100 μM)	47	30.3	7.4	61.5
BH3D:ATGD (300μM)	47	27.8	12.1	63.2

3.4. Discussion

In Chapter 2, we demonstrated, based on our 1D-NMR and CD spectra, that the BECN1 IDR extends through the BH3D beyond the conservative consensus IDR boundaries of 42-115. The first half of the BECN1 BH3D overlaps with the consensus IDR, while the second half constitutes an Anchor region. In this chapter, we successfully purified two BECN1 IDR-containing recombinant proteins and demonstrated that the prediction of the BECN1 consensus IDR in Chapter 2 is correct. Although our CD spectra show that there might be some structure in BECN1 residues 1-104, recently published NMR data show that residue BECN1 residues 1-150 are disordered (Lee, Perugini et al. 2016). It is possible that the highly ordered MBP at the N-terminus of our IDR-containing proteins resulted in overestimation of helical content since CD spectra may not accurately characterize secondary structure content in the presence of high helical content (Kelly, Jess et al. 2005).

The previously identified BH3D, comprising residues 107-128, is required and sufficient for binding to BCL2 homologs, and for autophagy inhibition by BCL2s (Feng, Huang et al. 2007, Maiuri, Le Toumelin et al. 2007, Oberstein, Jeffrey et al. 2007). The binding of the BECN1 BH3D to BCL2s facilitates the formation of a 4-turn helix in the BH3D. Therefore, the BECN1 BH3D is an α-MoRF as previously also shown for the BIM BH3D (Liu, Dai et al. 2003). Strikingly, in yeast, which do not encode BCL2s, the IDRs of BECN1 (called ATG6 or VPS30 in yeast) appear to lack BH3Ds (Sinha and Levine 2008). It is likely that other proteins interact with the IDR of ATG6/VPS30 to regulate autophagy in yeast. Considering the high sequence variability and structural flexibility of IDRs, it might enable IDRs to interaction with different proteins and adopt different functions.

We also showed in Chapter 2 that the last 13 residues (residues 116-128) of the 26-residue BECN1 BH3D appear to compose an Anchor region. Although the Anchor region constitutes only half the BH3D, it bears four of five residues that are critical for binding BCL2 (Table 3.3). We also note that L112 outside the Anchor region is also required for BCL2 interaction. Since the BECN1 BH3D is an α-MoRF (Figure 3.3), these results illuminate a distinction between Anchor regions and MORFs: Anchor regions may constitute the entire MoRF, or only a part of the MORF such as BH3D Anchor region that nucleates concomitant folding and binding of a larger IDR. It is probable that the BH3D Anchor region transitions between helical and disordered conformations on time scales faster than CD and NMR measurements, with a helical conformation stabilized only upon binding to BCL2s. The concomitant binding and stabilization of the BH3D Anchor region as a helix may then promote helicity in the remaining BH3D, which is in turn, further stabilized by BCL2 interactions. Abrogation of binding to BCL2, especially by mutations within the BH3D anchor region, prevents the formation of stable helical conformation in the BH3D (Figure 3.7 and Table 3.3). Beyond the BH3D Anchor region, there are four other Anchors regions in BECN1. So in the next chapter, we will further investigate the role of some of these interaction motifs to elucidate the function of BECN1 as a protein interaction hub.

Autophagy activation promotes survival during nutrition deprivation (Xu, Wu et al. 2013), while disruption of autophagy may also cause diseases, especially cancers (Yang, Chee et al. 2011). Therefore, it is important to study the BCL2:BH3D interaction for a better understanding of autophagy regulation. The BH3D, despite lacking any residues invariant amongst BECN1 homologs, bears residues conserved amongst BH3Ds: L112, L116, G120,

D121 and F123. The biophysical and biochemical experiments show that substitutions of these residues will decrease or abrogate the interaction between BECN1 and BCL2 homologs.

Our cellular autophagy assays show that down-regulation of autophagy mediated by BCL2 homologs can be inhibited by disrupting the interaction between BECN1 and BCL2s, especially by mutating residues in the Anchor region. Most residues in the Anchor region display similar regulatory effects on both BCLXL- and M11-mediated autophagy. However, the BECN1 G120E+D121A double mutant permits BCLXL-mediated autophagy inhibition under starvation condition while abrogating M11-mediated autophagy inhibition, indicating the BH3D-derived DS peptide might selectively bind to viral BCL2. The BAK BH3D derived mimetic ABT737 was shown to induce autophagy by disrupting the interaction between the BECN1 BH3D and cellular BCL2s (Maiuri, Le Toumelin et al. 2007). Our data might provide a new drug design method to mimic the BECN1 BH3D to selectively bind to viral BCL2 (M11) instead of cellular BCL2 (BCLXL), which could provide a potential therapeutic for use in cancer treatment.

Our attempts to use ITC to characterize the VMP1 ATGD:BECN1 BH3D interaction were inconclusive, apparently due to inconsistencies in the behavior of different batches of peptides. Though the interactions between two IDRs are occur frequently (Shimizu and Toh 2009), the features of this interaction are not fully understood.

In addition, although BH3D appears to be an α-MoRF upon binding to BCL2, perhaps it may be a σ-MoRF in the context of binding to VMP1 ATGD. Different conformational transitions have been seen in p53, of which residues 383-384 form a β-strand with two residues of the Sir2 enzyme (Avalos, Celic et al. 2002), and residues 378-384 have been shown to become helical upon binding Ca^{2+}-bound S100B (ββ) (Rustandi, Baldisseri et al. 2000). Therefore, the binding partners may determine the conformational changes of the BECN1 BH3D. It is possible

that the BECN1 BH3D is also a σ-MoRF that forms a stable coil upon binding to the VMP1 ATGD. On the other hand, we found that the VMP1 ATGD is not predicted to contain an Anchor region (data not shown here) that is likely to be stabilized in ordered structures upon binding (Meszaros, Simon et al. 2009). Therefore, it is also possible that the absence of an Anchor region in the VMP1 ATGD prevents a disorder-to-order transition as is observed in other IDRs lacking Anchor regions (Glover, Mei et al. 2016). Thus, further investigation of the interaction of VMP1 and VMP1:BECN1 complex is needed to further elucidate the conformational changes associated with the interaction between BECN1 and VMP1.

CHAPTER 4. TO PROBE THE STRUCTURE OF BECN1 RESIDUES 141-171, AND THEIR ROLE IN PROTEIN INTERACTION AND AUTOPHAGY REGULATION

4.1. Introduction

In the previous chapters, we have shown that the BECN1 IDR (residues 42-130) is poorly conserved amongst homologs. Residues 105-130 within the IDR constitute a BH3D, a functional domain necessary and sufficient for binding to diverse BCL2 homologs (Maiuri, Criollo et al. 2007, Sinha and Levine 2009). On the other hand, BECN1 residues 136-450 are highly conserved (Furuya, Yu et al. 2005, Huang, Choi et al. 2012).

Residues 141-171 located between the BH3D and the CCD were previously predicted to be part of the CCD (Liang, Jackson et al. 1999), but structural delineation of the boundaries of the BH3D (Sinha and Levine 2009) and CCD (Li, He et al. 2012) indicate that these residues comprise an independent domain. Here we report our structural, biophysical and functional studies characterizing the human BECN1 domain between the BH3D and CCD. We have used various methods: X-ray crystallography, CD spectroscopy, double electron-electron resonance (DEER)-electron-paramagnetic resonance (EPR) spectroscopy and SAXS to demonstrate that, while the C-terminal half of this domain forms an α-helix, the N-terminal half is disordered in the absence of a binding partner. Therefore, we name residues 141-171 the flexible helical domain (FHD). Interestingly, the FHD crystal structure and SAXS data indicate that the BECN1 FHD trimerizes in the absence of a binding partner. In order to better understand FHD conformations in the absence of binding partners we performed long time-scale molecular dynamic (MD) simulations, which based on fits of different conformers to the experimental SAXS data, also suggests that the FHD appears to exist as a trimer, wherein each FHD has a helical C-terminal part and an flexible N-terminal region that transiently samples helical

conformations. Highly conserved FHD residues map to one face of the helical part of the FHD, suggesting that this domain may be involved in binding. Additionally, we find that the FHD is predicted to fold upon binding, and show that this region undergoes environment-influenced disorder-to-helix transitions. Furthermore, we demonstrate that these conserved FHD residues are important for binding to AMBRA1, a WD40 protein that that has been shown to bind to this region of BECN1. Lastly, and most importantly, we show that conserved FHD residues are critical for starvation-triggered up-regulation of autophagy. In sum, our results indicate that the BECN1 FHD comprising residues 141-171 is partially disordered, but likely undergoes a disorder-to-helix transition positioning all conserved residues in this region on one face of the helix, which is essential for binding to appropriate protein partners, and for the starvation-induced up-regulation of autophagy.

4.2. Materials and Methods

4.2.1. Production of BECN1 Constructs

The human BECN1 FHD (residues 141-171) (Figure 4.1) was chemically synthesized and purified using HPLC to >95% purity as confirmed by electrospray mass spectrometry (Protein Chem. Tech. Core, UTSW or EZBioLabs). A 1 mM peptide stock solution in 25 mM HEPES pH 7.5, 150 mM NaCl, 2mM β-mercaptoethanol was prepared. For EPR analysis, chemical synthesis was used to obtain an FHD construct that includes a Cys preceding the FHD, while C159 was altered to a Ser.

The BECN1 CCD (residues 175-265) and FHD-CCD (residues 141-265) were cloned between the BamHI and NotI restriction enzyme sites of the pMBP-Parallel-1 vector (Sheffield, Garrard et al. 1999). BL21(DE3)pLysS cells were transformed by expression vectors and grown at 37°C to an OD_{600} of ~0.8 prior to induction of recombinant protein expression by addition of

0.5 mM IPTG at 20 °C and continue incubating for 16~18 hours. Soluble MBP-tagged fusion protein was purified from clarified crude cell lysate by amylose affinity chromatography. The MBP tag was removed by on-column cleavage using tobacco etch virus (TEV) protease. Subsequently, the protein was purified to homogeneity by SEC, using a 16/60 Superdex200 or 10/300 Tandem Superdex 200+75 (GE Lifesciences, Pittsburgh, US) columns. The total yield of BECN1 CCD and FHD-CCD are 2mg/L, 4.7mg/L and 1.25mg/L, respectively.

4.2.2. Sequence Analysis

Sequences of BECN1 homologs from eight diverse eukaryotes: *Homo sapiens, Mus musculus, Gallus gallus, Zenopus laevis, Drosophila melanogaster, Caenorhabditis elegans, Arabidopsis thaliana, and Saccharomyces cerevisiae*, were identified by BLASTP searches of Genomic RefSeq Protein databases (http://blast.ncbi.nlm.nih.gov/) for each organism. Multiple sequence alignment of these orthologs was performed with Jalview (http://www.jalview.org/). Disordered regions and Anchor regions within the FHD were predicted using the intrinsically unstructured protein predictor, IUPred, (http://upred.enzim.hu/), and ANCHOR (http://anchor.enzim.hu/) respectively (Dosztányi, Csizmok et al. 2005, Dosztányi, Mészáros et al. 2009, Meszaros, Simon et al. 2009).

4.2.3. CD Spectroscopy

CD spectra were recorded at 4 °C between 195 and 250 nm using a 300 μL quartz cell with a 0.1 cm path length on a Jasco J-815 spectropolarimeter equipped with thermoelectric temperature control. BECN1 constructs were diluted to 50-200 μM in CD buffer (10 mM potassium phosphate, pH 7.6; 100 mM ammonium sulfate). 2,2,2-trifluoroethanol (TFE) (Sigma Aldrich, St. Louis, MO) was premixed and incubated with three BECN1 constructs (FHD, CCD

and FHD-CCD) in CD buffer at different % v/v ratios: 0%, 10%, 25% or 40%. The data were analyzed using SELCON3 from the CDpro program suite (Sreerama, Venyaminov et al. 2001)

4.2.4. DEER-EPR Data Collection and Analysis

C140 preceding the FHD and C165 in the FHD domain were labeled with the 1-oxyl-2,2,5,5-tetramethylpyrroline-3-methyl methanethiosulfonate spin label (Hubbell, Lopez et al. 2013). Unreacted spin label was removed by washing the peptide/label mixture through a 3 kDa-cutoff Millipore concentrator. The sample concentration for each EPR experiment was ~ 200 μM, with 20 % (v/v) glycerol mixed in as a cryogenic protectant. Immediately prior to data collection, the sample was flash-cooled in quartz capillaries using a liquid nitrogen bath. All DEER-EPR measurements were performed on an Elexsys 580 spectrometer (Bruker Corp., Billerica, MA) equipped with a Super Q-FTu Bridge, a Bruker ER 5107DQ resonator and a 10 W Q-band signal amplifier. The Oxford temperature controller and liquid nitrogen were used to maintain the experimental temperature at 80 K. A standard pulse sequence and operation procedure were used for DEER-EPR as described (Lopez, Yang et al. 2013), with pulse lengths adjusted to 16 and 32 ns for a $\pi/2$ and π pulse, respectively. The time domain signal collected for each sample was about 3 μs. DEER-EPR data were analyzed using a model-free maximum-entropy analysis approach by Christian Altenbach (http://www.chemistry.ucla.edu/directory/hubbell-wayne-l). The reliable maximum average distance extracted from the DEER data, $r_{max<r>}$, can be estimated using $r_{max,<r>} \approx 5x[t_{max}/(2ms)]^{1/3}$ nm, where t_{max} is the maximum length of time domain signal (Jeschke 2012). In our case , $r_{max<r>}$ is approximately 60 Å. This work was performed by Dr. Zhongyu Yang at UCLA.

4.2.5. Crystallization, X-ray Diffraction Data Collection and Structure Solution

BECN1 FHD crystals were grown at 20 °C by sitting drop vapor diffusion from a drop consisting of 1 µl of 10 mg/ml FHD in 25 mM HEPES, pH 7.5; 250 mM NaCl; 2 mM β-mercaptoethanol and 1 µl of reservoir solution, comprising 100 mM sodium citrate tribasic dihydrate, pH 5.6; 250 mM potassium sodium tartrate tetrahydrate; and 2.2 M ammonium sulfate. Cubic crystals were observed within 4 days and harvested after two months. The 41µm ×39µm×41µm crystals were cryo-protected with MiTeGen LV Cryo-oil (MiTeGen, Ithaca, NY) and immediately flash-cooled in liquid N_2. Diffraction intensities from these crystals were recorded at 100 K using 1 second exposures per 0.5° crystal rotation per image on a MARCCD 300 detector at a crystal-to-detector distance of 150 mm at beamline 23ID-D of GMCA@APS, ANL, Chicago. The data used to solve the structure were collected at an X-ray wavelength of 1.3776 Å in a 360° sweep from a single crystal. Data were processed using XDS (Kabsch 2010). Diffraction data statistics are summarized in Table 4.1. The structure was solved by S-SAD using SHELXD (Sheldrick 2010). The model was built using Coot (Emsley, Lohkamp et al. 2010) and refined in PHENIX (Adams, Afonine et al. 2010) (Table 4.1). The final refined structure is deposited in the PDB under PDB ID 5EFM.

4.2.6. SAXS data Collection and Analysis

SAXS data were recorded at the BioCAT beamline (ID18) (APS, Argonne, IL) on a Mar165-CCD detector, at a sample to detector distance of 2.5 m, thereby covering a momentum transfer range of $0.006\ Å^{-1} < q < 0.32\ Å^{-1}$. Static SAXS measurements were recorded for BECN1 constructs smaller than 50 residues by loading into a quartz capillary at various sample concentrations (4 mg/ml, 2 mg/ml, 1 mg/ml, and 0.5 mg/ml). For larger BECN1 constructs, we performed SEC in tandem with SAXS data collection, to ensure that the SAXS data was

collected from a homogeneous sample. 4 mg/ml protein was injected onto a SEC column (GL 10/300 Superdex 200) and SAXS data recorded by exposing the column exposed to the X-ray beam for 1 second with a periodicity of 5 seconds.

Scattering data were normalized to the incident X-ray beam intensity and scattering from buffer was subtracted prior to analysis using Igor Pro macros (Ilavsky and Jemian 2009). Data analysis was performed using the ATSAS program suite (Petoukhov, Franke et al. 2012) (http://www.emblhamburg.de/biosaxs/crysol.html). The program PRIMUS (Konarev, Volkov et al. 2003) in the ATSAS suite was used to calculate Guinier extrapolations to evaluate sample dispersity and calculate the radius of gyration (R_g) and Kratky plots to evaluate disorder within the sample. The program GNOM was used to plot the P(*r*) function from the Fourier inversion of the scattering intensity, *I*(q). The *P*(r) function was used to calculate the R_g and maximum particle size (D_{max}), and also for the reconstruction of *ab initio* envelopes by the application of ten cycles in DAMMIF (Franke and Svergun 2009). The resulting bead models were sequentially analyzed using DAMSEL, DAMSUP, and DAMAVER to compare and identify the most probable model, align all models to the most probable model, average these aligned models and compute a probability map with the averaged model then filtered using DAMMFILT (Volkov and Svergun 2003). CRYSOL (Svergun, Barberato et al. 1995) was used to compare theoretical scattering curves calculated for FHD monomer and trimer atomic structures against the experimental SAXS scattering curve. The FHD monomer and trimer structures were superimposed into the final bead models using the program SUPCOMB (Kozin and Svergun 2001).

4.2.7. MD Simulations

MD simulations were initiated from five different starting models. One model was comprised of the entire FHD monomer modeled as a disordered structure. In the other four models, the C-terminal end of the FHD was retained as a helix, as observed in the crystal structure. In two of these models, the FHD N-terminal residues 141-159 were modeled in a random coil conformation, while in the other pair, the N-terminal residues were modeled as an α-helix such that the entire FHD was a single helix. The models were then placed in different oligomeric states: either a monomer or the trimer observed in the crystal structure. Long time-scale MD simulations were performed for each of the models. The simulations are summarized in Table 4.3. Briefly, the parm99SB.ildn force field in the AMBER 12.0 suite of molecular modeling software was used, as it is particularly well suited for running long time-scale simulations. After modeling the structures using standard amino acid residues, and determining the protonation state for each residue at pH 7.0, each system was neutralized using counter-ions placed in a solvated box of TIP3P water molecules that was at least 12 Å from the protein. Final box sizes and the total number of atoms in each simulation system are detailed in Table 4.3 Each system was minimized and equilibrated as previously described (Ramanathan and Agarwal 2009). Production runs were carried out using the 'constant number of particles, volume and energy ensemble with particle mesh Ewald's technique for electrostatics and a 10 Å cut-off for Lennard-Jones interactions. The SHAKE algorithm was used to restrict motions of all covalently bound hydrogen atoms. Simulations were performed at 1 atm pressure and at 300 K temperature and the data from the simulations were stored every 0.02 ns. The simulations are summarized in Table 4.3. The resulting ensembles were compared to SAXS experimental data using CRYSOL (Svergun, Barberato et al. 1995). The free chi value was calculated using the algorithm from

SCÅTTER suite to obtain a better assessment of similarity (Rambo and Tainer 2013). This was performed by Dr. Arvind Ramanathan at Oak Ridge National Laboratories.

4.2.8. Co-IP

Highly conserved residues within the FHD of human BECN1 (Figure 4.1) were mutated by site-directed mutagenesis (Agilent Technologies) using the primers ordered from Integrated DNA Technologies. The Flag-tagged CMV2-AMBRA1 is changed to a HA-tagged CMV2-AMBRA1 using site-direct mutagenesis by first mutating out the Flag tag and then inserting the HA tag. 7×10^6 MCF7 cells were seeded in 10 cm culture dish and cultured overnight in DMEM with 10% FBS to 80% ~confluence. The cells were co-transfected with a total of 24 μg plasmids in a 3:1 molar ratio of Flag-tagged WT or mutant BECN1 and HA-tagged WT AMBRA1, using lipofectamine 2000 (Invitrogen) according to the manufacturer's instructions. After transfection, the cells were cultured in starvation media (EBSS) respectively for 4 hours. Cells were lysed in lysis buffer consisting of 50 mM Tris-HCl pH 7.9, 150mM NaCl, 1% Triton X-100, 1mM DTT protease inhibitor cocktail (Roche Applied Sciences) and 1mM PMSF. Cell lysates were centrifuged at 14,800g for 10 min at 4°C and the supernatants subjected to immunoprecipitation using mouse monoclonal anti-Flag M2 antibodies (Sigma), followed by incubation with Protein G beads (Invitrogen) overnight. The samples were then eluted by 2× Laemmli buffer and analyzed by SDS-PAGE, followed by western blot using rabbit polyclonal anti-HA antibodies (Y-11, Santa Cruz), and detection by ECL western blotting substrate (Thermo Fisher) and imaging by a Storm Imager (GE Lifesciences).

4.2.9. Autophagy Assays

Cellular autophagy levels were evaluated by monitoring cellular localization of GFP-tagged LC3 (Kabeya, Mizushima et al. 2000). 3.0×10^5 MCF7 cells were seeded in each

chamber of a 4-well culture slide (Millipore EZ slides) and cultured overnight in DMEM with 10% FBS, until ~80% confluency. The cells were co-transfected with a total of 4 μg plasmids comprising 1.6 μg GFP-LC3 and 2.4 μg BECN1 WT or mutant expression plasmids, using lipofectamine 2000 (Invitrogen, Carlsbad, CA) according to the manufacturer's instructions. After transfection, the cells were cultured in either rich (DMEM, 10% FBS, 2X amino acid mixture) or starvation (EBSS) media respectively for 4 hours. Cells were then fixed with 2% paraformaldehyde in PBS. GFP-LC3-positive puncta were observed under a fluorescent microscope (Zeiss AxioObserver Z1) and quantified by counting a minimum of 100 cells for duplicate samples per condition using Imaris (Bitplane AG, Zurich, Switzerland) in three independent repeats. The significance of alterations in autophagy levels was determined by a two-tailed, heteroscedastic student's *t-test*, wherein $p \leq 0.05$ is considered significant.

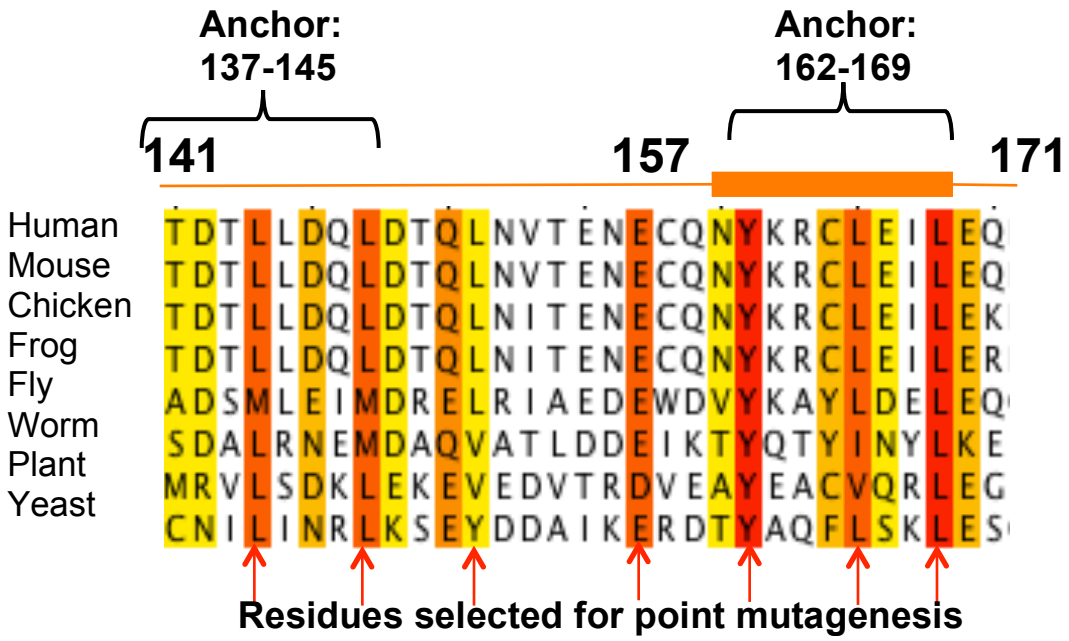

Figure 4.1. Sequence alignment of the BECN1 FHD from eight diverse eukaryotes. Residue numbers correspond to the human FHD. Yellow, orange and red backgrounds represent increasing sequence conservation with red corresponding to invariant residues. Secondary structure elements reported in this paper are displayed above the alignment with the orange line representing the disordered region and the orange cylinder representing the helical region. Residues predicted by the program ANCHOR (Dosztányi, Mészáros et al. 2009) to nucleate folding upon binding are indicated. Arrows indicate residues that were mutated to Ala for cellular assays.

4.3. Results

We applied CD spectroscopy, DEER-EPR, SAXS and X-ray crystallography to investigate the structural characteristics of the chemically synthesized BECN1 FHD (141-171) (Figure 4.1). Based on the sequence analyses, conserved residues (Figure 4.1) were mutated to alanine and their impact on AMBRA1 interaction and on autophagy was investigated by Co-IP and cellular autophagy assays respectively.

Table 4.1. X-ray diffraction data and refinement statistics.

Data collection	
Wavelength (Å)	1.3776
Data range (Å)	44.66-1.95
Space group	$P4_332$
Unit cell parameters	$a=b=c$=63.16 Å
Mosaicity (°)	0.093-0.200
Unique reflections	3514
Multiplicity	75.5 (78.1)
Completeness (%)	100 (100)
$CC_{1/2}$	1.00 (0.82)
[1]R_{meas}	0.16 (0.58)
I/σ_I	26.3 (1.8)
Refinement	
Model:	PDB ID: 5EFM
Residues	15
Water molecules	8
Sulfate molecules	1
Data Range (Å)	44.66-1.95
[2]R_{work} (%)	21.2
[2,3]R_{free} (%)	21.6
Average B-values (Å^2)	
Main Chain	46.4
Side Chain	61.4
Water	54.6
All Atoms	54.5
B-factor RMSDs between bonded atoms (Å^2)	
Main chain	5.722
Side Chain	11.287
RMSDs from target values:	
Bond Lengths (Å)	0.009
Bond Angles (°)	1.298
Ramachandran outliers	0

Values in parentheses pertain to the outermost shell of data.

[1] $R_{meas} = \sum_{hkl} (n/n-1)^{1/2} \sum_{h,i} |I_{hkl,i} - \langle I_{hkl} \rangle| / \sum_{hkl} \sum_{h,i} I_{hkl,i}$.

[2] R factor= $\sum_h |F_{obs} - |F_{calc}| / \sum_h |F_{obs}|$. [3] Test set for R_{free} consisted of 5.5 % of data.

4.3.1. The FHD is Partially Disordered in Solution

We first used CD spectroscopy to investigate the secondary structure of BECN1 FHD (Figure 4.2). SELCON3 was used to estimate secondary structure content since it is the best program for calculating random coil (Sreerama and Woody 2000). The results showed that FHD is 49.4% coil and 37.8% helix (Table 4.2). Although the secondary structure estimation shows it contains 17.8% β-strand (Table 4.2), that corresponds to five FHD residues in β-strand, which is not enough to form a stable β-sheet. Therefore, FHD likely contains 15-20 residues in coil.

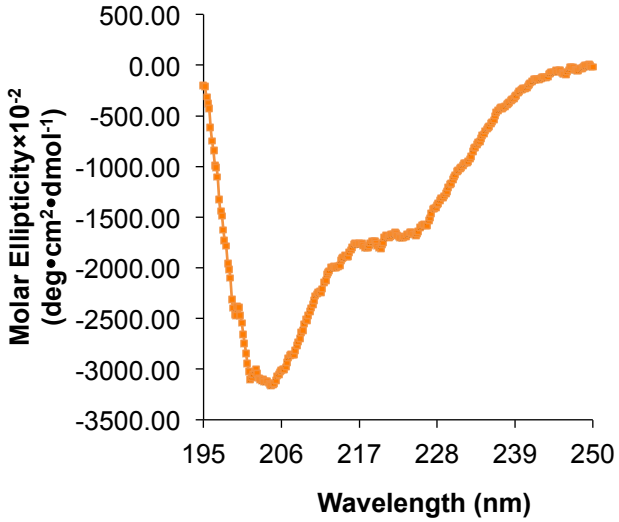

Figure 4.2. The CD spectra of BECN1 FHD.
The CD spectra of BECN1 FHD was collected between 195-250 nm and colored in orange.

In order to better understand the size and conformation of the FHD in solution, Dr. Zhongyu Yang at UCLA helped us to carried out residue-to-residue, intra-peptide distance measurement using DEER–EPR spectroscopy (Jeschke 2012) and Site-Directed Spin Labeling (Hubbell, Lopez et al. 2013). Residue C159 within the FHD was substituted with Ser, while C140, a residue preceding the FHD, and C165 located toward the FHD C-terminus, were spin-labeled with 1-oxyl-2,2,5,5-tetramethylpyrroline-3-methyl) methanethiosulfonate to create the spin labeled mutant 140R1/165R1, where R1 represents the spin label side chain. We analyzed

the time domain signals (Figure 4.3A) using a previously reported DEER data analysis program (Lopez, Yang et al. 2013). Since we anticipated that the FHD is structurally disordered, we used a Gaussian function to describe the inter-spin distance distribution in the data analysis. The resultant distance distribution extracted from the DEER data (Figure 4.3B) displays a broad spin-spin distance distribution, ranging from ~15 to 55 Å, qualitatively consistent with an intrinsically disordered, extended FHD structure. The DEER data were also analyzed using a model-free, unbiased analysis, which assumes that every distance between 15 and 100 Å contributes to the time domain signal, while the probability of each distance is plotted against the distance. Data analyzed by this approach also indicate an intrinsically disordered, extended FHD structure.

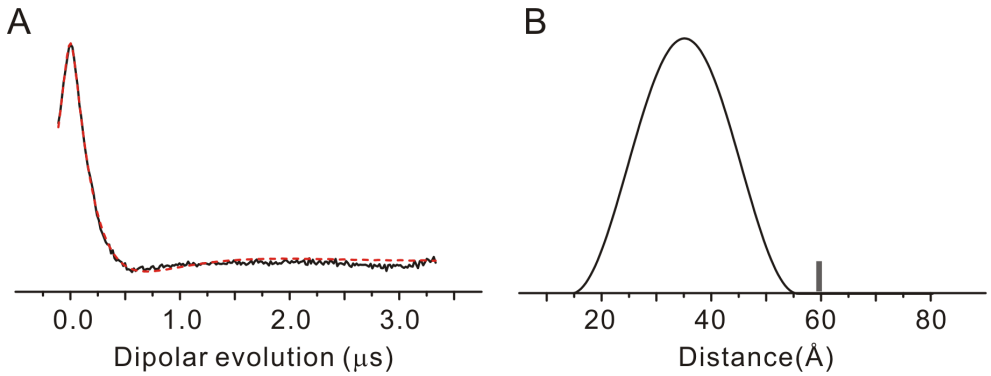

Figure 4.3. DEER-EPR data and data analysis on the spin labeled FHD.
(A) The time domain dipolar evolution from DEER (black curve). The data is analyzed by assuming that the distance distribution between the spin labels is a Gaussian function with the best fit shown by the red dotted curve. (B) The distance distribution derived from the analysis of the time domain signal in (A). The grey vertical bars indicate the approximate upper limit of reliable distances determined from DEER.

4.3.2. Only Half of the FHD Forms a 2.5-turn α-helix

We went on to investigate the atomic structure of FHD and were successful in crystallizing the construct comprising residues 141-171 (Figure 4.1). We finally got the cubic crystals with about 40 μm in each dimension after many trials with different conditions (Figure 4.4). These crystals belonged to the space group $P4_332$ with unit cell parameters of

a=*b*=*c*=63.2Å, and contained one copy of the BECN1 FHD per asymmetric unit (Table 4.1). The 2.0 Å crystal structure of the FHD was determined using Sulfur SAD methods. Consistent with the CD spectra, electron density was visible only for residues 157-171, of which residues 160-169 form a 2.5-turn amphipathic α-helix (Figure 4.5A). Electron density corresponding to residues 141-156 is missing, suggesting that similar to the BH3D preceding it (Chapter 3), this region may be partially unstructured in certain physiological contexts. Notably, the FHD was not identified as part of the consensus IDR delineated for BECN1 (Chapter 2), however, the programs IUPpred and PSIPRED predict that residues 141-152/154 are disordered.

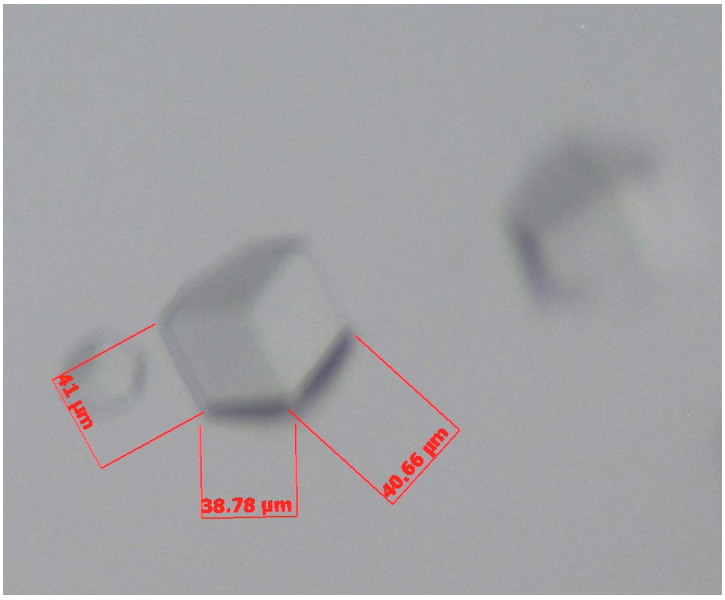

Figure 4.4. Cubic crystals of the BECN1 FHD.
The dimensions of the FHD crystal used to collect X-ray diffraction data is labeled in figure.

In the crystal structure, three FHD helices pack around the crystallographic three-fold to form a compact trimer (Figure 4.5B). The core of the trimer is stabilized by aromatic stacking of the conserved Y162 residues (Figure 4.5B) from each helix, with each Y162 being largely buried in the hydrophobic interface (Figure 4.5B). Other hydrophobic residues from each of the three helices, including conserved residues L166 and L169, also contribute to the hydrophobic packing

at the trimer center. The trimer is further stabilized by three disulfide bonds between C159 and C165 of adjacent FHD molecules. The formation of the trimer buries about one-third of the total surface area of 1773 $Å^2$ of each monomer.

One face of this trimer is negatively charged, primarily due to the glutamate at the C-terminus of each helix (Figure 4.5C). The opposite trimer face is positively charged, with the outside edge of this positive face bearing residues K163 and R164 from each monomer, and the center caving into a positively charged pocket created by the helix dipoles and lined by the side chain amides of N161 and backbone amides of Y162 from each FHD. A sulfate from the crystallization solution is bound at the crystallographic three-fold within this pocket (Figure 4.5C).

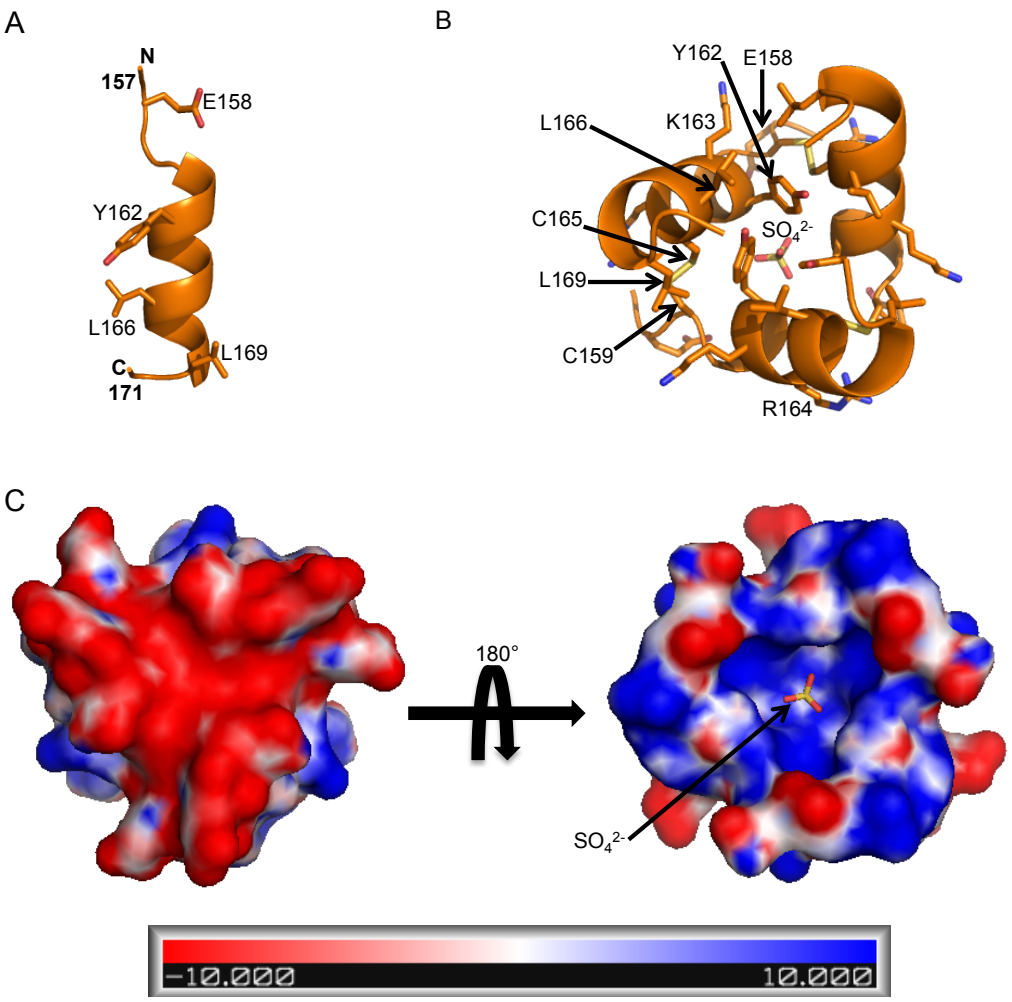

Figure 4.5. The FHD crystal structure.
(A) The FHD monomer. The FHD backbone is displayed in orange ribbon, while highly-conserved residues are labeled and rendered in stick, with atoms color-coded by type: C, orange; O, red; N, blue and S, yellow. This and all other molecular figures were made using PyMol. (B) The FHD trimer showing three molecules arranged around the crystallographic 3-fold are rendered as in (A). One set of highly conserved residues are labeled. (C) Electrostatic potential surface of the FHD trimer calculated using APBS. The figure on the left displays the face bearing the C-termini of the FHD monomers. The figure on the right displays the face bearing the N-termini of the FHD monomers. This face has a pocket that binds a sulfate molecule, rendered in stick and color-coded by atom type as in (A).

We then performed SAXS experiments to further investigate the size, shape and structure of the BECN1 FHD in solution. The Guinier plot of the SAXS data were linear in the region corresponding to 0.3*Radius of Gyration (R_g), indicating that the sample was not aggregated at concentrations analyzed. The R_g of the FHD, estimated from the Guinier plot and P(r)

distribution, was ~17 Å (Figure 4.6A, 4.6B), which is significantly larger than the R_g of 10 Å or ~12Å for the FHD monomer or trimer respectively, calculated from the crystal structure (Table 4.2). Similarly, the D_{max} obtained from the P(r) (Figure 4.6B) is 61Å (Table 4.2), nearly triple the length of the crystal structure (Table 4.2). This is consistent with the presence of additional disordered residues that were not visible in the crystal structure and the partial disorder estimated from analysis of the CD spectra. This partial disorder is confirmed by the Kratky plot (Figure 4.6C).

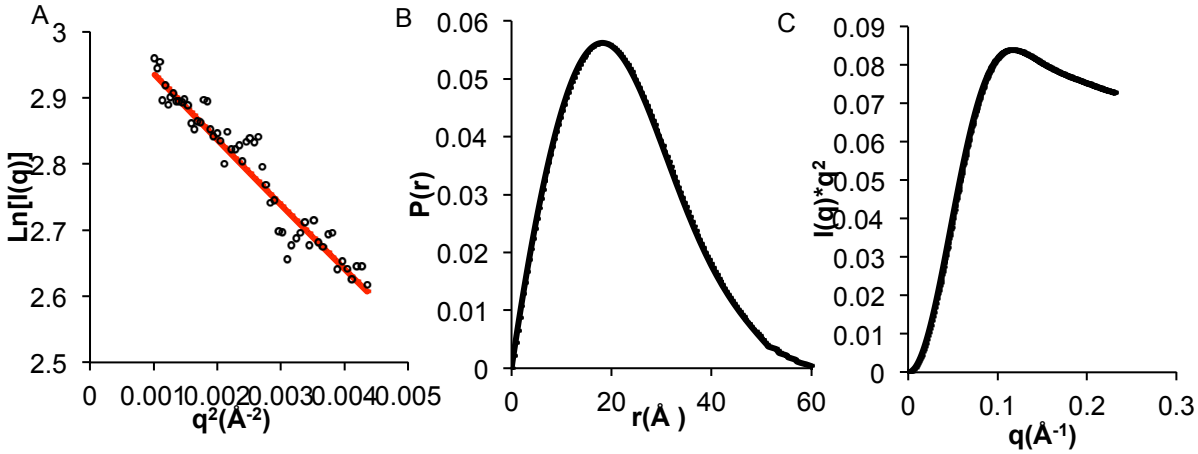

Figure 4.6. SAXS analysis of the BECN1 FHD.
(A) Guinier Plot. (B) P(r) pairwise distribution. (C) Kratky plot.

4.3.3. The FHD Appears to Transiently Sample Completely-helical Conformations

Next we fitted the crystal structures to the envelopes calculated from SAXS data. However, neither the FHD monomer, nor the trimer crystal structures fit well (χ^2 = 7.5 and 6.5 respectively) into molecular envelopes calculated from the SAXS data, leaving a lot of unoccupied space within the envelope indicative of disordered regions that were not modeled (Table 4.2, Figure 4.7).

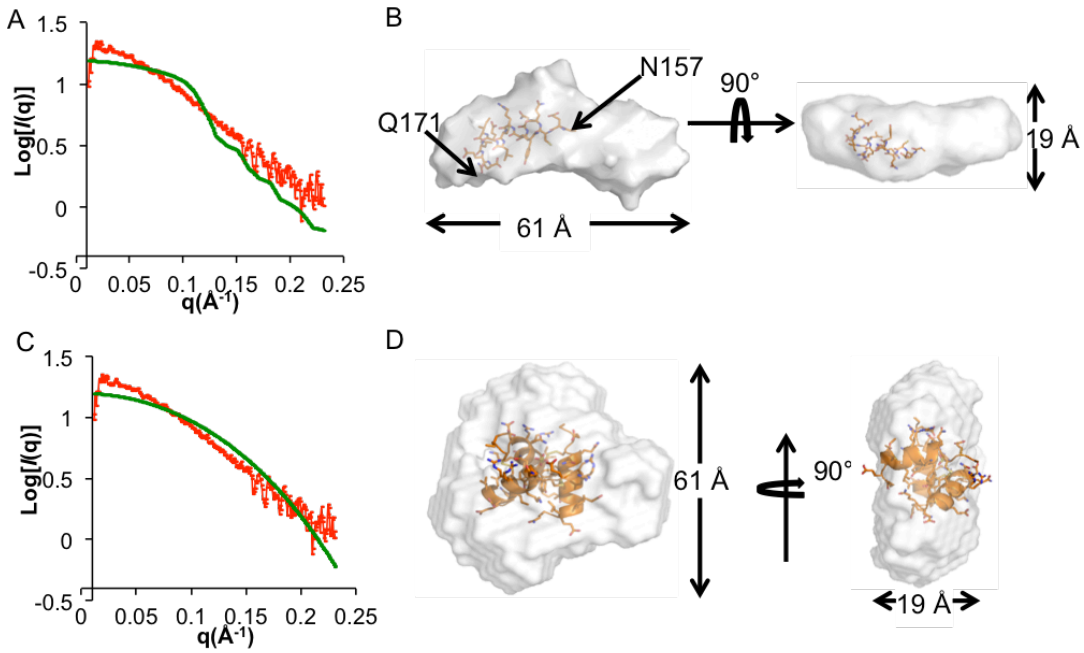

Figure 4.7. The FHD crystal structure fits poorly to the SAXS data.
(A) Comparison of the experimental scattering curve (red) with the theoretical scattering curve (green) calculated from the crystal structure of FHD monomer. (B) The FHD monomer crystal structure fitted to the SAXS envelope with P1 symmetry. (C) Comparison of the experimental scattering curve (red) with the theoretical scattering curve (green) calculated from the crystal structure of FHD trimer. (D) The FHD trimer crystal structure fitted to the SAXS envelope with P3 symmetry.

Table 4.2. Parameters of molecular parameters calculated from SAXS data and the X-ray crystal structure.

	Construct ->	FHD monomer	FHD trimer
From sequence	MW_T (KD)	3.7	11.1
SAXS parameters	Rg (Å)	17	
	P(r) R_g (Å)	17	
	D_{max} (Å)	61	
	MW from V_p (KD)	8	
	V_c ($Å^3$)	161	
	MW from V_c (KD)	12	
X-ray structure	Rg (Å)	10	12
	Length (Å)	22	22
χ^2	Atomic structure	7.5	6.5
	MD ensemble	~7	0.5-1.5
χ2 free	Atomic structure	9.0	13.3
	MD ensemble		1.0-3.1(FHD1) 1.6-3.2(FHD2)

MW_T: theoretical molecular weight from sequence; N/A: Not available.
*: For a single FHD conformer selected from two different starting models as described in text.

The SAXS analyses of the FHD provided gross structural details of its solution structure. To further probe the conformational heterogeneity and oligomerization of the FHD in solution and to enable atomistic characterization of the observed conformational disorder in FHD, we performed long time-scale all-atom MD simulations using five different FHD starting models (Table 4.3): (i) a completely disordered FHD monomer; (ii) a completely helical FHD monomer;

(iii) a part coil and part helical FHD monomer (as per the crystal structure); (iv) completely helical FHD trimer; and (v) part coil and part helical FHD trimer (as per the crystal structure). The sulfate was not included in the trimer models used for simulation. We found that regardless of the starting model, the C-terminus of the FHD retained, or folded into its helical state. Further, although the N-terminus tended to remain disordered, or unfold in simulations starting from models of a completely helical FHD; a majority of conformations sampled folded states during the course of the simulations.

We used a heuristic, similar to a recently developed approach (Chen and Hub 2014), to assess the fit of the MD conformational ensembles from different starting models to the experimental SAXS data using CRYSOL. In general, the scattering curves calculated from the ensembles of MD simulated conformations generated from the various monomer models did not fit well (average χ^2 of ~7), but the conformers generated from the trimer models fit the experimental SAXS curves quite well (average χ^2 of 2.7). This suggests that the FHD tends to form a trimer in solution. Therefore, we focused subsequent analyses on the simulations starting from the two trimer models.

In order to obtain a better fit to the SAXS experimental scattering curves, for each trimer simulation, we selected conformers with low χ^2 values (between 0.5 and 1.5) and reconstructed an ensemble representation of the FHD trimer. The free χ^2 values of the partial helical MD ensemble ranges from 1.0-3.1 while the completely helical MD ensemble has free χ^2 values ranging from 1.6-3.2 (Table 4.2). We fit both ensembles of conformers to the experimental data to obtain a better fit (Figure 4.8). Further, the ensembles of conformations that have the best fits show considerable heterogeneity (the partial coil partial helical ensemble) (Figure 4.8), including a high degree of conformational variation in residues 141-156, with many of the conformations

showing partial helices. These results strongly suggest that the FHD has an inherent propensity to interconvert between disorder and helical conformations.

Table 4.3. Summary of MD simulation parameters for the FHD system.

System	Conformer-state	Box size (Å^3)	# of atoms	Time Scale (μs)
FHD-monomer	Complete coil	66.3 x 46.9 x 45.2	14635	1.0
	Complete helical	66.3 x 46.9 x 45.2	14635	1.0
	Part-coil, part helix	66.3 x 46.9 x 45.2	14535	1.0
FHD-timer	Part-coil, part helix	70.0 x 72.8 x 61.5	32523	3.0
	Complete helical	55.3 x 71.4 x 70.3	28977	2.0

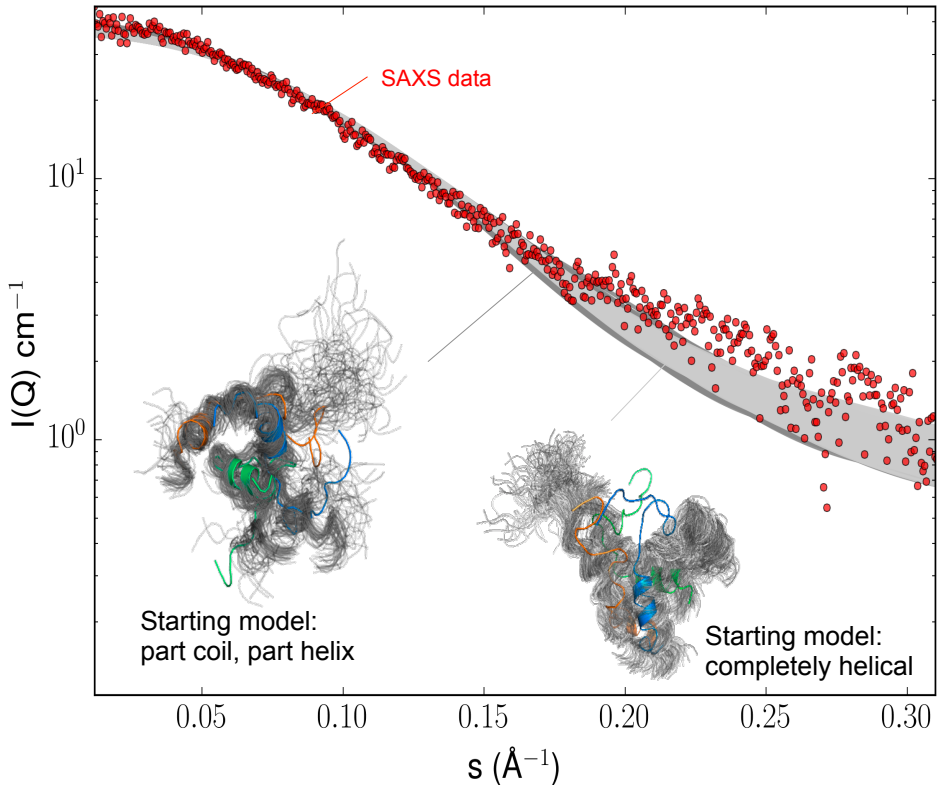

Figure 4.8. MD conformer ensembles of the FHD fit to experimental SAXS data.
The fits to the experimental SAXS data (red dots) are shown in dark grey and light grey for the MD simulations initiated from the part coil and part helical FHD trimer (left ensemble) and for the simulations initiated from the fully helical FHD trimer (right ensemble) respectively. An ensemble representation of conformers that show a good fit ($0.5 \leq \chi^2 \leq 1.5$) to the experimental SAXS data is shown for each set of simulations.

4.3.4. The FHD likely Undergoes a Binding-associated Disorder-to-helix Transition

The FHD has two invariant residues: Y162 and L169, as well as several highly conserved residues: L144, D146, L148, Q151, E158, and L166 (Figure 4.1). Of these, residues E158, Y162, L166 and L169 are ordered in the crystal structure. Y162, L166 and L169 map to one face of the FHD helix, while E158 maps to the coil preceding the helix (Figure 4.5A). Analysis by the program ANCHOR (Dosztányi, Mészáros et al. 2009) indicates that two regions of the FHD, residues 137-145 and residues 162-169 (Figure 1), may be energetically stabilized in ordered conformations upon binding to an appropriate partner. The BECN1 BH3D, which also contains an Anchor region, has previously been shown to be involved in protein interactions, and to nucleate a disorder-to-helix transition in the BECN1 BH3D upon binding to BCL2 (Chapter 3). Therefore, we decided to investigate whether the FHD is likely to become completely helical upon binding to a partner.

2,2,2-trifluoroethanol (TFE) is commonly used to mimic the hydrophobic environment experienced by proteins in protein-protein interactions (Buck, Radford et al. 1993, Buck 1998, Hua, Jia et al. 1998, Roccatano, Colombo et al. 2002); therefore, we measured CD spectra for the FHD, CCD, and FHD-CCD in the presence of increasing concentrations of TFE to determine if TFE treatment increased helicity (Bourhis, Johansson et al. 2004). Our CD spectra demonstrate that increasing TFE concentration results in increased helical content in the FHD and FHD-CCD (Figure 4.9, Table 4.4), with maximum helicity achieved at 25% TFE, which was maintained, or slightly decreased, at 40% TFE. The FHD undergoes a dramatic two-fold increase and the FHD-CCD undergoes a ~10% increase in helicity. In contrast to the FHD-containing BECN1 fragments, helicity of the highly helical CCD barely changes in different concentrations of TFE (Figure 4.9B and Table 4.4).

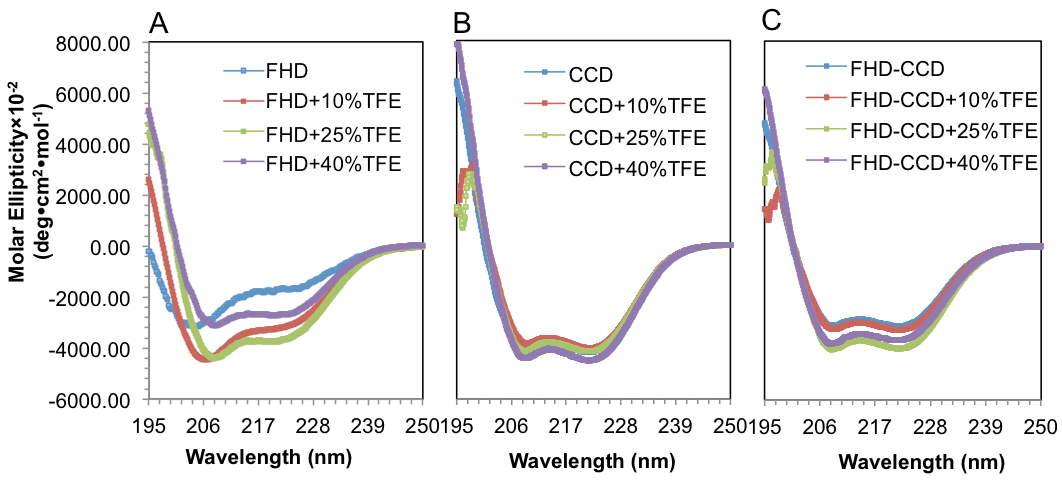

Figure 4.9. Effects of TFE on the secondary structure content in various BECN1 constructs. CD spectra for the (A) FHD, (B) CCD and (C) FHD-CCD recorded at four different TFE v/v concentrations: 0%, 10%, 25% and 40%.

Table 4.4. Secondary structure content of FHD-containing constructs in different TFE concentrations.

		% Estimated Secondary Structure Content											
		No TFE			10 % TFE			25 % TFE			40 % TFE		
BECN1 domain(s)	Length (residues)	α	β	O	α	β	O	α	β	O	α	β	O
FHD	31	37.8	17.8	49.4	36.3	7.5	57.5	80.6	0	19.4	76.5	0	28.4
FHD-CCD	128	80.6	0.2	20	79.4	7.8	12.9	86.6	3.2	10	85.1	4.1	10.7
CCD	97	81.6	0.9	21	83.3	0	19.9	80.9	0	19.1	82.5	0	20.5

α = helices; β = strands; O=coil + turns.

4.3.5. Highly Conserved BECN1 FHD Residues are Involved in Interaction with AMBRA1

BECN1 residues 140-150 have been shown to be necessary for binding to AMBRA1 (Strappazzon, Vietri-Rudan et al. 2011), and to date, AMBRA1 is the only BECN1 binding partner known to bind to BECN1 FHD. Given the evidence that the FHD may undergo binding-associated disorder-to-helix transitions, we decided to use cellular Co-IPs to investigate the role

of conserved FHD residues in binding to AMBRA1. A visual examination of the Co-IP results (Figure 4.10A) indicated that, relative to the binding of AMBRA1 to WT BECN1, the L144A and L148A mutants did not impact binding, the L144A mutant only slightly diminished binding, while the E158A, Y162A, L166A and L169A mutations reduced binding much more significantly.

In order to more quantitatively compare binding of AMBRA1 to WT and mutant BECN1 (Figure 4.10B), we quantified the intensities of the Co-IP bands by densitometric analysis, then normalized these intensities by BECN1 expression levels in the corresponding western blot, with the intensity of the WT BECN1 band assigned a value of 1. We found that mutation of the conserved residues that lie between the two FHD Anchors, i.e. the L148A and L152A mutants result in Co-IP bands that have 95 % of the intensity of the Co-IP band for WT BECN1. Thus the L148A and L152A BECN1 mutations have minimal impact on AMBRA1 binding. In contrast, mutation of residues that lie within the Anchor regions had a much more significant impact on binding of AMBRA1 to BECN1. The L144A mutation, which lies within the first FHD Anchor region reduces the intensity of the Co-IP band to 66 % of that of WT BECN1. Even more strikingly, for the E158A, Y162A, L166A and L169A mutants, the intensity of the Co-IP band was reduced to between 30-16% relative to WT BECN1, with L169A having the largest impact on AMBRA1 binding. Thus, the highly conserved residues within the FHD Anchor regions are essential for interaction with AMBRA 1. However, repeats of this Co-IP experiment are needed to further confirm the results.

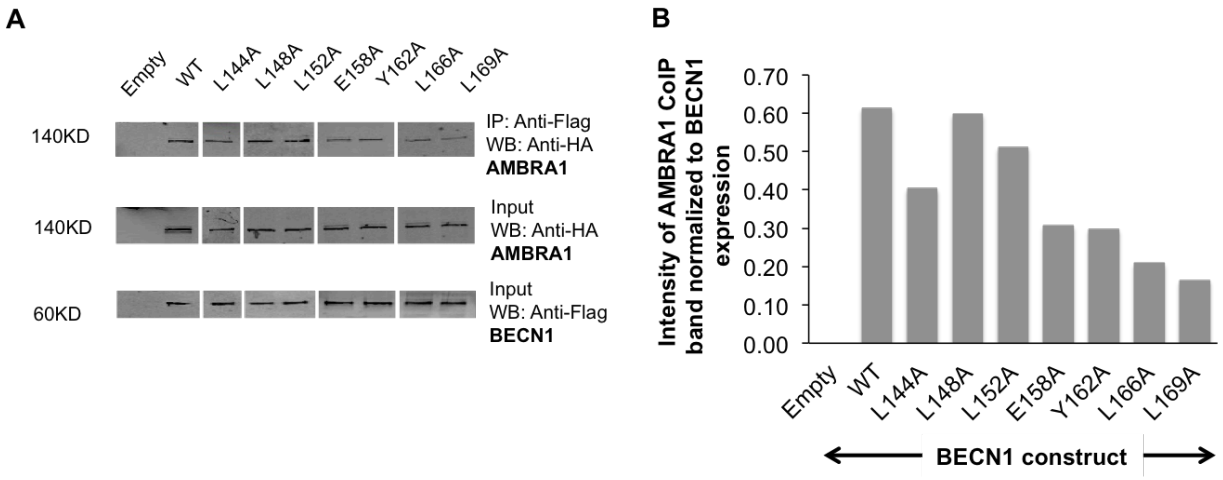

Figure 4.10. Effect of the mutation of conserved BECN1 on AMBRA1 interaction (A) Co-IP of Flag-BECN1 and HA-AMBRA1. IP with anti-flag and IB with anti-HA (top), western blot of lysate using anti-HA (middle) and anti-flag (bottom). (B) Quantification of AMBRA1 CoIP band intensity shown in (A) normalized to the intensity of the BECN1 western band in each sample, with WT BECN1 western band intensity set to 1.0.

4.3.6. Highly Conserved FHD Residues are Required for Starvation-induced Up-regulation of Autophagy

We then decided to investigate the impact of alanine mutagenesis of invariant and highly conserved residues within the FHD (Figure 4.1); L144, L148, L152, E158, Y162, L166 and L169; on autophagy levels within a cell by monitoring levels of GFP-LC3 labeled puncta in cells grown in nutrient-rich and starvation media. These experiments were performed in MCF7 cells that lack one BECN1 allele and express undetectable levels of endogenous BECN1 and have very low levels of autophagy, thereby enabling us to assess the impact of BECN1 mutations relative to WT BECN1.

We found that none of the BECN1 FHD mutants impact autophagy levels in nutrient rich media ($p > 0.05$ vs WT), indicating that these conserved FHD residues are not essential for mediating basal autophagy levels. However, these mutations have a much more dramatic impact on starvation-induced up-regulation of autophagy. Mutation of L144, a highly-conserved residue

that lies within the first Anchor region, diminishes, but does not completely abrogate, the starvation-induced up-regulation of autophagy ($p = 0.006$, vs WT). Mutation of another highly conserved residue, E158, which is the first ordered residue in the FHD structure, completely abrogates the starvation-induced up-regulation of autophagy ($p = 2.5E-4$, vs WT) (Figure 4.11A, 4.11B). Alanine mutagenesis of the invariant residues within the second Anchor region, Y162, L166, and L169, also completely abrogates the starvation-induced up-regulation of autophagy ($p = 1.2E-4$, $4.8E-4$, $4E-4$ respectively, vs WT) (Figure 4.11A, 4.11B). The only mutations that did not impact cellular autophagy levels were L148A and L152A. Strikingly, both these residues lie outside the two Anchor regions. Thus, residues within the FHD Anchor regions, especially the residues in the FHD helical region, are essential for the starvation-induced up-regulation of autophagy.

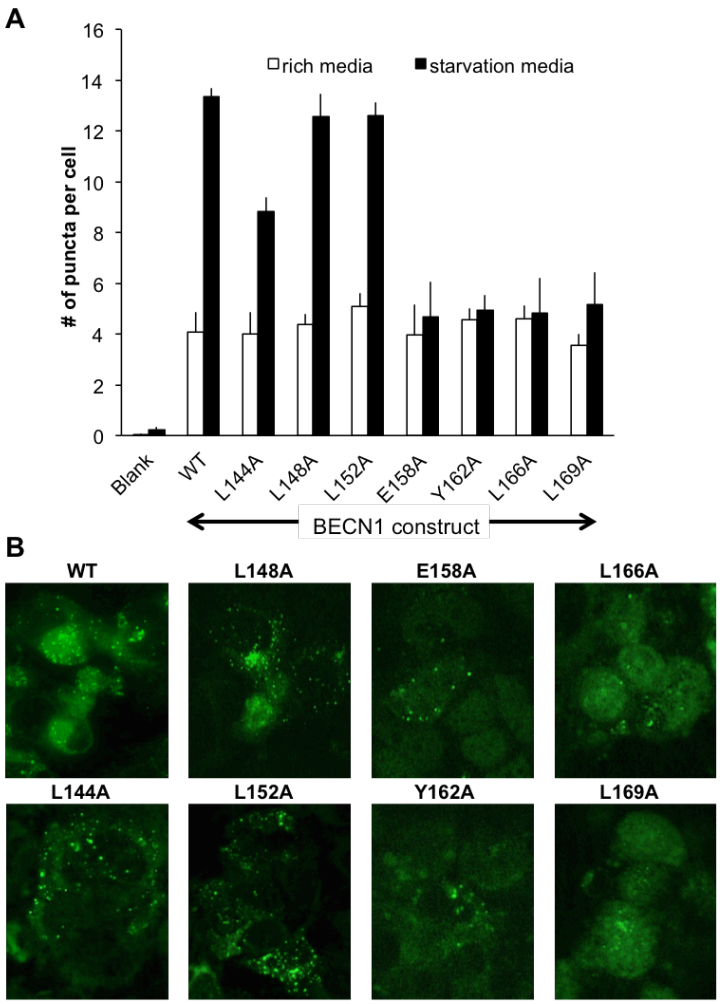

Figure 4.11. Effect of the mutation of conserved BECN1 residues on autophagy.
(A) Light microscopy quantification of discrete GFP-LC3 puncta per cell in GFP-positive MCF7 cells co-transfected with GFP-LC3, WT or mutant BECN1 as indicated below the X-axis. Bars represent number of puncta per cell for each construct. (B) Representative images of GFP- LC3 staining in cells grown in starvation media and transfected with mutant BECN1 as indicated.

4.4. Discussion

Based on the extensive biophysical and structural analyses reported here, we conclude that BECN1 contains a partially disordered domain in the absence of a binding partner between the functional BH3D, which constitutes the C-terminal end of the IDR, and the CCD, which is completely helical (Li, He et al. 2012). This is consistent with predictions by programs such as IUPred. Therefore, we named this BECN1 domain the FHD. SAXS and DEER-EPR analyses

indicate that the FHD has an extended conformation. Thus, conformational flexibility in BECN1 extends beyond the IDR (residues 42-130), into the N-terminal half of FHD (residues 141-156).

We further show that the FHD contains two Anchor regions, at its N- and C-termini. These regions are predicted to nucleate folding upon binding which is similar to the BH3D Anchor that is thought to nucleate folding of that domain (Chapter 3). If the entire FHD were to become helical, the register of the conserved residues indicates that these conserved residues would map to one face of this helix, further supporting the hypothesis that the FHD folds into a helix upon binding to appropriate partners. This hypothesis is consistent with the evidence that FHD-containing BECN1 fragments become more helical in the presence of TFE, a solvent that induces or stabilizes the local hydrophobic interaction of α-helices in sequence with intrinsic helical propensity (Shiraki, Nishikawa et al. 1995). Lastly, MD simulations fitted to SAXS data indicate that helicity is maintained at the FHD C-terminus, but the FHD N-terminal disordered region transiently samples helical conformations. A role for the FHD in binding different partners is consistent with the role of BECN1 as a cellular interaction hub that modulates autophagy.

Recently, a paper describing the 4.4 Å crystal structure (5DFZ) of full-length yeast VPS30 (BECN1 or ATG6) in a complex comprising VPS34 (PI3KC3), VPS15 (p150) and VPS38 (UVRAG) was published (Rostislavleva, Soler et al. 2015). In this complex the VPS30 CC1 forms an eight-turn helix by packing against the helical VPS38 CC1. The formation of this CC1 complex, as part of a coiled-coil heterodimer, is consistent with our results suggesting that this region undergoes a binding-associated disorder-to-helix transition. Curiously however, conserved FHD residues do not map to the interface with VPS38, but are completely solvent-

exposed. This would allow the FHD to be responsible for nucleating other interactions such as AMBRA1 that modulate the activity of the PI3KC3 complex.

Indeed, this BECN1 region has been shown to be required for interaction with another important autophagy protein AMBRA1 (Fimia, Stoykova et al. 2007, Strappazzon, Vietri-Rudan et al. 2011). The deficiency of AMBRA1 in mouse embryos leads to the neuroepithelial hyperplasia, associated with autophagy impairment. AMBRA1 specifically binds the dynein motor complex under normal conditions through a direct interaction with dynein light chain 1 (DLC1). When autophagy is induced under cellular stresses such as nutrient deprivation, AMBRA1 is released from the dynein motor complex in a ULK dependent manner to relocate to ER and enable autophagy nucleation. Co-IP results show that AMBRA1, a highly disordered 1300-amino acid protein, interacts with the BECN1 FHD (residues 140-150) (Strappazzon, Vietri-Rudan et al. 2011). BECN1 BH3D domain residues such as F123 and L125 are not required for the AMBRA1 interaction (Strappazzon, Vietri-Rudan et al. 2011), indicating that the BH3D is dispensable for AMBRA1 interaction. It would be interesting to determine if AMBRA1 can bind to BECN1 in the absence of binding to UVRAG (or ATG14), or whether the BECN1 FHD would need to be stabilized in a helical state prior to AMBRA1 binding.

Strikingly, we show that single point mutations of highly conserved FHD residues completely abrogate starvation-induced up-regulation of autophagy, but have no effect on basal autophagy levels. This implies that the FHD is responsible for transmitting signals for the up-regulation of autophagy in response to nutrient deprivation. To our knowledge, this is the first BECN1 region to be directly implicated in up-regulating autophagy in response to starvation, rather than impacting general autophagy levels. Our autophagy assays showed that all the residues that are essential for regulating the starvation-induced autophagy are located in FHD

Anchors, especially the residues in the second Anchor that forms α-helix. Moreover, our Co-IP results suggest these mutations of may abolish the interaction with AMBRA1, thereby abrogating the starvation-induced up-regulation of autophagy. Both AMBRA1 and UVRAG have previously been shown to also be important for the up-regulation of autophagy (Liang, Feng et al. 2006, Fimia, Stoykova et al. 2007, Gu, Wan et al. 2014). It is possible that these conserved residues also interact with UVRAG, or perhaps some other as yet uncharacterized interaction to regulate starvation-induced autophagy.

In the crystal structure reported here, the FHD trimer is stabilized by the partial packing of conserved hydrophobic residues. MD simulations fitted to SAXS data suggest that this trimer likely exists in solution. However, the FHD is unlikely to trimerize in this manner in the context of the PI3KC3 complex, as there would be extensive stearic clashes between three PI3KC3 complexes arranged based on superposition of the VPS30 CC1 on the FHD. Therefore, it is likely that this FHD trimer represents FHD structure and oligomerization in BECN1 states accessed while performing other biological functions. Notably, regions N-terminal to the CCD have been implicated in homo-oligomerization in other studies (Adi-Harel, Erlich et al. 2010, Rostislavleva, Soler et al. 2015), and it has been shown that the levels of homo-oligomerized BECN1 molecules in cells is not affected by induction of autophagy and association with the other core components of the PI3KC3 complex (Adi-Harel, Erlich et al. 2010). Lastly, it is tempting to speculate that the sulfate-binding site created by the formation of this trimer may represent a site of interaction with a phosphorylated partner.

BECN1 has important roles in cellular pathways that do not involve the other core proteins of the PI3KC3 complex. For instance, BECN1 has been shown to localize to the nucleus (Liang, Yu et al. 2001). It is unclear whether BECN1 interacts with other proteins in the

nucleus, but it appears to impact nuclear export of other autophagy proteins such as LC3 that are not part of the PI3KC3 complex (Ma, Liu et al. 2015). BECN1 proteolytic fragments have also been implicated in apoptosis (Cho, Jo et al. 2009, Wirawan, Vande Walle et al. 2010). The BECN1 FHD structure discussed here may have a role in either of these biological functions. Disorder-to-order transitions in different BECN1 regions have been shown to be essential for regulation of BECN1 function in autophagy by our (Chapter 3) group and more recently, by others (Wei, An et al. 2015). However, the mechanism by which BECN1 mediates its other biological functions, as well as the mechanism of regulation of these diverse BECN1 functions, is not understood. Thus, it is essential that we continue to explore and understand the structure and conformational flexibility of BECN1 in the absence of interactions with other proteins, as well as in the context of diverse interactions, to fully understand the mechanism by which BECN1 performs this diverse array of biological functions.

CHAPTER 5. TO INVESTIGATE THE STRUCTURE OF THE BECN1:ATG14 CCD HETERODIMER COMPLEXAND IDENTIFY CCD INTERFACE RESIDUES IMPORTANT FOR AUTOPHAGY

5.1. Introduction

BECN1 contains a highly helical CCD (Liang, Feng et al. 2006) that has now been shown to interact with other CCD-containing proteins such as ATG14, nPIST or UVRAG (Yue, Horton et al. 2002) to activate autophagy, or TAB2/3 (Criollo, Niso-Santano et al. 2011) to inhibit autophagy.

To date, detailed structural information on ATG14 has not been obtained. The predicted domain architecture of ATG14 contains (i) an-N-terminal region that includes two conserved CxxC motif encompassing residues 43-46 and 55-58 (Sun, Fan et al. 2008), that is required for homoligomerization and ER localization (Fan, Nassiri et al. 2011); (ii) a CCD region encompassing residues 71-180, that is variously predicted to contain either two or three CCDs (Itakura, Kishi et al. 2008, Sun, Fan et al. 2008, Matsunaga, Saitoh et al. 2009, Obara and Ohsumi 2011); and (iii) a functionally-defined domain called the BARKOR/ATG14 autophagosome-targeting sequence (BATS) domain comprising residues 412-492 (Fan, Nassiri et al. 2011, Obara and Ohsumi 2011) that includes an IDR comprising residues 442-472 (Chapter 2), and a C-terminal, amphipathic α-helix (Fan, Nassiri et al. 2011). The BATS domain senses membrane curvature and binds to the early autophagosomal membrane in a PI3P concentration-dependent manner to recruit downstream effectors such as LC3 to mediate autophagy (Fan, Nassiri et al. 2011, Diao, Liu et al. 2015). Co-IP experiments performed by different groups indicate that residues 75-95 and residues 148-178 within the larger CCD region are required and

indispensable for BECN1 binding (Itakura, Kishi et al. 2008, Sun, Fan et al. 2008, Matsunaga, Saitoh et al. 2009, Zhong, Wang et al. 2009).

Several studies have demonstrated that ATG14 binding to BECN1 is important for the up-regulation of autophagy (Itakura, Kishi et al. 2008, Sun, Fan et al. 2008, Itakura and Mizushima 2009, Matsunaga, Saitoh et al. 2009, Zhong, Wang et al. 2009, Fogel, Dlouhy et al. 2013). ATG14 influences the function of the PI3KC3:BECN1 complex by competing with UVRAG to bind to BECN1 (Itakura, Kishi et al. 2008, Sun, Fan et al. 2008, Itakura and Mizushima 2009, Matsunaga, Saitoh et al. 2009, Zhong, Wang et al. 2009). Thus, BECN1 forms two mutually exclusive, quaternary complexes: Complex I, PI3KC3:p150:BECN1:ATG14 or Complex 2, PI3KC3:p150:BECN1:UVRAG, to mediate autophagosome formation and maturation, respectively (Itakura, Kishi et al. 2008, Sun, Fan et al. 2008, Itakura and Mizushima 2009, Matsunaga, Saitoh et al. 2009, Zhong, Wang et al. 2009).

Recent 28Å cryo-EM envelopes of the quaternary complexes of PI3KC3:p150:BECN1:ATG14 and PI3KC3:p150:BECN1:UVRAG indicate that the BECN1 CCD forms a parallel heterodimer with either the ATG14 or UVRAG CCDs, thereby providing a scaffold for recruiting PI3KC3 and P150 (Baskaran, Carlson et al. 2014). The more recent structure of the VPS34:VPS15:VPS30:VPS38 complex confirms that the BECN1:UVRAG CCD heterodimer has a parallel arrangement (Rostislavleva, Soler et al. 2015). However, structural details of the BECN1:ATG14 CCD interaction are still unavailable. Further, given the moderate conservation of the ATG14 CCD and absence of residues that would constitute a clear hydrophobic CCD interface such as a leucine zipper, the identification of ATG14 residues important for the interaction with the BECN1 CCD is non-trivial.

Here we present the 1.46 Å resolution X-ray crystal structure of the human BECN1 CCD homodimer. This structure confirms that BECN1 forms an anti-parallel coiled-coil homodimer in the absence of interactions with other CCD-containing binding partners. Further, we investigate the interaction of human BECN1 and ATG14 CCDs by quantifying thermodynamics of binding using ITC, and use CD spectroscopy and tandem size-exclusion chromatography - small-angle X-ray scattering (SEC-SAXS) to probe the structure of the ATG14 CCD, both as a monomer, and in complex with the BECN1 CCD. We have built a pseudo-atomic model of a parallel BECN1:ATG14 CCD heterodimer based on optimal packing interactions, and verified it against experimental SAXS data. Based on this model, we identify BECN1 and ATG14 residues at the CCD heterodimer interface. We experimentally evaluate the role of selected BECN1 and ATG14 residues by using Co-IP to evaluate binding, and cellular autophagy assays to assess formation of GFP-LC3 labeled autophagosomes (Kabeya, Mizushima et al. 2003).The Co-IP assays demonstrate that mutation of all BECN1 residues and many of the ATG14 residues selected, adversely impacts heterodimerization. Lastly, we show that residues important for heterodimerization are also important for the starvation- induced increase in cellular autophagy levels. Thus, we have developed an accurate pseudo-atomic model of the BECN1:ATG14 heterodimer and identified interface residues essential for heterodimerization and autophagosome nucleation.

5.2. Materials and Methods

5.2.1. Sequence Analysis

Sequences of ATG14 homologs from five eukaryotes: *Homo sapiens, Rattusnorvegicus, Drosophila melanogaster, Arabidopsis thaliana,* and *Saccharomyces cerevisiae,* were identified by BLASTP searches of Genomic RefSeq Protein databases (http://blast.ncbi.nlm.nih.gov/) for

each organism. Multiple sequence alignments of these diverse orthologs were performed with CLUSTALW (Thompson, Gibson et al. 2002) and displayed using Jalview (http://www.jalview.org/).

5.2.2. Protein Expression and Purification

The human BECN1 CCD (residues 175-265) was cloned into the pET29b expression vector between NdeI and XhoI restriction enzyme sites to enable expression of the BECN1 CCD with a C-terminal His_6-tag, using Kanamycin as a selection marker. The human ATG14 CCD (residues 88-178) was cloned into the pMBP-parallel-1 (Sheffield, Garrard et al. 1999) expression vector between BamHI and NotI restriction enzyme sites to enable expression of an MBP-ATG14 CCD fusion protein, using Ampicillin as a selection marker. BL21(DE3)pLysS cells with Chloramphenicol as a selection marker were transformed with either one or both of these expression vectors. Expression of each protein individually or co-expression of both proteins was induced with 0.5mM IPTG. BECN1 CCD-His_6 was expressed at 20 °C overnight. However, in order to limit degradation of the ATG14 CCD, co-expression of the MBP-ATG14 CCD and the MBP-ATG14 CCD:BECN1 CCD-His_6 was performed at 37 °C for 2 hours. All proteins were first purified from cell lysate by affinity chromatography: two tandem 5 ml HisTrap columns (GE Lifesciences) were used for BECN1 CCD purification, while a 10 ml amylose column was used for MBP-ATG14 CCD purification. For the co-expressed proteins, a 10 ml amylose column was first used to bind the MBP-ATG14 CCD. The MBP-tag was removed by on-column cleavage by adding TEV protease in a 1:10 (w/w) ratio to the MBP-ATG14 CCD protein and incubating at 4°C for 8-10 hours. Subsequently, two 5 ml tandem HisTrap columns were used to further purify the BECN1 CCD-His_6 in complex with the ATG14 CCD. Finally, all proteins were purified to apparent homogeneity by SEC, using either a

Superdex 200 16/60 or tandem Superdex 200 10/300 - Superdex75 HR 10/300 columns (GE Lifesciences). MWs were estimated by K_{av} calculations based on SEC standards (BioRad).

5.2.3. Crystallization, X-ray Crystallography Data Collection and Structure Solution

BECN1 CCD crystals were grown at 20 °C by hanging drop vapor diffusion from a drop consisting of 1 µl of BECN1 CCD at 5.2 mg / ml in 25 mM Tris, pH 7.5, 150 mM NaCl and 2mM β-mercaptoethanol plus 1 µl of reservoir solution comprised of 39% v/v 2-methyl-2,4-pentadiol, 9% v/v polyethylene glycol 400 and 100 mM Tris buffer, pH 7.5 suspended over a reservoir of 1 ml. Crystals were harvested and cryo-protected in the reservoir solution and then immediately flash-cooled in liquid N_2.

Diffraction intensities from BECN1 CCD crystals were recorded at 100 K at an X-ray wavelength of 0.9792 Å at beamline 23ID-D of GMCA@APS, Argonne National Laboratories (ANL), Argonne, IL. Images were collected at 1 second exposure per 0.5° crystal rotation per image, in a 360° sweep from a single crystal, on a MAR*mosaic* 4X4 CCD detector (Rayonix) at a crystal-to-detector distance of 350 mm. Intensities were indexed, merged, and scaled using XDS. Data statistics are summarized in Table 5.1. The BECN1 CCD structure was solved by molecular replacement using Phaser-MR (McCoy, Grosse-Kunstleve et al. 2007) with a search model extracted from rat BECN1 CCD (residues 174-264) (PDB code 3Q8T). The model was refined using Phenix (Adams, Afonine et al. 2010) and model building performed in Coot (Emsley, Lohkamp et al. 2010) (Table 5.1). The final refined model is deposited in the PDB with ID 5HHE.

5.2.4. Construction of an Atomic Model of the BECN1:ATG14 CCD Complex

CCbuilder V 1.0 (Wood, Bruning et al. 2014) was used to build a series of parallel heterodimer models to determine the register of the BECN1 and ATG14 helices that would result

in optimal packing at the heterodimer interface. Based on the optimal heterodimer packing model selected and the ATG14 and BECN1 CCD sequences, the program Protein Structure Prediction Server ($(PS)^2$) Version 3.0, http://ps2v3.life.nctu.edu.tw) (Huang, Hwang et al. 2015), which builds a model for protein complexes based on considerations of the packing density in the complex and sequence alignments with known structures, was used to build a atomistic coiled-coil model of the BECN1:ATG14 CCD heterodimer. For comparison, another program, MODELLER (Sali and Blundell 1993, Evans, Bahri et al. 2014) was also used to build a coiled-coil model of the BECN1:ATG14 CCD heterodimer, based on the BECN1 CCD homodimer atomic structure and alignment of the ATG14 CCD and BECN1 CCD sequences.

5.2.5. CD Spectroscopy

CD spectra were recorded with a Jasco J-815 spectropolarimeter equipped with thermoelectric temperature control. The spectra were collected between 180 and 250 nm at 4 °C using a 300 µL quartz cell with a 0.1 cm path length. MBP-ATG14 CCD, MBP and the BECN1:ATG14 CCD complex were diluted to 50 µM and dialyzed in CD buffer (10 mM potassium phosphate, pH 7.6, 100 mM ammonium sulfate) overnight. Data were analyzed using CONTIN from the CDpro program suite (Provencher and Glöckner 1981) within the Jasco Spectra Manager software.

5.2.6. SEC-SAXS Data Collection and Analysis

SEC-SAXS data were recorded at beamline 18-ID of Bio-CAT at APS, ANL, Argonne, IL on a Pilatus 1M detector at a sample-to-detector distance of 3.5 m, covering a momentum transfer range of $0.0036 Å^{-1} < q < 0.4 Å^{-1}$. An aliquot of BECN1:ATG14 CCD complex at 5.9 mg/ml was injected onto a SEC column (Superdex 200 GL 10/300) and SAXS data were recorded by exposing the column eluate to the X-ray beam for one second with a periodicity of

three seconds. SAXS signal from parts of the diffraction curve immediately preceding the BECN1:ATG14 CCD heterodimer elution peak were selected, averaged and subtracted as the buffer blank from data points within the peak corresponding to the BECN1:ATG14 CCD heterodimer. Data analysis was performed using various programs within the ATSAS program suite (Petoukhov, Franke et al. 2012). Data were processed using PRIMUS (Konarev, Volkov et al. 2003) and the R_g was calculated from Guinier extrapolation. The pair distribution function P(r) was calculated by Fourier inversion of the scattering intensity *I*(q) using AutoGNOM. The P(r) function was used to calculate the R_g and D_{max}, and also for the reconstruction of an *ab initio* envelope by the application of ten cycles in DAMMIF (Franke and Svergun 2009). The resulting bead models were sequentially analyzed using DAMSEL, DAMSUP and DAMAVER, and then filtered using DAMMFILT (Volkov and Svergun 2003). CRYSOL (Svergun, Barberato et al. 1995) was used to fit and compare theoretical scattering curves, calculated from either the BECN1 CCD homodimer crystal structure or the BECN1:ATG14 CCD heterodimer model, for comparison with the experimental SAXS curve. The BECN1 CCD homodimer crystal structure and the BECN1:ATG14 CCD heterodimer model were then fit into appropriate *ab initio* envelopes using the program SUPCOMB (Kozin and Svergun 2001).

5.2.7. ITC

Separately purified BECN1 CCD and ATG14 CCD protein samples were loaded into separate dialysis cassettes, which were simultaneously dialyzed against 2 L of 50 mM HEPES, pH 8.0, 150 mM NaCl and 2 mM β-mercaptoethanol buffer to ensure matched buffers for the ITC experiments. ITC experiments were performed at 20 °C using a Low Volume Gold Nano ITC (TA Instruments). 400 μL of the BECN1 CCD at 0.18 mg/mL was placed in the cell and

32.4 mg/mL ATG14 CCD was titrated into the cell using 20 injections of 2.5 μL each. The data were analyzed using the NanoAnalyze Software (TA Instruments) with an independent model.

5.2.8. Co-IP of Exogenously Expressed BECN1 and ATG14 Mutants

Human ATG14 or BECN1 mutants were created by site-directed mutagenesis (Agilent Technologies) using the primers ordered from Integrated DNA Technologies. 5×10^5 COS7 or MCF7 cells / ml were seeded in a 10 cm culture dish and cultured overnight in DMEM (GIBCO) with 10% FBS (GIBCO) to ~80% confluence. Lipofectamine 2000 (Invitrogen, Carlsbad, CA) was used for transfection according to the manufacturer's instructions, using a total of 24 μg of plasmids in a 1:1 molar ratio of either Flag-tagged WT BECN1 and HA-tagged WT / mutant ATG14 to COS7 cells or HA-tagged WT ATG14 and Flag-tagged WT / mutant BECN1 to MCF7 cells. Cells were lysed in a buffer comprising 50 mM Tris HCl, pH 7.9, 150 mM NaCl, 1% Triton X-100, 1 mM DTT, protease inhibitor cocktail (1 tablet per 50 ml buffer) (Roche Applied Sciences) and 1 mM PMSF. Cell lysates were clarified by centrifugation at 14,800 x g for 10 min at 4 °C. The HA-tagged WT or mutant ATG14 supernatants were saved and subjected to immunoprecipitation using mouse monoclonal anti-Flag M2 antibodies (Sigma), whereas the Flag-tagged WT or mutant BECN1 supernatants were collected and immunoprecipitated using rabbit polyclonal anti-HA antibodies (Y-11, Santa Cruz), followed by overnight incubation with Protein G beads (Invitrogen). The samples were eluted by 2 × Laemmli buffer, analyzed by western blot using rabbit polyclonal anti-HA antibodies (Y-11, Santa Cruz) or monoclonal anti-Flag M2-HRP antibody (Sigma) detected by ECL western blotting substrate (Thermo Fisher) and imaged by a Storm Imager (GE Lifesciences).

5.2.9. Autophagy Assay

Autophagy levels were evaluated by monitoring cellular localization of GFP-tagged LC3 (Kabeya, Mizushima et al. 2000). 2×10^5 COS7 or MCF7 cells were seeded in each chamber of four-well culture slides (Millipore EZ slides) and cultured overnight in DMEM with 10% FBS until ~80% confluency. Lipofectamine 2000 was used for transfection as above, with cells in each chamber being co-transfected with 4 μg of total plasmids comprising 1.6 μg GFP-LC3; and either 1.2 μg WT BECN1 and 1.2 μg WT or mutant ATG14 expression plasmids for COS7 cells; or 1.6 μg GFP-LC3 and 1.2 μg WT ATG14 and 1.2 μg WT or mutant BECN1 expression plasmids for MCF7 cells. After transfection, the cells were cultured in either rich media (DMEM, 10% FBS, 2X amino acid mixture, GIBCO) or starvation media (Earle's balanced salt solution, GIBCO) for 4 hours. Then the cells were fixed with 4% paraformaldehyde in PBS. GFP-LC3-positive puncta were observed using a Zeiss AxioObserver Z1 fluorescent microscope and quantified by counting a minimum of 50 cells per condition in three independent repeats using the Imaris program (Bitplane). The significance of alterations in autophagy levels was determined by a two-tailed, heteroscedastic student's *t*-test, wherein $p \leq 0.05$ is considered significant.

5.3. Results

5.3.1. Human BECN1 CCD Forms an Anti-parallel Homodimer

We have determined the X-ray crystal structure of the human BECN1 CCD, comprising residues 175-265, to 1.46 Å resolution. The crystals belonged to space group *C*2 with unit cell parameters of a = 58.2 Å, b = 71.58 Å, c = 58.45 Å and β = 112.55° (Table 5.1) and contain two BECN1 CCD monomers per asymmetric unit. The structure was solved by molecular replacement using the rat BECN1 CCD structure (PDB code 3Q8T) (Li, He et al. 2012) as a

search model. The final model consists of residues 175-265 in each monomer and 255 water molecules. The two monomers in the asymmetric unit are almost identical; superimposing with an RMSD of 0.72 Å over 91 Cα atoms. Both molecular dimer axes coincide with crystallographic two-folds, thus each CCD monomer in the asymmetric unit forms an anti-parallel dimer with an equivalent symmetry related molecule, (A to A and B to B).

Table 5.1. X-ray Diffraction Data Collection and Refinement Statistics.

Data collection	
Wavelength (Å)	0.97921
Data range (Å)	40.15-1.46
Space group	C2
Unit Cell	a=58.20 Å, b=71.58 Å, c=58.45 Å, β=112.55°
Unique reflections	38596 (3766)
Avg. multiplicity	7.5 (7.1)
Ave. Mosaicity	0.21
Completeness (%)	99.70 (97.97)
$CC_{1/2}$	0.98 (0.86)
[1]R_{meas}	0.11 (0.70)
I/σI	15.91 (2.99)
Refinement	
Model:	
Chain A (number of residues)	93
Chain B (number of residues)	93
Water molecules	255
Data Range (Å)	40.15-1.46
[2]R_{work} (%)	17.2
[2,3]R_{free} (%)	20.8
Average B-values (Å^2):	
Main Chain	22.8
Side Chain	37.6
Water	43.0
All Atoms	32.3
RMSDs from target values:	
Bond Lengths (Å)	0.007
Bond Angles (°)	0.71
Ramachandran outliers	0

Values in parentheses pertain to the highest resolution shell.
[1]$R_{meas} = \sum_{hkl}(n/n-1)^{1/2}\sum_{h,i} |I_{hkl,i}-\langle I_{hkkl}\rangle|/\sum_{hkl}\sum_{h,i}I_{hkl,i}$;
[2]R factor= $\sum_{h,} |F_{obs}-|F_{calc}|/\sum_{h}|F_{obs}|$;
[3]Test set for R_{free} consisted of 5.0 % of data.

The human and rat BECN1 CCD (Li, He et al. 2012) have a similar structure, comprising of an anti-parallel, left handed coiled coil homodimr (Figure 5.1). The human and rant BECN1 CCD monomer superimpose with an RMSD of 1.38 Å over 91 Cα atoms. For the human BECN1 CCD, the surface area buried at the interface between the two monomers is 4849 $Å^2$, accounting for 26.4% of the total surface area of each monomer, while for the rat BECN1 CCD the surface area buried is 4969 $Å^2$, accounting for 27% of the total surface area of each monomer. Residues that are different between the human and rat BECN1 CCDs: residues M182, I207 and T259 in human correspond to R180, V205 and M257 in rat (Figure 5.1), are solvent-exposed and do not contribute to the BECN1 CCD homodimer interface. Half the residues comprising the BECN1 CCD homodimer are charged, with a predominance of acidic residues resulting in a very negatively charged surface. 40% of these charged residues are conserved.

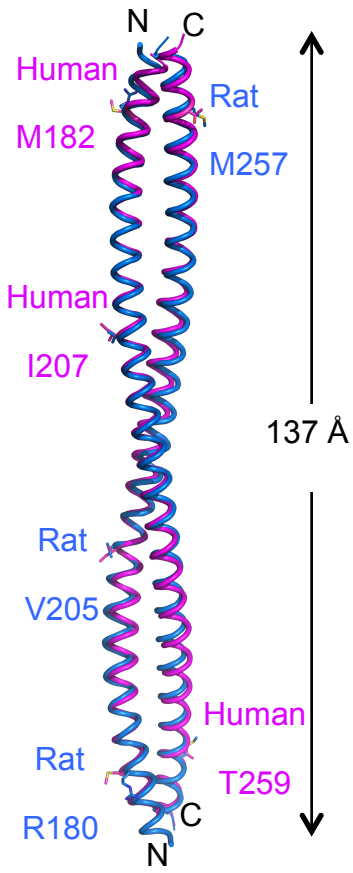

Figure 5.1. The crystal structure of the BECN1 CCD homodimer.
The human BECN1 CCD homodimer and the rat BECN1 CCD (PDB ID: 3Q8T) are superimposed and displayed in magenta and marine ribbon respectively. The three residues that are different between the human and rat CCDs are rendered in stick with atoms color-coded by atom type: C, magenta (human) or marine (rat); O, red; N, blue and S, yellow. The length of the homodimer is indicated. This and all other molecular figures were prepared using the program PyMol (DeLano 2002).

The human BECN1 CCD has 13 heptad repeats (*a-b-c-d-e-f-g*), that stabilize the homodimer by interactions of residues at the "a" and "d" positions, similar to the rat BECN1 CCD. The 26 interacting pairs are comprised of two sets of thirteen unique pairs related by the homodimer two-fold symmetry. Six of these thirteen unique "a" and "d" positions of the heptad repeats are occupied by hydrophobic residues that form acceptable interacting pairs, including three ideal pairs (Table 5.2). The remaining seven repeats bear bulky charged or polar residues

resulting in non-ideal pairings at these a and d positions (Table 5.2). For instance, the a and d positions of the first heptad repeat comprises of residues S177 and L180, which pack against L264 and L261 respectively, at the d' and a' positions of the last heptad repeat within the homodimer resulting in one imperfect and one perfect pairing (Table 5.2). The register of heptad interactions is maintained throughout the length of the BECN1 CCD homodimer.

Polar interactions also play an important role in stabilizing the BECN1 CCD in both rat and humans. The BECN1 CCD homodimer contains six pairs of inter-chain polar interactions. At the interaction interface, R205 forms a non-ideal pair with F236 of the partner helix, but in addition to the hydrophobic packing of the aliphatic part of the side chain, it also stabilizes the homodimer by forming two hydrogen bonds with Y233 and Q240 of the partner helix, two polar interface residues located a turn away on either side of F236. Further, while the aliphatic part of the interface E226 packs against the partner's V215, the charged end makes an inter-molecular polar interaction with Q216 of the partner helix. Therefore there are three unique pairs of inter-molecule polar interactions in the BECN1 CCD homodimer that compensate for the non-ideal pairings at the interaction interface and further stabilize the CCD. Lastly, intra-molecular polar networks between charged and polar surface exposed residues formed along the whole chain, including interacting triplets of charged residues, diminish potential Coulombic repulsion between chains and stabilize CCD structure.

Table 5.2. Residues at the interaction interface (a, d positions of heptad repeats) in the various BECN1/VPS30-containing dimers.

Dimer:	**BECN1 homodimer (anti-parallel)**		**Pairing**	**BECN1:ATG14 heterodimer (parallel)**		**Pairing**	**VPS30:VPS38 heterodimer (parallel)**	
Monomers:	BECN1			BECN1	ATG14		VPS30	VPS38
Heptad positions:	A	d’		a	a’		a	a’
Interface residues:	S177	L264	NI	S177	F92	NI		
	L184	A257	OK	L184	A99	OK		
	E191	V250	NI	E191	T106	P	E244	R224
	L198	L243	I	L198	I113	I	L251	E231
	R205	F236	NI	R205	I120	NI	D258	L238
	L212	Y229	NI	L212	I127	I	L265	K245
	A219	L222	OK	A219	M134	OK	K272	L252
	E226	V215	NI	E226	L141	NI	K279	N259
	Y233	V208	NI	Y233	N148	NI		
	Q240	V201	NI	Q240	A155	NI	N293	E272
	L247	L194	I	L247	K162	NI	L300	G279
	M254	L187	OK	M254	N169	NI	F307	V286
	L261	L180	I	L261	V176	I	L314	D293
Heptad positions:	D	a’		d	d’		d	d’
Interface residues:	L180	L261	I	L180	E95	NI		
	L187	M254	OK	L187	G102	NI		
	L194	L247	I	L194	L109	I	L247	Q227
	V201	Q240	NI	V201	C116	NI	L254	E234
	V208	Y233	NI	V208	L123	I	L261	K241
	V215	E226	NI	V215	G130	NI	L268	E248
	L222	A219	OK	L222	N137	NI	L275	N255
	Y229	L212	NI	Y229	T144	P	K282	T263
	F236	R205	NI	F236	L151	OK		
	L243	L198	I	L243	H158	NI	F296	N275
	V250	E191	NI	V250	I165	I	L303	Y282
	A257	L184	OK	A257	L172	OK	S310	K289
	L264	S177	NI					

Pairing Key: I: Ideal; NI: Non-Ideal; OK: Acceptable hydrophobic; P: paired polar residues

Despite this similarity in overall structure and interface residues, the human BECN1 CCD homodimer self-associates twice as tightly (K_d = 48.3 μM) (Figure 5.2A and Table 5.3) as the rat BECN1 CCD (K_d = 89 μM) (Li, He et al. 2012). For the human homodimer, the self-

association is driven by entropy rather than enthalpy (Table 5.3). The absence of enthalpic contributions to binding is likely a result of the lower number of favorable interface interactions, relative to the total buried surface area, and results in a metastable homodimer.

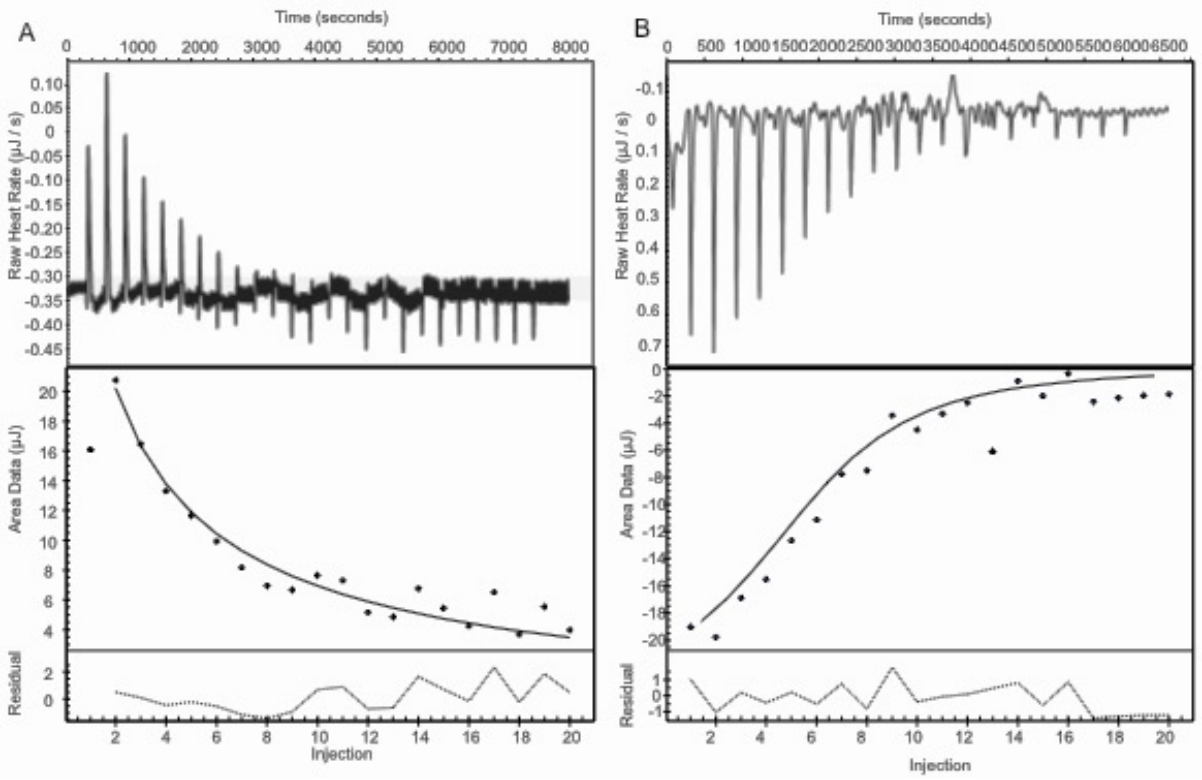

Figure 5.2. ITC data of BECN1 homodimer and BECN1:ATG14 heterodimer.
(A) BECN1 homodimer dissociation (B) BECN1:ATG14 heterodimer interaction with upper panel showing the raw data and lower panel showing the fitting curve.

Table 5.3. ITC measurements of BECN1 CCD homodimerization and heterodimerization with the ATG14 CCD.

Constructs	**K_d (µM)**	**ΔH (kJ/mol)**	**ΔG (kJ/mol)**	**ΔS (J/K•mol)**	**n**
Homodimer	48.3±13.47	161±105	-27.64± 0.40	627±356	
Heterodimer	4.44±0.08	-27.17± 5.65	-30.56± 0.04	11.361± 18.85	1

5.3.2. The ATG14 CCD is Less Helical than the BECN1 CCD

Sequence alignment of predicted ATG14 CCDs from five diverse eukaryotic organisms, ranging from human to yeast, shows that the ATG14 CCD is moderately conserved (Figure 5.3).

Its conservation is similar to the BECN1 CCD (Li, He et al. 2012). Secondary structure prediction using JPred4 (Drozdetskiy, Cole et al. 2015) indicates that the ATG14 CCD region spans residues 71-202 (Figure 5.3), similar to previously published sequence analyses. Cellular biology studies show that ATG14 residues 71-180 include all residues that are required for binding to the BECN1 CCD (Itakura, Kishi et al. 2008, Sun, Fan et al. 2008, Matsunaga, Saitoh et al. 2009, Zhong, Wang et al. 2009). Further, biophysical and biochemical studies using purified protein fragments show that residues 88-178 are sufficient for the interaction with the BECN1 CCD (Li, He et al. 2012). Therefore, we selected ATG14 residues 88-178, which matches the length of the BECN1 CCD (residues 175-265), as the nominal ATG14 CCD for structural studies (Figure 5.3).

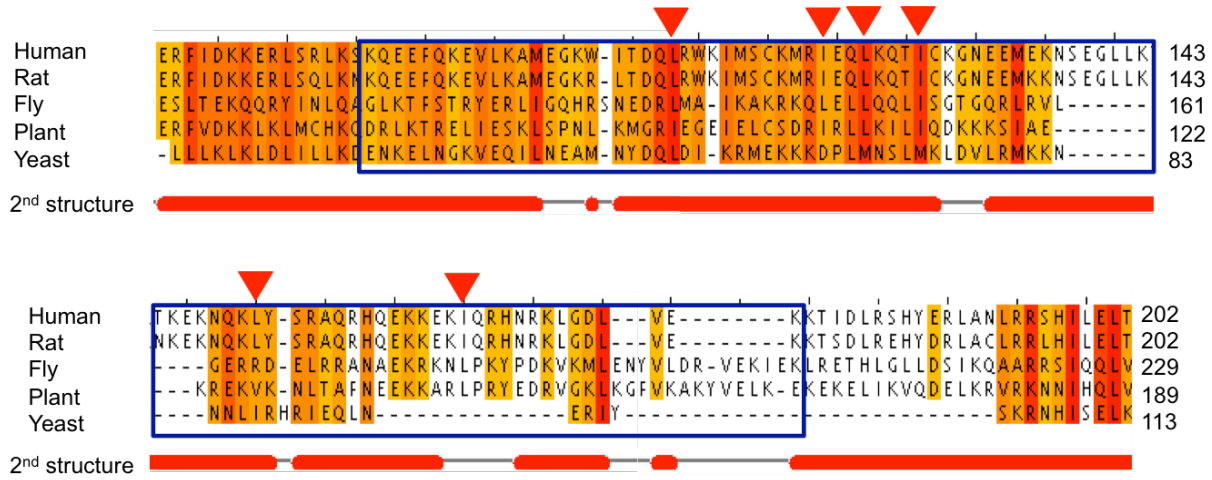

Figure 5.3. ATG14 Sequence Alignment.
Sequence alignment of predicted CCDs from five diverse eukaryotic ATG14 proteins. Yellow, orange and red represent increasing sequence conservation, with red corresponding to invariant residues. Predicted secondary structures are shown below the sequence alignment. The predicted CCD region used in this study is boxed. Conserved residues involved in hydrophobic pairing in the heterodimer, that were selected for mutagenesis are indicated by red arrowheads.

We utilized CD spectroscopy to analyze and compare the secondary structure content of the ATG14 CCD, BECN1 CCD homodimer and BECN1:ATG14 CCD heterodimer (Figure 5.4). Since the CCDs were expected to be highly helical, we used CONTIN (Provencher and Glöckner

1981), which has been shown to provide the most accurate estimation of α-helical content in proteins (Sreerama and Woody 2000), to calculate the secondary structure content from the CD spectra measured from each sample. Consistent with expectations, all spectra have strong helical features comprising a positive transition at 195 nm and two negative transitions at 208 nm at 222 nm (Figure 5.4). However, there are differences in the helical and coil content estimated for each CCD sample (Table 5.4). The 97-residue BECN1 CCD monomer construct comprising the 91-residue BECN1 CCD (175-265) and a His_6-tag is highly helical, with a helical conformation adopted by 168 residues within the 194-residue homodimer, or 84 residues within each 97-residue monomer (Table 5.4). However, this helicity is less than that observed in the BECN1 CCD X-ray crystal structure, wherein all observed residues adopt α-helix structure.

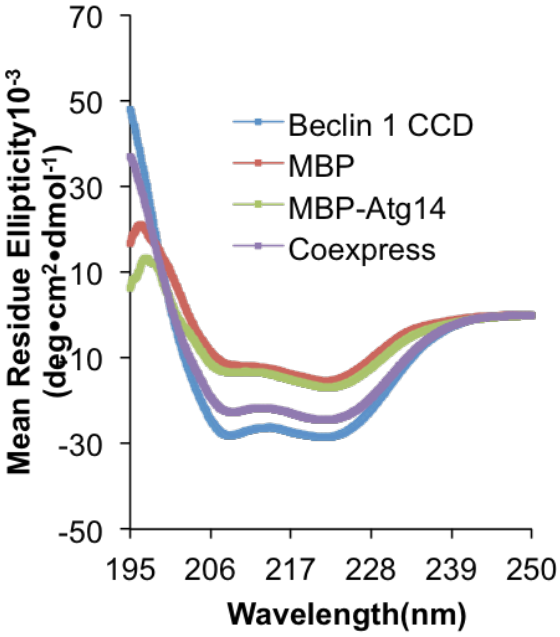

Figure 5.4. CD Spectra of Different CCDs.
The spectra for the MBP-ATG14 CCD fusion protein, the BECN1:ATG14 CCD complex, the BECN1 CCD-His_6, and MBP are color coded as indicated in the legend.

In the absence of an interacting partner, the purified ATG14 CCD is unstable upon cleavage of the MBP-tag, therefore CD spectra were recorded from the MBP-tagged ATG14

CCD. Analysis of this spectrum indicates that of the 487 residues in the fusion protein (371 residues from MBP, 25 in the linker and 91 in the ATG14 CCD); 277 residues are in a helical conformation, 53 are in β-conformation and 157 are in a random coil conformation (Table 5.4). Analysis of a CD spectrum recorded from MBP alone indicates that of the 371 total residues, 214 residues are in helical conformation, 52 in β-conformation and 105 in random coil-conformation (Table 5.4). Subtraction of the secondary structure content of MBP from the MBP-ATG14 CCD enables us to deduce the secondary structure content of the ATG14 CCD when not in complex with BECN1 or other partners. Assuming the secondary structure of MBP does not change between the isolated MBP and the fusion protein, and the 25-residue linker is a random coil, we find that only 63 of the 91 residues comprising the ATG14 CCD are helical and 27 residues exist in a coil conformation. Thus, the ATG14 CCD is significantly less helical and more disordered than the BECN1 CCD.

Table 5.4. Secondary structure content of different protein constructs estimated from CD.

Protein	**Residue number**	**% Estimated secondary structure content**			
		Helix	**Strand**	**Coil**	**Total**
BECN1 CCD	194 (dimer)	86.8	0.8	12.4	100
MBP-ATG14	487	56.9	10.8	32.3	100
MBP	371	57.6	14.1	28.3	100
BECN1:ATG14	191 (heterodimer)	79.6	0.5	19.9	100

The ATG14 CCD does not appear to form a homodimer, and no detectable heat of self-association was recorded in ITC measurements. Our ITC measurements (Figure 5.2B and Table 5.3) indicate that the human ATG14 CCD binds to the BECN1 CCD with a 1:1 stoichiometry with a moderate affinity (K_d = 4.44 μM), that is ~10-fold tighter than BECN1 self-association under the same conditions. Further, this heterodimerization is both enthalpically and entropically favorable, in contrast to BECN1 homodimerization, which is driven entirely by entropy (Table 5.3).

To further understand the structural basis of heterodimerization, we purified the BECN1:ATG14 CCD complex (Figure 5.5). We confirmed the presence of both proteins in the purified sample using SDS-PAGE (Figure 5.5) and mass spectrometry (data not shown). Analysis of CD spectra measured for the purified heterodimer indicates that 152 of the 182 residues in the BECN1:ATG14 CCD heterodimer are in a helical conformation (Table 5.4), sixteen residues less than that observed for the BECN1 CCD homodimer; while 38 residues are in a random coil conformation, compared to the 24 in the BECN1 CCD homodimer. Assuming the helicity of the BECN1 CCD does not change relative to that observed within a BECN1 homodimer, the ATG14 CCD has 68 residues in a helical conformation. Alternately, assuming that the helicity of both, the BECN1 and ATG14 CCDs are comparable within the heterodimer, the ATG14 CCD will have ~76 residues in helical conformation. Thus, compared to that ATG14 CCD helicity in the monomeric state, the helicity of the ATG14 CCD in the context of the BECN1:ATG14 CCD homodimer is increased by five to thirteen residues.

5.3.3. The BECN1:ATG14 CCD Heterodimer has a Partially Disordered, Elongated Structure

We conducted extensive crystallization trials of both, the MBP-ATG14 CCD fusion protein and the ATG14:BECN1 CCD heterodimer. Although both SDS-PAGE and mass spectroscopy show that the protein samples used for crystallization contained the appropriate protein, we were unable to obtain crystals of either the fusion protein or the complex. Indeed, we find that the ATG14 CCD is very unstable even in complex with the BECN1 CCD. Careful monitoring by SDS-PAGE shows that it degrades in approximately three days even at 4 °C (data not shown). It is likely that this rapid degradation of ATG14 CCD, combined with its inherent structural flexibility, prevented crystallization.

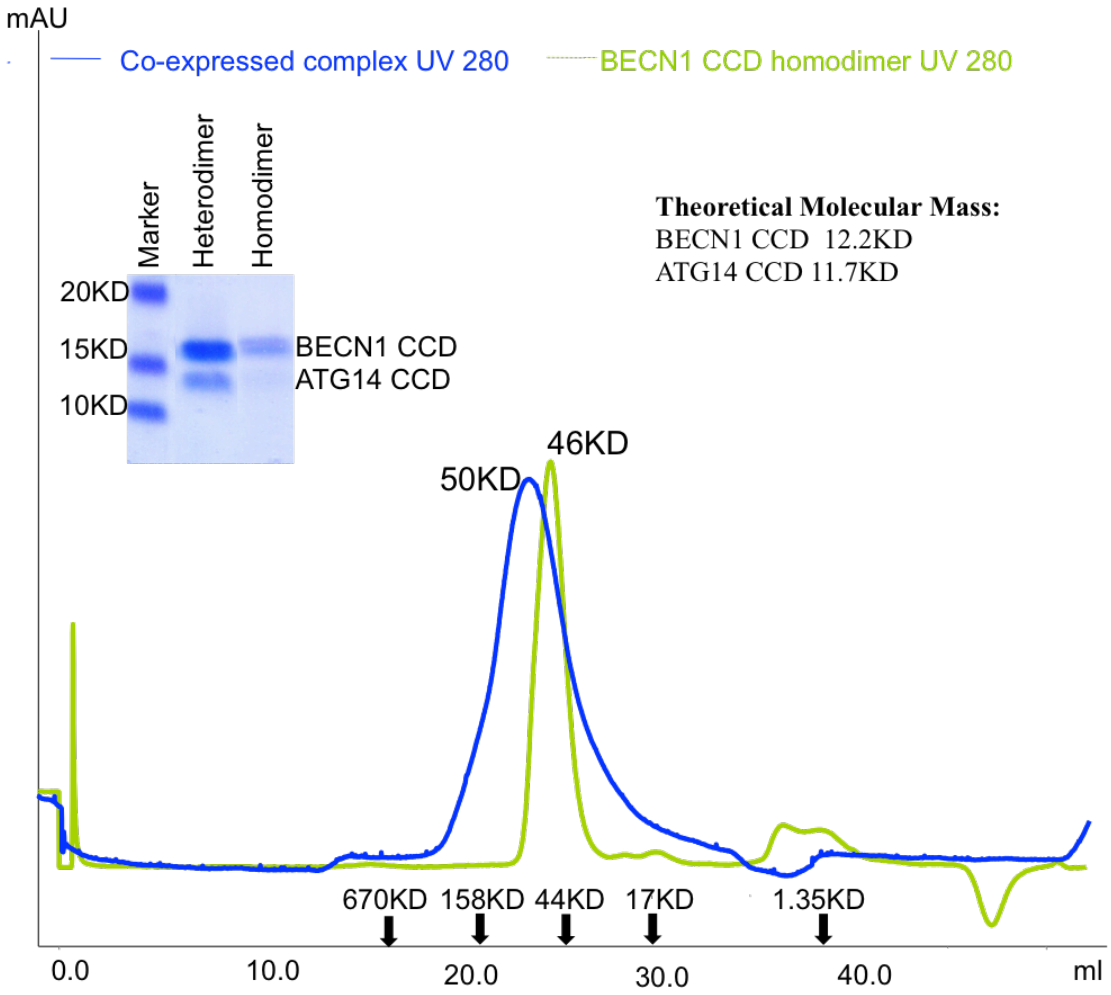

Figure 5.5. Size exclusion chromatogram and the corresponding SDS-PAGE.
SEC curves correspond to BECN1 CCD (green) and BECN1:ATG14 CCD (blue). Elution positions for different molecular weight markers are indicated. The molecular weight calculated from SEC is indicated.

Therefore, in order to gain a better insight into the size and shape of BECN1:ATG14 CCD heterodimer, we performed SAXS on samples frozen immediately after purification. For comparison, we also performed SAXS on BECN1 CCD homodimer. To ensure that the SAXS data were collected from a homogeneous sample, SAXS was performed in tandem with size exclusion chromatography (SEC-SAXS). The SEC profile of the complex as well as the homodimer comprises a single peak, indicating the absence of aggregated protein in both constructs (Figure 5.5). The low q-range region in the Guinier plot is linear in the range of $q \times R_g$

< 1.3. The Radius of Gyration (R_g) of BECN1:ATG14 CCD complex calculated from the Guinier plot and the P(r) distribution function is 34 Å and 37 Å, respectively (Figure 5.6 and Table 5.5), which is close to those values of the elongated BECN1 CCD, with 34 Å from Guinier plot, and 36 Å from P(r) distribution function (Figure 5.7A and Table 5.5). The P(r) distribution was also used to calculate a D_{max} of 125 Å for SAXS experimental data of BECN1:ATG14 CCD heterodimer (Figure 5.6B), which is comparable to the D_{max} of 121 Å calculated from the SAXS experimental data of BECN1 CCD complex(Figure 5.7B and Table 5.5), indicating that the heterodimer has an elongated structure, similar to the BECN1 CCD homodimer. The MW derived from the Porod Volume of the heterodimer is 25KD, close to its theoretical MW of 23.9 KD (Table 5.5). While the MW derived from the Porod Volume of the homodimer is 22 KD, a little bit smaller than its theoretical MW of 24.4 KD (Table 5.5). The most striking difference between the BECN1:ATG14 CCD heterodimer and the BECN1 CCD homodimer is observed in the Kratky plots (Figure 5.6C and Figure 5.7C). The Kratky plot calculated for SAXS data recorded from the BECN1:ATG14 CCD heterodimer indicates that it is not well unfolded (Figure 5.6C), which is consistent with our estimation of secondary structure content from the CD spectrum of the complex. But the Kratky plot calculated for SAXS data recorded from the BECN1 CCD homodimer indicates that this domain is well folded (Figure 5.7C), consistent with the X-ray crystal structure. Therefore, both CD spectroscopy and SAXS indicate that the BECN1:ATG14 CCD heterodimer is unstructured relative to the BECN1 CCD homodimer.

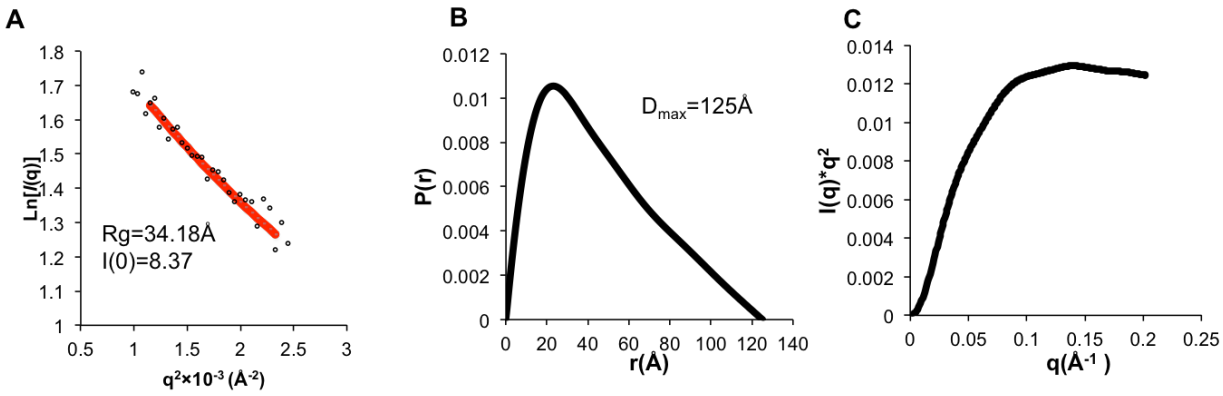

Figure 5.6. SAXS analysis of BECN1:ATG14 CCD complex.
(A) Guinier plot; (B) P(r) pairwise distribution; (C) Kratky plot

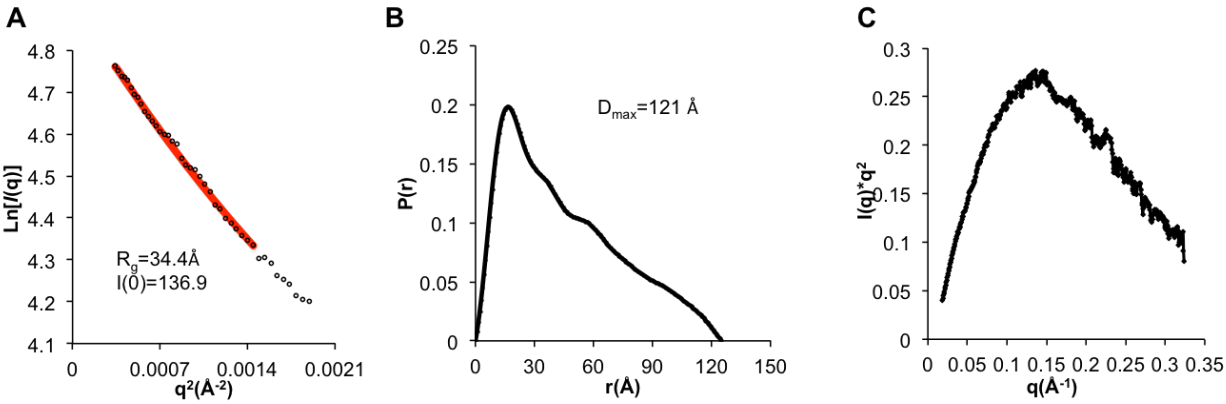

Figure 5.7. SEC SAXS analysis of BECN1 CCD.
(**A**) Guinier Plot. (**B**) P(r) pairwise distribution. (**C**) Kratky plot.

Table 5.5. Comparison of molecular parameters calculated from SAXS data and either the X-ray crystal structure or computational model.

Protein	**SAXS Parameters**					**X-ray structure or model**		**Fit of BECN1 CCD SAXS data to atomic structure / model (χ^2)**	**Fit of BECN1:ATG14 SAXS data to atomic structure / model (χ^2)**
	MW_T (KD)	MW_{ex} (KD)	R_g (Å)	R_g (Å) from P(r) plot	D_{max} (Å)	R_g (Å)	Length (Å)		
BECN1 Homodimer	24.4	22	34	36	121	40.0	137.3	1.5	2.1
BECN1: ATG14 Heterodimer	23.9	25	34	37	125	38.0	127.4	1.2	1.1

MW_{ex}: molecular weight calculated from the SAXS scattering curve; MW_T: theoretical molecular weight expected from sequence

5.3.4. BECN1 and ATG14 Form a Curved CCD Heterodimer

The low-resolution envelope calculated for the BECN1:ATG14 CCD heterodimer from the SAXS data has an elongated shape (Figure 5.8A and B), similar to that of the BECN1 CCD homodimer (Figure 5.8 C and D). However, unlike the BECN1 CCD homodimer envelope, the heterodimer envelope has a pronounced curvature, fitting a radius of 15 nm. In order to further investigate structural details of the BECN1:ATG14 CCD heterodimer interaction interface, we built an atomistic model of the heterodimer, as a parallel CCD, based on information from the Cryo-EM reconstruction of the human BECN1:ATG14:p150:PI3KC3 quaternary complex (Baskaran, Carlson et al. 2014). This is also analogous to the parallel heterodimer formed by the CCDs of VPS30 and VPS38, which correlate to BECN1 and UVRAG, in the X-ray crystal structure of the yeast VPS30:VPS38:VPS15:VPS34 quaternary complex (Rostislavleva, Soler et al. 2015).

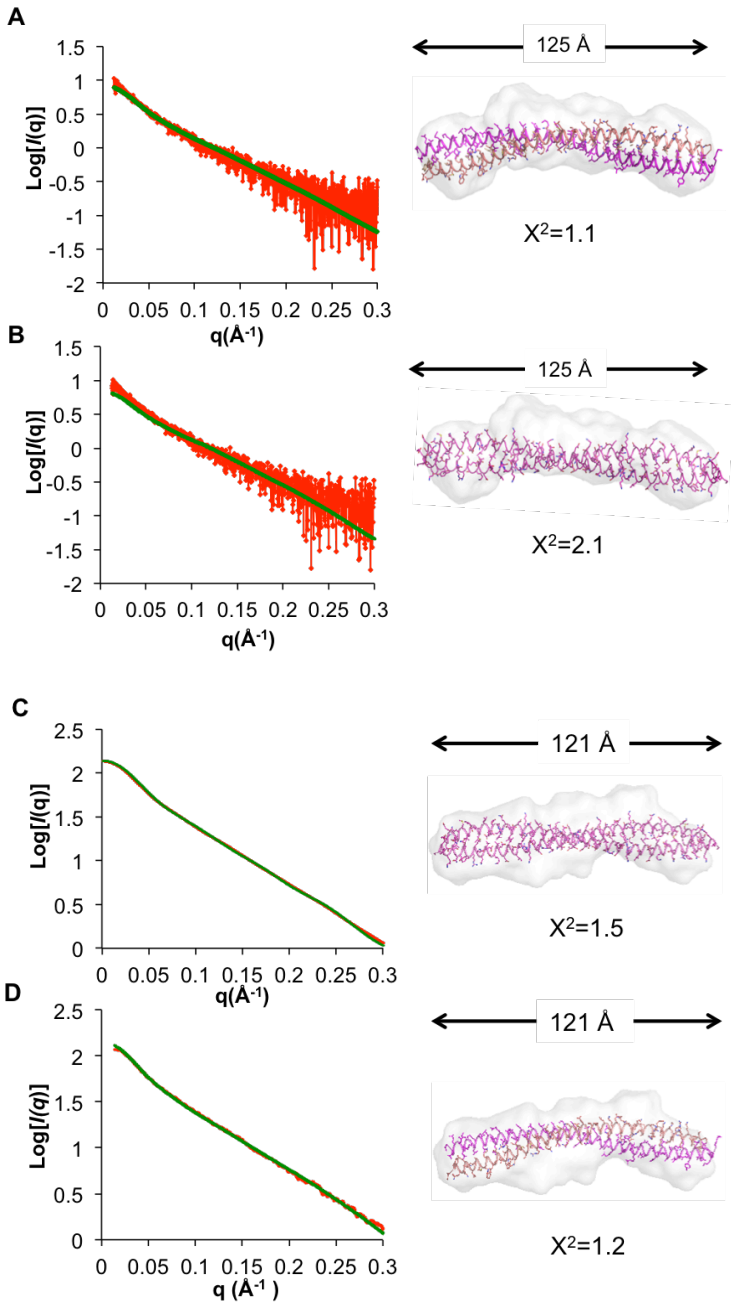

Figure 5.8. The BECN1:ATG14 heterodimer model agrees well with the experimental SAXS data.

Fits of experimental SAXS data recorded from the BECN1:ATG14 CCD heterodimer to (A) the BECN1:ATG14 CCD heterodimer and (B) BECN1 CCD homodimer. Fits of experimental SAXS data recorded from the BECN1 CCD homodimer to (C) the BECN1 CCD homodimer and (D) BECN1:ATG14 CCD heterodimer. The left panels show fits of the experimental scattering curve (red) measured from the BECN1 CCD homodimer or BECN1:ATG14 CCD heterodimer and the theoretical scattering curve (green) calculated from the two different atomic models. The right panels show the fit of these two atomic models into the molecular envelope calculated from the SAXS data. The D_{max} obtained from the P(r) function is indicated.

Strikingly, the similar heterodimer models obtained from the programs $(PS)^2$ and Modeller are both curved, with a curvature radius of 14 or 15 nm respectively (Figure 5.9A), similar to the curvature radius observed for the experimental SAXS envelope (Figure 5.8A, right panel), but different from the BECN1 CCD homodimer, which forms a flat structure (Figure 5.9 B and C). Subsequent analysis primarily uses the model obtained from $(PS)^2$. This model is structurally different from the BECN1 CCD homodimer, superimposing with a poor RMSD of 43.6 Å over 150 Cα atoms of the homodimer (Figure 5.10A). This curvature results in a heterodimer CCD length of 126 Å (Figure 5.9A), significantly shorter than the BECN1 CCD homodimer (Figure 5.9B), and agrees well with the D_{max} of 125 Å calculated from the P(r) function derived from the heterodimer SAXS data.

Next, we compared the experimental SAXS data recorded from the BECN1:ATG14 CCD heterodimer to the theoretical scattering curves calculated from the BECN1:ATG14 CCD heterodimer model and the BECN1 CCD homodimer structure. The experimental SAXS scattering curve fit nicely to the theoretical scattering curve calculated from the heterodimer model, with a χ^2 of 1.1 (Figure 5.8A, left panel). Consistent with this, the envelope encloses the heterodimer model very well (Figure 5.8A right panel). In contrast, the experimental SAXS data recorded for the BECN1:ATG14 CCD heterodimer does not fit well to the theoretical scattering curve calculated from the BECN1 CCD homodimer crystal structure, with a relatively higher χ^2 of 2.1 (Figure 5.8B, left panel). Consistent with this, the BECN1 CCD homodimer crystal structure fits poorly into the molecular envelope calculated from the BECN1:ATG14 CCD heterodimer SAXS data, with both termini of the 137 Å long BECN1 CCD extending beyond the envelope and the curvature of the heterodimer envelope resulting in poor agreement along the center of the BECN1 CCD homodimer (Figure 5.8B, right panel). Thus, the BECN1:ATG14

CCD heterodimer model fits better than the BECN1 CCD homodimer structure to the SAXS data recorded from samples of the heterodimer (Table 5.5).

Consistent with this, the BECN1 CCD homodimer crystal structure fits poorly into the molecular envelope calculated from the BECN1:ATG14 CCD heterodimer SAXS data, with both termini of the 137 Å long BECN1 CCD extending beyond the envelope and the curvature of the heterodimer envelope resulting in poor agreement along the center of the BECN1 CCD homodimer (Figure 5.8B, right panel). Meanwhile the experimental SAXS curve recorded from the homodimer also fits fairly well with homodimer structure with a relatively low χ^2 of 1.5 (Figure 5.8C, left panel). The envelope of BECN1 CCD homodimer forms a rod shape but is a little bent at one end (Figure 5.8C and D, right panel). Therefore, this envelope covers most of the straight BECN1 CCD homodimer with just the terminal residues exposed (Figure 5.8C, right panel). However, contrary to our expectations but perhaps not surprisingly, the fits of the experimental scattering curve of BECN1 homodimer to the calculated curve from heterodimer model show little difference with χ^2 of 1.2 (Figure 5.8D, left panel). This is because the heterodimer model is curved and the homodimer envelope is bent, which enables the homodimer envelope to cover most of the heterodimer model (Figure 5.8D, right panel). But the terminal residues of heterodimer are still exposed. Thus, the model of the BECN1:ATG14 CCD heterodimer fits best to the SAXS data recorded from samples of the heterodimer among all these fits (Table 5.5).

A comparison of the BECN1:ATG14 CCD heterodimer model to the analogous CCD heterodimer structure of the BECN1:UVRAG yeast homologs VPS30:VPS38 within the VPS34:VPS30:VPS38:VPS15 complex, shows that the 159 Å long VPS30:VPS38 CCD heterodimer is less curved, with a radius of curvature of ~17 nm (Figure 5.9C). Thus, the

BECN1:ATG14 CCD heterodimer is more curved relative to both, the BECN1 CCD homodimer and BECN1:UVRAG CCD heterodimer (Figure 5.9). As modeled, the BECN1:ATG14 CCD heterodimer (pI=7.0) has a more neutral surface (Figure 5.9A) than the highly negatively charged BECN1 homodimer (pI=4.3) (Figure 5.9B). In the BECN1:ATG14 CCD heterodimer, the N-terminal and central regions are negatively charged, while the C-terminal ends are positively charged (Figure 5.9A). The electrostatic surface of the VPS30:VPS38 CCD heterodimer (pI=6.2) is also closer to neutral, with the N-terminal region being positively charged while the central and C-terminal parts are negatively charged (Figure 5.9C).

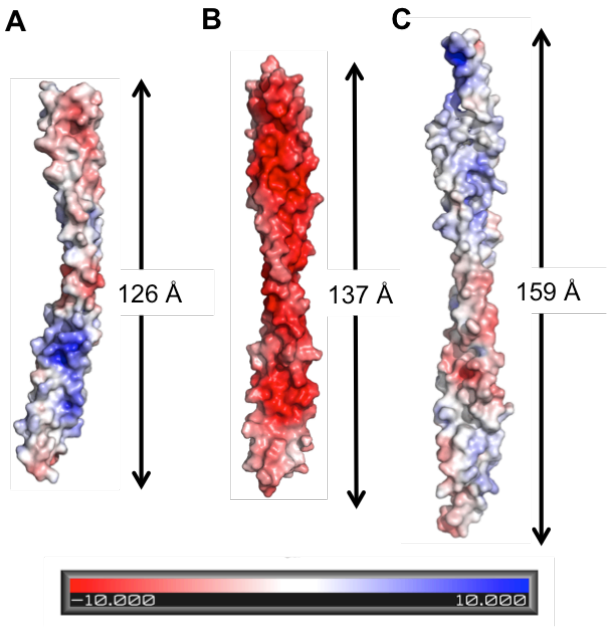

Figure 5.9. Comparison of the electrostatic potential surface of different. BECN1/VPS30 CCD-containing dimers. The length of each dimer is indicated. (A) BECN1:ATG14 CCD heterodimer (B) BECN1 CCD homodimer (C) VPS30:VPS38 CCD heterodimer (PDB ID: 5DFZ).

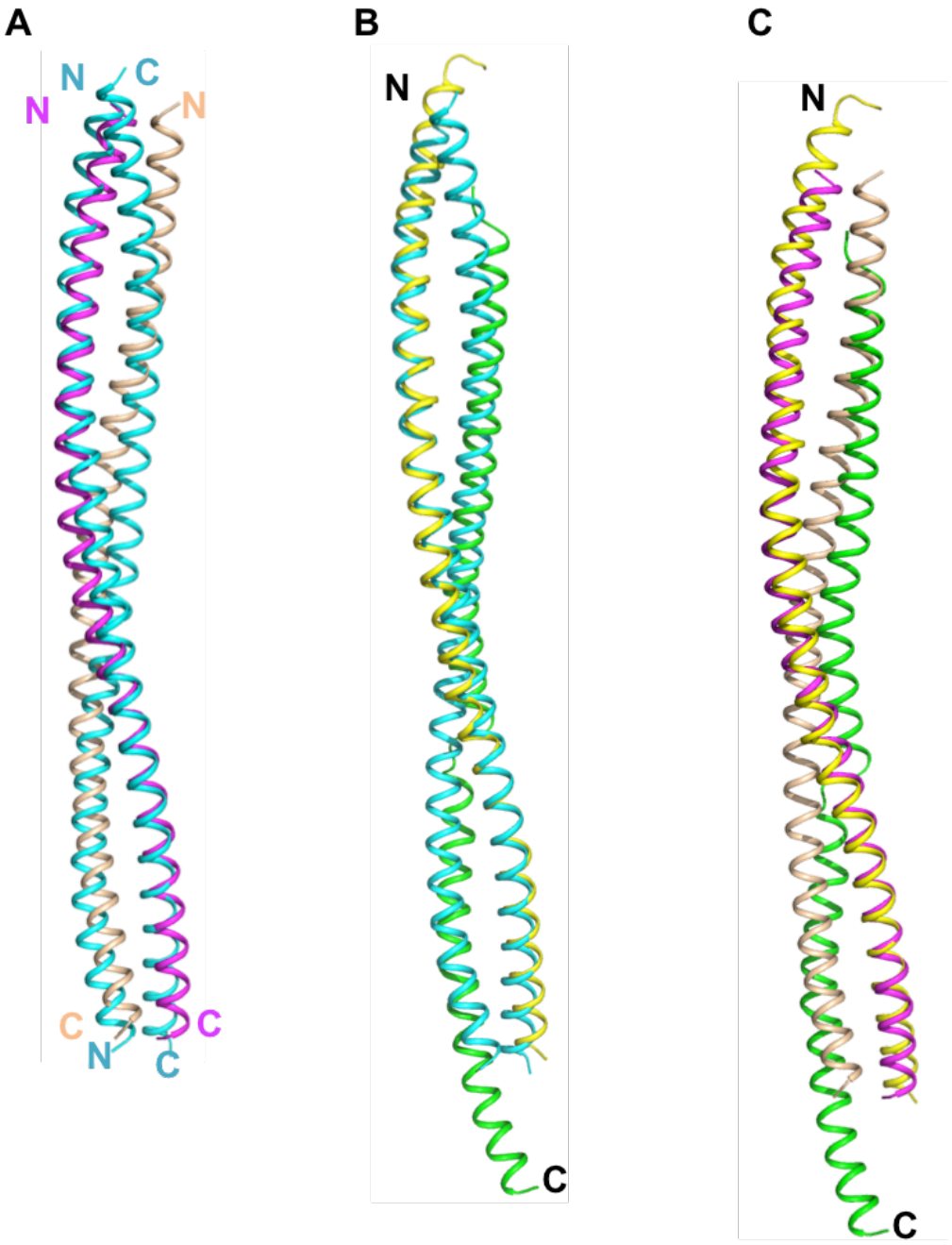

Figure 5.10. Comparison of the three different BECN1 dimers.
All proteins are shown in ribbon, colored as follows: BECN1, magenta; ATG14, wheat; VPS30, yellow and VPS38, green. The residues involved in interface interactions are shown in stick with atoms color-coded by atom type: O, red; N, blue; S, yellow; and C, colored according to main chain ribbon for that molecule. Superposition of BECN1 CCD homodimer on (A) BECN1:ATG14 CCD complex, (B) VPS30:VPS38 CCD complex (PDB ID: 5DFZ), and (C) superposition of BECN1:ATG14 CCD complex on VPS30:VPS38 CCD complex (PDB ID: 5DFZ).

5.3.5. The BECN1:ATG14 CCD Heterodimer Interface

Examination of the BECN1:ATG14 CCD heterodimer model shows that the total surface area buried at the interface in the heterodimer is 4389 $Å^2$, accounting for 24.3% of the ATG14 CCD surface area and 25.5% of the BECN1 CCD surface area. This buried area is less than in the BECN1 CCD homodimer, which is 4849 $Å^2$. In contrast, the CCD heterodimer of VPS30:VPS38 buries a total surface area of 3319 $Å^2$, accounting for 16.8% and 15.9% of the surface area of VPS30 and VPS38, respectively, which is much less than that observed for either the BECN1:ATG14 CCD heterodimer or the BECN1 CCD homodimer.

Superposition of the BECN1:ATG14 CCD heterodimer on the BECN1 homodimer (Rostislavleva, Soler et al. 2015) (Figure 5.10A) shows that the BECN1 CCD in the two structures aligns moderately well, with an RMSD of 2.6 Å over 91 Cα atoms. Superposition of the VPS30:VPS38 CCD heterodimer (Rostislavleva, Soler et al. 2015) (Figure 5.10B) on the BECN1 CCD homodimer is somewhat worse, with the VPS30 and BECN1 CCDs aligning with an RMSD of 3.5 for 91 Cα atoms. Superposition of the BECN1:ATG14 CCD heterodimer on equivalent regions of the VPS30:VPS38 CCD heterodimer (Rostislavleva, Soler et al. 2015) (Figure 5.10C) shows that the BECN1 CCD also aligns moderately well with equivalent VPS30 residues, with an RMSD of 2.7 Å for 91 Cα atoms; however, the partner ATG14 CCD superimposes more poorly upon the VPS38 CCD, with an RMSD of 4.1 Å for 82 Cα atoms.

In all three CCD dimer structures, the same BECN1 or equivalent VPS30 residues are pointed toward complementary residues from the partner CCD either from BECN1 or ATG14 or VPS38 (Figure 5.11 and Table 5.2). The BECN1:ATG14 CCDs are modeled in a parallel coiled-coil heterodimer, therefore, the residues at the a and d positions of heptad repeats from the BECN1 CCD interact with residues at the a’ and d’ positions of heptad repeats from the ATG14

CCD, to form 25 interacting pairs (Figure 5.11 and Table 5.2). A comparison of the residues at the interaction interfaces of the homodimer and heterodimer (Figure 5.11A and 5.11B), shows that all the BECN1 residues that contribute to the homodimer interface are also involved in the heterodimer interactions with ATG14 (Table 5.2), except for L264 from the last BECN1 heptad repeat. Analysis of the BECN1:ATG14 CCD heterodimer interface, shows that of the 25 interface pairs, only ten form acceptable hydrophobic interactions, including six ideal pairs (Figure 5.11A and Table 5.2). In the heterodimer, BECN1 residues S177 and L180, from the first heptad repeat, pack against ATG14 residues F92 and E95 (Figure 5.11A and Table 5.2). This register is maintained through the whole chain of interactions starting with BECN1 S177 and ATG14 F92, to BECN1 L261 and ATG14 V176.

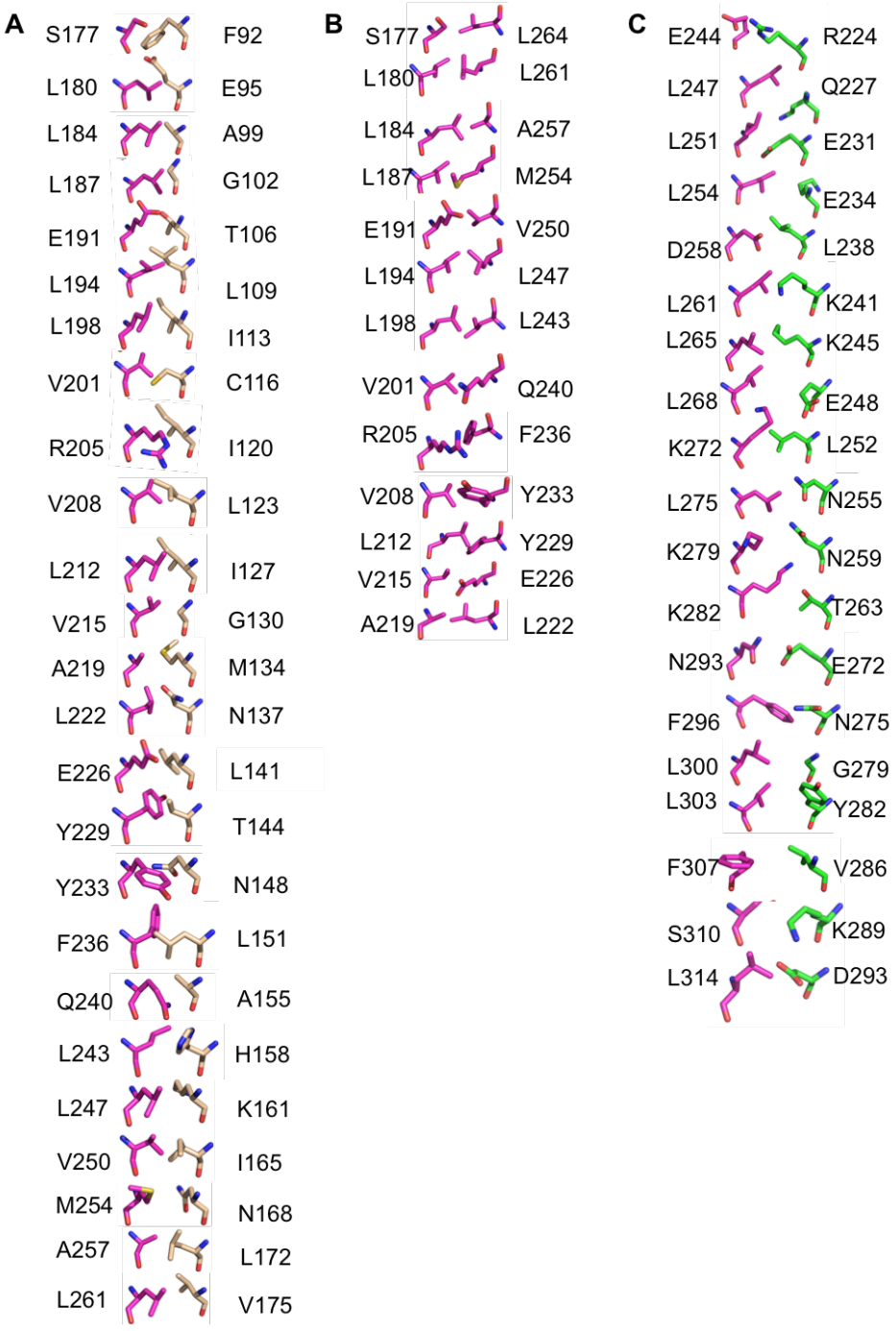

Figure 5.11. Comparison of the interface interactions among different. BECN1/VPS30 CCD-containing dimers. Residues are shown in stick and color-coded by atom-type: O, red; N, blue; S, yellow; and C, magenta (BECN1 / VPS30), wheat (ATG14), and green (VPS38). (A) BECN1:ATG14 CCD heterodimer. Black dotted circles indicate regions where the heterodimer helix is kinked. (B) BECN1 CCD homodimer. Thirteen interaction pairs are shown, as the remaining thirteen are related by two-fold molecular and crystallographic symmetry. (C) VPS30:VPS38 CCD heterodimer (PDB ID: 5DFZ).

Ten of the 25 BECN1:ATG14 interface pairs are hydrophobic: L184:A99, L194:L109, L198:I113, V208:L123, L212:I127, A219:M134, F236:L151, V250:I165, A257:L172 and L216:V176 (Figure 5.11A, Table 5.2). Interestingly, most of these interface pairs are conserved amongst diverse eukaryotes, except for BECN1 A219, F236, and L261. This is particularly striking because amongst these pairs, BECN1 residues V208, L212, F236 and V250 are paired with conserved polar residues from the partner BECN1 CCD in the homodimer, and therefore make better hydrophobic interactions in the modeled heterodimer than in the BECN1 homodimer (Figure 5.11 and Table 5.2). We find that toward the center of the heterodimer, BECN1 V208:ATG14 L123 and BECN1 L212:ATG14 I127 form two consecutive ideal hydrophobic pairings (Figure 5.11) and these residues are conserved in both BECN1 and ATG14 (Table 5.2), indicative of their importance in heterodimer formation. In addition, the variant BECN1 V215 that was paired with a glutamate is paired with the neutral G130 from ATG14 in the heterodimer (Table 5.2).

The invariant, charged BECN1 residue, E191, participates in 'imperfect' pairing with the highly conserved BECN1 V250 within the CCD homodimer (Figure 5.11B and Table 5.2). However, in the heterodimer, BECN1 V250 packs against the hydrophobic ATG14 I165, which is highly conserved amongst higher eukaryotes, but not in yeast (Figure 5.3, Figure 5.11B and Table 5.2); while BECN1 E191 pairs with the conserved ATG14 T106, with the pairing stabilized by hydrogen bonds. Further, the polar BECN1 Q240, which is partnered with hydrophobic V201 in homodimer, makes better interactions as it partnered with the conserved small residue, A155, in the heterodimer.

BECN1 S177 and Q240 form non-ideal interface pairs with ATG14 F92 and A155 respectively, however, they are stabilized by inter-molecular polar interactions with two polar

ATG14 interface residues, E95 and H158, located one turn away from the paired ATG14 residues. Further, the conserved BECN1 interface residue, Y233, is stabilized by an inter-chain polar interaction with the solvent-exposed, conserved ATG14 R154. Lastly, the heterodimer is also stabilized by a salt-bridge between the solvent-exposed conserved residues, BECN1 E190 and ATG14 R110. Thus, the interaction of the ATG14 CCD with the BECN1 CCD appears to involve many conserved, hydrophobic residues, as well as conserved, polar residues that are paired with conserved, polar BECN1 residues.

We used the numbering and positions in the 4.4 Å poly-alanine model of the VPS34:VPS30:VPS38:VPS15 complex, to model the residue side chains. Based on this, our analysis indicates that residues of the yeast VPS30 homolog that are equivalent to the BECN1 CCD interface residues are also pointed toward and involved in binding VPS38 (Figure 5.11 and Table 5.2). However, residues contributed to the interface by VPS38 are mostly polar and charged (Figure 5.11 and Table 5.2). Amongst 19 VPS38 residues involved in heterodimer interaction, only L238, L252 and V286 are hydrophobic (Figure 5.11C), but they interact with polar BECN1 D258, K272 and large side-chain F307 respectively. Thus the VPS30:VPS38 interface comprises entirely of non-ideal pairings. Further, the CCDs of VPS30 and VPS38 are physically shifted relative to each other, therefore VPS30 residues corresponding to four BECN1 interface residues from the N-terminal heptads, S177, L180, L184 and L187; as well as one residue from the C-terminal heptad, L264, do not interact with VPS38 residues (Figure 5.11C and Table 5.2). Lastly, a loop inserted in the center of the VPS38 CCD results in BECN1 residues Q286 and M289 not being paired at the interface.

Thus, overall, the VPS30:VPS38 heterodimer has very few hydrophobic interactions, with an interface that is not as extensive or well-packed as either the BECN1 CCD homodimer

or BECN1:ATG14 heterodimer interfaces. The BECN1:ATG14 interface is marginally more extensive than that of the BECN1 homodimer with some non-ideal packing interactions involving paired hydrophobic and polar residues in the homodimer, being replaced in the heterodimer by either better hydrophobic interactions or polar pairings. This differential packing of BECN1 homodimer and different heterodimer interfaces, likely impacts competitive binding of diverse BECN1 partners within cells. These improved interactions result in a significant enthalpic contribution to BECN1:ATG14 CCD binding.

5.3.6. BECN1 CCD Interface Residues are Important for Binding the ATG14 CCD and are Required for Starvation-induced Autophagy

In order to assess the importance of residues at the CCD interface, we mutated selected interface residues to alanine in full-length BECN1, then assessed the impact of these mutations on Co-IP with full-length ATG14 and on cellular autophagy levels. The hydrophobic BECN1 residues L184, L194, V208, L212, L222, Y233, F236 and V250 (Figure 5.11A) were selected for alanine-mutagenesis. Of these selected BECN1 residues, L194 is invariant and F236 is not conserved, while the remaining residues are conserved. Based on the heterodimer model, L194, V208, L212, and V250 form ideal hydrophobic pairings with conserved ATG14 residues. BECN1 F236 interacts with the highly conserved ATG14 L151; while L184, L222, Y233 participate in non-ideal interactions with polar or small ATG14 interface residues (Figure 5.11 and Table 5.2).

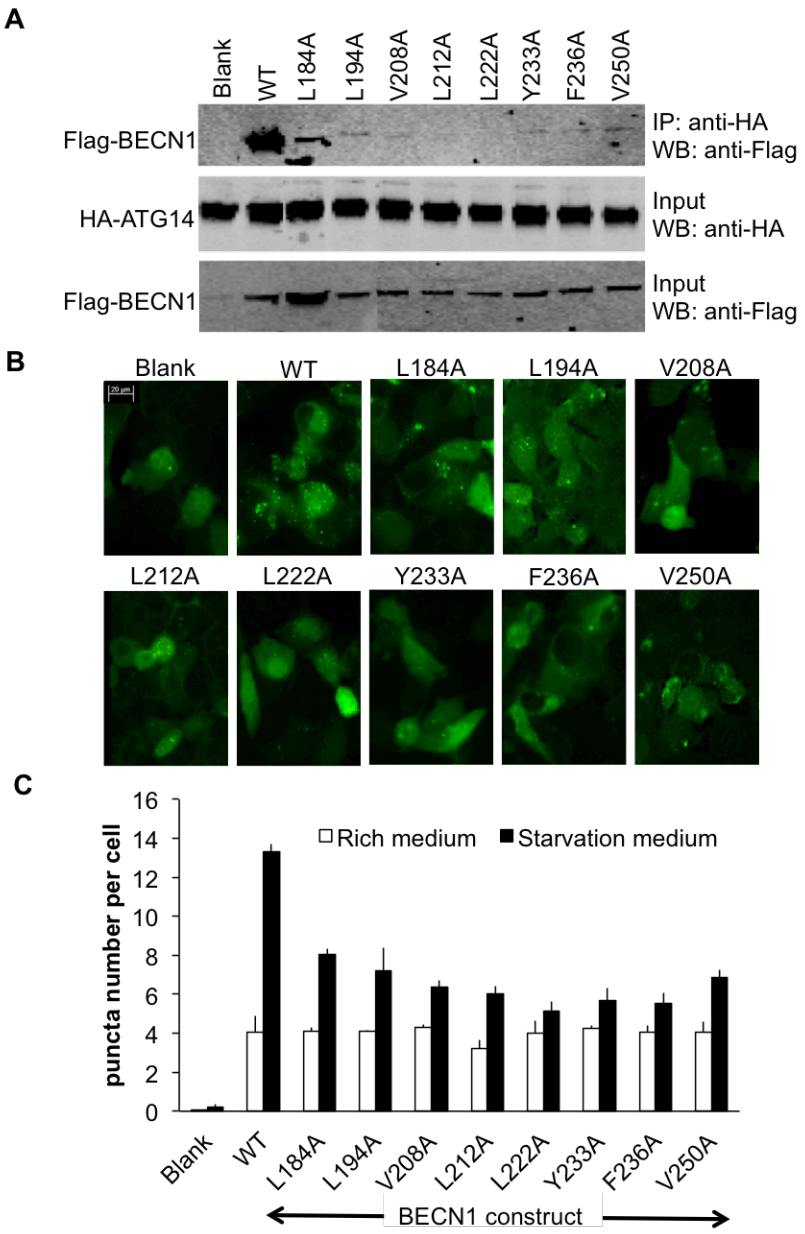

Figure 5.12. Effect of single alanine mutagenesis of conserved BECN1 interface residues. (A) Impact on ATG14 binding as assessed by Co-IP of HA-ATG14 and WT or single mutant Flag-BECN1. IP with anti-HA and western blot with anti-Flag (top); Western blot with anti-HA (middle); Western blot of lysate using anti-Flag (bottom). (B) Representative images of GFP-LC3 staining in cells grown in growth media (top) and starvation media (bottom), transfected with WT ATG14 and WT or mutant BECN1 as indicated. (C) Bars represent fluorescent microscopy quantification of discrete GFP-LC3 labeled autophagic puncta per cell in GFP-positive MCF7 cells co-transfected with GFP-LC3, WT ATG14, and WT or single mutant BECN1 as indicated below the x-axis.

The cellular assays were performed using MCF7 cells, which have a defective *becn1* gene and express low levels of BECN1 (Liang, Jackson et al. 1999, Liang, Yu et al. 2001, Furuya, Yu et al. 2005, Pattingre, Tassa et al. 2005), thereby allowing the effect of BECN1 mutations to be assayed in the absence of endogenous BECN1. Our Co-IP results show that all the BECN1 interface mutations dramatically decreased interaction with ATG14 (Figure 5.12A). Amongst these, the L212A and L222A mutations completely abolish interaction with ATG14; the L194A, V208A, Y233A, F236A and V250A mutations result in barely detectable interaction with ATG14, and only the L184A mutant shows clear interaction with ATG14, although the interaction is substantially diminished relative WT BECN1 (Figure 5.12A). These results confirm the essential role of these BECN1 residues identified from our BECN1:ATG14 heterodimer model in mediating the interaction of full-length BECN1 and ATG14 in cells.

Earlier studies have conclusively shown that the interaction of BECN1 and ATG14 is required for autophagosome nucleation (Yorimitsu and Klionsky 2005, Itakura, Kishi et al. 2008, Obara and Ohsumi 2011). Therefore, here we monitored autophagy levels simply by quantifying the change in cellular localization of a GFP-tagged, transiently expressed mammalian autophagy-specific marker, LC3 (GFP-LC3) from a diffuse cytoplasmic distribution to localized puncta corresponding to autophagosomal structures (Kabeya, Mizushima et al. 2000). Due to low BECN1 expression levels, MCF7 cells do not show starvation-induced increases in autophagy unless BECN1 is ectopically expressed (Liang, Jackson et al. 1999, Liang, Yu et al. 2001, Furuya, Yu et al. 2005, Pattingre, Tassa et al. 2005) (Holt, Thompson et al. 1996, Liang, Jackson et al. 1999). Transient expression of BECN1 in MCF7 cells led to a marked increase in autophagy upon starvation ($p = 6.0\times10^{-4}$ for starved versus nutrient-rich cells; Figure 5.12B, 5.12C).

Basal autophagy levels in nutrient-rich media are typically lower and less consistent than in starvation conditions. Nevertheless, in nutrient rich conditions, the expression of the BECN1 CCD interface mutants results in basal autophagy levels similar to WT BECN1, (ranging between $p = 0.20$ to 0.98 for mutants versus WT BECN1; Figure 5.12C). In contrast, a pronounced effect is seen on starvation-induced autophagy levels. Starvation triggers an increase in autophagy regardless of whether WT or mutant BECN1 is expressed (ranging between $p = 4\times10^{-5}$ to 0.02) for starvation versus rich conditions; Figure 5.12C), except in the case of BECN1 L222A that abrogates starvation-induced autophagy ($p = 0.07$ for starvation versus rich conditions; Figure 5.12C). However, the starvation-induced increase in autophagy is markedly diminished when upon expression of each of the BECN1 mutants (ranging between $p = 2\times10^{-5}$ to 0.008 for mutants versus WT BECN1; Figure 5.12C), with the decrease in starvation-induced autophagy caused by each mutation being somewhat co-related with the ability of the mutant to bind ATG14. This suggests that the BECN1 CCD interface residues are not essential for basal levels of autophagy in nutrient-rich conditions, but are critical for the interaction with ATG14 and for starvation-induced up-regulation of autophagy.

5.3.7. ATG14 CCD Residues Important for Interacting with the BECN1 CCD are Also Required for the Starvation-induced Autophagy

Based on our analysis of the BECN1:ATG14 CCD interface, hydrophobic ATG14 interface residues L109, I120, L123, I127, L151 and I165 (Figure 5.11A) were selected for alanine-mutagenesis, to investigate their role in heterodimerization with BECN1, as well as in mediating autophagy. Each of these residues is conserved and also paired with a conserved BECN1 residue within the BECN1:ATG14 CCD heterodimer.

Co-IP experiments were used to assess the impact of these mutations on the interaction between exogenously expressed full-length BECN1 and ATG14 (Figure 5.13A). Our results show that compared to WT ATG14, expression of mutant ATG14 constructs decreases interaction with WT BECN1 (Figure 5.13A). Expression of I120A or I165A ATG14 mutants abolishes binding to BECN1; expression of the L123A or I127A mutants substantially decreases binding; while expression of the L109A or L151A mutants only marginally decreases binding to BECN1 (Figure 5.13A). Therefore, ATG14 I120 and I165 appear to be required for binding to BECN1, while L109A and L151A are less important.

Next we investigated the effect of these mutations on cellular autophagy, by quantifying transiently-expressed, GFP-LC3 labeled, autophagosomal puncta in mammalian cells in both nutrient-rich and starvation media. Since earlier studies have used diverse methods to establish the critical role of ATG14 and BECN1 in autophagosome nucleation, and show that in starvation conditions, ATG14 promotes autophagic flux via binding to BECN1 (Itakura, Kishi et al. 2008, Sun, Fan et al. 2008, Itakura and Mizushima 2009, Matsunaga, Saitoh et al. 2009, Zhong, Wang et al. 2009, Fogel, Dlouhy et al. 2013); the quantification of the cellular localization of the GFP-LC3 labeled, autophagosomal puncta is adequate for assessing the impact of ATG14 mutations on cellular autophagy levels (Figure 5.13B and C). Monkey kidney COS7 cells were selected for this experiment as they have reduced endogenous expression of some autophagy-related genes including ATG14, and do not show a starvation-induced increase in autophagy unless ATG14 is ectopically expressed (Figure 5.13B and C) (Xiong, Tao et al. 2012). This allows us to assess the impact of ATG14 mutants on autophagy without background effects due to endogenous ATG14 expression.

We find that in nutrient-rich conditions, the number of autophagic puncta are comparable, regardless of whether ATG14 is exogenously expressed or not ($p = 0.24$ for absence vs. presence of ectopically-expressed ATG14). Indeed, in nutrient rich conditions, none of the ATG14 CCD mutants significantly impact cellular autophagy levels, as indicated by the similar numbers of autophagosome puncta per cell ($p > 0.05$ for mutants vs. WT ATG14) (Figure 5.13C). Strikingly however, starvation does not increase the number of autophagosomes ($p = 0.89$, for starvation vs. nutrient rich conditions in absence of ectopically-expressed ATG14), unless ATG14 is exogenously expressed ($p = 0.007$ for starvation vs. nutrient rich conditions when ATG14 is exogenously expressed). This suggests that ATG14 expression, and consequently the BECN1:ATG14 interaction, is not essential for basal levels of autophagosome nucleation in nutrient-rich conditions, but is critical for the starvation-induced up-regulation of autophagy.

All the ATG14 mutations tested adversely impact starvation-induced up-regulation of autophagy. Consistent with the Co-IP results, up-regulation of autophagy in response to starvation is significantly diminished upon exogenous expression of either the I120A or I165A ATG14 mutant ($p = 0.005$ and 0.009, for mutant vs. WT ATG14 respectively, Figure 5.13B and C), for which no BECN1 binding was detected. Interestingly, there is a comparable reduction in the starvation-induced up-regulation of autophagy even when the L123A and I127A ATG14 mutants are expressed ($p = 0.005$ and 0.01, for mutant vs. WT ATG14 respectively, Figure 5.13B and C), which show weak binding to BECN1. Further, even the L151A ATG14 mutant that shows only a marginal decrease in binding to BECN1, shows a significant decrease in starvation-induced up-regulation of autophagy ($p = 0.01$, for L151A vs. WT ATG14), although the levels of starvation-induced autophagy are higher than for the preceding four mutants (Figure 5.13C).

Only the L109A ATG14 mutant does not significantly diminish starvation-induced up-regulation of autophagy ($p = 0.11$ for L109A vs. WT ATG14, Figure 5.13B and C), consistent with the marginal decrease in BECN1 binding observed for this mutant.

Thus, the starvation-induced up-regulation of autophagy is correlated with the ability of the ATG14 CCD to interact with the BECN1 CCD. However, this correlation is not perfect, as the reduction in starvation-induced autophagy is more dramatic than would be expected from a response that was proportional to the reduction of interaction between ATG14 and BECN1 due to each mutation. From a biochemical mechanism perspective, this suggests that even a marginal decrease in the binding of BECN1 and ATG14 can have larger physiological effects within a cell.

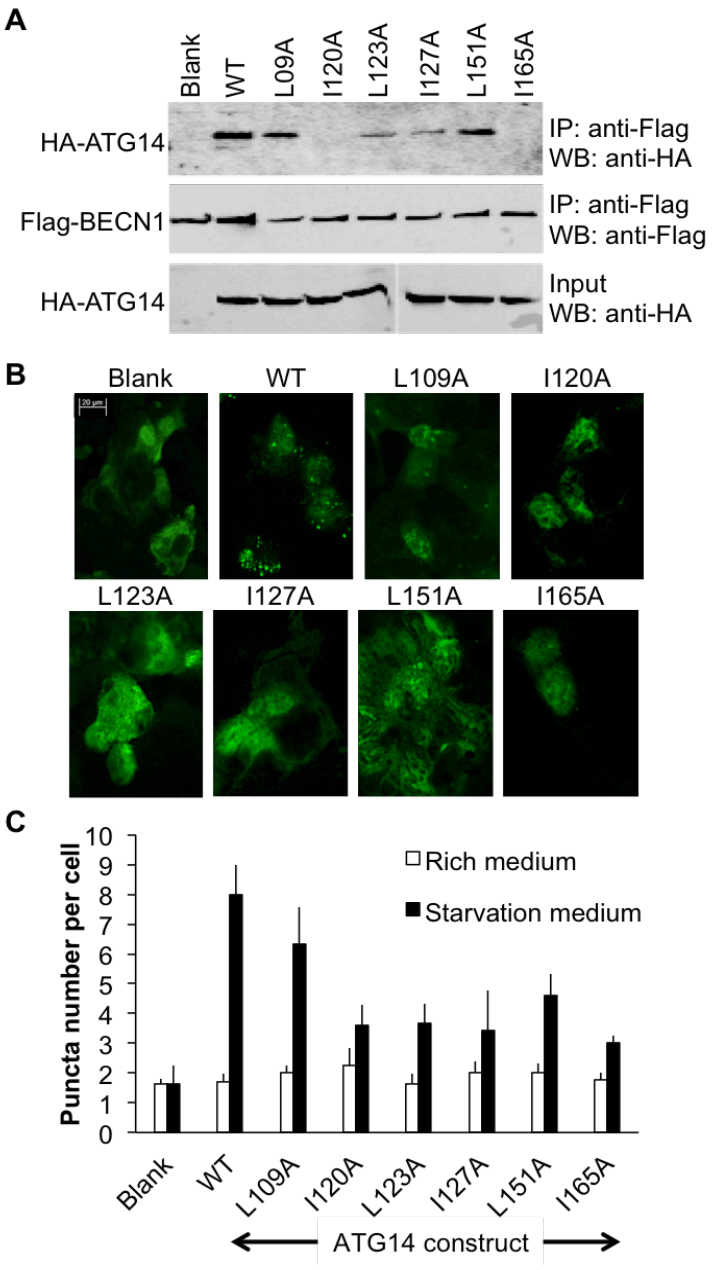

Figure 5.13. Impact of alanine mutagenesis of conserved ATG14 interface residues. (A) Impact on BECN1 binding as assessed by Co-IP of Flag-BECN1 and WT and single mutant HA-ATG14. IP with anti-flag and western blot with anti-HA (top); Western blot with anti-Flag (middle); Western blot of lysate using anti-HA (bottom). (B) Co-IP of Flag-BECN1 and WT or single mutant HA-ATG14. IP with anti-flag and western blot with anti-HA (top). (B) Representative images of GFP-LC3 staining in cells grown in growth media (top) and starvation media (bottom), transfected with WT BECN1 and WT or mutant ATG14 as indicated. (C) Bars represent fluorescent microscopy quantification of discrete GFP-LC3 autophagic puncta per cell in GFP-positive COS7 cells co-transfected with GFP-LC3, WT BECN1, and WT or mutant ATG14 as indicated below the x-axis.

5.4. Discussion

BECN1 and ATG14 both contain CCDs that are essential to their role in autophagosome biogenesis and mediate a variety of interactions. However, there are many differences between the CCDs of the two proteins. The BECN1 CCD self-associates to form a stable, highly-helical, anti-parallel homodimer in the absence of other partners that interact via the CCD. BECN1 CCD N-terminal contains a leucine-rich nuclear export signal motif (NES, residues 180-190) that binds the chromosomal maintenance protein 1 (CRM1). Mutation of the conserved Leu184 and Leu187 block the CRM1-dependent nuclear export of BECN1 as well as the autophagy and tumor suppressor functions in MCF7 cells (Liang, Yu et al. 2001). In BECN1 CCD homodimer, the C-terminal overlap helix (residues 248-265) between BECN1 CCD and BARAD packs against this BECN1 NES motif via L184:A257 and L187: M254. Therefore, in the process of nuclear export, the overlap helix would be free to adopt the conformer in BECN1 BARAD. In contrast, the ATG14 CCD has no detectable homodimerization, and approximately 30% of the CCD appears to be disordered in the monomeric state, and only marginally less within the BECN1:ATG14 heterodimer. It is likely that this disordered structure makes ATG14 particularly prone to proteases, preventing purification in the absence of a stabilizing tag such as MBP and complicating structural studies. Indeed, contrary to our expectations, but consistent with the comparable disorder in monomeric and heterodimeric states, the heterodimerization with BECN1 did not completely protect ATG14 from degradation, only somewhat delayed degradation. This conformational flexibility is likely an important structural and biochemical property of ATG14, perhaps facilitating interactions with diverse partners or simultaneous interaction with multiple partners as well as structural elasticity within different complexes, thereby enabling ATG14 to adopt different conformations to perform diverse functions.

Both BECN1 and ATG14 are moderately conserved amongst eukaryotes. The CCD of each protein constitutes one of the best-conserved domains within each protein. As expected, the sequences, overall structures and interactions stabilizing the human and rat BECN1 CCD homodimer are very similar, but differ markedly from the structure and interactions of the BECN1:ATG14 heterodimer. The pseudo-atomic BECN1:ATG14 CCD model, verified by good fits to experimental SAXS data, enables identification of potential ATG14 and BECN1 CCD residues that contribute to the BECN1:ATG14 interaction.

Our mutagenesis combined with cellular Co-IP assays confirms that almost all of the selected BECN1 and ATG14 interface residues are important for heterodimerization, verifying the BECN1:ATG14 CCD pseudo-atomic model presented. Further, the heterodimer model presented here is also supported by previously published studies using ITC to investigate the potential role of alanines and/or charged BECN1 residues located at the interface of the BECN1 homodimer, in binding ATG14. Interaction with the ATG14 CCD is abolished by the BECN1 single mutations: E191L and R205L; double mutations: E191L+A257L and A219L+E226L; triple mutation A219L+E226L+A257L; and tetrad mutation E191L+A219L+E226L+A257L (Li, He et al. 2012).

Strikingly, exogenous expression of ATG14, in cell lines reported to have no detectable ATG14 expression, does not result in an increase in the number of autophagic puncta in nutrient-rich conditions. However, starvation-induced up-regulation of autophagy is observed in these cells only upon exogenous expression of ATG14, consistent with previous studies that indicate ATG14 is primarily required for the starvation-mediated up-regulation of autophagy (Itakura, Kishi et al. 2008, Sun, Fan et al. 2008, Itakura and Mizushima 2009, Hamasaki, Furuta et al. 2013). Our studies further indicate that the BECN1:ATG14 interaction is not essential for low,

basal levels of autophagosome formation, but is critical for starvation-induced up-regulation of autophagy. Further, it appears that even a slight reduction of the BECN1:ATG14 interaction dramatically abrogates the increase in autophagy in response to starvation. Perhaps, in cells undergoing autophagy, a slight reduction in binding affinity is sufficient to allow other BECN1 interactions to out-compete the interaction with ATG14 thereby altering the biochemical equilibrium of complex formation and preventing an up-regulation of autophagy.

BECN1 and ATG14 play critical roles in autophagosome biogenesis, specifically in autophagy nucleation. Neither BECN1 nor ATG14 have been shown to have any catalytic activity, but the association of BECN1:ATG14, or BECN1:UVRAG, with the PI3KC3:P150 binary complex has been shown to increase PI3KC3 catalytic activity, resulting in an increased production of PI3P (Fan, Nassiri et al. 2011), a signaling molecule critical for the recruitment of other autophagy proteins to the developing autophagosome and the up-regulation of autophagy. Further, BECN1 and ATG14 associate with membranes, serving as a sensor of membrane lipid composition and, in the case of ATG14, membrane curvature.

Lastly, both BECN1 and ATG14 are implicated in additional interactions, with BECN1 specifically appearing to serve as an interaction hub for autophagy regulators (He and Levine 2010, Kang, Zeh et al. 2011, Mei, Su et al. 2014, Levine, Liu et al. 2015). For example, the yeast two-hybrid experiment indicates that the nPIST CCD (residues 34-231) may form the heterodimer with BECN1 CCD and act synergistically to induce autophagy. This interaction may be facilitated by the nPIST PDZ domain together with other proteins such as Gluδ2 to induce autophagy (Yue, Horton et al. 2002). Therefore, the combined role of these proteins appears to be to serve as a scaffold for the autophagosome nucleation complex, thereby up-regulating

catalytic activity of PI3KC3, to sense and influence membrane curvature and lipid composition and to serve as an interaction hub for autophagy regulators.

Our results show that the BECN1:ATG14 CCD heterodimer is shorter and more curved than the VPS30:VPS38 CCD heterodimer, which would alter the conformation of and interactions within and outside the quaternary complex. For instance, the different structure and curvature of the BECN1:ATG14 CCD heterodimer would result in changes in the relative positioning of membrane-binding domains within the quaternary complex (Figure 5.14). The C-terminal BECN1 BARAD and ATG14 BATS domain that are required for membrane association and for sensing membrane composition; and the PI3KC3 catalytic domain, which binds to PI-rich membranes, are located at the tips of the two arms of the V-shaped complex. The altered curvature would result in ~14 Å displacement of the BECN1 BARAD from the position occupied by the VPS30 BARAD within the quaternary complex, relative to PI3KC3 (Figure 5.14). Such changes in Complex I may dictate the preferential binding to more curved membranes.

The association of BECN1:ATG14 with PI3KC3:p150 increases PI3KC3 catalytic activity. However the mechanism by which this occurs is unclear. The different positions, curvatures and sequences of the two different heterodimers would also necessitate altered positioning and interactions of the VPS15/p150 WD40 domain within the quaternary structure. This may, in turn, alter P150:PI3KC3 interactions, resulting in stabilization of a more catalytically-active conformation of PI3KC3. As formation of the autophagosome nucleation complex increases PI3P content in the membranes, it would lead to formation of additional quaternary complexes as well as recruitment of other PI3P-binding autophagy proteins.

Numerous studies have shown that the CCDs of each protein are required and sufficient for the interactions of BECN1 with either ATG14 or UVRAG (Liang, Feng et al. 2006, Itakura, Kishi et al. 2008, Liang, Lee et al. 2008, Sun, Fan et al. 2008, Itakura and Mizushima 2009, Matsunaga, Saitoh et al. 2009, Zhong, Wang et al. 2009), however, other domains from each protein likely also support these interactions. For instance, the BECN1 C-terminal BARAD packs against a BARAD at the C-terminus of UVRAG; and the FHD, a short helical region preceding the CCD in both BECN1 and UVRAG, also forms a heterodimeric coiled-coil structure in the quaternary structure complex (Rostislavleva, Soler et al. 2015). Therefore, it is possible that the ATG14 BATS domain packs against the BECN1 BARAD. Moreover, the conserved residues in BECN1 BARAD are found to cluster on the surface which contains N terminus of BARAD, indicating these residues could form a continuous surface with the C-terminus of BECN1:ATG14 CCD complex. Therefore, the conserved residues in BARAD may also facilitate the recruitment of other proteins to ATG14-containing PI3KC3 complex I to activate the kinase activity of PI3KC3 (Noda, Kobayashi et al. 2012). Further, although ATG14 is not predicted to contain a helical region preceding the BECN1 CCD, the existence of such a helical interacting region is not impossible given the known ATG14 domain architecture.

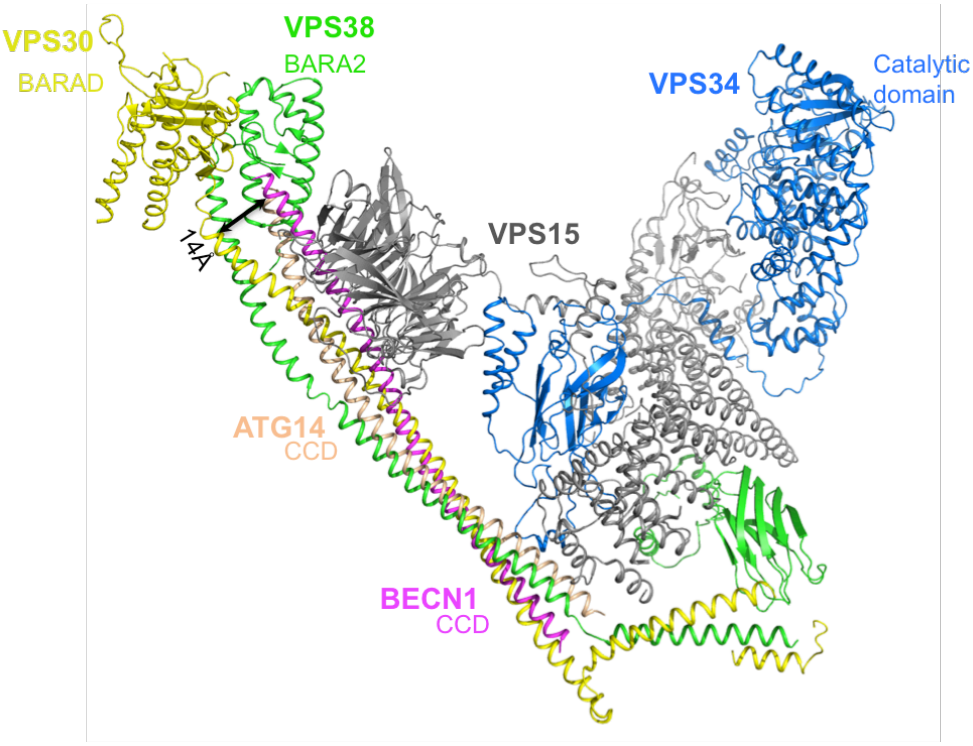

Figure 5.14. Displacement of the BECN1 BARAD domain due to the curved BECN1:ATG14 quaternary structure.
All proteins are shown in ribbon, colored as follows: BECN1, magenta; ATG14, wheat; VPS30, yellow; VPS38, green; VPS15, grey, and VPS34, blue. Protein domains implicated in membrane interaction, the BECN1 BARAD, ATG14 BARAD and PI3KC3 catalytic domain are labeled. Arrows indicate altered positions of equivalent residues.

The CCDs of BECN1 and ATG14 have also been implicated in other, mutually exclusive interactions. The BECN1 CCD also interacts with CCDs from diverse proteins such as UVRAG/VSP38 (Liang, Feng et al. 2006, Liang, Feng et al. 2007), TAB2 and TAB3 (Criollo, Niso-Santano et al. 2011, Niso-Santano, Criollo et al. 2012). While the interaction of the BECN1 CCD with the UVRAG CCD up-regulates autophagy (Liang, Feng et al. 2006, Liang, Feng et al. 2007, Itakura, Kishi et al. 2008, Liang, Lee et al. 2008), BECN1 CCD interaction with CCDs of either TAB2 or TAB3 down-regulates autophagy (Criollo, Niso-Santano et al. 2011, Niso-Santano, Criollo et al. 2012). The ATG14 CCD also binds to the SNARE core domain of STX17, thereby stabilizing the STX17:SNAP29 binary t-SNARE complex on autophagosomes

and facilitating subsequent fusion of the autophagosome and lysosome upon association of the t-SNARE and v-SNARE VAMP8 (Hamasaki, Furuta et al. 2013, Diao, Liu et al. 2015). ATG14 binds to either STX17 or the STX17-SNAP29 binary t-SNARE ternary membrane fusion complex, but not to the STX17:SNAP29:VAMP8 complex. Further, the BECN1:ATG14 CCD and ATG14:STX17 CCD heterodimers are mutually exclusive, indicating that ATG14 plays a role in autophagy, independent of BECN1. The STX17:SNAP29:VAMP8 crystal structure (Diao, Liu et al. 2015) has a radius of curvature of 16 nm, comparable to the 15 nm radius of curvature for the BECN1:ATG14 complex. The relative curvature of these different CCDs dimers likely also affects their competitive association and function in the cell.

Similarly, the CCD-containing region (residues 393-849) of Run domain protein as BECN1 interacting and cysteine-rich containing protein (RUBICON) (Matsunaga, Saitoh et al. 2009) interacts with UVRAG CCD to prevent the BECN1:UVRAG CCD complex formation, inhibit the autophagosome maturation and negatively regulate autophagy (Sun, Zhang et al. 2011). Therefore, CCDs play important roles for various protein-protein interactions in PI3KC3 complexes in autophagy.

In summary, our studies of the BECN1:ATG14 heterodimer provide important structural and biochemical insight into the potential architecture and mechanism of Complex I. We show that the BECN1:ATG14 interaction is critical for the eukaryotic cellular response to stressors such as starvation, and elucidate key structural details of this interaction. This study provides clues to the structural details of the mechanism by which competitive formation of BECN1 homodimers, BECN1:ATG14 heterodimers, and perhaps BECN1:UVRAG heterodimers, occurs in cells. It also provides clues to the conformational changes within proteins, especially in ATG14, as well as to how different BECN1 CCD interactions may affect formation and structure

of different quaternary complexes that function in different stages of vesicle trafficking. Substantial additional studies will be required to elucidate details of the mechanisms by which these complexes up-regulate PI3KC3-mediated PI phosphorylation and influence membrane association and curvature, and how these functions are themselves regulated by additional diverse interactions. Further, extensive structural, thermodynamic and cellular studies of these diverse BECN1 and ATG14 interactions are required in order to fully understand how these interactions complement and compete with each other to mediate and differentially modulate cellular autophagy levels. The information regarding the BECN1:ATG14 interaction presented here provides important insight that can be used to design future studies to ultimately elucidate the mechanism of membrane association and PI3KC3 activation. A detailed understanding of BECN1 interactions with cellular and viral BCL2 proteins recently enabled development of a potent, yet very specific, cell penetrating peptide, designed to disrupt viral BCL2-BECN1 interactions, and induce autophagy in cultured cells, without affecting normal regulation of BECN1-mediated by cellular BCL2 proteins (Su, Mei et al. 2014). Therefore, we expect that given the importance of autophagy to human health, elucidating a detailed structure-based understanding of the various protein interactions that modulate cellular autophagy levels will greatly facilitate the future development of new therapeutics.

CHAPTER 6. INVARIANT RESIDUES IN THE BECN1 BARAD ARE IMPORTANT FOR STARVATION-INDUCED AUTOPHAGY

6.1. Introduction

The highly conserved C-terminal region of BECN1 was formerly referred to as the ECD, based upon analysis of sequence alignment among homologs that indicate that most of the conserved residues of BECN1 are located within this region. However, X-ray crystal structures of the yeast VPS30 residues 320-557 and human BECN1 residues 248-450 (Huang, Choi et al. 2012, Noda, Kobayashi et al. 2012), indicate this region adopts a new structural fold consisting of three repeats of a three-stranded, anti-parallel β-sheet followed by a helix; with the three repeats arranged around an approximate central 3-fold such that the helices form a central three-helix bundle surrounded by the β-sheets. Largely conserved, hydrophobic residues in BARAD stabilize the packing of the helices, as well as the β-sheets, against the three-helix bundle (Noda, Kobayashi et al. 2012). This novel domain is required for autophagy but not vacuolar sorting, and was therefore re-named the β-α repeated autophagy-specific domain.

Liposome binding and cellular autophagy assays have revealed that autophagy induction is dependent upon the membrane-binding function of an "aromatic finger" composed of BARAD residues F259, F360 and W361. WT BARAD, but not a F259D+F360D+W361D mutant, co-sediment with liposomes and co-localizes with lipid membranes (Huang, Choi et al. 2012). Loss of the aromatic finger also reduces starvation-induced autophagy. Although the aromatic finger is not well conserved in yeast VPS30, hydrogen-deuterium exchange mass spectrometry analysis of the yeast VPS30 identified a region analogous to the aromatic finger that directly interacts with lipid membranes (Rostislavleva, Soler et al. 2015, Rostislavleva, Soler et al. 2015).

A recent 4.4 Å crystal structure of yeast PI3KC3 Complex II (Rostislavleva, Soler et al. 2015) reveals that VPS30 BARAD interacts with a C-terminal VPS38 domain that has a similar to BARAD, but with only two repeats of the three-stranded, anti-parallel β-sheet and helix unit, and was therefore named the VPS38 BARA2 domain. The VPS30 BARAD:VPS38 BARA2 domain interactions involve the first α-helix and second β-sheet of the VPS30 BARAD and the second α-helix of the VPS38 BARA2. The VPS30 BARAD:VPS38 BARA2 interaction is located at the tip of one arm of the V-shaped yeast PI3KC3 Complex II, which allows these domains to bind membranes and trigger membrane phosphorylation by PI3KC3.

Several other proteins target the BARAD to regulate autophagy. BARAD residues 267-284 are essential for autophagy, and also necessary and sufficient for *in vivo* interaction with the endogenous autophagy inhibitor GAPR1 (Golgi-associated plant pathogenesis-related protein 1), and HIV-encoded Nef, which induces autophagy (Shoji-Kawata, Sumpter et al. 2013).

However, the impact of the conserved BARAD residues on BECN1-dependent starvation-induced autophagy has not been investigated. We first performed a sequence alignment of human BECN1 orthologs from eight eukaryotes ranging from humans to yeast, to identify the highly conserved residues in the BECN1 BARAD. We then transfected mammalian cells with alanine mutants of these highly conserved residues, generated by site-directed mutagenesis, to investigate the impact of these mutants on starvation-induced autophagy. We found that the invariant residues within the BECN1 BARAD region comprising residues 268-286 are important for starvation-induced up-regulation of autophagy.

6.2. Materials and Methods

6.2.1. Sequence Analysis

Sequences of BECN1 homologs from eight eukaryotes: *Homo sapiens, Mus musculus, Gallus gallus, Xenopus tropicalis, Drosophila melanogaster, Caenorhabditis elegans, Arabidopsis thaliana,* and *Saccharomyces cerevisiae* were identified by BLASTP searches of the Genomic RefSeq Protein databases (http://blast.ncbi.nlm.nih.gov/) for each organism. Multiple sequence alignments of these diverse orthologs were performed with CLUSTALW (Thompson, Gibson et al. 2002) and displayed using Jalview (Waterhouse, Procter et al. 2009).

6.2.2. Autophagy Assay

The selected invariant or conserved residues within human BECN1 BARAD were mutated by site-directed mutagenesis (Agilent Technologies) using primers ordered from Integrated DNA Technologies. James Moulton made all theses mutants. 2×10^5 MCF7 cells were seeded in each chamber of four-well culture slides (Millipore EZ slides) and incubated overnight in DMEM with 10% FBS (growth medium) until ~80% confluence. Lipofectamine 2000 (Invitrogen) was used according to the manufacturer's method to co-transfect MCF7 cells with 4 μg of total plasmids comprising 1.6 μg GFP-LC3; and 2.4 μg WT BECN1 or mutant BECN1 expression plasmids. 24 hours after transfection, the cells were either starved (Earle's balanced salt solution, GIBCO), or grown in growth medium enriched with 2X amino acid mixture (GIBCO) for four hours. Then the cells were fixed with 4% paraformaldehyde in PBS. GFP-LC3-positive puncta were observed using a Zeiss AxioObserver Z1 fluorescent microscope and quantified by counting a minimum of 50 cells per condition in three independent repeats using the Imaris program (Bitplane). The significance of alterations in autophagy levels was

determined by a two-tailed, heteroscedastic student's *t*-test, wherein $p \leq 0.05$ is considered significant.

6.2.3. Western Blotting

1×10^6 MCF7 cells were seeded into each well of a 6-well plate and cultured in DMEM plus 10% FBS. Lipofectamine 2000 (Invitrogen) was used according to the manufacturer's method to co-transfect MCF7 sells with 4μg WT or mutant BECN1 expression plasmids. Cells were then lysed with 50mM Tris-HCl (pH 7.5), 150mM NaCl, 1mM DTT, 1mM EDTA, 1% Triton X-100 and cOmplete-EDTA free protease inhibitor tablet (Roche). Cells were rocked at 4 °C for 30 minutes to complete lysis and then centrifuged at 14000 x g for 10 minutes at 4 °C. The supernatant of the cell lysate was collected for SDS-PAGE. Expression levels of Flag-tagged WT and mutant BECN1 in MCF7 cells were verified by western blot analysis using commercial mouse monoclonal anti-Flag M2-peroxidase antibody (Sigma). As a loading control, the levels of Actin in MCF7 cell lysates were detected with mouse anti-Actin (Chemicon).

6.3. Results

6.3.1. BECN1 BARAD Contains Most of the Conserved Residues of BECN1

The various BECN1 domains have different degrees of conservation (Figure 6.1). Except for the N-terminal residues 16-27, the IDR and BH3D are poorly conserved, and the natively structured domains; the FHD, CCD, and BARAD, are all well conserved. However, the BARAD contains the majority of the invariant and conserved BECN1 residues. Invariant BECN1 BARAD residues include: N268, F274, I276, G280, I285, N286, R289, L290, G291, V298, E302, I303, N304, A305, A306, G308, Q309, L312, L313, L314, G334, D366, L373, P393, Y394, W425, T426, A428, L433, and K437 (Figure 6.1). Although the aromatic finger (residues

F259, F360 and W361) is not conserved in yeast VPS30, equivalent positions contain basic residues (Figure 6.1) that may also promote interactions with acidic lipid head-groups.

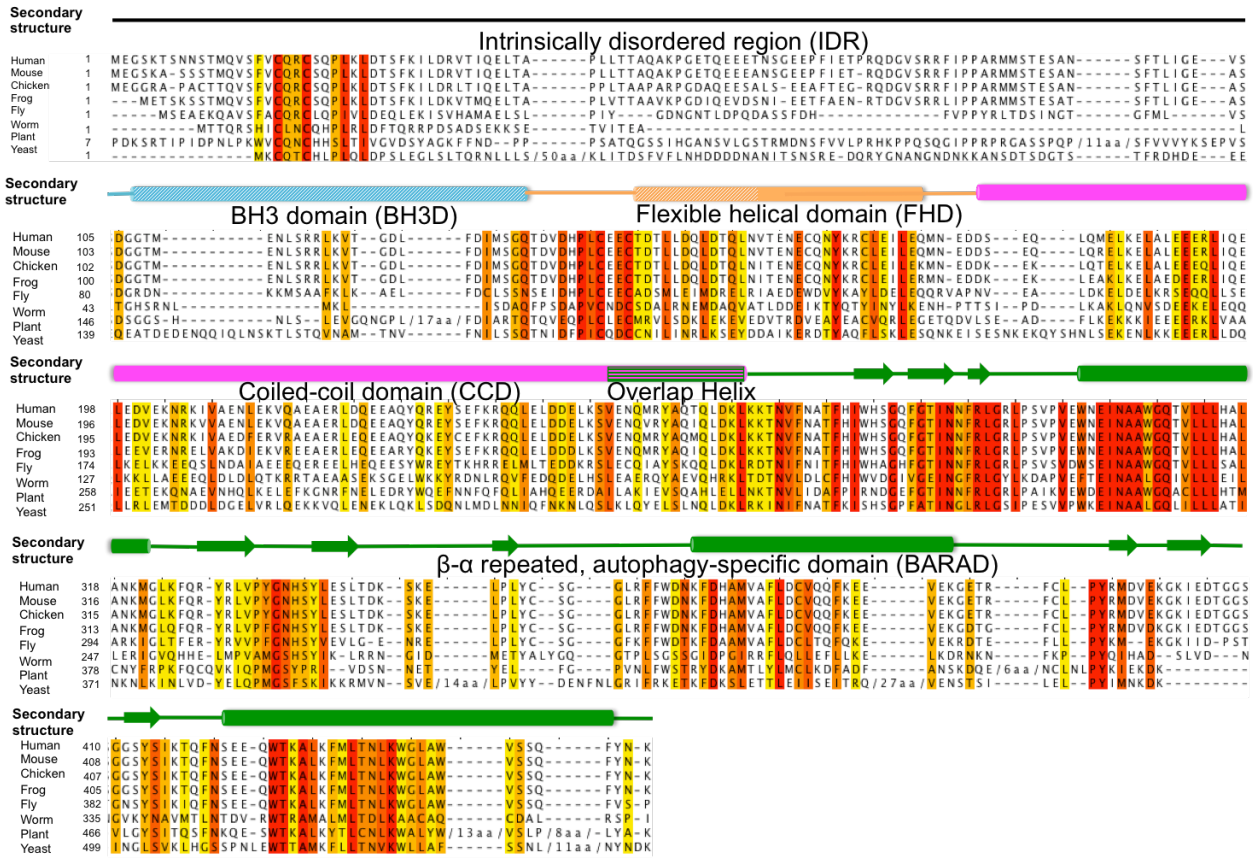

Figure 6.1. The sequence alignment of BECN1 orthologs from eight eukaryotes. Increasing background color intensity corresponds to increasing residue conservation: with red corresponding to invariant residues. Secondary structure for human BECN1 is displayed above the alignment, with cylinders representing helices, arrows representing strands, and lines representing coils. Solid outlines represent experimentally determined structures. Domains are color-coded as follows: IDR (black), BH3D (cyan), FHD (orange), CCD (magenta), and BARAD (green). Solid colors indicate natively folded stable structural elements, horizontal stripes indicate elements that may fold as part of two domain and diagonal stripes indicate binding-induced secondary structure.

Since the first half of the BARAD contains most of the invariant residues (Figure 6.1), we then selected the invariant residues within this region (N268, F274, I285, N286, R289, L290, G291, E302, I303, and D366) for single, double and triple alanine mutagenesis to investigate their roles in autophagy regulation. Mutations included N268A+N271A (N271 is invariant

amongst human, mouse, chicken, frog, fly and yeast), F274A, I285A+N286A, R289A+L290A+G291V, E302A+I303A, and D366A.

6.3.2. Identification of BECN1 BARAD Residues Required for Starvation-Induced Autophagy

As mentioned in the previous chapters, GFP-tagged LC3 (Kabeya, Mizushima et al. 2000) were cotransfected with various BECN1 mutants into MCF7 cells that have undetectable endogenously expressed BECN1 (Liang, Jackson et al. 1999, Liang, Yu et al. 2001, Furuya, Yu et al. 2005, Pattingre, Tassa et al. 2005) to assay the effects of BECN1 mutants on autophagy by quantifying the change in cellular localization of the transiently expressed mammalian autophagy-specific marker, LC3 (GFP-LC3) from a diffuse cytoplasmic distribution to membrane-localized punctae corresponding to autophagosomal structures.

Our autophagy assays confirm that GFP-LC3 puncta are undetectable in MCF7 cells without ectopically expressed BECN1 (Figure 6.2A, B). Under nutrient rich conditions, WT BECN1 and all mutants induce similar basal autophagy levels ($p=0.35$-0.91, for mutants *vs*. WT) and have similar BECN1 expression levels (Figure 6.2C). However, under starvation conditions, different mutants differentially impact autophagy induction. For N268A+N271A, F274A, I285A+N286A, and E302A+I202A mutants, starvation-induced autophagy decreases dramatically compared to WT ($p=0.007$-0.04, for starvation media *vs.* rich media) (Figure 6.2 A, B). Among these mutants, only N268A+N271A abolishes starvation-induced autophagy, resulting in basal autophagy levels ($p=0.56$, for starvation media *vs.* rich media). For the other two mutants, R289A+L290A+G291V and D366A, starvation-induced autophagy levels are not affected ($p=0.45$ and 0.07, for R289A+L290A+G291V and D366A *vs.* WT, respectively) (Figure 6.2 A, B), indicating R289, L290, G291, and D366 are probably not required for starvation-

induced autophagy. All mutants were expressed at levels similar to WT BECN1 (Figure 6.2 C) regardless of their impact on starvation-induced autophagy, confirming that their impact on starvation-induced autophagy is likely due to their importance in protein functions such as protein-protein interactions, rather than changes in expression levels.

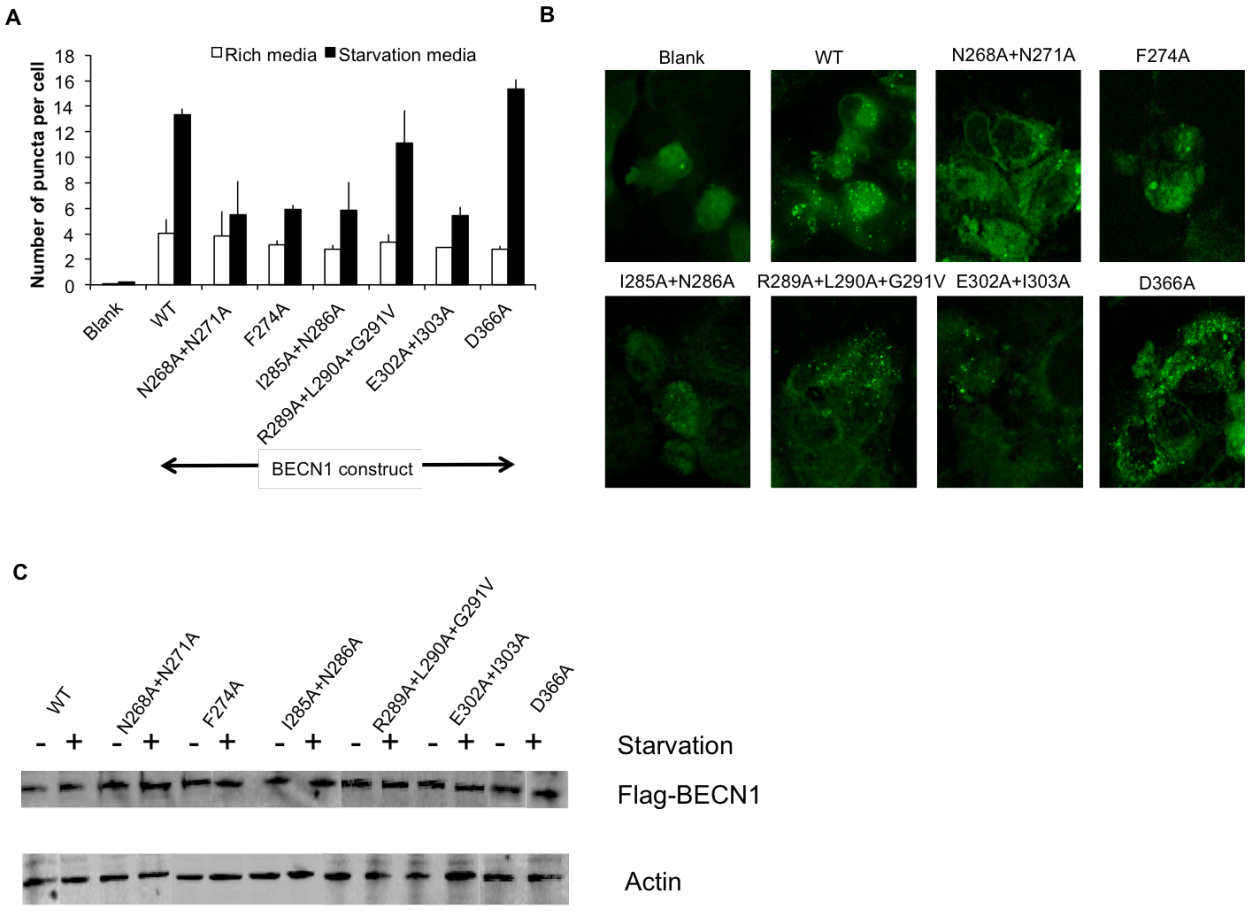

Figure 6.2. The effects of BECN1 BARAD mutants on starvation-induced autophagy.
(A) Bar graphs representing fluorescent light microscoppy quantification of the number of GFP-LC3 puncta per cell in GFP-positive MCF7 cells co-transfected with GFP-LC3 and BECN1 WT or mutant BECN1 in nutrient rich (white bar) or starvation (black bar) conditions. (B) Representative images of GLP-LC3 labeled puntae in MCF7 co-transfected with GFP-LC3 and BECN1 WT or mutant BECN1 cells in starvation-induced condition. (C) Western blots of MCF7 cell extracts indicating expression levels of WT and mutant Flag-tagged BECN1 constructs, in nutrient rich and starvation conditions.

6.4. Discussion

Before the determination of the X-ray crystal structure of the BECN1 BARAD (Huang, Choi et al. 2012, Noda, Kobayashi et al. 2012), part of this domain was called ECD (Furuya, Yu et al. 2005) due the significant sequence conservation in this domain. Cellular assays have shown that this domain is required for autophagy function (Furuya, Yu et al. 2005). Although the BECN1 ECD co-immunoprecipitates the PI3KC3/VPS34 (Furuya, Yu et al. 2005) to regulate autophagy, the recent 4.4Å crystal structure of PI3KC3 complex II (Rostislavleva, Soler et al. 2015) conclusively shows that there is no direct interaction of the BECN1/VPS30 BARAD with VPS34/PI3KC3, rather VPS15 mediates the BECN1/VPS30:VPS34 interaction. The first α-helix and second β-sheet of the BECN1/VPS30 BARAD interacts with UVRAG/VPS38 BARA2 and directly binds membrane to activate the lipid kinase activity of PI3KC3/VPS34 and induce autophagosome formation. Since the autophagy function is conserved in eukaryotes, the conserved BARAD residues BARAD are likely especially important for the autophagy regulation.

Deletion of BECN1 residues 268-284 was shown to decrease the starvation-induced autophagy to basal autophagy levels under nutrient normal conditions (Shoji-Kawata, Sumpter et al. 2013). This is consistent with our cellular autophagy assays in which mutations in this region (N268A+N271A, F274A, I285A+N286A, and E302A+I202A) highly decrease starvation-induced autophagy. Moreover, mutation of residues of the first α-helix of the BARAD (E302A+I303A) also dramatically decreased autophagy level under starvation conditions. Since the first α-helix of BECN1/VPS30 BARAD is involved in the interaction with UVRAG/VPS38 BARA2 (Rostislavleva, Soler et al. 2015), the failure of this mutant to up-regulate starvation-induced autophagy suggests that the E302A+I303A mutation may disrupt the interaction with

UVRAG/VPS38. Further investigations on the effects of other invariant BARAD residues are needed to fully understand the mechanism of the BECN1 BARAD in autophagy regulation.

In conclusion, we successfully identify the invariant residues required for the starvation-induced autophagy; this might provide important targets for therapeutic design to mediate autophagy.

CHAPTER 7. TO INVESTIGATE STRUCTURES OF AND INTERACTIONS WITHIN BECN1 MULTI-DOMAIN CONSTRUCTS

7.1. Introduction

A better understanding of BECN1 structural characteristics will enable a better understanding of BECN1 function. Despite the extensive structural biology research on BECN1, the structure of full-length (FL) BECN1 is unsolved due to the presence of the N-terminal IDR (Chapter 2 and 3) preventing the formation of the stable structure (Mei, Su et al. 2014). In the previous chapters, we have discussed the structures of the individual domains. Here we will probe the structure and function of multi-domain or FL BECN1.

Some of these multi-domain fragments also have distinct biological function. It was shown that caspases cleave BECN1 at D133, D146 or D149 to generate two fragments that fail to interact normally with PI3KC3/VPS34 and impair autophagy induction (Luo and Rubinsztein 2010, Wirawan, Vande Walle et al. 2010, Rohn, Wirawan et al. 2011). The two fragments also show reduced autophagy response to starvation or staurosporine, indicating that each domain of BECN1 is indispensible for autophagy (Zhu, Zhao et al. 2010). Meanwhile, the C-terminal fragment of the cleaved BECN1 translocates to mitochondria and triggers apoptosis (Djavaheri-Mergny, Maiuri et al. 2010).

In chronic lymphocytic leukemia cells, signaling lymphocyte-activation molecule family 1 (SLAMF1) helps to dissociate BECN1 from BCL2 to form the PI3KC3 complex and promote autophagic flux (Bologna, Buonincontri et al. 2016). Further Co-IP shows that SLAMF1 associates with the PI3KC3/BECN1/UVRAG complex via binding to BECN1 BH3D-FHD-CCD, which in turn activates the lipid kinase activity of PI3KC3 to regulate the phasosome/endosome fusion (Ma, Wang et al. 2012).

The BH3-only, pro-apoptotic protein BIM also binds to the BECN1 FHD-CCD (residues 149-243) (Adams and Cory 1998). BIM and BECN1 can pull down each other in vitro, however, the binding between BIM and BECN1 doesn't affect the BECN1:BCL-X_L interaction (Luo, Garcia-Arencibia et al. 2012). Further experiments show that the BECN1 BH3D interacts with BCL2/BCL-X_L, while the BECN1 FHD-CCD is crucial for binding BIM (Luo, Garcia-Arencibia et al. 2012). The regulation of autophagy by BIM is dependent on its interaction with BECN1 and DLC1/LC8 (dynein light chain 1), a protein localized on microtubules. In nutrient rich condition, the LC8-bound BIM recruits BECN1 to form a LC8:BIM:BECN1 tertiary complex, leading to the mislocalization of BECN1 to microtubules. Thus, the BECN1-dependent autophagy is inhibited. However, upon starvation, the phosphorylation of BIM by JNK at T116 facilitates its dissociation from LC8 and BECN1, leading to the decrease of mislocalized BECN1 in microtubules. Then the autophagy is activated (Luo, Garcia-Arencibia et al. 2012).

Meanwhile, between the disordered BH3D and partially ordered FHD, BECN1 has a conserved CxxC motif whose function is unknown. CxxC motifs have been found to be important for DNA binding (Voo, Carlone et al. 2000), native disulfide bond formation in protein folding (Chivers, Laboissiere et al. 1996, Woycechowsky and Raines 2000) and metal binding (Voskoboinik, Strausak et al. 1999, Woycechowsky and Raines 2000). However, the effect of the ^{137}CxxC^{140} motif on BECN1 structure and function is unknown.

To investigate the structure of multi-domain BECN1 constructs, we successfully expressed and purified mg quantities of the BECN1 FHD-CCD, BECN1 BH3D-FHD-CCD and full-length (FL) BECN1. CD spectroscopy was used to investigate the secondary structure of these constructs to demonstrate that each individual domain retains its secondary structure in multi-domain constructs. We then performed ITC to show that there is no intra-domain

interaction among BH3D, FHD and CCD, which agrees with the CD spectra results. SAXS experiments were performed to assess the size and shape of these multi-domain constructs. The structural information on multi-domain BECN1 constructs provides insights into the arrangement of BECN1 individual domains and the mechanism by which different BECN1 domains contribute to its function as an interaction hub. We also use CD spectroscopy to investigate conformational changes of different CxxC-containing BECN1 constructs to demonstrate that oxidizing conditions increase the helical content and decrease the coil content. Additionally, the CxxC motif is required not only for starvation-induced autophagy under oxidizing and non-oxidizing conditions, but also important for the autophagy up-regulation under oxidized condition.

7.2. Material and Methods

7.2.1. Production of BECN1 Constructs

BECN1 BH3D (residues 105-130) and FHD (residues 141-171) were chemically synthesized as described in previous chapters. The BECN1 CCD (residues 175-265) and FHD-CCD (residues 141-265) were purified as mentioned in the previous chapters. The BECN1 CxxC-FHD (137-171) and BH3D-FHD (residues 105-171) were chemically synthesized and purified using HPLC to >95% purity as confirmed by electrospray mass spectrometry (Protein Chem. Tech. Core, UTSW or EZBioLabs). BECN1 BH3D-FHD-CCD (residues 105-265) and BECN1 FL (residues 1-450) were cloned between the BamHI and NotI restriction enzyme sites of the pMBP-Parallel-1 vector (Sheffield, Garrard et al. 1999). BL21(DE3)pLysS cells were transformed by expression vectors and grown at 37°C with 100μg/L ampicillin and 35μg/L chloramphenicol to an OD_{600} of ~0.8 prior to induction of recombinant protein expression of BECN1 BH3D-FHD-CCD by addition of 0.5 mM IPTG at 20 °C overnight, while BECN1 FL

was induced at OD_{600} of ~1.0 with 0.5 mM IPTG at 37 °C for two hours. Soluble MBP-tagged fusion protein was purified from clarified crude cell lysate that was first loaded onto 10 mL amylose affinity columns. The unbound protein was washed off by wash buffer containing 25mM HEPES pH 7.5, 150 mM NaCl, 0.05% mM βME and 1 mM ethylenediaminetetraacetic acid. The MBP-tag was removed by on-column cleavage by adding TEV protease in a 1:10 (w/w) ratio to the BECN1 protein and incubating at 4°C for 8-10 hours. Subsequently, the protein was purified to homogeneity by ion-exchange chromatography, using an 8 ml HR 10/10 MonoQ column (GE) and SEC, using 16/60 Superdex200 or 10/300 Tandem Superdex 200+75 (GE Lifesciences, Pittsburgh, US) columns as necessary. The total yield of BECN1 BH3D-FHD-CCD and MBP-BECN1 FL are 4.7mg/L and 0.25mg/L, respectively.

7.2.2. CD Spectroscopy

CD spectra were recorded at 4 °C between 195 and 250 nm using a 300 µL quartz cell with a 0.1 cm path length on a Jasco J-815 spectropolarimeter equipped with thermoelectric temperature control. BECN1 constructs were diluted to 50-200 µM, injected into dialysis cassettes separately and dialyzed in 2L CD buffer (10 mM potassium phosphate, pH 7.6; 100 mM ammonium sulfate) overnight to ensure the buffer match. To assess redox-dependent conformational change, BECN1 constructs were dialyzed in 2 L CD buffer added with either 2 mM BME (reducing condition) or 0.5 mM H_2O_2 (oxidizing condition) overnight. Different % v/v ratios: 0%, 10%, 25% or 40% TFE (Sigma Aldrich, St. Louis, MO) was then mixed with dialyzed samples and incubated for 60 minutes on ice. The data were analyzed using either SELCON3 or CONTIN from the CDpro program suite (Sreerama, Venyaminov et al. 2001).

7.2.3. ITC

The BECN1 BH3D, FHD and CCD were injected into the dialysis cassettes separately and then dialyzed with buffer containing 50 mM HEPES pH 7.5, 150 mM NaCl and 2 mM BME to ensure the buffer match. The titration experiment was performed at 20 °C using a TA Instruments Low Volume Gold Nano ITC (TA Instruments) with 25 injections of 2.0 μL each. 1 mM FHD was loaded in the syringe and 100 mM BH3D or CCD in the sample cell to measure the interaction between FHD and BH3D, as well as, FHD and CCD. 1 mM BH3D and 100 mM CCD were added into syringe and sample cell separately to measure the interaction between BH3D and CCD. Data were plotted and analyzed with NanoAnalyze software, using an independent binding model.

7.2.4. SAXS Data Collection and Analysis

SAXS data were recorded at the BioCAT beamline (ID18) (APS, Argonne, IL) on a Mar165-CCD detector, at a sample to detector distance of 2.5 m, thereby covering a momentum transfer range of $0.006\ Å^{-1} < q < 0.32\ Å^{-1}$. SAXS measurements were recorded for BECN1 BH3D-FHD by loading a quartz capillary at various sample concentrations (4 mg/ml, 2 mg/ml, 1 mg/ml, and 0.5 mg/ml). For BECN1 FHD-CCD and BH3D-FHD-CCD constructs, we performed SEC in tandem with SAXS data collection, to ensure that the SAXS data was collected from a homogeneous sample. 4 mg/ml protein was injected onto a SEC column (GL 10/300 Superdex 200) and SAXS data recorded by exposing the column exposed to the X-ray beam for 1 second with a periodicity of 5 seconds.

Scattering data were normalized to the incident X-ray beam intensity and scattering from buffer was subtracted prior to analysis using Igor Pro macros (Ilavsky and Jemian 2009). Data analysis was performed using the ATSAS program suite (Petoukhov, Franke et al. 2012)

(http://www.emblhamburg.de/biosaxs/crysol.html). The program PRIMUS (Konarev, Volkov et al. 2003) in the ATSAS suite was used to calculate Guinier extrapolations to evaluate sample dispersity and calculate the radius of gyration (R_g) and Kratky plots to evaluate disorder within the sample. The program GNOM was used to plot the P(*r*) function from the Fourier inversion of the scattering intensity, *I*(q). The P(r) function was used to calculate the R_g and maximum particle size (D_{max}), and also for the reconstruction of *ab initio* envelopes by the application of ten cycles in DAMMIF (Franke and Svergun 2009). The resulting bead models were sequentially analyzed using DAMSEL, DAMSUP, and DAMAVER to compare and identify the most probable model, align all models to the most probable model, average these aligned models and compute a probability map with the averaged model then filtered using DAMMFILT (Volkov and Svergun 2003). For BECN1 BH3D-FHD construct, EOM (Bernado, Mylonas et al. 2007, Tria, Mertens et al. 2015) was used to calculate the pseudo atomic model based on the sequence and monomer extracted from two FHD MD conformers described in Chapter 4 to obtain a model that best fit the corresponding SAXS data. For the BECN1 FHD-CCD construct, the crystal structure of the BECN1 CCD homodimer and MD simulation of two FHD conformers described in Chapter 4 were used in SASREF (Petoukhov and Svergun 2005) to build and fit a model against the corresponding SAXS data sets. For the BECN1 BH3D-FHD-CCD construct, SASREF (Petoukhov and Svergun 2005) was used to calculate and fit the atomic models against its SAXS data set with the crystal structure of the BECN1 CCD dimer flanked by pseudo-atomic models of the BH3D-FHD (partial FHD or fully helical FHD) calculated by EOM (Bernado, Mylonas et al. 2007, Tria, Mertens et al. 2015). The four-residue gap between the FHD and CCD was set to 10Å (the average length between an α helical motif and fully extended motif with 4 residues), and P1 symmetry was imposed on all models. CRYSOL (Svergun, Barberato et al.

1995) and χ^2 free algorithm from SCÅTTER suite were used to compare theoretical scattering curves calculated for the models from EOM (Bernado, Mylonas et al. 2007, Tria, Mertens et al. 2015) or SASREF (Petoukhov and Svergun 2005) against the experimental SAXS scattering curve. The multi-domain models were superimposed into the final bead models using the program SUPCOMB (Kozin and Svergun 2001).

7.2.5. Autophagy Assays

Primers for each mutant used in site-directed mutagenesis (Agilent Technologies) were ordered from Integrated DNA Technologies. James Moulton made the human BECN1 C137A+C140A mutant. Cellular autophagy levels were evaluated by monitoring cellular localization of GFP-tagged LC3 (Kabeya, Mizushima et al. 2000). 3.0×10^5 MCF7 cells were seeded in each chamber of a 4-well culture slide (Millipore EZ slides) and cultured overnight in DMEM with 10% FBS until ~80% confluence. The cells were co-transfected with a total of 4 μg plasmids comprising 1.6 μg GFP-LC3 and 2.4 μg BECN1 WT or C137AC140A mutant expression plasmids, using lipofectamine 2000 (Invitrogen, Carlsbad, CA) according to the manufacturer's instructions. After transfection, the cells were divided into two groups, with one group being cultured in either nutrient-rich, non-oxidizing (DMEM, 10% FBS, 2X amino acid mixture) or starvation, non-oxidizing (EBSS) media; while the other group cultured in either nutrient-rich, oxidizing (DMEM, 10% FBS, 2X amino acid mixture and 0.5 mM hydrogen peroxide (H_2O_2)) or starvation, oxidizing (EBSS and 0.5mM H_2O_2) media, for 4 hours each. Cells were then fixed with 2% paraformaldehyde in PBS. GFP-LC3-positive puncta were observed under a fluorescent microscope (Zeiss AxioObserver Z1) and quantified by counting a minimum of 100 cells for duplicate samples per condition using Imaris (Bitplane AG, Zurich, Switzerland) in three independent repeats. The significance of alterations in autophagy levels

was determined by a two-tailed, heteroscedastic student's *t-test*, wherein $p \leq 0.05$ is considered significant.

7.3. Results

7.3.1. Protein Purification of Multi-domain Constructs

In order to characterize the structures of the multi-domain BECN1 constructs, we successfully purified the multi-domain BECN1 constructs of FHD-CCD (Figure 7.1A) and BH3D-FHD-CCD (Figure 7.1B) and cut the MBP tag from them. The theoretical MW for FHD-CCD and BH3D-FHD-CCD from the SEC profile are 26KD and 64KD, corresponding to the dimer of FHD-CCD and trimer of BH3D-FHD-CCD, respectively. There are two peaks in the SEC chromatogram of BECN1 FHD-CCD. Peak 1 is in void volume, therefore we did not collect it. Both BECN1 FHD-CCD and BH3D-FHD-CCD appear as a single band corresponding to their MW upon SDS-PAGE. These BECN1 fragments are very stable even after cleaving of the MBP tag. Therefore, we set up the crystal trays for these two BECN1 constructs together with the chemically synthesized BH3D-FHD. Unfortunately, all crystallization screens were unsuccessful. Therefore, we continued to apply other methods such as CD spectroscopy and SAXS experiments to investigate their structural features. The SEC chromatogram for FL BECN1 shows three overlapping peaks, and the SDS-PAGE shows degradation in every fraction (Figure 7.1C), indicating that we failed to obtain pure and stable protein suitable for further characterization.

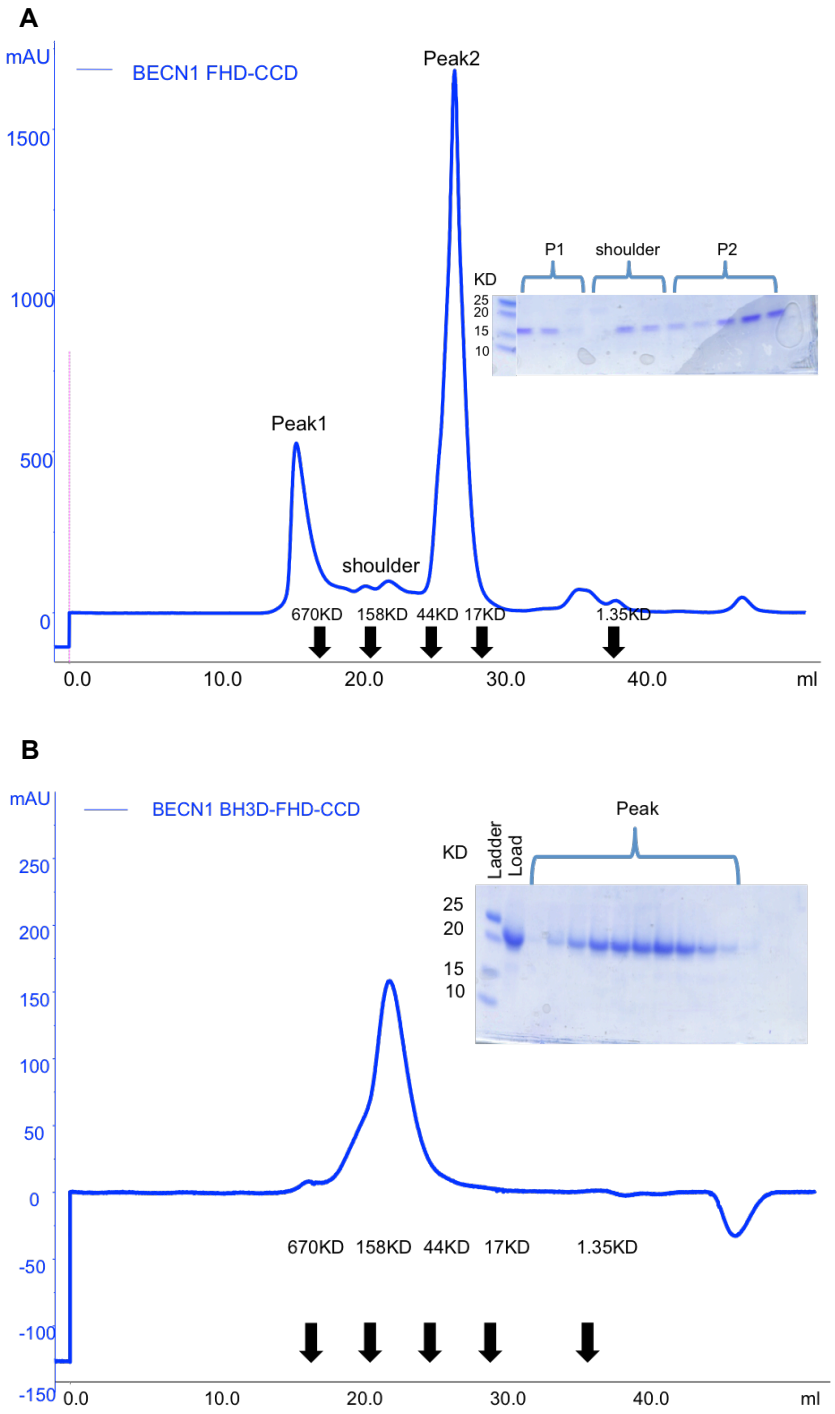

Figure 7.1. Size exclusion chromatograms of three BECN1 constructs and corresponding SDS-PAGE.
The SEC chromatograms of (A) BECN1 FHD-CCD, (B) BECN1 BH3D-FHD-CCD and (C) BECN1 full-length) are shown in blue. Elution positions for different molecular weight markers are indicated with arrows. The peaks presented in each chromatogram are labeled accordingly. The corresponding fractions from each peak shown in SDS-PAGE and the molecular weight marker are also labeled in figure.

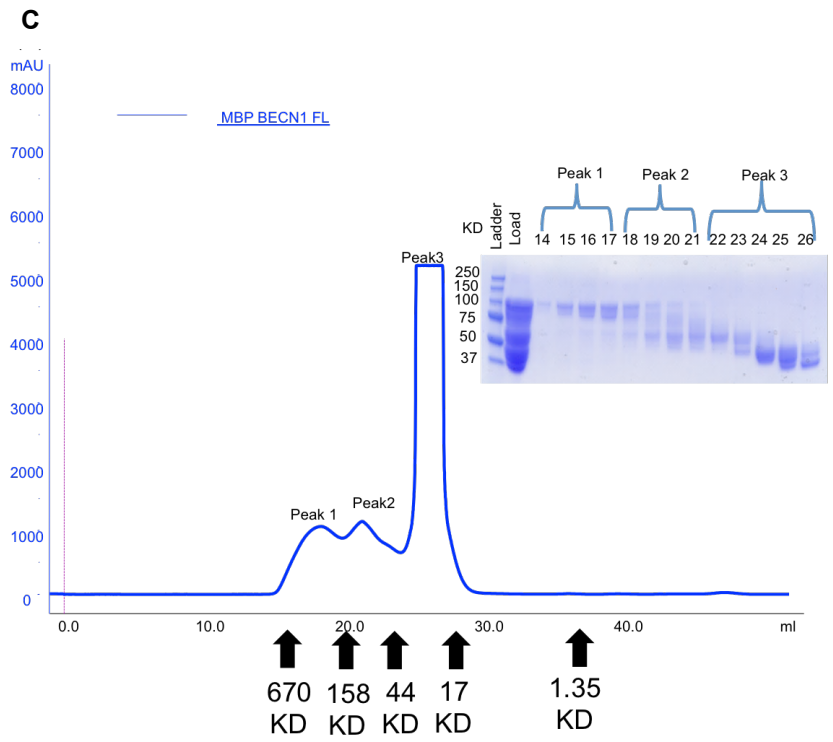

Figure 7.1. Size exclusion chromatograms of three BECN1 constructs and corresponding SDS-PAGE (continued).
The SEC chromatograms of (A) BECN1 FHD-CCD, (B) BECN1 BH3D-FHD-CCD and (C) BECN1 full-length) are shown in blue. Elution positions for different molecular weight markers are indicated with arrows. The peaks presented in each chromatogram are labeled accordingly. The corresponding fractions from each peak shown in SDS-PAGE and the molecular weight marker are also labeled in figure.

7.3.2. The Individual Domains of BECN1 Remain the Secondary Structural Contents with the Presence of Adjacent Domains

We used CD spectroscopy to investigate the secondary structure content of each multi-domain construct (Figure 7.2). We analyzed the secondary content using different programs in the CDpro suite (Sreerama and Woody 1993, Sreerama, Venyaminov et al. 1999, Sreerama and Woody 2000): SELCON3, a program optimized for estimation of coil in the CDpro suite, and CONTIN, a program optimized for estimation of helical content.

As mentioned before, BECN1 BH3D (residue 105-130) is highly disordered so all 26 residues are in random coil conformation (Figure 7.2, cyan curve and Table 7.1). The FHD (141-

171) is partially helical with 15 residues in random coil conformation (Figure 7.2, orange curve and Table 7.1). The CCD (residues 175-265) is highly helical with 79-84 residues being α-helix (Figure 7.2, magenta curve and Table 7.1), although the X-ray structure shows all 91 residues are α-helical (Li, He et al. 2012).

The BECN1 BH3D-FHD (residues 105-171) construct containing the highly disordered BH3D and partially disordered FHD, shows a high negative peak at around 200 nm and a slightly negative transition at 220 nm (Figure 7.2, blue curve). This spectrum shows more disorder than a helical features, which is consistent with the SELCON3 estimation that almost 60% (39 residues) of this construct is random coil and only 22.1% (15 residues) are α-helical (Table 7.1). However, for the disordered BH3D and BH3D-FHD, the estimations by CONTIN are not very accurate (Table 7.1), as CONTIN underestimates disorder (Greenfield 2006). Both the FHD-CCD (residues 141-265) and BH3D-FHD-CCD (residues 105-265) constructs show the typical α-helical curves with a positive peak at 195nm and two negative peaks at 208nm and 222nm (Figure 7.2, green and red curves). Both the SELCON3 and CONTIN estimations agree well with each other for these two constructs. In the FHD-CCD, about 80% (100-103 residues) of this construct is α-helical and 20% (25-28 residues) are in random coil (Table 7.1). In BH3D-FHD-CCD, about 65% (106-113 residues) is α-helical and about 32% (51-57 residues) is random coil (Table 7.1). A comparison of the secondary structure content estimated for the individual domains of BH3D, FHD and CCD, indicates that the secondary structure content remains unchanged in the multi-domain constructs.

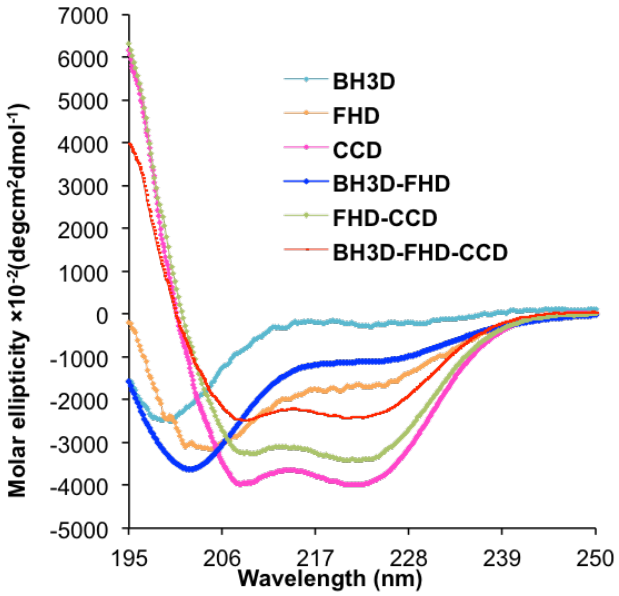

Figure 7.2. CD spectra of 6 BECN1 constructs.
The color of each BECN1 construct is labeled as in figure legend.

Table 7.1. CD spectra analysis of BECN1 constructs.

Domain(s)	**Length (residues)**	**% Secondary Structure Estimation by SELCON3**			**% Secondary Structure Estimation by CONTIN**		
		Helix	**Strand**	**Coil**	**Helix**	**Strand**	**Coil**
BH3D	26	4.0	3.8	92	0	42.1	57.9
FHD	31	37.8	17.8	49.4	51.5	2.7	45.9
CCD	97	81.6	0.9	20.5	86.8	0.8	12.4
BH3D-FHD	67	22.1	24.6	57.5	58.1	0	41.9
FHD-CCD	128	80.6	0.2	20	78.1	0.2	21.7
BH3D-FHD-CCD	164	64.4	5.2	34.6	68.7	0	31.3

7.3.3. No Intra-domain Interaction amongst BH3D, FHD and CCD

We then applied ITC to measure the interaction between the BH3D, FHD and CCD. Consistent with the CD spectra, no interaction was detected between any two of the three domains (Figure 7.3). The height of peak measured in each interaction is just 0.1 μJ/s, close to the dilution heat. Thus, none of these domains pack against each other to stabilize additional structure.

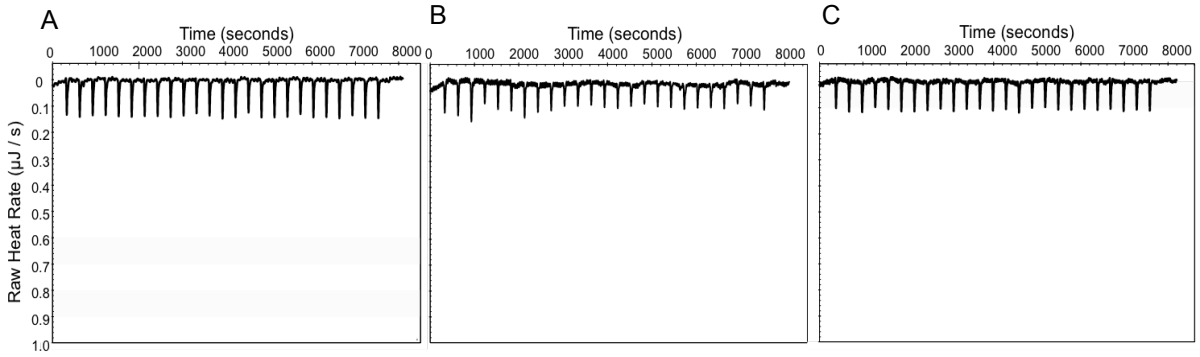

Figure 7.3. ITC experiments assessing interaction amongst BECN1 domains.
(A) interaction between BH3D and FHD (B) interaction between FHD and CCD (C) interaction between BH3D and CCD

7.3.4. Multi-domain Constructs Adopt an Extended Conformation

We next used SAXS to investigate the size and shape of these multi-domain constructs. For the BECN1 BH3D-FHD, the Guinier plot (Figure 7.4A) and P(r) distribution function (Figure 7.4B) indicate this construct has a R_g of 22-23Å (Table 7.2), a little bigger than the R_g of FHD (17Å, Chapter 4). The D_{max} calculated form P(r) distribution function is 86 Å (Figure 7.4 B and Table 7.2). The Krakty plot (Figure 7.4C) indicated this construct is partially disordered, which is consistent with the CD results (Figure 7.2, blue curve and Table 7.1). The molecular weight calculated from the V_c (Rambo and Tainer 2013) is almost two-fold that of its theoretical molar mass, although the FHD appears to trimerize in both solution and crystal structure (Chapter 4) (Mei, Ramanathan et al. 2016). We applied P1 symmetry to calculate the envelope of

the BH3D-FHD to avoid imposition of artificial symmetry constraints. We used a FHD monomer with a (i) disordered N-terminal model extracted from an MD simulation conformer that agreed well with the experimental FHD SAXS data (χ^2 ~ 1.0) or (ii) completely helical N-terminus extracted from an MD simulation conformer that also agreed well with the experimental FHD SAXS data (χ^2 ~ 1.0) (Chapter 4) to calculate the best BH3D-FHD pseudo-atomic model using EOM (Bernado, Mylonas et al. 2007, Tria, Mertens et al. 2015). The models that fit best are shown in Figure 7.5. Both models have relatively low χ^2 and χ^2 free values close to 1.0 (Table 7.2). However, when the model is fit to the envelope, the terminal BH3D residues are not covered (Figure 7.5, lower panels). This is probably due to the high flexibility of BH3D. Meanwhile, the envelopes also show that there is no space for another BH3D-FHD monomer, contradicting expectations from the V_c (Rambo and Tainer 2013) calculations. Both models show no interaction between BH3D and FHD, consistent with our ITC data (Figure 7.3A)

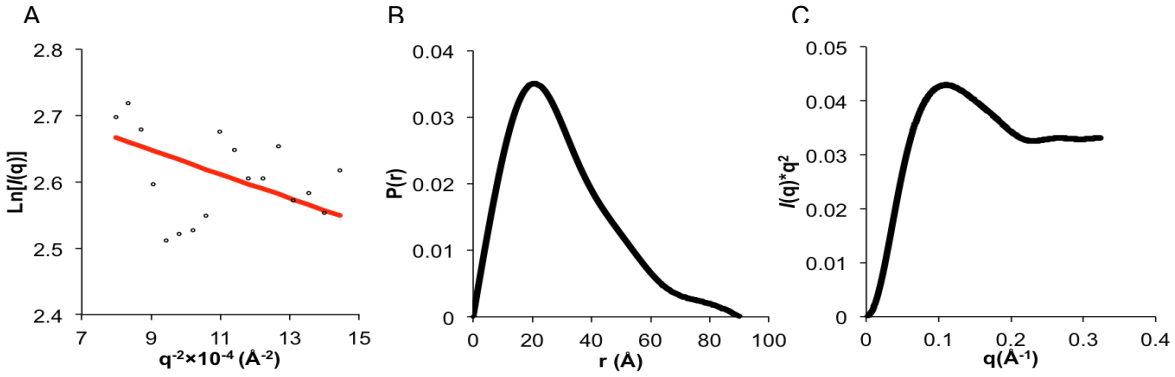

Figure 7.4. SAXS analysis of BECN1 BH3D-FHD.
(A) Guinier Plot; (B) P(r) pairwise distribution; (C) Kratky plot.

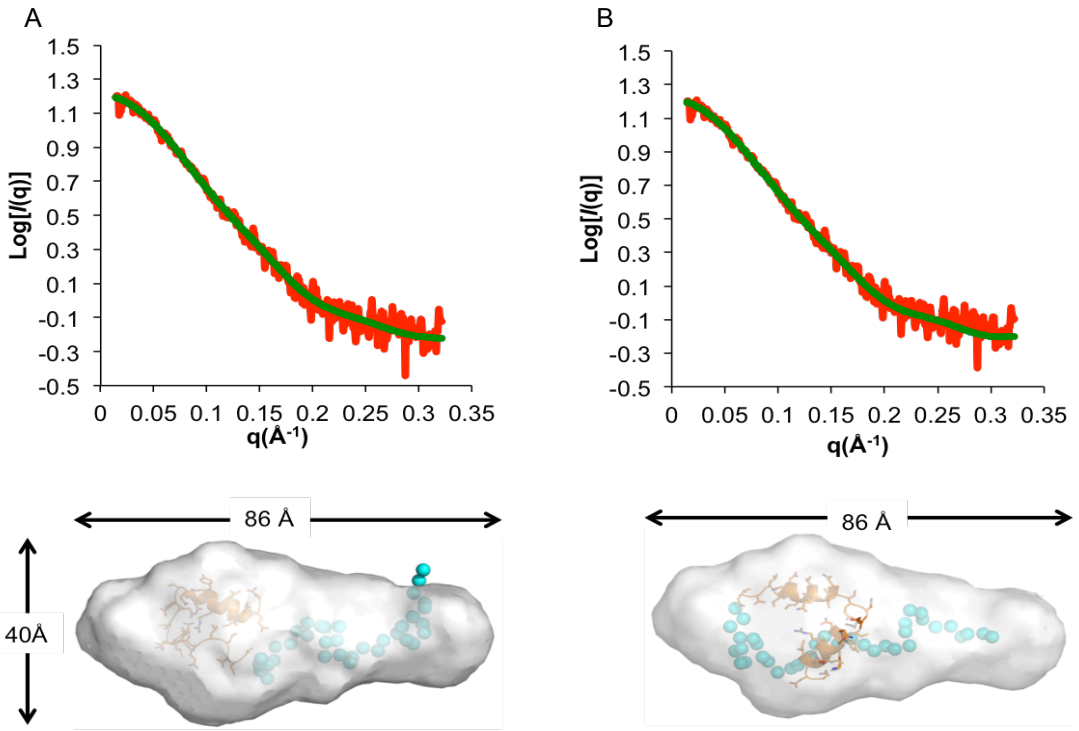

Figure 7.5. Pseudo-atomic model of BECN1 BH3D-FHD.
Top panels compare the experimental scattering curve (red) with the theoretical scattering curves (green) calculated from the pseudo-atomic models of two different FHD MD conformers generated using EOM. Bottom panels show each of the two different pseudo-atomic models of the BH3D-FHD fitted into SAXS envelopes of fits to the BH3D-FHD SAXS envelopes (grey envelope). The two different BH3D-FHD models were generated in EOM using: (A) an MD simulation conformer with a disordered N-terminus; (B) an MD simulation conformer with a partially helical N-terminus.

SAXS data were also measured concurrently with isocratic elution of peaks corresponding to the FHD-CCD and BH3D-FHD-CCD, previously verified by SDS-PAGE (Figure 7.1).

SAXS analysis of the FHD-CCD was complicated by the disorder within the FHD. However, the combined SAXS analysis clearly indicates that the FHD-CCD is a dimer, rather than a trimer. The Guinier plot (Figure 7.6A) and P(r) plot (Figure 7.6B) indicate that this construct has a R_g of 76-80 Å (Table 7.2). The P(r) plot indicates that the FHD-CCD is a long molecule with a D_{max} of 252 Å (Table 7.2 and Figure 7.6B). The D_{max} is consistent with that

expected for a model wherein a FHD (D_{max}=61 Å, Chapter 4) flanks the anti-parallel CCD homodimer (D_{max}=121 Å, Chapter 5) at each end. This oligomerization state is confirmed by the estimation of molecular weight from the V_c (Rambo and Tainer 2013), which is consistent with that expected for a dimer, rather than a trimer (Table 3). Strikingly, the Kratky plot indicates that the FHD-CCD construct is partly disordered (Figure 7.6C), consistent with the CD data recorded from this construct (Figure 7.2 and Table 7.1). This demonstrates that the FHD does not become more ordered in the context of the adjacent CCD.

The SAXS envelope for the FHD-CCD calculated with the P1 symmetry indicates that it is an elongated molecule, similar to the anti-parallel CCD homodimer envelope (Figure 7.7) and consistent with the formation of a CCD dimer. The different oligomerization states of the FHD and the FHD-CCD, combined with the fact that the CCD forms an anti-parallel homodimer, indicate that these are alternate conformational states of BECN1. The R_g, D_{max} and shape of the envelope suggest that the FHD-CCD likely consists of a central anti-parallel CCD homodimer, with flanking FHDs at either end. Therefore, we used SASREF (Petoukhov and Svergun 2005) to build a model of the FHD-CCD using a FHD monomer with either a disordered N-terminal model or a completely helical N-terminal model. As before, relevant parts of the resulting pseudo-atomic model were superimposed upon the individual FHD and CCD envelopes and then the entire model was docked into the FHD-CCD envelope (Figure 7.7). This resulted in a fit with a χ^2 of 2.0 and χ^2 free of 1.6 for the FHD-CCD model containing a partially disordered FHD, and a χ^2 of 2.7 and χ^2 free of 1.7 for the FHD-CCD model containing a completely helical FHD (Table 7.2).

Thus, our SAXS analysis of the BECN1 FHD-CCD fragment indicates that this two-domain fragment exists as a homodimer with unpaired FHDs flanking a CCD dimer. Further,

there is no interaction between the CCD and FHD that would stabilize the structure of FHD. This is also consistent with ITC experiments (Figure 7.2B) indicating that there is no direct interaction between the FHD and CCD. Further, the best fit to the experimental SAXS data is obtained when the FHD-CCD model incorporates a partially disordered model of the FHD.

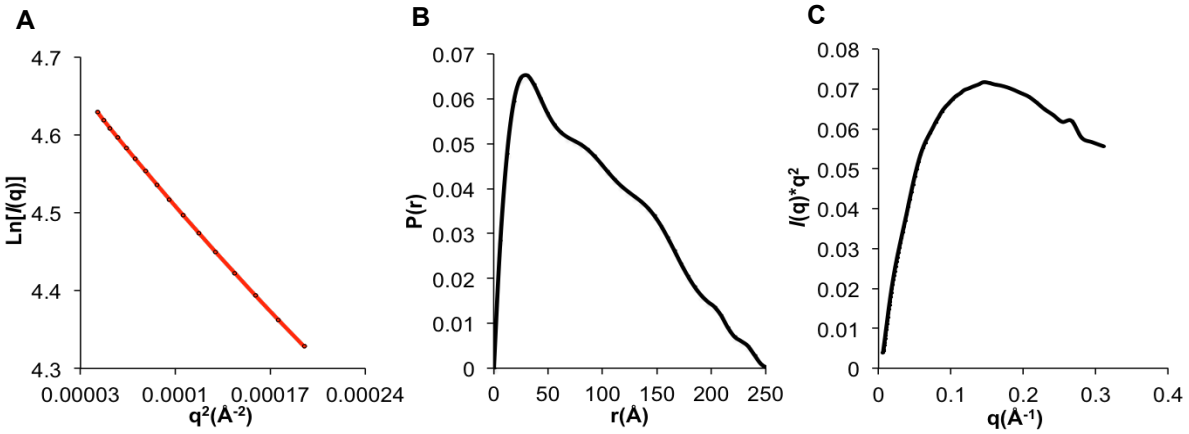

Figure 7.6. SAXS analysis of BECN1 BH3D-FHD.
(A) Guinier Plot; (B) P(r) pairwise distribution; (C) Kratky plot.

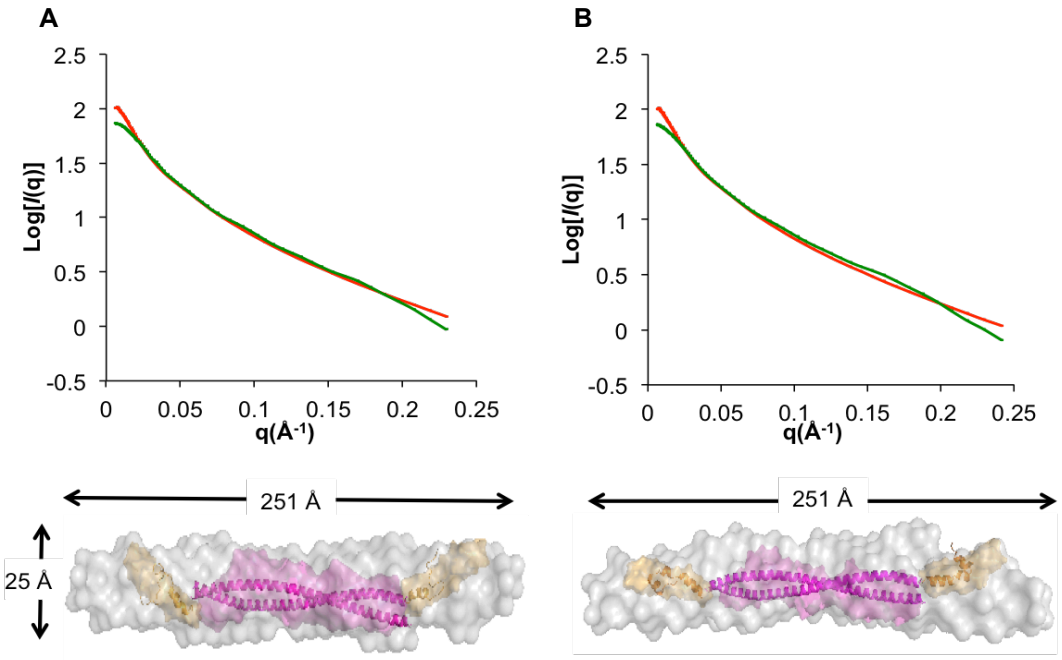

Figure 7.7. Pseudo-atomic model of the BECN1 FHD-CCD.
Top panels compare the experimental scattering curve (red) with the theoretical scattering curves (green) calculated from the pseudo-atomic models generated using SASREF using the CCD crystal structure and one of two different FHD models. Bottom panels show each of the three different pseudo-atomic models of the FHD-CCD fitted into SAXS envelopes of the isolated FHD (orange) and CCD (magenta), followed by fits to the FHD-CCD SAXS envelopes (grey envelope). The two different FHD-models were generated using the CCD crystal structure and: (A) an MD simulation conformer with a disordered N-terminus; (B) an MD simulation conformer with a partially helical N-terminus.

SAXS analysis of the BECN1 BH3D-FHD-CCD construct was also complicated by the disorder of the BH3D and FHD. The Guinier plot (Figure 7.8A) shows the BH3D-FHD-CCD has a R_g of 71 Å (Table 7.2), close to the R_g of 74 Å (Table 7.2) calculated from P(r) plot (Figure 7.8B). Unexpectedly these R_g of the BH3D-FHD-CCD are a little smaller than the FHD-CCD (Table 7.2). Meanwhile the P(r) plot also shows that this construct has a D_{max} of 238 Å, also smaller than the D_{max} of the FHD-CCD. The Kratky plot indicates this construct is partially folded, consistent with the CD spectra (Table 7.1). The molecular weight calculated from V_c is 44 KD, about 2 fold of its theoretical molar mass.

The envelopes calculated for this data also show an extended long rod (Figure 7.9). Therefore, SASREF (Petoukhov and Svergun 2005) was used to build the BH3D-FHD-CCD model using the crystal structure of BECN1 CCD dimer with BH3D-FHD flanking on either side. The BH3D-FHD models calculated by EOM (Bernado, Mylonas et al. 2007, Tria, Mertens et al. 2015) using the FHD monomers extracted from two MD conformers were both tried by SASREF (Petoukhov and Svergun 2005) to calculate the BH3D-FHD-CCD models. However, the results show that the two models fit poorly with the SAXS data (Figure 7.9). The model containing the partially disordered FHD fits with a χ^2 value of 2.8 and χ^2 free value of 3.2 (Figure 7.9A and Table 7.2). On the other hand, the model containing the completely helical FHD fits with a χ^2 value of 3.2 and χ^2 free value of 3.6. Similar to BECN1 FHD-CCD, the model containing the partial disordered FHD fits better than the model containing completely folded FHD, however Due some of the BH3D residues are located outside the envelope, while there is unoccupied space within the envelope. Consistent with the CD spectra and ITC data, the models show no obvious interaction amongst the BH3D, FHD and CCD.

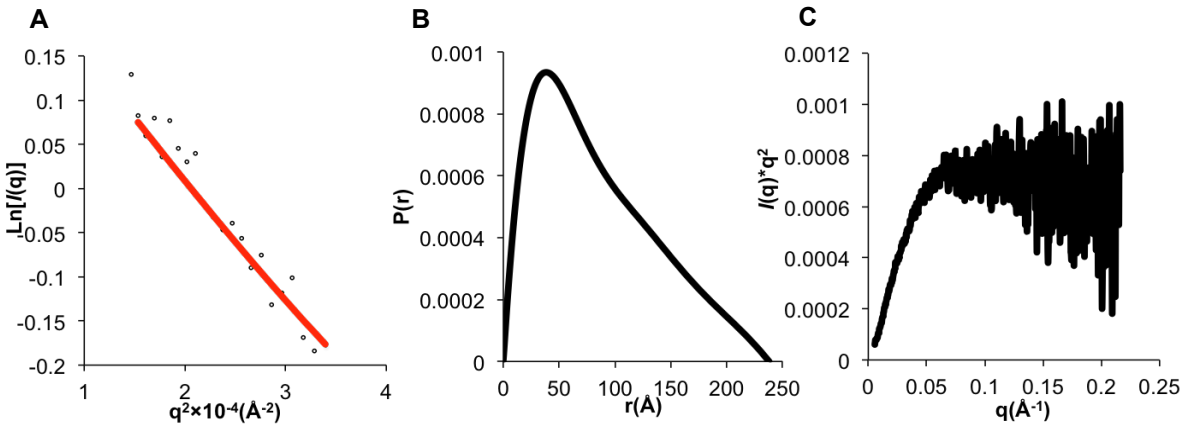

Figure 7.8. SAXS analysis of BECN1 BH3D-FHD-CCD.
(A) Guinier plot; (B)P(r) pairwise distribution; (C) Kratky plot.

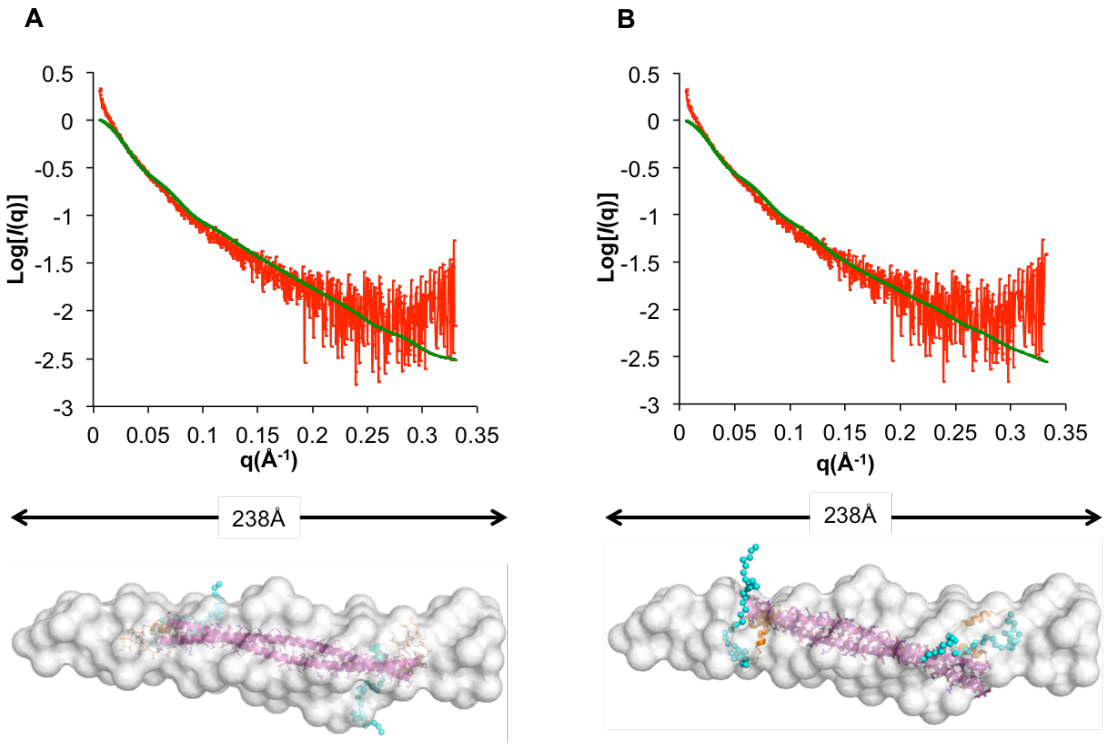

Figure 7.9. Pseudo-atomic model of the BECN1 BH3D-FHD-CCD.
Top panels compare the experimental scattering curve (red) with the theoretical scattering curves (green) calculated from the pseudo-atomic models generated using SASREF using the CCD crystal structure and one of two different BH3D-FHD models. Bottom panels show each of the three different pseudo-atomic models of the BH3D-FHD-CCD fitted into SAXS envelopes of the isolated BH3D(cyan), FHD (orange) and CCD (magenta), followed by fits to the BH3D-FHD-CCD SAXS envelopes (grey envelope). The two different BH3D-FHD-CCD models were generated using the CCD crystal structure and: (A) an EOM calculated pseudo-atomic model containing the MD simulation conformer with a disordered N-terminus; (B) an EOM calculated pseudo-atomic model containing the MD simulation conformer with a partially helical N-terminus.

Table 7.2. Comparison of SAXS data and pseudo-atomic structure of three BECN1 multi-domain constructs.

BECN1 fragment ->		**BH3D-FHD**		**FHD-CCD**		**BH3D-FHD-CCD**	
From sequence	MW_T (KD)	7.7		15.1		19.0	
SAXS parameters	R_g (Å)	22		80		71	
	P(r) R_g (Å)	23		76		74	
	D_{max} (Å)	86		251		238	
	MW from V_c (KD	13.5		27		44	
χ^2	Pseudo atomic model	1.1*	1.0**	2.0*	2.7**	2.8*	3.2**
χ^2 free	Pseudo atomic model	1.0*	1.0**	1.6*	1.7**	3.2*	3.6**

MW_T: theoretical molecular weight from sequence;*: a single FHD conformer selected from MD ensembles with partial helix; **: a single FHD conformer selected from MD ensembles with fully helix.

7.3.5. The Invariant CxxC Motif is Important for the Disorder-to-Helix Changes of CxxC-Containing Constructs under Oxidizing Conditions

We noticed that there is an invariant CxxC-motif of ^{137}CxxC^{140} between the disordered BH3D and partially ordered FHD. We used CD spectroscopy to investigate the impact of this CxxC motif on BECN1 secondary structure under different oxidizing conditions. The results show that in the absence of the CxxC motif, such as in the FHD construct, there is no difference under either reducing or oxidizing conditions (Figure 7.10, orange curve and Table 7.3). However the other CxxC-containing constructs: CxxC-FHD, BH3D-FHD and BH3D-FHD-CCD become more helical under oxidizing conditions (Figure 7.10, Table 7.3). This might be because the oxidizing conditions facilitates the formation of disulfide bond between the two cysteines to stabilize the native structure of protein (Chivers, Laboissiere et al. 1996).

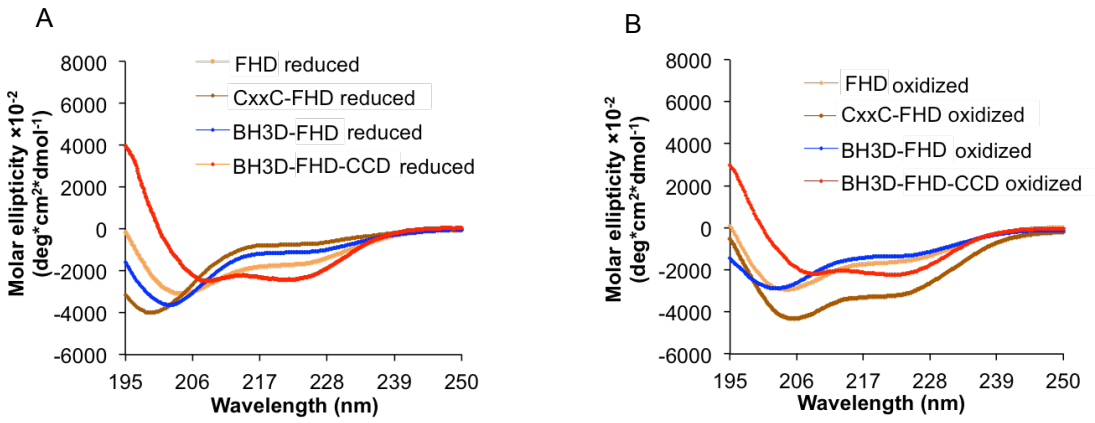

Figure 7.10. CD spectra of CxxC-containing constructs under different oxidizing conditions. (A) reducing condition; (B) oxidizing condition.

Table 7.3. Secondary structure content of CxxC-containing constructs under reducing and oxidizing conditions estimated from CD spectra.

Constructs	Length (residues)	% Secondary Structure Estimation by SELCON3					
		Reducing			Oxidizing		
		Helix	Strand	Coil	Helix	Strand	Coil
FHD	31	37.8	17.8	49.4	37.6	15.1	50
CxxC-FHD	36	20.2	11.2	71.9	44	4.4	51.3
BH3D-FHD	67	22.1	24.6	57.5	38.5	14.2	51.4
BH3D-FHD-CCD	164	64.4	5.2	34.6	90.4	0.6	12.9

Since BH3D and FHD both contain Anchor regions that nucleate interactions and undergo TFE-induces helical transitions, we further investigated the effects of oxidizing conditions on the conformational changes of CxxC motif-containing BECN1 constructs in the presence of TFE. Although the number of helical residues in the 164-residue BH3D-FHD-CCD increases from 106 under reducing condition to 148 under oxidizing condition (Table 7.3), we did not include this construct to investigate the effects of CxxC motif on disorder-to-helix changes under oxidizing condition because (i) there is no extra Anchor region in the highly-helical CCD, (ii) there are no intra-domain interactions between the CCD and other domains that

affect the conformational change, and (iii) it will be hard to assess TFE-induced changes in helicity in the context of the high helicity of the BH3D-FHD-CCD under oxidizing condition. Indeed, the BH3D-FHD-CCD does not show obvious conformational changes with the increased TFE concentration under reducing conditions (Figure 7.11, Table 7.4). It is likely that TFE will have negligible impact on the conformational changes of protein constructs with high helical content.

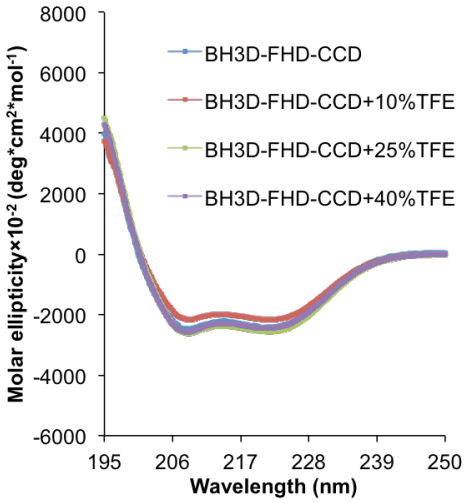

Figure 7.11. Effects of TFE on the secondary structure content in BECN1 BH3D-FHD-CCD.

Table 7.4. Secondary structure content of 164-residue BECN1 BH3D-FHD-CCD estimated from CD spectra recorded in different TFE concentrations.

% Secondary Structure Estimation by SELCON3											
NO TFE			**10% TFE**			**25%TFE**			**40% TFE**		
Helix	Strand	Coil	Helix	Strand	Coil	Helix	Strand	Coil	Helix	Strand	Coil
64.4	5.2	34.6	59.5	14.3	28.7	67.6	8.1	26.8	64.2	11.2	26.4

Under both reducing and oxidizing conditions, the highest helical content and the lowest coil content of FHD, CxxC-FHD and BH3D-FHD occur at 25% TFE and fluctuates somewhat at

40% TFE. For FHD and CxxC-FHD, the β-strand content is less than 6 residues under all conditions, which is not enough to form a stable β-strand (Kabsch and Sander 1983, Frishman and Argos 1995). Therefore, the increase of helicity is offset by the decrease of coil in these two constructs. For the BH3D-FHD, the β-strand content fluctuates inconsistently in different conditions. Under reducing conditions, the BH3D-FHD has a relatively high β-strand content of about 16-21 residues at low TFE concentrations (0 and 10%), and a relatively low β-strand content of about 4-9 residues at high TFE concentrations (25% and 40%) (Table 7.5, 7.6). On the other hand, BH3D-FHD is estimated to contain 9 residues of β-strand content in the absence of TFE under oxidizing condition (Table 7.5, 7.6). But there is no stable β-strand formed when TFE is added under oxidizing condition (Table 7.5, 7.6). Though the CD spectra results indicate there might be some β-strand content in BH3D-FHD under both reducing and oxidizing conditions (Table 7.5, 7.6), the available structural information of BH3D and FHD do not indicate there is any β-strand content in either domain. Therefore, the BH3D-FHD may have some unstable β-strand content in solution.

The FHD undergoes similar TFE-induced conformational changes in reducing and oxidizing conditions (Figure 7.12A, 6.13A and Table 7.5, 6.6). With the presence of two Anchors, the helical content of FHD increases by 2.5-fold in 25% TFE or higher (Table 7.5, 6.6). In contrast, the presence of CxxC motif in CxxC-FHD and BH3D-FHD appears to further increase the helical content under oxidizing condition (Figure 7.12B, C, Figure 7.13B, C and Table 7.5, 7.6). At 25% TFE, the helical content in CxxC-FHD and BH3D-CCD increases from 22 and 55 residues under reducing condition, to 25 and 62 residues respectively under oxidizing condition (Table 7.5 and Table 7.6); while, the coil content is decreased by 5 and 6 residues, respectively (Table 7.5, 6.6).

Amongst these three constructs, the most striking helix transition occurs in BH3D-FHD, in which the helical content increases from 15 residues with no TFE under reducing conditions, to 62 residues with 25% TFE under oxidizing conditions.

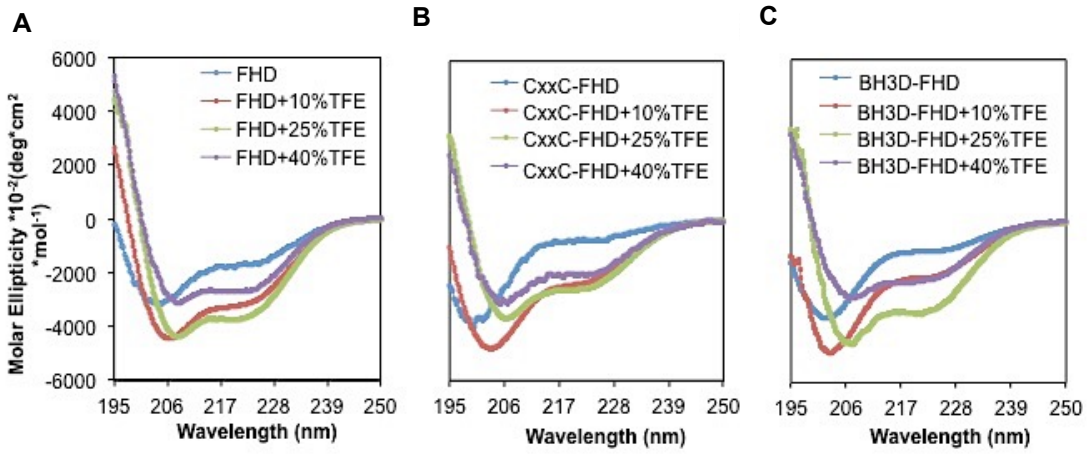

Figure 7.12. Effect of TFE on the secondary structure content in various CxxC-containing constructs under reducing condition.
CD spectra for (A) FHD, (B) CxxC-FHD and (C) BH3D-FHD recorded at four different TFE v/v concentrations.

Table 7.5. Secondary structure content of CxxC-containing constructs under reducing condition estimated from CD spectra.

BECN1 Constructs	**Length (Number of residues)**	**% Secondary Structure Estimation by SELCON3**											
		NO TFE			**10% TFE**			**25%TFE**			**40% TFE**		
		Helix	Strand	Coil	Helix	Strand	Coil	Helix	Strand	Coil	Helix	Strand	Coil
FHD	31	37.8	17.8	49.4	36.3	7.5	57.5	80.6	0	19.4	76.5	0	28.4
CxxC-FHD	36	20.2	11.2	71.9	31.5	16.2	56.3	61.3	3.9	39.0	61.5	13.0	30.4
BH3D-FHD	67	22.1	24.6	57.5	33.4	31.8	35.2	82.6	6.7	17.4	78.8	14.2	7.8

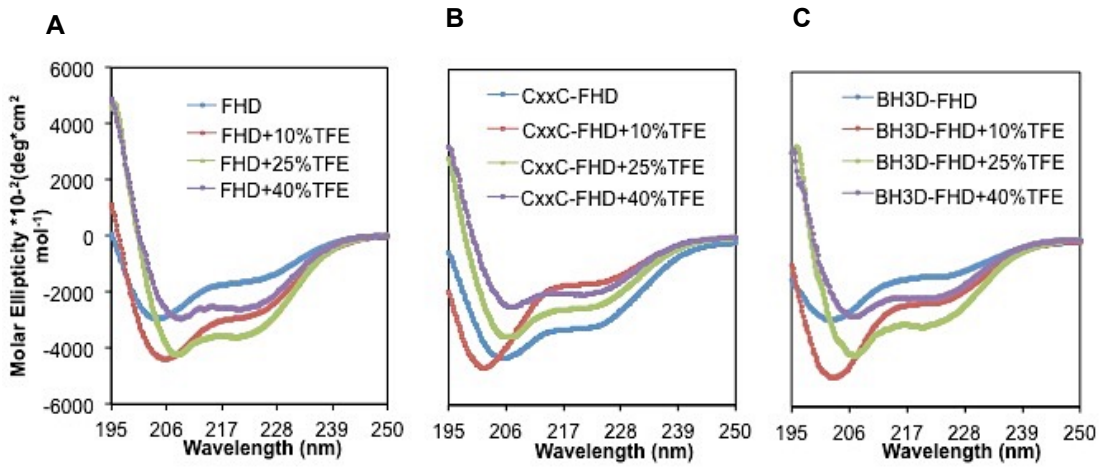

Figure 7.13. Effect of TFE on the secondary structure content in various CxxC-containing constructs under oxdizing condition.
CD spectra for (A) FHD, (B) CxxC-FHD and (C) BH3D-FHD recorded at fourt different TFE v/v concetrations

Table 7.6. Secondary structure content of CxxC-containing constructs under oxidizing condition estimated from CD spectra.

BECN1 Constructs	Length (Resi-dues)	% Secondary Structure Estimation by SELCON3											
		NO TFE			10% TFE			25%TFE			40% TFE		
		Helix	Strand	Coil	Helix	Strand	Coil	Helix	Strand	Coil	Helix	Strand	Coil
FHD	31	37.6	15.1	50	39.7	6.7	53.3	81.2	0	19.8	80.9	0	20
CxxC-FHD	36	44	4.4	51.3	36.4	7.7	60	70.3	7.5	24.8	73.2	7.8	21.7
BH3D-FHD	67	38.5	14.2	51.4	35.2	0	66.1	93	0.1	9	86.6	4.6	10.5

7.3.6. The Invariant CxxC Motif is Important for Autophagy under Oxidizing Conditions

Next we performed autophagy assays using MCF7 cells, which have no detectable endogenous BECN1 expression, to investigate the role of CxxC motifs in autophagy regulation (Liang, Jackson et al. 1999). We used site-directed mutagenesis to simultaneously mutate both C137 and C140 of BECN1 to alanine in order to determine whether these invariant cysteines are

important for autophagy up-regulation. In non-oxidizing (normal), nutrient-rich media, there is no difference between autophagy levels mediated by WT and C137A+C140A BECN1 (p=0.65, WT *vs.* C137A+C140A mutant) (Figure 7.14). When cells are treated with 0.5 mM H_2O_2, autophagy levels increase in both WT BECN1 ($p=1.9\times10^{-4}$, oxidizing *vs.* normal) and C137A+C140A mutant ($p=5.8\times10^{-4}$, oxidizing *vs.* normal) under nutrient rich conditions. However, autophagy levels in rich media under oxidizing condition mediated by the C137A+C140A mutant is significantly lower compared to WT BECN1 ($p=4.0\times10^{-3}$, WT *vs.* C137A+C140A) (Figure 7.14). Therefore the CxxC motif appears to be important for the up-regulation of autophagy under oxidative stress in nutrient rich condition.

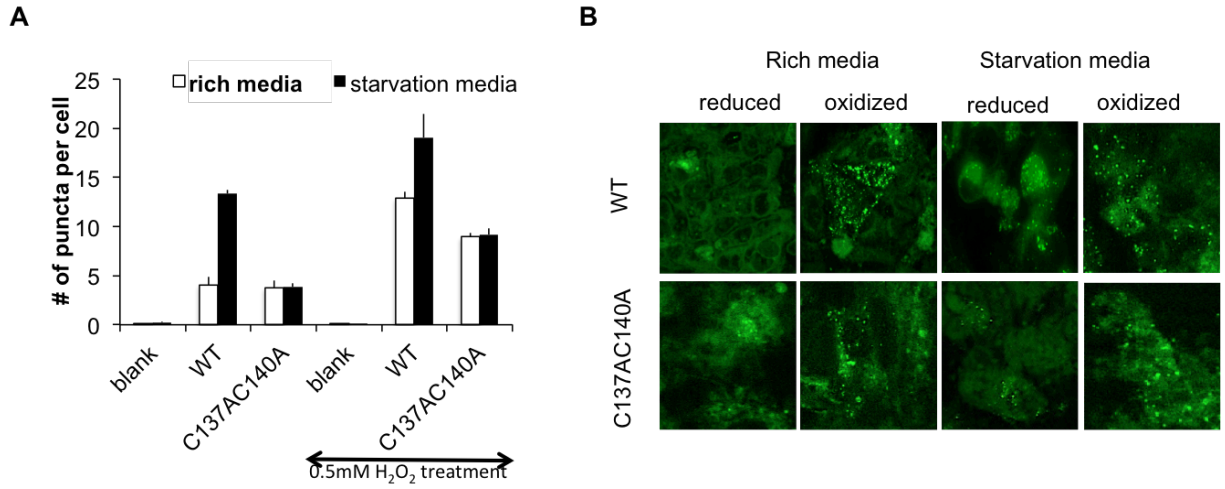

Figure 7.14. Effect of the BECN1 C137A+C140A mutant on autophagy under different oxidizing conditions.
(A) Light microscopy quantification of discrete GFP-LC3 puncta per cell in GFP-positive MCF7 cells co-transfected with GFP-LC3 and WT or mutant BECN1 as indicated below the X-axis. Bars represent number of puncta per cell for each construct in nutrient rich (white bar) and starvation (black bar) conditions. The arrow below the X-axis indicates oxidation conditions.
(B) Representative images of GFP- LC3 staining in cells grown in both rich and starvation media under non-oxidizing or oxidizing conditions transfected with WT and mutant BECN1 as indicated.

Starvation significantly increases autophagy levels mediated by WT BECN1 under both normal ($p= 6.0\times10^{-4}$, rich *vs.* starvation) and oxidizing conditions (p= 0.035, rich *vs.* starvation).

However, the C137A+C140A mutation abolishes starvation-induced increase in autophagy under oxidizing conditions (p=0.014, WT *vs.* C137A+C140A) and autophagy levels remain similar to those observed in nutrient-rich, oxidizing media (p=0.59, rich *vs* starvation) (Figure 7.14). Hence, the CxxC motif is required for starvation-induced autophagy in both normal and oxidizing conditions.

7.4. Discussion

In this chapter, we show that there is no intra-domain interaction amongst BH3D, FHD and CCD by CD spectroscopy and ITC. It is likely that each of these domains has its own interaction proteins to regulate autophagy. This property might also enable BECN1 to recruit many interaction proteins and lead to the BECN1 interaction hub. Little information is available considering the multi-domain or FL BECN1. Recently, a 4.4Å crystal structure of the yeast PI3KC3 complex comprising VPS34:VPS30:VPS38:VPS15 (Rostislavleva, Soler et al. 2015) agrees with our data that BECN1 adopts an extended conformation with each BECN1 domain involved in an interaction with other protein binding partners. This conformational arrangement might enable BECN1 to interact with more proteins in autophagy or other cell signaling regulation and makes it an interaction hub. This also indicates that autophagy is a complicated regulation system that a lot of proteins are involved in this process via interaction with BECN1 (He and Levine 2010). The recent Cryo-EM structure of PI3KC3 complex I comprising VPS34:BECN1:ATG14:VPS15 also indicates that the heterodimer of BECN1:ATG14 might form a scaffold to recruit other interaction proteins in the autophagy process. Further study on the detailed structural information of FL BECN1 and its complex is needed to elucidate the mechanism of BECN1 in autophagy regulation via interacting with various proteins.

Though, we showed that there is no intra-domain interaction amongst three domains, in the large construct of BH3D-FHD-CCD, it showed a smaller R_g and D_{max} than the smaller construct of FHD-CCD, indicating BH3D-FHD-CCD might adopt a more compact conformation. The presence of compact IDRs is not uncommon (Mittag and Forman-Kay 2007, Blocquel, Habchi et al. 2012, Kurzbach, Platzer et al. 2013). It is probably that BECN1 forms a compact conformation without its binding partners, while the binding of a partner to BECN1 causes a more extended conformation of BECN1 to recruit more proteins to form the complex such as PI3KC3 to regulate autophagy.

The multiple domains of BECN1 might cooperate with each in protein interaction. Several proteins (Luo, Garcia-Arencibia et al. 2012) Ma, Wang et al. 2012) such as SLAMF1 (Ma, Wang et al. 2012) are shown to interact with multi-domain regions to regulate autophagy. Especially, it is indicated in a recent 4.4Å PI3KC3 complex II (Rostislavleva, Soler et al. 2015) that BECN1/VPS30 FHD, CCD and BARAD interact with UVRAG/VPS38 CC1, CC2 and BARA-like domain respectively. This interaction triggers the disorder-to-helix change of FHD and comprises one arm of the PI3KC3 complex II to facilitate membrane-binding and activate the kinase activity of PI3KC3 during autophagy.

The estimated molecular weight from SEC is 3 fold of the BH3D-FHD-CCD, while molar mass estimated from V_c is about 2 fold of the theoretical molar mass of BH3D-FHD-CCD. This might also indicate there is a transition between the BECN1 monomer and oligomer in solution. Previously, we showed that the FHD appears to form a trimer when isolated (Mei, Ramanathan et al. 2016), but in the context of a larger construct comprising the BH3D-FHD, FHD-CCD or BH3D-FHD-CCD, it may either present as a monomer with the presence of BH3D or homodimerized with the presence of anti-parallel BECN1 CCD. The anti-paralleled

homodimer of FHD-CCD and BH3D-FHD-CCD may form via the CCD homodimer flanking with the BH3D-FHD on either side. Thus, it appears that there is a transition between the parallel FHD-homotrimer and the anti-parallel FHD-CCD or BH3D-FHD-CCD homodimer. They may exist in two mutually exclusive conformational states of BECN1. We expect that the CCD homodimer state is accessed in the absence of other partners that interact with the CCD, while the FHD trimer state is primarily accessed when BECN1 forms a complex with other CCD-containing partners that appear to lack regions that interact with the FHD. FHD could also present as the monomer state with the presence of its interacting proteins. For example, the 4.4Å crystal structure of PI3KC3 complex II (Rostislavleva, Soler et al. 2015) shows that the FHD exists as the helical monomer when interacting with UVRAG/VPS38, which also indicates that the monomer state of FHD may be important for the autophagy activation. On the other hand, the trimer FHD might associate with the oligomerization of BECN1 under normal condition and act as a platform for protein-protein interaction (Adi-Harel, Erlich et al. 2010). We also tried to investigate the structure of FL BECN1, but unfortunately the FL BECN1 has severe degradation due to its N-terminal IDR even with the presence of MBP-tag. This prevents us from further structurally characterizing it. In the future, it may worth trying to delete the IDR from the BECN1 FL.

There are two conserved CxxC motifs in BECN1: ^{18}CxxC^{21} and ^{137}CxxC^{140}, but their function in BECN1 is often neglected. Here, we show that the ^{137}CxxC^{140} might function as an oxidative stress sensor to increase BECN1 folding and induce autophagy under oxidizing condition. But the mechanism by which CxxC motif enhances the nucleation effects of Anchor on binding-associated folding under oxidizing condition is not clear yet. The previous studies showed that the CxxC motif allows the oxidoreductases to form the disulfide bond in protein

folding process, especially in ER (Chivers, Laboissiere et al. 1996, Shimizu and Hendershot 2009, Jedrychowski, Liu et al. 2015). Meanwhile, the conserved CxxC motif is also found in ATG14 and required for targeting complex to ER (Matsunaga, Morita et al. 2010). It is also possible that the BECN1 CxxC motifs contain functions in ER or associated with ER. Other research also shows that CxxC motif has important roles in binding metals such as zinc, copper and nickel (Nash and Mowatt 1993, Badarau, Basle et al. 2013, Kolkowska, Krzywoszynska et al. 2015). However, it is unclear which BECN1 CxxC motifs are involved in metal binding. Moreover, if and how the two CxxC motifs associate with each other to regulate BECN1 folding, metal binding or other known functions in autophagy need to be further investigated.

CHAPTER 8. SUMMARY AND FUTURE DIRECTIONS

8.1. Summary

In this study, we tried to elucidate the mechanisms of BECN1 in autophagy by investigating the structural features of human BECN1 individual- and multi-domains with or without binding partners and identifying residues important for protein-protein interactions, binding-associated conformational changes, and autophagy regulation. I have seven major conclusions as follows (Figure 8.1):

1. Intrinsically disordered regions (IDRs) with no stable secondary or ordered tertiary structure are present in 57% of key autophagy-related proteins. These regions are predicted to contain many binding and phosphorylation sites. The inherent evolutionary flexibility of IDRs enables them to adopt different conformations, allowing them to interact with different proteins. Therefore, IDRs may have important biological roles in autophagy and many cell signaling pathways.
2. The BECN1 IDR (residues 1-140) likely facilitates many BECN1 interactions. The IDR includes a functional BH3D (residue 105-130) that undergoes disorder-to-helix change upon binding to BCL2. This transition is nucleated by an Anchor region in the C-terminal half of the BH3D. The Anchor region residues are important for the inhibition of autophagy mediated by BCL2 proteins. However, there is no significant conformational change upon the mixing the disordered BH3D and VMP1 ATGD.
3. BECN1 residues 141-171 form a flexible helical domain (FHD) with its N-terminal half disordered and C-terminal half forming a 2.5-turn helix. The disordered part contains an Anchor that could nucleate the conformational changes upon binding to partners. Meanwhile, the conserved residues position on one side in helix part and are

required for the starvation-induced autophagy, probably due to their important role in AMBRA1 interaction.

4. The metastable, straight, anti-parallel BECN1 coiled-coil domain (CCD, residues 175-265) homodimer self-dissociates to bind to ATG14 CCD (residues 88-178) to form a parallel heterodimer with a curvature radius of 15 nm to trigger autophagy. The interface residues in the BECN1 homodimer are also involved in the heterodimer interface, while the hydrophobic ATG14 CCD residues are important for the BECN1 interaction to regulate starvation-induced autophagy.
5. The invariant BARAD residues, especially those in the range of residues 268-286, are important for the starvation-induced autophagy.

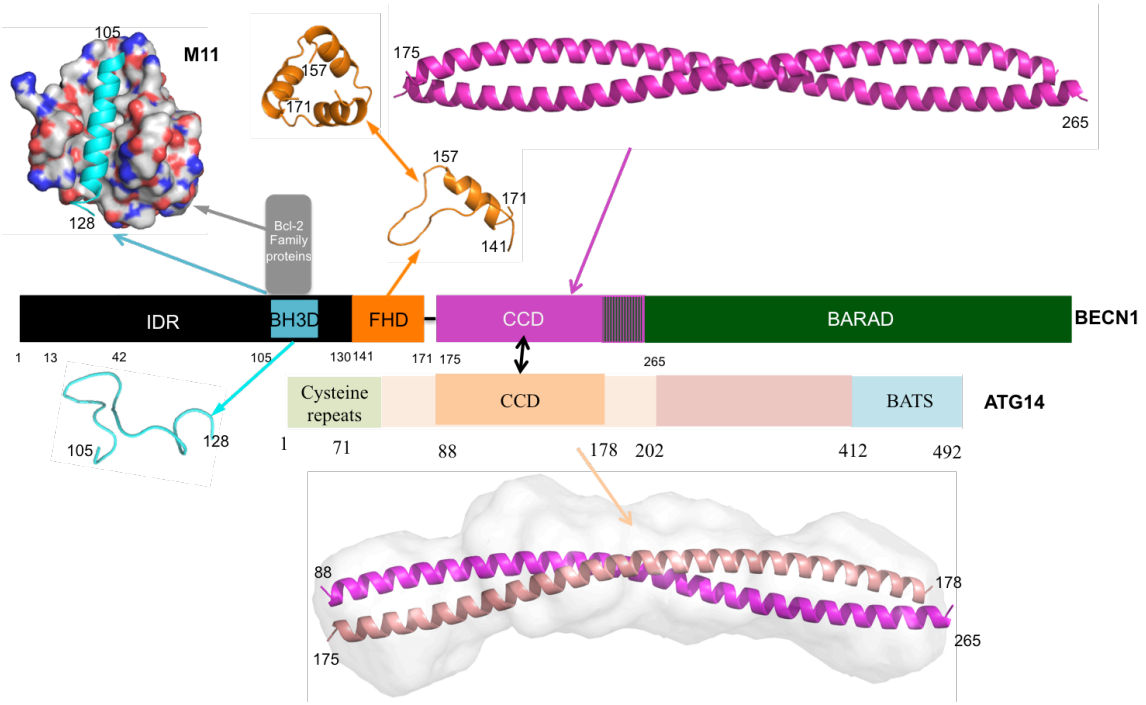

Figure 8.1. Summary of the structures of BECN1 domains and the interactions examined in this dissertation.
BECN1 and ATG14 domain architecture is indicated in the schematic. Boundaries of each domain are labeled by terminal residues. BCL2 homologs that down-regulate autophagy are displayed.

6. There is no intra-domain interaction amongst BH3D, FHD and CCD. The multi-domain constructs show extended conformation enabling each domain to interact with different binding partners.
7. The invariant CxxC-motif in BECN1 may respond to the oxidative stress to facilitate BECN1 folding and autophagy up-regulation under oxidizing condition.

8.2. Future Directions

Though we have delineated the individual domains of BECN1, and obtained information about their structures, conformational transitions and possible molecular mechanisms in autophagy, there are many unanswered questions.

In addition, there are two conserved CxxC motifs in the BECN1 IDR: ^{18}CxxC^{21} and ^{137}CxxC^{140}. Here we reported only preliminary studies on the role of ^{137}CxxC^{140} in BECN1 structure and autophagy regulation under oxidizing conditions. The molecular mechanism of these two CxxC motifs in determining BECN1 fold and its roles in autophagy or other cell signaling pathways has not yet been investigated. The potential role of these two CxxC motifs in metal binding, redox sensing, or protein-protein interaction needs to be investigated in the future. It was shown that ATG14 contains a conserved CxxC motif at its N terminus to target ATG14 to ER (Matsunaga, Morita et al. 2010) to fulfill its function in autophagy. Therefore, it is likely that the CxxC motif may also has important functions in ER to mediate BECN1 interaction, thereby playing an indispensable role in autophagy regulation, especially in PI3KC3 complex.

The individual BECN1 FHD forms a trimer in both crystal structure and solution. But the trimer structure cannot exist in the PI3KC3 complex, as the 4.4 Å crystal structure of PI3KC3 complex II also shows that it exists as a monomer when binding to its partner (Rostislavleva, Soler et al. 2015). Our SAXS data indicates it might exist as a monomer in the presence of the

BH3D or homodimerize together with the CCD homodimer. Meanwhile, BECN1 homotrimers and homodimers, formed by the oligomerization of the FHD and CCD respectively, cannot exist in the context of PI3KC3 complexes that mediate autophagy. However, the stable BECN1 oligomers exist under both normal and autophagy conditions (Adi-Harel, Erlich et al. 2010). Therefore, how the FHD trimer contributes to BECN1 oligomerization and the biological role of this trimer needs to be further elucidated.

The biological importance of the overlap region between BECN1 CCD and BARAD, which exists in two different conformations is often neglected. The X-ray structure of yeast VPS34:VPS30:VPS38:VPS15 (Rostislavleva, Soler et al. 2015) shows that this region is part of the CCD within the complex. However, this overlap region packs against the N-terminal nuclear export signal (NES) composed of a leucine zipper in CCD (Liang, Yu et al. 2001), therefore if it packs against the BARAD, the overlap region may be released from the BECN1 CCD homodimer freeing the NES to interact with proteins that facilitate nuclear export. However, further investigation is needed to explain this conformationally-flexible region and its impact on autophagy and other cellular functions.

The large number of invariant residues in the BECN1 BARAD indicates these residues are required for autophagy. But the impact of these residues on autophagy regulation has barely been investigated. Such studies could provide new targets for therapeutic design to regulate autophagy.

Though the structures of four individual BECN1 domains have been determined, the structure of full-length (FL) BECN1 in the absence of interaction partners is still unknown, perhaps due to the presence of the IDR at its N-terminal. The knowledge of the FL BECN1 structure would facilitate a better understanding of the mechanism and regulation of BECN1 in

protein interactions and cell signaling. Different strategies could be applied to demonstrate the structure of FL BECN1 such as using NMR to solve the solution structure or using a construct of FL BECN1 lacking the IDR to increase the possibility of crystal formation.

Additionally, the structure of BECN1 in complex with different proteins remains to be studies. Though the low-resolution structures of PI3KC3 complexes (Baskaran, Carlson et al. 2014, Rostislavleva, Soler et al. 2015) have been elucidated the domain arrangement of the structured BECN1 domains, high-resolution structures that enable identification of interacting side-chains in protein interaction is still unknown. Moreover, although interactions with a few proteins have been investigated in these structures, BECN1 interacts with about 20 other proteins. Much remains to be understood about the conformation and role of BECN1 in these protein interactions. Particularly, an understanding of how the flexibility of the BECN1 IDR facilitates protein interactions and perhaps simultaneously undergoes conformational changes to recruit or prevent binding of other proteins is missing. Such studies would also help to better understand the structure and function of FL BECN1 in protein complexes.

REFERENCES

Abergel, C. (2013). Molecular replacement: tricks and treats. *Acta Crystallogr D Biol Crystallogr* **69**(Pt 11): 2167-2173.

Adams, J. M. and S. Cory (1998). The Bcl-2 protein family: arbiters of cell survival. *Science* **281**(5381): 1322-1326.

Adams, P. D., P. V. Afonine, G. Bunkoczi, V. B. Chen, I. W. Davis, N. Echols, J. J. Headd, L. W. Hung, G. J. Kapral, R. W. Grosse-Kunstleve, A. J. McCoy, N. W. Moriarty, R. Oeffner, R. J. Read, D. C. Richardson, J. S. Richardson, T. C. Terwilliger and P. H. Zwart (2010). PHENIX: a comprehensive Python-based system for macromolecular structure solution. *Acta Crystallogr D Biol Crystallogr* **66**(Pt 2): 213-221.

Adi-Harel, S., S. Erlich, E. Schmukler, S. Cohen-Kedar, O. Segev, L. Mizrachy, J. A. Hirsch and R. Pinkas-Kramarski (2010). Beclin 1 self-association is independent of autophagy induction by amino acid deprivation and rapamycin treatment. *J Cell Biochem* **110**(5): 1262-1271.

Alexander, A. and C. L. Walker (2011). The role of LKB1 and AMPK in cellular responses to stress and damage. *FEBS Lett* **585**(7): 952-957.

Altomare, D. A. and J. R. Testa (2005). Perturbations of the AKT signaling pathway in human cancer. *Oncogene* **24**(50): 7455-7464.

Altschul, S. F., T. L. Madden, A. A. Schäffer, J. Zhang, Z. Zhang, W. Miller and D. J. Lipman (1997). Gapped BLAST and PSI-BLAST: a new generation of protein database search programs. *Nucleic Acids Res*. **25**: 3389-3402.

Amartely, H., A. David, M. Lebendiker, H. Benyamini, S. Izraeli and A. Friedler (2014). The STIL protein contains intrinsically disordered regions that mediate its protein-protein interactions. *Chemical Communications* **50**(40): 5245-5247.

Avalos, J. L., I. Celic, S. Muhammad, M. S. Cosgrove, J. D. Boeke and C. Wolberger (2002). Structure of a Sir2 enzyme bound to an acetylated p53 peptide. *Mol Cell* **10**(3): 523-535.

Axe, E. L., S. A. Walker, M. Manifava, P. Chandra, H. L. Roderick, A. Habermann, G. Griffiths and N. T. Ktistakis (2008). Autophagosome formation from membrane compartments enriched in phosphatidylinositol 3-phosphate and dynamically connected to the endoplasmic reticulum. *J Cell Biochem* **182**(4): 685-701.

Bach, M., M. Larance, D. E. James and G. Ramm (2011). The serine/threonine kinase ULK1 is a target of multiple phosphorylation events. *Biochem J* **440**: 283-291.

Backer, J. M. (2008). The regulation and function of Class III PI3Ks: novel roles for Vps34. *Biochem J* **410**(1): 1-17.

Badarau, A., A. Basle, S. J. Firbank and C. Dennison (2013). Investigating the Role of Zinc and Copper Binding Motifs of Trafficking Sites in the Cyanobacterium Synechocystis PCC 6803. *Biochemistry* **52**(39): 6816-6823.

Baskaran, S., L.-A. Carlson, G. Stjepanovic, L. N. Young, D. J. Kim, P. Grob, R. E. Stanley, E. Nogales and J. H. Hurley (2014). Architecture and dynamics of the autophagic phosphatidylinositol 3-kinase complex. *eLife* **3**: e05115.

Battye, T. G. G., L. Kontogiannis, O. Johnson, H. R. Powell and A. G. W. Leslie (2011). iMOSFLM: a new graphical interface for diffraction-image processing with MOSFLM. *Acta Crystallogr D Biol Crystallogr* **67**: 271-281.

Behrends, C., M. E. Sowa, S. P. Gygi and J. W. Harper (2010). Network organization of the human autophagy system. *Nature* **466**(7302): 68-84.

Bernado, P., E. Mylonas, M. V. Petoukhov, M. Blackledge and D. I. Svergun (2007). Structural characterization of flexible proteins using small-angle X-ray scattering. *J Am Chem Soc* **129**(17): 5656-5664.

Binder, L. I., A. L. Guillozet-Bongaarts, F. Garcia-Sierra and R. W. Berry (2005). Tau, tangles, and Alzheimer's disease. *Biochimica Et Biophysica Acta-Molecular Basis of Disease* **1739**(2-3): 216-223.

Blanchet, C. E. and D. I. Svergun (2013). Small-angle X-ray scattering on biological macromolecules and nanocomposites in solution. *Annu Rev Phys Chem* **64**: 37-54.

Blocquel, D., J. Habchi, A. Gruet, S. Blangy and S. Longhi (2012). Compaction and binding properties of the intrinsically disordered C-terminal domain of Henipavirus nucleoprotein as unveiled by deletion studies. *Molecular Biosystems* **8**(1): 392-410.

Blom, N., S. Gammeltoft and S. Brunak (1999). Sequence and structure-based prediction of eukaryotic protein phosphorylation sites. *Journal of Molecular Biology* **294**(5): 1351-1362.

Blow, D. M. and F. H. C. Crick (1959). The Treatment of Errors in the Isomorphous Replacement Method. *Acta Crystallographica* **12**(10): 794-802.

Bologna, C., R. Buonincontri, S. Serra, T. Vaisitti, V. Audrito, D. Brusa, A. Pagnani, M. Coscia, G. D'Arena, E. Mereu, R. Piva, R. R. Furman, D. Rossi, G. Gaidano, C. Terhorst and S. Deaglio (2016). SLAMF1 regulation of chemotaxis and autophagy determines CLL patient response. *Journal of Clinical Investigation* **126**(1): 181-194.

Bourhis, J. M., K. Johansson, V. Receveur-Brechot, C. J. Oldfield, K. A. Dunker, B. Canard and S. Longhi (2004). The C-terminal domain of measles virus nucleoprotein belongs to the class of intrinsically disordered proteins that fold upon binding to their physiological partner. *Virus Research* **99**(2): 157-167.

Brugarolas, J., K. Lei, R. L. Hurley, B. D. Manning, J. H. Reiling, E. Hafen, L. A. Witter, L. W. Ellisen and W. G. Kaelin (2004). Regulation of mTOR function in response to hypoxia by REDD1 and the TSC1/TSC2 tumor suppressor complex. *Genes & Development* **18**(23): 2893-2904.

Brunger, A. T. (1992). Free R value: a novel statistical quantity for assessing the accuracy of crystal structures. *Nature* **355**(6359): 472-475.

Buck, M. (1998). Trifluoroethanol and colleagues: cosolvents come of age. Recent studies with peptides and proteins. *Quarterly reviews of biophysics* **31**(3): 297-355.

Buck, M., S. E. Radford and C. M. Dobson (1993). A partially folded state of hen egg white lysozyme in trifluoroethanol: structural characterization and implications for protein folding. *Biochemistry* **32**: 669-678.

Budovskaya, Y. V., H. Hama, D. B. DeWald and P. K. Herman (2002). The C terminus of the Vps34p phosphoinositide 3-kinase is necessary and sufficient for the interaction with the Vps15p protein kinase. *Journal of Biological Chemistry* **277**(1): 287-294.

Chen, N. and J. Debnath (2010). Autophagy and tumorigenesis. *FEBS Lett* **584**(7): 1427-1435.

Chen, P.-c. and J. S. Hub (2014). Validating solution ensembles from molecular dynamics simulations by wide-angle X-ray scattering data. *Biophysical Journal* **107**(2): 435-447.

Cherra, S. J., 3rd, S. M. Kulich, G. Uechi, M. Balasubramani, J. Mountzouris, B. W. Day and C. T. Chu (2010). Regulation of the autophagy protein LC3 by phosphorylation. *J Cell Biol* **190**(4): 533-539.

Chittenden, T., C. Flemington, A. B. Houghton, R. G. Ebb, G. J. Gallo, B. Elangovan, G. Chinnadurai and R. J. Lutz (1995). A conserved domain in Bak, distinct from BH1 and BH2, mediates cell death and protein binding functions. *EMBO J* **14**(22): 5589-5596.

Chivers, P. T., M. C. Laboissiere and R. T. Raines (1996). The CXXC motif: imperatives for the formation of native disulfide bonds in the cell. *EMBO J* **15**(11): 2659-2667.

Cho, D.-H., Y. K. Jo, J. J. Hwang, Y. M. Lee, S. A. Roh and J. C. Kim (2009). Caspase-mediated cleavage of ATG6/Beclin-1 links apoptosis to autophagy in HeLa cells. *Cancer Letters* **274**: 95-100.

Colecchia, D., A. Strambi, S. Sanzone, C. Iavarone, M. Rossi, C. Dall'Armi, F. Piccioni, A. Verrotti di Pianella and M. Chiariello (2012). MAPK15/ERK8 stimulates autophagy by interacting with LC3 and GABARAP proteins. *Autophagy* **8**(12): 1724-1740.

Cowtan, K. (2006). The Buccaneer software for automated model building. 1. Tracing protein chains. *Acta Crystallogr D Biol Crystallogr* **62**(Pt 9): 1002-1011.

Criollo, A., M. Niso-Santano, S. A. Malik, M. Michaud, E. Morselli, G. Marino, S. Lachkar, A. V. Arkhipenko, F. Harper, G. Pierron, J. C. Rain, J. Ninomiya-Tsuji, J. M. Fuentes, S.

Lavandero, L. Galluzzi, M. C. Maiuri and G. Kroemer (2011). Inhibition of autophagy by TAB2 and TAB3. *Embo Journal* **30**(24): 4908-4920.

DeLano, W. L. (2002). The PyMOL Molecular Graphics System. San Carlos, CA, USA., *DeLano Scientific*.

Deretic, V., T. Saitoh and S. Akira (2013). Autophagy in infection, inflammation and immunity. *Nature Reviews Immunology* **13**(10): 722-737.

Dessau, M. A. and Y. Modis (2011). Protein Crystallization for X-ray Crystallography. *Jove-Journal of Visualized Experiments*(47).

Diao, J. J., R. Liu, Y. G. Rong, M. L. Zhao, J. Zhang, Y. Lai, Q. J. Zhou, L. M. Wilz, J. X. Li, S. Vivona, R. A. Pfuetzner, A. T. Brunger and Q. Zhong (2015). ATG14 promotes membrane tethering and fusion of autophagosomes to endolysosomes. *Nature* **520**(7548): 563-566.

Dinkel, H., S. Michael, R. J. Weatheritt, N. E. Davey, K. V. Roey, B. Altenberg, G. Toedt, B. Uyar, M. Seiler, A. Budd, L. Jödicke, M. A. Dammert, C. Schroeter, M. Hammer, T. Schmidt, P. Jehl, C. McGuigan, M. Dymecka, C. Chica, K. Luck, A. Via, A. Chatraryamontri, N. Haslam, G. Grebnev, R. J. Edwards, M. O. Steinmetz, H. Meiselbach, F. Diella and T. J. Gibson (2012). ELM—the database of eukaryotic linear motifs. *Nucleic Acids Res* **40**(D1): D242-251.

Djavaheri-Mergny, M., M. C. Maiuri and G. Kroemer (2010). Cross talk between apoptosis and autophagy by caspase-mediated cleavage of Beclin 1. *Oncogene* **29**(49): 6508-6508.

Dosztányi, Z., V. Csizmok, P. Tompa and I. n. Simon (2005). IUPred: web server for the prediction of intrinsically unstructured regions of proteins based on estimated energy content. *Bioinformatics* **21**(16): 3433-3434.

Dosztányi, Z., B. Mészáros and I. Simon (2009). ANCHOR: web server for predicting protein binding regions in disordered proteins. *Bioinformatics* **25**(20): 2745–2746.

Dowdle, W. E., B. Nyfeler, J. Nagel, R. A. Elling, S. Liu, E. Triantafellow, S. Menon, Z. Wang, A. Honda, G. Pardee, J. Cantwell, C. Luu, I. Cornella-Taracido, E. Harrington, P. Fekkes, H. Lei, Q. Fang, M. E. Digan, D. Burdick, A. F. Powers, S. B. Helliwell, S. D'Aquin, J. Bastien, H. Wang, D. Wiederschain, J. Kuerth, P. Bergman, D. Schwalb, J. Thomas, S. Ugwonali, F. Harbinski, J. Tallarico, C. J. Wilson, V. E. Myer, J. A. Porter, D. E. Bussiere, P. M. Finan, M. A. Labow, X. Mao, L. G. Hamann, B. D. Manning, R. A. Valdez, T. Nicholson, M. Schirle, M. S. Knapp, E. P. Keaney and L. O. Murphy (2014). Selective VPS34 inhibitor blocks autophagy and uncovers a role for NCOA4 in ferritin degradation and iron homeostasis in vivo. *Nat Cell Biol* **16**(11): 1069-1079.

Drozdetskiy, A., C. Cole, J. Procter and G. Barton (2015). JPred4: a protein secondary structure prediction server. *Nucleic Acids Research* **43**(W1): W389-W394.

Dunlap, T. B., J. M. Kirk, E. A. Pena, M. S. Yoder and T. P. Creamer (2013). Thermodynamics of binding by calmodulin correlates with target peptide α-helical propensity. *Proteins* **81**: 607–612.

Dunlop, E. A., D. K. Hunt, H. A. Acosta-Jaquez, D. C. Fingar and A. R. Tee (2011). "ULK1 inhibits mTORC1 signaling, promotes multisite Raptor phosphorylation and hinders substrate binding." Autophagy **7**(7): 737-747.

Dusetti, N. J., Y. F. Jiang, M. I. Vaccaro, R. Tomasini, A. A. Samir, E. L. Calvo, A. Ropolo, F. Fiedler, G. V. Mallo, J. C. Dagorn and J. L. Iovanna (2002). Cloning and expression of the rat vacuole membrane protein 1 (VMP1), a new gene activated in pancreas with acute pancreatitis, which promotes vacuole formation. B*iochemical and Biophysical Research Communications* **290**(2): 641-649.

Dyson, H. and P. E. Wright (2002). Coupling of folding and binding for unstructured proteins. *Curr Opin Struct Biol* **12**(1): 54-60.

Dyson, H. J. and P. E. Wright (2005). Intrinsically unstructured proteins and their functions. *Nat Rev Mol Cell Biol* **6**(3): 197-208.

Eisenberg-Lerner, A. and A. Kimchi (2012). PKD is a kinase of Vps34 that mediates ROS-induced autophagy downstream of DAPk. *Cell Death and Differentiation* **19**(5): 788-797.

Emsley, P., B. Lohkamp, W. G. Scott and K. Cowtan (2010). Features and development of Coot. *Acta Crystallogr D Biol Crystallogr* **66**(Pt 4): 486-501.

Emsley, P., B. Lohkamp, W. G. Scott and K. Cowtand (2010). Features and development of *Coot*. *Acta crystallographica*. *Section D, Biological crystallography* **66**(Pt 4): 486-501.

Erlich, S., L. Mizrachy, O. Segev, L. Lindenboim, O. Zmira, S. Adi-Harel, J. A. Hirsch, R. Stein and R. Pinkas-Kramarski (2007). Differential Interactions Between Beclin 1 and Bcl-2 Family Members. *Autophagy* **3**(6): 561-568.

Evans, H. A., P. A. Bahri, L. T. T. Vu and K. R. Barnard (2014). Modelling Cobalt Solvent Extraction using Aspen Custom Modeler. *24th European Symposium on Computer Aided Process Engineering*, *Pts A and B* **33**: 505-510.

Fan, W., A. Nassiri and Q. Zhong (2011). Autophagosome targeting and membrane curvature sensing by Barkor/Atg14(L). *Proceedings of the National Academy of Sciences of the United States of America* **108**(19): 7769-7774.

Feng, W., S. Huang, H. Wu and M. Zhang (2007). Molecular basis of Bcl-xL's target recognition versatility revealed by the structure of Bcl-xL in complex with the BH3 domain of Beclin-1. *J Mol Biol* **372**(1): 223-235.

Feng, W. Z., T. Wu, X. Y. Dan, Y. L. Chen, L. Li, S. Chen, D. Miao, H. T. Deng, X. Q. Gong and L. Yu (2015). Phosphorylation of Atg31 is required for autophagy. *Protein & Cell* **6**(4): 288-296.

Feng, Z., H. Zhang, A. J. Levine and S. Jin (2005). The coordinate regulation of the p53 and mTOR pathways in cells. *Proc Natl Acad Sci U S A* **102**(23): 8204-8209.

Fimia, G., A. Stoykova, A. Romagnoli, L. Giunta, S. Bartolomeo, R. Nardacci, M. Corazzari, C. Fuoco, A. Ucar, P. Schwartz, P. Gruss, M. Piacentini, K. Chowdhury and F. Cecconi (2007). Ambra1 regulates autophagy and development of the nervous system. *Nature* **447**(7148): 1121-1125.

Fogel, A. I., B. J. Dlouhy, C. X. Wang, S. W. Ryu, A. Neutzner, S. A. Hasson, D. P. Sideris, H. Abeliovich and R. J. Youle (2013). "Role of Membrane Association and Atg14-Dependent Phosphorylation in Beclin-1-Mediated Autophagy." Molecular and Cellular Biology **33**(18): 3675-3688.

Franke, D. and D. I. Svergun (2009). DAMMIF, a program for rapid ab-initio shape determination in small-angle scattering. *Journal of Applied Crystallography* **42**: 342-346.

Frishman, D. and P. Argos (1995). Knowledge-based protein secondary structure assignment. *Proteins* **23**(4): 566-579.

Fujioka, Y., N. N. Noda, K. Fujii, K. Yoshimoto, Y. Ohsumi and F. Inagaki (2008). In vitro reconstitution of plant ATG8 and ATG12 conjugation systems essential for autophagy. *Journal of Biological Chemistry* **283**(4): 1921-1928.

Fujioka, Y., S. W. Suzuki, H. Yamamoto, C. Kondo-Kakuta, Y. Kimura, H. Hirano, R. Akada, F. Inagaki, Y. Ohsumi and N. N. Noda (2014). Structural basis of starvation-induced assembly of the autophagy initiation complex. *Nature Structural & Molecular Biology* **21**(6): 513-521.

Fujita, N., T. Itoh, H. Omori, M. Fukuda, T. Noda and T. Yoshimori (2008). The Atg16L complex specifies the site of LC3 lipidation for membrane biogenesis in autophagy. *Molecular Biology of the Cell* **19**(5): 2092-2100.

Furuya, N., F. Yu, M. Byfield, S. Pattingre and B. Levine (2005). The evolutionarily conserved domain of Beclin 1 is required for Vps34 binding, autophagy and tumor suppressor function. *Autophagy* **1**(1): 46-52.

Furuya, T., M. Kim, M. Lipinski, J. Li, D. Kim, T. Lu, Y. Shen, L. Rameh, B. Yankner, L. H. Tsai and J. Yuan (2010). Negative regulation of Vps34 by Cdk mediated phosphorylation. *Mol Cell* **38**(4): 500-511.

Ganley, I. G., D. H. Lam, J. R. Wang, X. J. Ding, S. Chen and X. J. Jiang (2009). ULK1 center dot ATG13 center dot FIP200 Complex Mediates mTOR Signaling and Is Essential for Autophagy. *Journal of Biological Chemistry* **284**(18): 12297-12305.

Geng, J. F. and D. J. Klionsky (2008). The Atg8 and Atg12 ubiquitin-like conjugation systems in macroautophagy. *Embo Reports* **9**(9): 859-864.

Geng, J. F. and D. J. Klionsky (2010). The Golgi as a potential membrane source for autophagy. *Autophagy* **6**(7): 950-951.

Glover, K., Y. Mei and S. C. Sinha (2016). Identifying intrinsically disordered protein regions likely to undergo binding-induced helical transitions. *Biochim Biophys Acta*. In Press

Gnad, F., J. Gunawardena and M. Mann (2011). PHOSIDA 2011: the posttranslational modification database. *Nucleic Acids Research* **39**: D253-D260.

Gnad, F., S. B. Ren, J. Cox, J. V. Olsen, B. Macek, M. Oroshi and M. Mann (2007). PHOSIDA (phosphorylation site database): management, structural and evolutionary investigation, and prediction of phosphosites. *Genome Biology* **8**(11).

Greenfield, N. (2006). Using circular dichroism spectra to estimate protein secondary structure. *Nat. Protoc.* **1**(6): 2876-2890.

Gu, W., D. Wan, Q. Qian, B. Yi, Z. He, Y. Gu, L. Wang and S. He (2014). Ambra1 is an essential regulator of autophagy and apoptosis in SW620 cells: pro-survival role of Ambra1. *PloS One* **9**(2): e90151.

Gurkar, A., K. Chu, L. Raj, R. Bouley, S. Lee, Y. Kim, S. Dunn, A. Mandinova and S. Lee (2013). Identification of ROCK1 kinase as a critical regulator of Beclin1-mediated autophagy during metabolic stress. *Nature Communications* **4**.

Hailey, D. W., A. S. Rambold, P. Satpute-Krishnan, K. Mitra, R. Sougrat, P. K. Kim and J. Lippincott-Schwartz (2010). Mitochondria Supply Membranes for Autophagosome Biogenesis during Starvation. *Cell* **141**(4): 656-667.

Hamasaki, M., N. Furuta, A. Matsuda, A. Nezu, A. Yamamoto, N. Fujita, H. Oomori, T. Noda, T. Haraguchi, Y. Hiraoka, A. Amano and T. Yoshimori (2013). Autophagosomes form at ER-mitochondria contact sites. *Nature* **495**(7441): 389-393.

Hanada, T., N. N. Noda, Y. Satomi, Y. Ichimura, Y. Fujioka, T. Takao, F. Inagaki and Y. Ohsumi (2007). The Atg12-Atg5 conjugate has a novel E3-like activity for protein lipidation in autophagy. *Journal of Biological Chemistry* **282**(52): 37298-37302.

Hashimoto, M., N. Kodera, Y. Tsunaka, M. Oda, M. Tanimoto, T. Ando, K. Morikawa and S. Tate (2013). Phosphorylation-Coupled Intramolecular Dynamics of Unstructured Regions in Chromatin Remodeler FACT. *Biophysical Journal* **104**(10): 2222-2234.

Hauptman, H. A. (1991). The Phase Problem of X-Ray Crystallography. *Reports on Progress in Physics* **54**(11): 1427-1454.

Hayashi-Nishino, M., N. Fujita, T. Noda, A. Yamaguchi, T. Yoshimori and A. Yamamoto (2010). Electron tomography reveals the endoplasmic reticulum as a membrane source for autophagosome formation. *Autophagy* **6**(2): 301-303.

He, C. and B. Levine (2010). The Beclin 1 interactome. *Current Opinion in Cell Biology* **22**(2): 140-149.

Hegedus, K., P. Nagy, Z. Gaspari and G. Juhasz (2014). The Putative HORMA Domain Protein Atg101 Dimerizes and Is Required for Starvation-Induced and Selective Autophagy in Drosophila. B*iomed Research International*.

Hill, J. M. (2008). NMR Screening for Rapid Protein Characterization in Structural Proteomics. Methods in Molecular Biology: Structural Proteomics: High-throughput Methods. B. Kobe, M. Guss and T. Huber. *Totowa, NJ., Humana Press*. **426:** 437-446.

Hirsch, D. S., Y. Shen, M. Dokmanovic and W. J. Wu (2010). pp60c-Src phosphorylates and activates vacuolar protein sorting 34 to mediate cellular transformation. *Cancer Res* **70**(14): 5974-5983.

Holt, J. T., M. E. Thompson, C. Szabo, C. RobinsonBenion, C. L. Arteaga, M. C. King and R. A. Jensen (1996). Growth retardation and tumour inhibition by BRCA1. *Nature Genetics* **12**(3): 298-302.

Hosokawa, N., T. Sasaki, S. Iemura, T. Natsume, T. Hara and N. Mizushima (2009). Atg101, a novel mammalian autophagy protein interacting with Atg13. *Autophagy* **5**(7): 973-979.

Hsu, W. L., C. Oldfield, J. Meng, F. Huang, B. Xue, V. N. Uversky, P. Romero and A. K. Dunker (2012). Intrinsic protein disorder and protein-protein interactions. *Pac Symp Biocomput*: 116-127.

Hua, Q. X., W. H. Jia, B. P. Bullock, J. F. Habener and M. A. Weiss (1998). Transcriptional activator-coactivator recognition: Nascent folding of a kinase-inducible transactivation domain predicts its structure on coactivator binding. *Biochemistry* **37**(17): 5858-5866.

Huang, K. L., A. B. Chadee, C. Y. A. Chen, Y. Q. Zhang and A. B. Shyu (2013). Phosphorylation at intrinsically disordered regions of PAM2 motif-containing proteins modulates their interactions with PABPC1 and influences mRNA fate. *Rna-a Publication of the Rna Society* **19**(3): 295-305.

Huang, T. T., J. K. Hwang, C. H. Chen, C. S. Chu, C. W. Lee and C. C. Chen (2015). (PS)2: protein structure prediction server version 3.0. *Nucleic Acids Res* **43**(W1): W338-342.

Huang, W., W. Choi, W. Hu, N. Mi, Q. Guo, M. Ma, M. Liu, Y. Tian, P. Lu, F.-L. Wang, H. Deng, L. Liu, N. Gao, L. Yu and Y. Shi (2012). Crystal structure and biochemical analyses reveal Beclin 1 as a novel membrane binding protein. *Cell Research* **22**(3): 473-489.

Hubbell, W. L., C. J. Lopez, C. Altenbach and Z. Yang (2013). Technological advances in site-directed spin labeling of proteins. *Curr Opin Struct Biol* **23**(5): 725-733.

Hynes, N. E. and H. A. Lane (2005). ERBB receptors and cancer: The complexity of targeted inhibitors. *Nature Reviews Cancer* **5**(7): 341-354

Iakoucheva, L. M., P. Radivojac, C. J. Brown, T. R. O'Connor, J. G. Sikes, Z. Obradovic and A. K. Dunker (2004). The importance of intrinsic disorder for protein phosphorylation. *Nucleic Acids Res* **32**(3): 1037-1049.

Ilavsky, J. and P. R. Jemian (2009). Irena: tool suite for modeling and analysis of small-angle scattering. *Journal of Applied Crystallography* **42**: 347-353.

Inoki, K., Y. Li, T. Q. Zhu, J. Wu and K. L. Guan (2002). TSC2 is phosphorylated and inhibited by Akt and suppresses mTOR signalling. *Nature Cell Biology* **4**(9): 648-657.

Ishida, T. and K. Kinoshita (2007). PrDOS: prediction of disordered protein regions from amino acid sequence. *Nucleic Acids Res.* **35**: W460-W464.

Itakura, E., C. Kishi, K. Inoue and N. Mizushima (2008). Beclin 1 Forms Two Distinct Phosphatidylinositol 3-Kinase Complexes with Mammalian Atg14 and UVRAG. *Molecular Biology of the Cell* **19**(12): 5360-5372.

Itakura, E. and N. Mizushima (2009). Atg14 and UVRAG Mutually exclusive subunits of mammalian Beclin 1-PI3K complexes. *Autophagy* **5**(4): 534-536.

Janus, A., T. Robak and P. Smolewski (2005). The mammalian target of the rapamycin (mTOR) kinase pathway: Its role in tumourigenesis and targeted antitumour therapy. *Cellular & Molecular Biology Letters* **10**(3): 479-498.

Jedrychowski, M. P., L. Liu, C. J. Laflamme, K. Karastergiou, T. Meshulam, S. Y. Ding, Y. Wu, M. J. Lee, S. P. Gygi, S. K. Fried and P. F. Pilch (2015). Adiporedoxin, an upstream regulator of ER oxidative folding and protein secretion in adipocytes. *Mol Metab* **4**(11): 758-770.

Jeschke, G. (2012). DEER Distance Measurements on Proteins. *Annual Review of Physical Chemistry* **63**: 419-446.

Jiang, H., D. Cheng, W. Liu, J. Peng and J. Feng (2010). Protein kinase C inhibits autophagy and phosphorylates LC3. *Biochem Biophys Res Commun* **395**(4): 471-476.

Jiang, P. H., Y. Motoo, M. I. Vaccaro, J. L. Iovanna, G. Okada and N. Sawabu (2004). Expression of vacuole membrane protein 1 (VMP1) in spontaneous chronic pancreatitis in the WBN/Kob rat. *Pancreas* **29**(3): 225-230.

Jin, S. (2005). p53, Autophagy and tumor suppression. *Autophagy* **1**(3): 171-173.

Johnson, W. C., Jr. (1990). Protein secondary structure and circular dichroism: a practical guide. *Proteins* **7**(3): 205-214.

Jones, D. T. (1999). Protein secondary structure prediction based on position-specific scoring matrices. *J Mol Biol* **292**(2): 195-202.

Joo, J. H., F. C. Dorsey, A. Joshi, K. M. Hennessy-Walters, K. L. Rose, K. McCastlain, J. Zhang, R. Iyengar, C. H. Jung, D. F. Suen, M. A. Steeves, C. Y. Yang, S. M. Prater, D. H. Kim, C. B. Thompson, R. J. Youle, P. A. Ney, J. L. Cleveland and M. Kundu (2011). Hsp90-Cdc37 Chaperone Complex Regulates Ulk1-and Atg13-Mediated Mitophagy. *Molecular Cell* **43**(4): 572-585.

Kabeya, Y., N. Mizushima, T. Ueno, A. Yamamoto, T. Kirisako, T. Noda, E. Kominami, Y. Ohsumi and T. Yoshimori (2000). LC3, a mammalian homologue of yeast Apg8p, is localized in autophagosome membranes after processing. *The EMBO Journal* **19**(21): 5720-5728.

Kabeya, Y., N. Mizushima, A. Yamamoto, S. Oshitani-Okamoto, Y. Ohsumi and T. Yoshimori (2004). "LC3, GABARAP and GATE16 localize to autophagosomal membrane depending on form-II formation." Journal of Cell Science **117**(13): 2805-2812.

Kabsch, W. (1988). Automatic-Indexing of Rotation Diffraction Patterns. *Journal of Applied Crystallography* **21**: 67-71.

Kabsch, W. (2010). Integration, scaling, space-group assignment and post-refinement. *Acta Crystallographica Section D-Biological Crystallography* **66**: 133-144.

Kabsch, W. and C. Sander (1983). Dictionary of protein secondary structure: pattern recognition of hydrogen-bonded and geometrical features. *Biopolymers* **22**(12): 2577-2637.

Kaiser, S. E., Y. Qiu, J. E. Coats, K. Mao, D. J. Klionsky and B. A. Schulman (2013). Structures of Atg7-Atg3 and Atg7-Atg10 reveal noncanonical mechanisms of E2 recruitment by the autophagy E1. *Autophagy* **9**(5): 778-780.

Kang, R., H. Zeh, M. Lotze and D. Tang (2011). The Beclin 1 network regulates autophagy and apoptosis. *Cell Death and Differentiation* **18**(4): 571-580.

Keil, E., R. Hocker, M. Schuster, F. Essmann, N. Ueffing, B. Hoffman, D. A. Liebermann, K. Pfeffer, K. Schulze-Osthoff and I. Schmitz (2013). Phosphorylation of Atg5 by the Gadd45 beta-MEKK4-p38 pathway inhibits autophagy. *Cell Death and Differentiation* **20**(2): 321-332.

Kelekar, A. and C. B. Thompson (1998). Bcl-2-family proteins: the role of the BH3 domain in apoptosis. *Trends in Cell Biology* **8**(8): 324-330.

Kelly, S. M., T. J. Jess and N. C. Price (2005). How to study proteins by circular dichroism. *Biochimica Et Biophysica Acta-Proteins and Proteomics* **1751**(2): 119-139.

Khan, S. H. and R. Kumar (2012). Role of an intrinsically disordered conformation in AMPK-mediated phosphorylation of ULK1 and regulation of autophagy. *Mol Biosyst* **8**(1): 91-96.

Kihara, A., T. Noda, N. Ishihara and Y. Ohsumi (2001). Two distinct Vps34 phosphatidylinositol 3-kinase complexes function in autophagy and carboxypeptidase Y sorting in Saccharomyces cerevisiae. *J Cell Biol* **152**(3): 519-530.

Kikhney, A. G. and D. I. Svergun (2015). A practical guide to small angle X-ray scattering (SAXS) of flexible and intrinsically disordered proteins. *Febs Letters* **589**(19): 2570-2577.

Kim, J., Y. C. Kim, C. Fang, R. C. Russell, J. H. Kim, W. Fan, R. Liu, Q. Zhong and K. L. Guan (2013). Differential Regulation of Distinct Vps34 Complexes by AMPK in Nutrient Stress and Autophagy. *Cell* **152**(1-2): 290-303.

Kim, J., M. Kundu, B. Viollet and K. L. Guan (2011). AMPK and mTOR regulate autophagy through direct phosphorylation of Ulk1. *Nature Cell Biology* **13**(2): 132-U171.

Klionsky, D. J. (2010). The autophagy connection. *Dev Cell* **19**(1): 11-12.

Klionsky, D. J. and S. D. Emr (2000). Autophagy as a regulated pathway of cellular degradation. *Science* **290**(5497): 1717-1721.

Kolkowska, P., K. Krzywoszynska, S. Potocki, P. R. Chetana, M. Spodzieja, S. Rodziewicz-Motowidlo and H. Kozlowski (2015). Specificity of the Zn(2+), Cd(2+) and Ni(2+) ion binding sites in the loop domain of the HypA protein. *Dalton Trans* **44**(21): 9887-9900.

Komatsu, M., T. Ueno, S. Waguri, Y. Uchiyama, E. Kominami and K. Tanaka (2007). Constitutive autophagy: vital role in clearance of unfavorable proteins in neurons. *Cell Death and Differentiation* **14**(5): 887-894.

Konarev, P. V., V. V. Volkov, A. V. Sokolova, M. H. J. Koch and D. I. Svergun (2003). PRIMUS: a Windows PC-based system for small-angle scattering data analysis. J*ournal of Applied Crystallography* **36**: 1277-1282.

Koneri, K., T. Goi, Y. Hirono, K. Katayama and A. Yamaguchi (2007). Beclin 1 gene inhibits tumor growth in colon cancer cell lines. *Anticancer Res* **27**(3B): 1453-1457.

Kozin, M. B. and D. I. Svergun (2001). Automated matching of high- and low-resolution structural models. *Journal of Applied Crystallography* **34**: 33-41.

Ku, B., J.-S. Woo, C. Liang, K.-H. Lee, H.-S. Hong, E. Xiaofei, K.-S. Kim, J. U. Jung and B.-H. Oh (2008). Structural and biochemical bases for the inhibition of autophagy and apoptosis by viral Bcl-2 of murine γ-Herpesvirus 68. *PLoS Pathogens* **4**(2): e25.

Ku, B., J.-S. Woo, C. Liang, K.-H. Lee, J. J. U. and B.-H. Oh (2008). An insight into the mechanistic role of Beclin 1 and its inhibition by prosurvival Bcl-2 family proteins. *Autophagy* **4**(4): 519-520.

Kurzbach, D., G. Platzer, T. C. Schwarz, M. A. Henen, R. Konrat and D. Hinderberger (2013). Cooperative unfolding of compact conformations of the intrinsically disordered protein osteopontin. *Biochemistry* **52**(31): 5167-5175.

Lang, T., S. Reiche, M. Straub, M. Bredschneider and M. Thumm (2000). Autophagy and the cvt pathway both depend on AUT9. *Journal of Bacteriology* **182**(8): 2125-2133.

Lazarus, M. B., C. J. Novotny and K. M. Shokat (2015). Structure of the Human Autophagy Initiating Kinase ULK1 in Complex with Potent Inhibitors. *Acs Chemical Biology* **10**(1): 257-261.

Lee, C. (2007). Coimmunoprecipitation assay. *Methods Mol Biol* **362**: 401-406.

Lee, E. F., M. A. Perugini, A. Pettikiriarachchi, M. Evangelista, D. W. Keizer, S. Yao and W. D. Fairlie (2016). The BECN1 N-terminal domain is intrinsically disordered. *Autophagy* **12**(3): 460-471.

Lee, H. W., J. Y. Ryu, J. Yoo, B. Choi, K. Kim and T. Y. Yoon (2013). "Real-time single-molecule coimmunoprecipitation of weak protein-protein interactions." Nat Protoc **8**(10): 2045-2060.

Legakis, J. E. and D. J. Klionski (2006). Overview of autophagy. Autophagy in immunity and infection. *V. Deretic. Weinheim, Germany, Wiley-VCH Verlag GmbH & Co. KGaA***:** 3-17.

Levine, B. and D. J. Klionsky (2004). Development by self-digestion: Molecular mechanisms and biological functions of autophagy. *Dev. Cell* **6**(4): 463-477.

Levine, B. and G. Kroemer (2008). Autophagy in the pathogenesis of disease. *Cell* **132**(1): 27-42.

Levine, B., R. Liu, X. Dong and Q. Zhong (2015). Beclin orthologs: integrative hubs of cell signaling, membrane trafficking, and physiology. *Trends in Cell Biology* **25**(9): 533-544.

Levine, B., N. Mizushima and H. W. Virgin (2011). Autophagy in immunity and inflammation. *Nature* **469**(7330): 323-335.

Li, S. H., G. Schilling, W. S. Young, 3rd, X. J. Li, R. L. Margolis, O. C. Stine, M. V. Wagster, M. H. Abbott, M. L. Franz, N. G. Ranen and et al. (1993). Huntington's disease gene (IT15) is widely expressed in human and rat tissues. *Neuron* **11**(5): 985-993.

Li, X., L. He, K. H. Che, S. F. Funderburk, L. Pan, N. Pan, M. Zhang, Z. Yue and Y. Zhao (2012). Imperfect interface of Beclin1 coiled-coil domain regulates homodimer and heterodimer formation with Atg14L and UVRAG. *Nature communications* **3**: 662.

Li, Z., B. Chen, Y. Wu, F. Jin, Y. Xia and X. Liu (2010). Genetic and epigenetic silencing of the beclin 1 gene in sporadic breast tumors. *BMC Cancer* **10**: 98.

Liang, C., P. Feng, B. Ku, O. B-H and J. U. Jung (2007). UVRAG: A new player in autophagy and tumor cell growth. *Autophagy* **3**(1): 69-71.

Liang, C., P. Feng, B. Ku, I. Dotan, D. Canaani, B. H. Oh and J. U. Jung (2006). Autophagic and tumour suppressor activity of a novel Beclin1-binding protein UVRAG. *Nat Cell Biol* **8**(7): 688-699.

Liang, C., J.-s. Lee, K.-S. Inn, M. U. Gack, Q. Li, E. A. Roberts, I. Vergne, V. Deretic, P. Feng, C. Akazawa and J. U. Jung (2008). Beclin1-binding UVRAG targets the class C Vps complex to coordinate autophagosome maturation and endocytic trafficking. *Nat Cell Biol* **10**(7): 776-787.

Liang, X. H., S. Jackson, M. Seaman, K. Brown, B. Kempkes, H. Hibshoosh and B. Levine (1999). Induction of autophagy and inhibition of tumorigenesis by beclin 1. *Nature* **402**(6762): 672-676.

Liang, X. H., L. K. Kleeman, H. H. Jiang, G. Gordon, J. E. Goldman, G. Berry, B. Herman and B. Levine (1998). Protection against fatal Sindbis virus encephalitis by beclin, a novel Bcl-2-interacting protein. *J Virol* **72**(11): 8586-8596.

Liang, X. H., J. Yu, K. Brown and B. Levine (2001). Beclin 1 contains a leucine-rich nuclear export signal that is required for its autophagy and tumor suppressor function. *Cancer Res* **61**(8): 3443-3449.

Lindmo, K., A. Brech, K. D. Finley, S. Gaumer, D. Contamine, T. E. Rusten and H. Stenmark (2008). The PI 3-kinase regulator Vps15 is required for autophagic clearance of protein aggregates. *Autophagy* **4**(4): 500-506.

Liu, Q., Q. Liu and W. A. Hendrickson (2013). Robust structural analysis of native biological macromolecules from multi-crystal anomalous diffraction data. *Acta Crystallogr D Biol Crystallogr* **69**(Pt 7): 1314-1332.

Liu, X., S. C. Dai, Y. Zhu, P. Marrack and J. W. Kappler (2003). The structure of a Bcl-x_L/Bim fragment complex: implications for Bim function. *Immunity* **19**: 341-352.

Longatti, A. and S. A. Tooze (2009). Vesicular trafficking and autophagosome formation. *Cell Death Differ* **16**(7): 956-965.

Lopez, C. J., Z. Yang, C. Altenbach and W. L. Hubbell (2013). Conformational selection and adaptation to ligand binding in T4 lysozyme cavity mutants. *Proc Natl Acad Sci U S A* **110**(46): E4306-4315.

Luo, J., M. Li, Y. Tang, M. Laszkowska, R. G. Roeder and W. Gu (2004). "Acetylation of p53 augments its site-specific DNA binding both in vitro and in vivo." Proc Natl Acad Sci U S A **101**(8): 2259-2264.

Luo, S. and D. C. Rubinsztein (2010). Apoptosis blocks Beclin 1-dependent autophagosome synthesis: an effect rescued by Bcl-xL. *Cell Death Differ* **17**(2): 268-277.

Luo, S. Q., M. Garcia-Arencibia, R. Zhao, C. Puri, P. P. C. Toh, O. Sadiq and D. C. Rubinsztein (2012). Bim Inhibits Autophagy by Recruiting Beclin 1 to Microtubules. *Molecular Cell* **47**(3): 359-370.

Ma, C. Y., N. H. Wang, C. Detre, G. X. Wang, M. O'Keeffe and C. Terhorst (2012). Receptor Signaling Lymphocyte-activation Molecule Family 1 (Slamf1) Regulates Membrane Fusion and NADPH Oxidase 2 (NOX2) Activity by Recruiting a Beclin-1/Vps34/Ultraviolet Radiation Resistance-associated Gene (UVRAG) Complex. J*ournal of Biological Chemistry* **287**(22): 18359-18365.

Ma, L., Z. B. Chen, H. Erdjument-Bromage, P. Tempst and P. P. Pandolfi (2005). Phosphorylation and functional inactivation of TSC2 by Erk: Implications for tuberous sclerosis and cancer pathogenesis. *Cell* **121**(2): 179-193.

Ma, X., H. Liu, J. T. Murphy, S. R. Foyil, R. J. Godar, H. Abuirqeba, C. J. Weinheimer, P. M. Barger and A. Diwan (2015). Regulation of the transcription factor EB-PGC1alpha axis by beclin-1 controls mitochondrial quality and cardiomyocyte death under stress. *Mol Cell Biol* **35**(6): 956-976.

Mack, H. I. D., B. Zheng, J. M. Asara and S. M. Thomas (2012). AMPK-dependent phosphorylation of ULK1 regulates ATG9 localization. *Autophagy* **8**(8): 1197-1214.

Maejima, Y., S. Kyoi, P. Zhai, T. Liu, H. Li, A. Ivessa, S. Sciarretta, D. P. Del Re, D. K. Zablocki, C.-P. Hsu, D.-S. Lim, M. Isobe and J. Sadoshima (2013). Mst1 inhibits autophagy by promoting the interaction between Beclin1 and Bcl-2. *Nat Med* **19**(11): 1478-1488.

Maiuri, M., A. Criollo, E. Tasdemir, J. Vicencio, N. Tajeddine, J. Hickman, O. Geneste and G. Kroemer (2007). BH3-only proteins and BH3 mimetics induce autophagy by competitively disrupting the interaction between Beclin 1 and Bcl-2/Bcl-X_L. *Autophagy* **3**(4): 374-476.

Maiuri, M., G. Le Toumelin, A. Criollo, J. Rain, F. Gautier, P. Juin, E. Tasdemir, G. Pierron, K. Troulinaki, N. Tavernarakis, J. Hickman, O. Geneste and G. Kroemer (2007). Functional and physical interaction between Bcl-X_L and a BH3-like domain in Beclin-1. *EMBO J.* **26**(10): 2527-2539.

Maiuri, M. C., A. Criollo, E. Tasdemir, J. M. Vicencio, N. Tajeddine, J. A. Hickman, O. Geneste and G. Kroemer (2007). BH3-only proteins and BH3 mimetics induce autophagy by competitively disrupting the interaction between Beclin 1 and Bcl-2/Bcl-X-L. *Autophagy* **3**(4): 374-376.

Mao, K., L. H. Chew, Y. Inoue-Aono, H. Cheong, U. Nair, H. Popelka, C. K. Yip and D. J. Klionsky (2013). Atg29 phosphorylation regulates coordination of the Atg17-Atg31-Atg29 complex with the Atg11 scaffold during autophagy initiation. *Proc Natl Acad Sci* U S A **110**(31): E2875-2884.

Mapelli, M., L. Massimiliano, S. Santaguida and A. Musacchio (2007). The mad2 conformational dimer: Structure and implications for the spindle assembly checkpoint. *Cell* **131**(4): 730-743.

Mark, W. Y., J. C. Liao, Y. Lu, A. Ayed, R. Laister, B. Szymczyna, A. Chakrabartty and C. H. Arrowsmith (2005). Characterization of segments from the central region of BRCA1: an intrinsically disordered scaffold for multiple protein-protein and protein-DNA interactions? *J Mol Biol* **345**(2): 275-287.

Matsuda, N., S. Sato, K. Shiba, K. Okatsu, K. Saisho, C. A. Gautier, Y. S. Sou, S. Saiki, S. Kawajiri, F. Sato, M. Kimura, M. Komatsu, N. Hattori and K. Tanaka (2010). PINK1 stabilized by mitochondrial depolarization recruits Parkin to damaged mitochondria and activates latent Parkin for mitophagy. *J Cell Biol* **189**(2): 211-221.

Matsumoto, G., K. Wada, M. Okuno, M. Kurosawa and N. Nukina (2011). Serine 403 Phosphorylation of p62/SQSTM1 Regulates Selective Autophagic Clearance of Ubiquitinated Proteins. *Molecular Cell* **44**(2): 279-289.

Matsunaga, K., E. Morita, T. Saitoh, S. Akira, N. T. Ktistakis, T. Izumi, T. Noda and T. Yoshimori (2010). Autophagy requires endoplasmic reticulum targeting of the PI3-kinase complex via Atg14L. *J Cell Biol* **190**(4): 511-521.

Matsunaga, K., T. Saitoh, K. Tabata, H. Omori, T. Satoh, N. Kurotori, I. Maejima, K. Shirahama-Noda, T. Ichimura, T. Isobe, S. Akira, T. Noda and T. Yoshimori (2009). Two Beclin 1-binding proteins, Atg14L and Rubicon, reciprocally regulate autophagy at different stages. *Nature Cell Biology* **11**(4): 385-396.

McCoy, A. J., R. W. Grosse-Kunstleve, P. D. Adams, M. D. Winn, L. C. Storoni and R. J. Read (2007). Phaser crystallographic software. *J Appl Crystallogr* **40**(Pt 4): 658-674.

Mei, Y., A. Ramanathan, K. Glover, Christopher , C. Stanley, R. Sanishvili, S. Chakravarthy, Z. Yang, C. L. Colbert and S. C. Sinha (2016). Conformational Flexibility Enables Function of a BECN1 Region Essential for Starvation-Mediated Autophagy. *Biochemistry* **55**(13): 1945–1958.

Mei, Y., M. Su, R. Sanishvili, S. Chakravarthy, C. L. Colbert and S. C. Sinha (2016). Identification of BECN1 and ATG14 coiled-coil interface residues important for starvation-induced autophagy. *Biochemistry*. In Press.

Mei, Y., M. Su, G. Soni, S. Salem, C. Colbert and S. Sinha (2014). Intrinsically disordered regions in autophagy proteins. *PROTEINS: Structure, Function and Bioinformatics* **82**(4): 565–578.

Mei, Y., M. Su, G. Soni, S. Salem, C. L. Colbert and S. C. Sinha (2014). "Intrinsically disordered regions in autophagy proteins." Proteins **82**(4): 565-578.

Mercer, C. A., A. Kaliappan and P. B. Dennis (2009). A novel, human Atg13 binding protein, Atg101, interacts with ULK1 and is essential for macroautophagy. *Autophagy* **5**(5): 649-662.

Meszaros, B., I. Simon and Z. Dosztanyi (2009). Prediction of protein binding regions in disordered proteins. *PLoS computational biology* **5**(5): e1000376.

Michel, M., M. Schwarten, C. Decker, L. Nagel-Steger, D. Willbold and O. H. Weiergraber (2015). The mammalian autophagy initiator complex contains 2 HORMA domain proteins. *Autophagy* **11**(12): 2300-2308.

Miller, S., B. Tavshanjian, A. Oleksy, O. Perisic, B. T. Houseman, K. M. Shokat and R. L. Williams (2010). Shaping Development of Autophagy Inhibitors with the Structure of the Lipid Kinase Vps34. *Science* **327**(5973): 1638-1642.

Miracco, C., E. Cosci, G. Oliveri, P. Luzi, L. Pacenti, I. Monciatti, S. Mannucci, M. C. De Nisi, M. Toscano, V. Malagnino, S. M. Falzarano, L. Pirtoli and P. Tosi (2007). Protein and mRNA expression of autophagy gene Beclin 1 in human brain tumours. *Int J Oncol* **30**(2): 429-436.

Mittag, T. and J. D. Forman-Kay (2007). Atomic-level characterization of disordered protein ensembles. *Curr Opin Struct Biol* **17**(1): 3-14.

Mizushima, N. (2007). Autophagy: process and function. *Genes Dev* **21**(22): 2861-2873.

Mizushima, N. and D. J. Klionsky (2007). Protein turnover via autophagy: implications for metabolism. *Annu Rev Nutr* **27**: 19-40.

Mizushima, N., A. Kuma, Y. Kobayashi, A. Yamamoto, M. Matsubae, T. Takao, T. Natsume, Y. Ohsumi and T. Yoshimori (2003). Mouse Apg16L, a novel WD-repeat protein, targets to the autophagic isolation membrane with the Apg12-Apg5 conjugate. *J Cell Sci* **116**(Pt 9): 1679-1688.

Mizushima, N., B. Levine, A. Cuervo and D. Klionsky (2008). "Autophagy fights disease through cellular self-digestion." Nature **451**: 1069-1075.

Mizushima, N., T. Noda and Y. Ohsumi (1999). Apg16p is required for the function of the Apg12p-Apg5p conjugate in the yeast autophagy pathway. *Embo Journal* **18**(14): 3888-3896.

Mizushima, N., H. Sugita, T. Yoshimori and Y. Ohsumi (1998). A new protein conjugation system in human - The counterpart of the yeast Apg12p conjugation system essential for autophagy. *Journal of Biological Chemistry* **273**(51): 33889-33892.

Mizushima, N., A. Yamamoto, M. Hatano, Y. Kobayashi, Y. Kabeya, K. Suzuki, T. Tokuhisa, Y. Ohsumi and T. Yoshimori (2001). Dissection of autophagosome formation using Apg5-deficient mouse embryonic stem cells. *Journal of Cell Biology* **152**(4): 657-667.

Mizushima, N., T. Yoshimori and Y. Ohsumi (2011). The role of Atg proteins in autophagosome formation. *Annu. Rev. Cell Dev. Biol*. **27**: 107-132.

Mohan, A., C. Oldfield, P. Radivojac, V. Vacic, M. Cortese, A. Dunker and V. Uversky (2006). Analysis of molecular recognition features (MoRFs). *J. Mol. Biol.* **362**(5): 1043-1059.

Mohan, A., C. J. Oldfield, P. Radivojac, V. Vacic, M. S. Cortese, A. K. Dunker and V. N. Uversky (2006). Analysis of molecular recognition features (MoRFs). *J Mol Biol* **362**(5): 1043-1059.

Molejon, M. I., A. Ropolo, A. L. Re, V. Boggio and M. I. Vaccaro (2013). The VMP1-Beclin 1 interaction regulates autophagy induction. *Sci Rep* **3**: 1055.

Morris, D. H., C. K. Yip, Y. Shi, B. T. Chait and Q. J. Wang (2015). Beclin 1-Vps34 Complex Architecture: Understanding the Nuts and Bolts of Therapeutic Targets. *Front Biol* (Beijing) **10**(5): 398-426.

Morselli, E., L. Galluzzi, O. Kepp, G. Marino, M. Michaud, I. Vitale, M. C. Maiuri and G. Kroemer (2011). Oncosuppressive Functions of Autophagy. Antioxidants & Redox Signaling **14**(11): 2251-2269.

Murray, J. T., C. Panaretou, H. Stenmark, M. Miaczynska and J. M. Backer (2002). Role of Rab5 in the recruitment of hVps34/p150 to the early endosome. *Traffic* **3**(6): 416-427.

Murshudov, G. N., A. A. Vagin and E. J. Dodson (1997). Refinement of macromolecular structures by the maximum-likelihood method. *Acta Crystallogr D Biol Crystallogr* **53**(Pt 3): 240-255.

Nakai, A., O. Yamaguchi, T. Takeda, Y. Higuchi, S. Hikoso, M. Taniike, S. Omiya, I. Mizote, Y. Matsumura, M. Asahi, K. Nishida, M. Hori, N. Mizushima and K. Otsu (2007). The role of autophagy in cardiomyocytes in the basal state and in response to hemodynamic stress. *Nat Med* **13**(5): 619-624.

Nakamura, T., H. Asakawa, Y. Nakase, J. Kashiwazaki, Y. Hiraoka and C. Shimoda (2008). Live observation of forespore membrane formation in fission yeast. *Mol Biol Cell* **19**(8): 3544-3553.

Nanao, M. H., G. M. Sheldrick and R. B. Ravelli (2005). Improving radiation-damage substructures for RIP. *Acta Crystallogr D Biol Crystallogr* **61**(Pt 9): 1227-1237.

Narendra, D., A. Tanaka, D. F. Suen and R. J. Youle (2008). Parkin is recruited selectively to impaired mitochondria and promotes their autophagy. *Journal of Cell Biology* **183**(5): 795-803.

Nascimento, E. B. M., M. Snel, B. Guigas, G. C. M. van der Zon, J. Kriek, J. A. Maassen, I. M. Jazet, M. Diamant and D. M. Ouwens (2010). Phosphorylation of PRAS40 on Thr246 by PKB/AKT facilitates efficient phosphorylation of Ser183 by mTORC1. *Cellular Signalling* **22**(6): 961-967.

Nash, T. E. and M. R. Mowatt (1993). Variant-Specific Surface-Proteins of Giardia-Lamblia Are Zinc-Binding Proteins. *Proceedings of the National Academy of Sciences of the United States of America* **90**(12): 5489-5493.

Niso-Santano, M., A. Criollo, S. A. Malik, M. Michaud, E. Morselli, G. Marino, S. Lachkar, L. Galluzzi, M. C. Maiuri and G. Kroemer (2012). Direct molecular interactions between Beclin 1 and the canonical NF kappa B activation pathway. *Autophagy* **8**(2): 268-270.

Noble, C., J. Dong, E. Manser and H. Song (2008). Bcl-xL and UVRAG cause a monomer-dimer switch in Beclin1. *Journal of Biological Chemistry* **283**(38): 26274-26282.

Noda, N. N. and Y. Fujioka (2015). Atg1 family kinases in autophagy initiation. *Cell Mol Life* Sci **72**(16): 3083-3096.

Noda, N. N., Y. Fujioka, T. Hanada, Y. Ohsumi and F. Inagaki (2013). Structure of the Atg12-Atg5 conjugate reveals a platform for stimulating Atg8-PE conjugation. *Embo Reports* **14**(2): 206-211.

Noda, N. N., T. Kobayashi, W. Adachi, Y. Fujioka, Y. Ohsumi and F. Inagaki (2012). Structure of the novel C-terminal domain of vacuolar protein sorting 30/autophagy-related protein 6 and its specific role in autophagy. *The Journal of biological chemistry* **287**(20): 16256-16266.

Noda, T., J. Kim, W. P. Huang, M. Baba, C. Tokunaga, Y. Ohsumi and D. J. Klionsky (2000). Apg9p/Cvt7p is an integral membrane protein required for transport vesicle formation in the Cvt and autophagy pathways. *Journal of Cell Biology* **148**(3): 465-479.

Obara, K., T. Noda, K. Niimi and Y. Ohsumi (2008). Transport of phosphatidylinositol 3-phosphate into the vacuole via autophagic membranes in Saccharomyces cerevisiae. *Genes to Cells* **13**(6): 537-547.

Obara, K. and Y. Ohsumi (2008). Dynamics and function of PtdIns(3)P in autophagy. *Autophagy* **4**(7): 952-954.

Obara, K. and Y. Ohsumi (2011). Atg14: a key player in orchestrating autophagy. *International journal of cell biology* **2011**: 713435.

Oberstein, A., P. D. Jeffrey and Y. Shi (2007). Crystal structure of the Bcl-XL-Beclin 1 peptide complex: Beclin 1 is a novel BH3 only protein. *J. Biol. Chem*. **282**(17): 13123-13132.

Obradovic, Z., K. Peng, S. Vucetic, P. Radivojac and A. K. Dunker (2005). Exploiting Heterogeneous Sequence Properties Improves Prediction of Protein Disorder. *Proteins* **61**(S7): 176-182.

Otwinowski, Z. and W. Minor (1997). Processing of X-ray diffraction data collected in oscillation mode. *Macromolecular Crystallography, Pt A* **276**: 307-326.

Pace, C. and J. M. Scholtz (1998). A helix propensity scale based on experimental studies of peptides and proteins. *Biophys* J. **75**(1): 422-427.

Page, R., W. Peti, I. A. Wilson, R. C. Stevens and K. Wüthrich (2004). NMR screening and crystal quality of bacterially expressed prokaryotic and eukaryotic proteins in a structural genomics pipeline. *Proceedings National Academy of Science, USA* **102**(6): 1901–1905.

Papinski, D., M. Schuschnig, W. Reiter, L. Wilhelm, C. A. Barnes, A. Maiolica, I. Hansmann, T. Pfaffenwimmer, M. Kijanska, I. Stoffel, S. S. Lee, A. Brezovich, J. H. Lou, B. E. Turk, R. Aebersold, G. Ammerer, M. Peter and C. Kraft (2014). Early Steps in Autophagy Depend on Direct Phosphorylation of Atg9 by the Atg1 Kinase. *Molecular Cell* **53**(3): 515-515.

Pasquier, B., Y. El-Ahmad, B. Filoche-Romme, C. Dureuil, F. Fassy, P. Y. Abecassis, M. Mathieu, T. Bertrand, T. Benard, C. Barriere, S. El Batti, J. P. Letallec, V. Sonnefraud, M. Brollo, L. Delbarre, V. Loyau, F. Pilorge, L. Bertin, P. Richepin, J. Arigon, J. R. Labrosse, J. Clement, F. Durand, R. Combet, P. Perraut, V. Leroy, F. Gay, D. Lefrancois, F. Bretin, J. P. Marquette, N. Michot, A. Caron, C. Castell, L. Schio, G. McCort, H. Goulaouic, C. Garcia-Echeverria and B. Ronan (2015). Discovery of (2S)-8-[(3R)-3-methylmorpholin-4-yl]-1-(3-methyl-2-oxobutyl)-2-(trifluoromethyl)- 3,4-dihydro-2H-pyrimido[1,2-a]pyrimidin-6-one: a novel potent and selective inhibitor of Vps34 for the treatment of solid tumors. *J Med Chem* **58**(1): 376-400.

Pattingre, S., C. Bauvy, T. Levade, B. Levine and P. Codogno (2009). Ceramide-induced autophagy. *Autophagy* **5**(4): 558-560.

Pattingre, S., A. Tassa, X. Qu, R. Garuti, X. H. Liang, N. Mizushima, M. Packer, M. D. Schneider and B. Levine (2005). Bcl-2 antiapoptotic proteins inhibit Beclin 1-dependent autophagy. *Cell* **122**(6): 927-939.

Peng, K., P. Radivojac, S. Vucetic, D. A.K. and Z. Obradovic (2006). Length-Dependent Prediction of Protein Intrinsic Disorder. B*MC Bioinformatics* **7**: 208.

Perez, H. L., P. Banfi, J. Bertrand, Z. W. Cai, J. W. Grebinski, K. Kim, J. Lippy, M. Modugno, J. Naglich, R. J. Schmidt, A. Tebben, P. Vianello, D. D. Wei, L. P. Zhang, A. Galvani, L. J. Lombardo and R. M. Borzilleri (2012). Identification of a phenylacylsulfonamide series of dual Bcl-2/Bcl-xL antagonists. *Bioorganic & Medicinal Chemistry Letter*s **22**(12): 3946-3950.

Perez-Iratxeta, C. and M. A. Andrade-Navarro (2008). K2D2: estimation of protein secondary structure from circular dichroism spectra. *BMC Struct Biol* **8**: 25.

Petoukhov, M. V., D. Franke, A. V. Shkumatov, G. Tria, A. G. Kikhney, M. Gajda, C. Gorba, H. D. T. Mertens, P. V. Konarev and D. I. Svergun (2012). New developments in the ATSAS program package for small-angle scattering data analysis. *Journal of Applied Crystallography* **45**: 342-350.

Petoukhov, M. V. and D. I. Svergun (2005). Global rigid body modeling of macromolecular complexes against small-angle scattering data. *Biophys J* **89**(2): 1237-1250.

Petros, A. M., A. Medek, D. G. Nettesheim, D. H. Kim, H. S. Yoon, K. Swift, E. D. Matayoshi, T. Oltersdorf and S. W. Fesik (2001). Solution structure of the antiapoptotic protein bcl-2. *Proc Natl Acad Sci U S A* **98**(6): 3012-3017.

Pierce, M. M., C. S. Raman and B. T. Nall (1999). Isothermal titration calorimetry of protein-protein interactions. *Methods* **19**(2): 213-221.

Platta, H. W., H. Abrahamsen, S. B. Thoresen and H. Stenmark (2012). Nedd4-dependent lysine-11-linked polyubiquitination of the tumour suppressor Beclin 1. *Biochem J* **441**(1): 399-406.

Popelka, H., V. N. Uversky and D. J. Klionsky (2014). Identification of Atg3 as an intrinsically disordered polypeptide yields insights into the molecular dynamics of autophagy-related proteins in yeast. *Autophagy* **10**(6): 1093-1104.

Porter, J., A. Payne, B. de Candole, D. Ford, B. Hutchinson, G. Trevitt, J. Turner, C. Edwards, C. Watkins, I. Whitcombe, J. Davis and C. Stubberfield (2009). Tetrahydroisoquinoline amide substituted phenyl pyrazoles as selective Bcl-2 inhibitors. *Bioorganic & Medicinal Chemistry Letters* **19**(1): 230-233.

Potter, C. J., L. G. Pedraza and T. Xu (2002). Akt regulates growth by directly phosphorylating Tsc2. *Nature Cell Biology* **4**(9): 658-665.

Provencher, S. W. and J. Glöckner (1981). Estimation of globular protein secondary structure from circular dichroism. *Biochemistry* **20**(1): 33-37.

Puente, C., R. C. Hendrickson and X. Jiang (2016). Nutrient-Regulated Phosphorylation of ATG13 Inhibits Starvation-Induced Autophagy. *J Biol Chem.* **291**(11):6026-6035

Putnam, C. D., M. Hammel, G. L. Hura and J. A. Tainer (2007). X-ray solution scattering (SAXS) combined with crystallography and computation: defining accurate macromolecular structures, conformations and assemblies in solution. *Q Rev Biophys* **40**(3): 191-285.

Qi, S. Q., D. J. Kim, G. Stjepanovic and J. H. Hurley (2015). Structure of the Human Atg13-Atg101 HORMA Heterodimer: an Interaction Hub within the ULK1 Complex. *Structure* **23**(10): 1848-1857.

Qu, X., J. Yu, G. Bhagat, N. Furuya, H. Hibshoosh, A. Troxel, J. Rosen, E. L. Eskelinen, N. Mizushima, Y. Ohsumi, G. Cattoretti and B. Levine (2003). Promotion of tumorigenesis by heterozygous disruption of the beclin 1 autophagy gene. *J Clin Inves*t **112**(12): 1809-1820.

Ragusa, M. J., R. E. Stanley and J. H. Hurley (2012). Architecture of the Atg17 Complex as a Scaffold for Autophagosome Biogenesis. *Cell* **151**(7): 1501-1512.

Ramanathan, A. and P. K. Agarwal (2009). Computational identification of slow conformational fluctuations in proteins. *J. Phys. Chem.* B **113**(52): 16669-16680.

Rambo, R. P. and J. A. Tainer (2013). Accurate assessment of mass, models and resolution by small-angle scattering. *Nature* **496**(7446): 477-481.

Reed, J. C., T. Miyashita, S. Takayama, H. G. Wang, T. Sato, S. Krajewski, C. AimeSempe, S. Bodrug, S. Kitada and M. Hanada (1996). BCL-2 family proteins: Regulators of cell death involved in the pathogenesis of cancer and resistance to therapy. *Journal of Cellular Biochemistry* **60**(1): 23-32.

Reggiori, F., T. Shintani, U. Nair and D. J. Klionsky (2005). Atg9 cycles between mitochondria and the pre-autophagosomal structure in yeasts. *Autophagy* **1**(2): 101-109.

Reggiori, F., K. A. Tucker, P. E. Stromhaug and D. J. Klionsky (2004). The Atg1-Atg13 complex regulates Atg9 and Atg23 retrieval transport from the pre-autophagosomal structure. *Developmental Cell* **6**(1): 79-90.

Rehm, T., R. Huber and T. Holak (2002). Application of NMR in structural proteomics: screening for proteins amenable to structural analysis. *Structure* **10**(12): 1613-1618.

Roccatano, D., G. Colombo, M. Fioroni and A. E. Mark (2002). Mechanism by which 2,2,2-trifluoroethanol/water mixtures stabilize secondary-structure formation in peptides: A molecular dynamics study. *Proceedings of the National Academy of Sciences of the United States of America* **99**(19): 12179-12184.

Rohn, T. T., E. Wirawan, R. J. Brown, J. R. Harris, E. Masliah and P. Vandenabeele (2011). Depletion of Beclin-1 due to proteolytic cleavage by caspases in the Alzheimer's disease brain. *Neurobiology of Disease* **43**(1): 68-78.

Romero, P., Z. Obradovic, X. Li, E. C. Garner, C. J. Brown and A. K. Dunker (2001). Sequence complexity of disordered protein. *Proteins* **42**(1): 38-48.

Ronan, B., O. Flamand, L. Vescovi, C. Dureuil, L. Durand, F. Fassy, M. F. Bachelot, A. Lamberton, M. Mathieu, T. Bertrand, J. P. Marquette, Y. El-Ahmad, B. Filoche-Romme, L. Schio, C. Garcia-Echeverria, H. Goulaouic and B. Pasquier (2014). A highly potent and selective Vps34 inhibitor alters vesicle trafficking and autophagy. *Nat Chem Biol* **10**(12): 1013-1019.

Ropolo, A., D. Grasso, R. Pardo, M. L. Sacchetti, C. Archange, A. Lo Re, M. Seux, J. Nowak, C. D. Gonzalez, J. L. Iovanna and M. I. Vaccaro (2007). The pancreatitis-induced vacuole membrane protein 1 triggers autophagy in mammalian cells. *J Biol Chem* **282**(51): 37124-37133.

Rostislavleva, K., N. Soler, Y. Ohashi, L. Zhang, E. Pardon, J. E. Burke, G. R. Masson, C. Johnson, J. Steyaert, N. T. Ktistakis and R. L. Williams (2015). Structure and flexibility of the endosomal Vps34 complex reveals the basis of its function on membranes. *Science* **350**(6257): 178-181.

Roux, P. P., B. A. Ballif, R. Anjum, S. P. Gygi and J. Blenis (2004). Tumor-promoting phorbol esters and activated Ras inactivate the tuberous sclerosis tumor suppressor complex via p90 ribosomal S6 kinase. *Proceedings of the National Academy of Sciences of the United States of America* **101**(37): 13489-13494.

Rumi-Masante, J., F. I. Rusinga, T. E. Lester, T. B. Dunlap, T. D. Williams, A. K. Dunker, D. D. Weis and T. P. Creamer (2012). Structural basis for activation of calcineurin by calmodulin. *Journal of molecular biology* **415**(2): 307-317.

Russell, R. C., Y. Tian, H. Yuan, H. W. Park, Y. Y. Chang, J. Kim, H. Kim, T. P. Neufeld, A. Dillin and K. L. Guan (2013). ULK1 induces autophagy by phosphorylating Beclin-1 and activating VPS34 lipid kinase. *Nature Cell Biology* **15**(7): 741-750.

Rustandi, R. R., D. M. Baldisseri and D. J. Weber (2000). Structure of the negative regulatory domain of p53 bound to S100B(betabeta). *Nat Struct Biol* **7**(7): 570-574.

Saftig, P., Y. Tanaka, R. Lullmann-Rauch and K. von Figura (2001). Disease model: LAMP-2 enlightens Danon disease. *Trends in Molecular Medicine* **7**(1): 37-39.

Sakaguchi, K., H. Sakamoto, D. Xie, J. W. Erickson, M. S. Lewis, C. W. Anderson and E. Appella (1997). Effect of phosphorylation on tetramerization of the tumor suppressor protein p53. *J Protein Chem* **16**(5): 553-556.

Sali, A. and T. L. Blundell (1993). Comparative Protein Modeling by Satisfaction of Spatial Restraints. *Journal of Molecular Biology* **234**(3): 779-815.

Sancak, Y., C. C. Thoreen, T. R. Peterson, R. A. Lindquist, S. A. Kang, E. Spooner, S. A. Carr and D. M. Sabatini (2007). PRAS40 is an insulin-regulated inhibitor of the mTORC1 protein kinase. *Molecular Cell* **25**(6): 903-915.

Sheffield, P., S. Garrard and Z. Derewenda (1999). Overcoming expression and purification problems of RhoGDI using a family of "Parallel" expression vectors. *Prot. Express. and Purif.* **15**: 34-39.

Sheldrick, G. M. (2010). Experimental phasing with SHELXC/D/E: combining chain tracing with density modification. *Acta Crystallographica Section D-Biological Crystallography* **66**: 479-485.

Shelly, S., N. Lukinova, S. Bambina, A. Berman and S. Cherry (2009). "Autophagy Is an Essential Component of Drosophila Immunity against Vesicular Stomatitis Virus." Immunity **30**(4): 588-598.

Shi, C. H., J. Wu, M. Fu, B. H. Zhang, J. Wang, X. Yang and Y. P. Chi (2014). Ambra1 modulates starvation-induced autophagy through AMPK signaling pathway in cardiomyocytes. *Biochemical and Biophysical Research Communications* **452**(3): 308-314.

Shi, C. S. and J. H. Kehrl (2010). Traf6 and A20 differentially regulate TLR4-induced autophagy by affecting the ubiquitination of Beclin 1. *Autophagy* **6**(7): 986-987.

Shi, Z., C. Y. Li, S. Zhao, Y. Yu, N. An, Y. X. Liu, C. F. Wu, B. S. Yue and J. K. Bao (2013). A systems biology analysis of autophagy in cancer therapy. *Cancer Lett* **337**(2): 149-160.

Shimizu, K. and H. Toh (2009). Interaction between Intrinsically Disordered Proteins Frequently Occurs in a Human Protein-Protein Interaction Network. *Journal of Molecular Biology* **392**(5): 1253-1265.

Shimizu, Y. and L. M. Hendershot (2009). Oxidative folding: cellular strategies for dealing with the resultant equimolar production of reactive oxygen species. *Antioxid Redox Signal* **11**(9): 2317-2331.

Shintani, T. and D. J. Klionsky (2004). Autophagy in health and disease: A double-edged sword. *Science* **306**(5698): 990-995.

Shintani, T., N. Mizushima, Y. Ogawa, A. Matsuura, T. Noda and Y. Ohsumi (1999). Apg10p, a novel protein-conjugating enzyme essential for autophagy in yeast. *Embo Journal* **18**(19): 5234-5241.

Shiraki, K., K. Nishikawa and Y. Goto (1995). Trifluoroethanol-induced stabilization of the alpha-helical structure of beta-lactoglobulin: implication for non-hierarchical protein folding. *J Mol Biol* **245**(2): 180-194.

Shoji-Kawata, S., R. Sumpter, M. Leveno, G. R. Campbell, Z. Zou, L. Kinch, A. D. Wilkins, Q. Sun, K. Pallauf, D. MacDuff, C. Huerta, H. W. Virgin, J. B. Helms, R. Eerland, S. A. Tooze, R. Xavier, D. J. Lenschow, A. Yamamoto, D. King, O. Lichtarge, N. V. Grishin, S. A. Spector, D. V. Kaloyanova and B. Levine (2013). Identification of a candidate therapeutic autophagy-inducing peptide. *Nature* **494**: 201-206.

Siliciano, J. D., C. E. Canman, Y. Taya, K. Sakaguchi, E. Appella and M. B. Kastan (1997). DNA damage induces phosphorylation of the amino terminus of p53. *Genes Dev* **11**(24): 3471-3481.

Sinha, S., C. L. Colbert, N. Becker, Y. Wei and B. Levine (2008). Molecular basis of the regulation of Beclin 1-dependent autophagy by the gamma-herpesvirus 68 Bcl-2 homolog M11. *Autophagy* **4**(8): 989-997.

Sinha, S. and B. Levine (2008). The autophagy effector Beclin 1: a novel BH3-only protein." *Oncogene* **27 Suppl 1**: S137-S148.

Smyth, M. S. and J. H. Martin (2000). x ray crystallography. *Mol Pathol* **53**(1): 8-14.

Sofer, A., K. Lei, C. M. Johannessen and L. W. Ellisen (2005). Regulation of mTOR and cell growth in response to energy stress by REDD1. *Mol Cell Biol* **25**(14): 5834-5845.

Song, X., S. Y. Kim, L. Zhang, D. Tang, D. L. Bartlett, Y. T. Kwon and Y. J. Lee (2014). Role of AMP-activated protein kinase in cross-talk between apoptosis and autophagy in human colon cancer. *Cell Death Dis* **5**: e1504.

Souers, A. J., J. D. Leverson, E. R. Boghaert, S. L. Ackler, N. D. Catron, J. Chen, B. D. Dayton, H. Ding, S. H. Enschede, W. J. Fairbrother, D. C. S. Huang, S. G. Hymowitz, S. Jin, S. L. Khaw, P. J. Kovar, L. T. Lam, J. Lee, H. L. Maecker, K. C. Marsh, K. D. Mason, M. J. Mitten, P. M. Nimmer, A. Oleksijew, C. H. Park, C. M. Park, D. C. Phillips, A. W. Roberts, D. Sampath, J. F. Seymour, M. L. Smith, G. M. Sullivan, S. K. Tahir, C. Tse, M. D. Wendt, Y. Xiao, J. C. Xue, H. C. Zhang, R. A. Humerickhouse, S. H. Rosenberg and S. W. Elmore (2013). ABT-199, a potent and selective BCL-2 inhibitor, achieves antitumor activity while sparing platelets. *Nature Medicine* **19**(2): 202-208.

Sreerama, N., S. Y. Venyaminov and R. W. Woody (1999). Estimation of the number of alpha-helical and beta-strand segments in proteins using CD spectroscopy. *Biophysical Journal* **76**(1): A381-A381.

Sreerama, N., S. Y. Venyaminov and R. W. Woody (2001). Analysis of protein circular dichroism spectra based on the tertiary structure classification. *Analytical biochemistry* **299**(2): 271-274.

Sreerama, N. and R. W. Woody (1993). A self-consistent method for the analysis of protein secondary structure from circular dichroism. *Anal Biochem* **209**: 32-44.

Sreerama, N. and R. W. Woody (2000). Estimation of protein secondary structure from circular dichroism spectra: Comparison of CONTIN, SELCON, and CDSSTR methods with an expanded reference set. *Analytical Biochemistry* **287**(2): 252-260.

Stack, J. H., P. K. Herman, P. V. Schu and S. D. Emr (1993). A Membrane-Associated Complex Containing the Vps15 Protein-Kinase and the Vps34 Pi 3-Kinase Is Essential for Protein Sorting to the Yeast Lysosome-Like Vacuole. *Embo Journal* **12**(5): 2195-2204.

Stark, C., B.-J. Breitkreutz, T. Reguly, L. Boucher, A. Breitkreutz and M. Tyers (2006). BioGRID: a general repository for interaction datasets. *Nucleic Acids Research*. **34**(Database issue): D535–D539.

Stein, M. P., Y. Feng, K. L. Cooper, A. M. Welford and A. Wandinger-Ness (2003). Human VPS34 and p150 are Rab7 interacting partners. *Traffic* **4**(11): 754-771.

Strappazzon, F., M. Vietri-Rudan, S. Campello, F. Nazio, F. Florenzano, G. M. Fimia, M. Piacentini, B. Levine and F. Cecconi (2011). Mitochondrial BCL-2 inhibits AMBRA1-induced autophagy. *EMBO J* **30**(7): 1195-1208.

Su, M., Y. Mei, R. Sanishvili, B. Levine, C. L. Colbert and S. Sinha (2014). Targeting gamma-herpesvirus 68 Bcl-2-mediated down-regulation of autophagy. *J Biol Chem* **289**(12): 8029-8050.

Sun, Q. M., W. L. Fan, K. L. Chen, X. J. Ding, S. Chen and Q. Zhong (2008). Identification of Barkor as a mammalian autophagy-specific factor for Beclin 1 and class III phosphatidylinositol 3-kinase. *Proceedings of the National Academy of Sciences of the United States of America* **105**(49): 19211-19216.

Sun, Q. M., J. Zhang, W. L. Fan, K. N. Wong, X. J. Ding, S. Chen and Q. Zhong (2011). The RUN Domain of Rubicon Is Important for hVps34 Binding, Lipid Kinase Inhibition, and Autophagy Suppression. *Journal of Biological Chemistry* **286**(1): 185-191.

Sun, T., X. Li, P. Zhang, W. D. Chen, H. L. Zhang, D. D. Li, R. Deng, X. J. Qian, L. Jiao, J. Ji, Y. T. Li, R. Y. Wu, Y. Yu, G. K. Feng and X. F. Zhu (2015). Acetylation of Beclin 1 inhibits autophagosome maturation and promotes tumour growth. *Nat Commun* **6**: 7215.

Suzuki, H., T. Kaizuka, N. Mizushima and N. N. Noda (2015). Structure of the Atg101-Atg13 complex reveals essential roles of Atg101 in autophagy initiation. *Nature Structural & Molecular Biology* **22**(7): 572-580.

Suzuki, K., T. Kirisako, Y. Kamada, N. Mizushima, T. Noda and Y. Ohsumi (2001). The pre-autophagosomal structure organized by concerted functions of APG genes is essential for autophagosome formation. *Embo Journal* **20**(21): 5971-5981.

Suzuki, K., Y. Kubota, T. Sekito and Y. Ohsumi (2007). Hierarchy of Atg proteins in pre-autophagosomal structure organization. *Genes to Cells* **12**(2): 209-218.

Svergun, D., C. Barberato and M. H. J. Koch (1995). CRYSOL - A program to evaluate x-ray solution scattering of biological macromolecules from atomic coordinates. J*ournal of Applied Crystallography* **28**: 768-773.

Svergun, D. I. (1992). Determination of the Regularization Parameter in Indirect-Transform Methods Using Perceptual Criteria. *Journal of Applied Crystallography* **25**: 495-503.

Svergun, D. I. (1999). Restoring low resolution structure of biological macromolecules from solution scattering using simulated annealing. *Biophysical Journal* **76**(6): 2879-2886.

Svergun, D. I., M. V. Petoukhov and M. H. J. Koch (2001). Determination of domain structure of proteins from X-ray solution scattering. *Biophysical Journal* **80**(6): 2946-2953.

Tang, H. W., Y. B. Wang, S. L. Wang, M. H. Wu, S. Y. Lin and G. C. Chen (2011). Atg1-mediated myosin II activation regulates autophagosome formation during starvation-induced autophagy. *Embo Journal* **30**(4): 636-651.

Tanida, I., N. Mizushima, M. Kiyooka, M. Ohsumi, T. Ueno, Y. Ohsumi and E. Kominami (1999). Apg7p/Cvt2p: A novel protein-activating enzyme essential for autophagy. *Molecular Biology of the Cell* **10**(5): 1367-1379.

Tanida, I., E. Tanida-Miyake, M. Komatsu, T. Ueno and E. Kominami (2002). Human Apg3p/Aut1p homologue is an authentic E2 enzyme for multiple substrates, GATE-16,

GABARAP, and MAP-LC3, and facilitates the conjugation of hApg12p to hApg5p. *Journal of Biological Chemistry* **277**(16): 13739-13744.

Tanida, I., E. Tanida-Miyake, T. Ueno and E. Kominami (2001). The human homolog of Saccharomyces cerevisiae Apg7p is a protein-activating enzyme for multiple substrates including human Apg12p, GATE-16, GABARAP, and MAP-LC3. *Journal of Biological Chemistry* **276**(3): 1701-1706.

Tattoli, I., M. T. Sorbara, D. Vuckovic, A. Ling, F. Soares, L. A. M. Carneiro, C. Yang, A. Emili, D. J. Philpott and S. E. Girardin (2012). Amino Acid Starvation Induced by Invasive Bacterial Pathogens Triggers an Innate Host Defense Program. *Cell Host & Microbe* **11**(6): 563-575.

Taylor, G. L. (2010). Introduction to phasing. *Acta Crystallogr D Biol Crystallogr* **66**(Pt 4): 325-338.

Terman, A. (2001). Garbage catastrophe theory of aging: imperfect removal of oxidative damage? *Redox Report* **6**(1): 15-26.

Terman, A. and U. T. Brunk (2005). Autophagy in cardiac myocyte homeostasis, aging, and pathology. *Cardiovascular Research* **68**(3): 355-365.

Thompson, J. D., T. J. Gibson and D. G. Higgins (2002). Multiple sequence alignment using ClustalW and ClustalX. *Curr Protoc Bioinformatics* **Chapter 2**: Unit 2 3.

Thompson, J. D., D. G. Higgins and T. J. Gibson (1994). CLUSTAL W: improving the sensitivity of progressive multiple sequence alignment through sequence weighting, position specific gap penalities and weight matrix choice. *Nucleic Acids Res.* **22**: 4673-4680.

Tompa, P. (2002). Intrinsically unstructured proteins. *Trends Biochem Sci* **27**(10): 527-533.

Towler, M. C. and D. G. Hardie (2007). AMP-activated protein kinase in metabolic control and insulin signaling. *Circulation Research* **100**(3): 328-341.

Tria, G., H. D. T. Mertens, M. Kachala and D. I. Svergun (2015). Advanced ensemble modelling of flexible macromolecules using X-ray solution scattering. *Iucrj* **2**: 207-217.

Ueno, T., W. Sato, Y. Horie, M. Komatsu, I. Tanida, M. Yoshida, S. Ohshima, T. W. Mak, S. Watanabe and E. Kominami (2008). Loss of Pten, a tumor suppressor, causes the strong inhibition of autophagy without affecting LC3 lipidation. *Autophagy* **4**(5): 692-700.

Vaccaro, M. I., A. Ropolo, D. Grasso and J. L. Iovanna (2008). A novel mammalian trans-membrane protein reveals an alternative initiation pathway for autophagy. *Autophagy* **4**(3): 388-390.

Velazquez-Campoy, A., S. A. Leavitt and E. Freire (2004). Characterization of protein-protein interactions by isothermal titration calorimetry. *Methods Mol Biol* **261**: 35-54.

Volkov, V. V. and D. I. Svergun (2003). Uniqueness of ab initio shape determination in small-angle scattering. *Journal of Applied Crystallography* **36**: 860-864.

Voo, K. S., D. L. Carlone, B. M. Jacobsen, A. Flodin and D. G. Skalnik (2000). Cloning of a mammalian transcriptional activator that binds unmethylated CpG motifs and shares a CXXC domain with DNA methyltransferase, human trithorax, and methyl-CpG binding domain protein 1. *Molecular and Cellular Biology* **20**(6): 2108-2121.

Voskoboinik, I., D. Strausak, M. Greenough, H. Brooks, M. Petris, S. Smith, J. F. Mercer and J. Camakaris (1999). Functional analysis of the N-terminal CXXC metal-binding motifs in the human Menkes copper-transporting P-type ATPase expressed in cultured mammalian cells. *J Biol Chem* **274**(31): 22008-22012.

Walker, E. H., O. Perisic, C. Ried, L. Stephens and R. L. Williams (1999). Structural insights into phosphoinositide 3-kinase catalysis and signalling. *Nature* **402**(6759): 313-320.

Wang, M. C., A. G. Wu, Y. Z. Huang, G. L. Shao, S. F. Ji, R. W. Wang, H. J. Yuan, X. L. Fan, L. H. Zheng and Q. L. Jiao (2015). Autophagic regulation of cell growth by altered expression of Beclin 1 in triple-negative breast cancer. I*nt J Clin Exp Med* **8**(5): 7049-7058.

Wang, R. C., Y. J. Wei, Z. Y. An, Z. J. Zou, G. H. Xiao, G. Bhagat, M. White, J. Reichelt and B. Levine (2012). Akt-Mediated Regulation of Autophagy and Tumorigenesis Through Beclin 1 Phosphorylation. *Science* **338**(6109): 956-959.

Wang, W., H. Fan, Y. Zhou, P. Duan, G. Zhao and G. Wu (2013). Knockdown of autophagy-related gene BECLIN1 promotes cell growth and inhibits apoptosis in the A549 human lung cancer cell line. *Mol Med Rep* **7**(5): 1501-1505.

Ward, J., L. McGuffin, K. Bryson, B. Buxton and D. T. Jones (2004). The DISOPRED server for the prediction of protein disorder. *Bioinformatics* **20**(13): 2138-2139.

Ward, J. J., J. S. Sodhi, L. J. McGuffin, B. F. Buxton and D. T. Jones (2004). Prediction and functional analysis of native disorder in proteins from the three kingdoms of life. *J Mol Biol* **337**(3): 635-645.

Waterhouse, A. M., J. B. Procter, D. M. Martin, M. Clamp and G. J. Barton (2009). Jalview Version 2--a multiple sequence alignment editor and analysis workbench. *Bioinformatics* **25**(9): 1189-1191.

Webber, J. L. and S. A. Tooze (2010). Coordinated regulation of autophagy by p38 alpha MAPK through mAtg9 and p38IP. *Embo Journal* **29**(1): 27-40.

Wei, Y., Z. An, Z. Zou, R. Sumpter, M. Su, X. Zang, S. Sinha, M. Gaestel and B. Levine (2015). The stress-responsive kinases MAPKAPK2/MAPKAPK3 activate starvation-induced autophagy through Beclin 1 phosphorylation. *eLife* **4**: e05289.

Wei, Y., S. Pattingre, S. Sinha, M. Bassik and B. Levine (2008). JNK1-mediated phosphorylation of Bcl-2 regulates starvation-induced autophagy. *Mol Cell* **30**(6): 678-688.

Wei, Y., Z. Zou, N. Becker, M. Anderson, R. Sumpter, G. Xiao, L. Kinch, P. Koduru, C. S. Christudass, R. W. Veltri, N. V. Grishin, M. Peyton, J. Minna, G. Bhagat and B. Levine (2013). EGFR-mediated Beclin 1 phosphorylation in autophagy suppression, tumor progression, and tumor chemoresistance. *Cell* **154**(6): 1269-1284.

Wei, Y. J., Z. Y. An, Z. J. Zou, R. Sumpter, M. F. Su, X. Zang, S. Sinha, M. Gaestel and B. Levine (2015). The stress-responsive kinases MAPKAPK2/MAPKAPK3 activate starvation-induced autophagy through Beclin 1 phosphorylation. *Elife* **4**.

Weng, J., C. Wang, Y. Wang, H. Tang, J. Liang, X. Liu, H. Huang and J. Hou (2014). Beclin1 inhibits proliferation, migration and invasion in tongue squamous cell carcinoma cell lines. *Oral Oncol* **50**(10): 983-990.

Winn, M. D., C. C. Ballard, K. D. Cowtan, E. J. Dodson, P. Emsley, P. R. Evans, R. M. Keegan, E. B. Krissinel, A. G. Leslie, A. McCoy, S. J. McNicholas, G. N. Murshudov, N. S. Pannu, E. A. Potterton, H. R. Powell, R. J. Read, A. Vagin and K. S. Wilson (2011). Overview of the CCP4 suite and current developments. *Acta Crystallogr D Biol Crystallogr* **67**(Pt 4): 235-242.

Wirawan, E., L. Vande Walle, K. Kersse, S. Cornelis, S. Claerhout, I. Vanoverberghe, R. Roelandt, R. De Rycke, J. Verspurten, W. Declercq, P. Agostinis, T. Vanden Berghe, S. Lippens and P. Vandenabeele (2010). Caspase-mediated cleavage of Beclin-1 inactivates Beclin-1-induced autophagy and enhances apoptosis by promoting the release of proapoptotic factors from mitochondria. *Cell Death Dis* **1**: e18.

Wong, P. M., C. Puente, I. G. Ganley and X. J. Jiang (2013). The ULK1 complex Sensing nutrient signals for autophagy activation. *Autophagy* **9**(2): 124-137.

Wood, C. W., M. Bruning, A. A. Ibarra, G. J. Bartlett, A. R. Thomson, R. B. Sessions, R. L. Brady and D. N. Woolfson (2014). CCBuilder: an interactive web-based tool for building, designing and assessing coiled-coil protein assemblies. *Bioinformatics* **30**(21): 3029-3035.

Woycechowsky, K. J. and R. T. Raines (2000). Native disulfide bond formation in proteins. *Curr Opin Chem Biol* **4**(5): 533-539.

Xia, P. Y., S. Wang, Y. Du, Z. N. Zhao, L. Shi, L. Sun, G. L. Huang, B. Q. Ye, C. Li, Z. H. Dai, N. Hou, X. Cheng, Q. Y. Sun, L. Li, X. Yang and Z. S. Fan (2013). WASH inhibits autophagy through suppression of Beclin 1 ubiquitination. *Embo Journal* **32**(20): 2685-2696.

Xiong, X. W., R. Y. Tao, R. A. DePinho and X. C. Dong (2012). The Autophagy-related Gene 14 (Atg14) Is Regulated by Forkhead Box O Transcription Factors and Circadian

Rhythms and Plays a Critical Role in Hepatic Autophagy and Lipid Metabolism. *Journal of Biological Chemistry* **287**(46): 39107-39114.

Xu, H. D., D. Wu, J. H. Gu, J. B. Ge, J. C. Wu, R. Han, Z. Q. Liang and Z. H. Qin (2013). The Pro-Survival Role of Autophagy Depends on Bcl-2 Under Nutrition Stress Conditions. *Plos One* **8**(5).

Xu, P., D. M. Duong, N. T. Seyfried, D. Cheng, Y. Xie, J. Robert, J. Rush, M. Hochstrasser, D. Finley and J. Peng (2009). Quantitative proteomics reveals the function of unconventional ubiquitin chains in proteasomal degradation. *Cell* **137**(1): 133-145.

Yamahara, K., M. Yasuda, S. Kume, D. Koya, H. Maegawa and T. Uzu (2013). The Role of Autophagy in the Pathogenesis of Diabetic Nephropathy. *Journal of Diabetes Research.*

Yamamoto, H., S. Kakuta, T. M. Watanabe, A. Kitamura, T. Sekito, C. Kondo-Kakuta, R. Ichikawa, M. Kinjo and Y. Ohsumi (2012). Atg9 vesicles are an important membrane source during early steps of autophagosome formation. *Journal of Cell Biology* **198**(2): 219-233.

Yang, C., V. Kaushal, S. V. Shah and G. P. Kaushal (2008). Autophagy is associated with apoptosis in cisplatin injury to renal tubular epithelial cells. *American Journal of Physiology-Renal Physiology* **294**(4): F777-F787.

Yang, S. and A. G. Rosenwald (2014). The roles of monomeric GTP-binding proteins in macroautophagy in Saccharomyces cerevisiae. *Int J Mol Sci* **15**(10): 18084-18101.

Yang, Z. N. J., C. E. Chee, S. B. Huang and F. A. Sinicrope (2011). The Role of Autophagy in Cancer: Therapeutic Implications. *Molecular Cancer Therapeutics* **10**(9): 1533-1541.

Yee, A., X. Chang, A. Pineda-Lucena, B. Wu, A. Semesi, B. Le, T. Ramelot, G. M. Lee, S. Bhattacharyya, P. Gutierrez, A. Denisov, C.-H. Lee, J. R. Cort, G. Kozlov, J. Liao, G. Finak, L. Chen, D. Wishart, W. Lee, L. P. McIntosh, K. Gehring, M. A. Kennedy, A. M. Edwards and C. H. Arrowsmith (2002). An NMR approach to structural proteomics. *Proceedings of the National Academy of Sciences* **99**(4): 1825-1830.

Yorimitsu, T. and D. J. Klionsky (2005). Autophagy: molecular machinery for self-eating. *Cell Death Differ* **12 Suppl 2**: 1542-1552.

Young, A. R. J., E. Y. W. Chan, X. W. Hu, R. Koch, S. G. Crawshaw, S. High, D. W. Hailey, J. Lippincott-Schwartz and S. A. Tooze (2006). Starvation and ULK1-dependent cycling of mammalian Atg9 between the TGN and endosomes. *Journal of Cell Science* **119**(18): 3888-3900.

Yuan, T., A. V. Gomes, J. A. Barnes, H. N. Hunter and H. J. Vogel (2004). Spectroscopic characterization of the calmodulin-binding and autoinhibitory domains of calcium/calmodulin-dependent protein kinase I. *Archives of biochemistry and biophysics* **421**(2): 192-206.

Yue, Z. Y., A. Horton, M. Bravin, P. L. DeJager, F. Selimi and N. Heintz (2002). A novel protein complex linking the delta 2 glutamate receptor and autophagy: Implications for neurodegeneration in Lurcher mice. *Neuron* **35**(5): 921-933.

Yue, Z. Y., S. K. Jin, C. W. Yang, A. J. Levine and N. Heintz (2003). Beclin 1, an autophagy gene essential for early embryonic development, is a haploinsufficient tumor suppressor. *Proceedings of the National Academy of Sciences of the United States of America* **100**(25): 15077-15082.

Zalckvar, E., H. Berissi, M. Eisenstein and A. Kimchi (2009). Phosphorylation of Beclin 1 by DAP-kinase promotes autophagy by weakening its interactions with Bcl-2 and Bcl-XL. *Autophagy* **5**(5): 720-722.

Zalckvar, E., H. Berissi, L. Mizrachy, Y. Idelchuk, I. Koren, M. Eisenstein, H. Sabanay, R. Pinkas-Kramarski and A. Kimchi (2009). DAP-kinase-mediated phosphorylation on the BH3 domain of beclin 1 promotes dissociation of beclin 1 from Bcl-XL and induction of autophagy. *EMBO Rep* **10**(3): 285-292.

Zha, H., C. Aime-Sempe, T. Sato and J. C. Reed (1996). Proapoptotic protein Bax heterodimerizes with Bcl-2 and homodimerizes with Bax via a novel domain (BH3) distinct from BH1 and BH2. *J Biol Chem* **271**(13): 7440-7444.

Zhong, Y., Q. J. Wang, X. T. Li, Y. Yan, J. M. Backer, B. T. Chait, N. Heintz and Z. Y. Yue (2009). Distinct regulation of autophagic activity by Atg14L and Rubicon associated with Beclin 1-phosphatidylinositol-3-kinase complex. *Nature Cell Biology* **11**(4): 468-476.

Zhu, Y., L. Zhao, L. Liu, P. Gao, W. Tian, X. Wang, H. Jin, H. Xu and Q. Chen (2010). Beclin 1 cleavage by caspase-3 inactivates autophagy and promotes apoptosis. *Protein Cell* **1**(5): 468-477.

APPENDIX A. PRIMERS DESIGNED FOR EACH CHAPTER

Primer Number	Primer Name	Sequence	Function	Chapter
1.	pMBP-BECN1 (aa1)-For	ACCGAAAACCTGT ATTTTCAGGGCGC CATGGATCCGATG GAAGGGTCTAAGA CGTCC	Cloning	3, 7
2.	pMBP-BECN1 (aa135)-Rev	GCGGCGGCGGCCG CTTCATGGGTGAT CCACATCTGTCTG GCCCGA	Cloning	3
3.	BECN (aa104)-For	ATTGGGGAGGTAT CTTGATGGCGGCA CCATG	Site-directed mutagenesis	3
4.	BECN (aa104)-Rev	CATGGTGCCGCCA TCAAGATACCTCC CCAAT	Site-directed mutagenesis	3
5.	pCR3.1 BECN1 (G120ED121A)-For	CGAAGACTGAAG GTCACTGAGGCCC TTTTTGACATC	Site-directed mutagenesis	3
6.	pCR3.1 BECN1 (G120ED121A)-Rev	GATGTCAAAAAGG GCCTCAGTGACCT TCAGTCTTCG	Site-direct mutagenesis	3
7.	pMBP-BECN1 (aa141)-For	GCGGCGATGGATC CGACAGATACTCT TTTAGACCAGCTG GACACTCAGC	Cloning	4
8.	pMBP-BECN1 (aa175)-For	GCGGCGGCCATGG ATGACAGTGAACA GTTACAGATGGAG CTAAAG	Cloning	4
9.	pMBP-BECN1 (aa265)-Rev	GCGGCGGCGGCCG CTTCACTTCAGCT TATCCAG CTGCGTCTGGGC	Cloning	4, 7
10.	pCR3.1- BECN1 (L144A)-For	GAGGAATGCACA GATACTGCGTTAG ACCAGCTGGACAC TCAG	Site-directed mutagenesis	4

Primer Number	Primer Name	Sequence	Function	Chapter
11.	pCR3.1- BECN1 (L144A)-Rev	CTGAGTGTCCAGCTGGTCTAACGCAGTATCTGTGCATTCCTC	Site-directed mutagenesis	4
12.	pCR3.1- BECN1 (L148A)-For	GATACTCTTTTAGACCAGGCGGACACTCAGCTCAACGTC	Site-directed mutagenesis	4
13.	pCR3.1- BECN1 (L148A)-Rev	GACGTTGAGCTGAGTGTCCGCCTGGTCTAAAAGAGTATC	Site-directed mutagenesis	4
14.	pCR3.1- BECN1 (L152A)-For	GACCAGCTGGACACTCAGGCGAACGTCACTGAAAATGAG	Site-directed mutagenesis	4
15.	pCR3.1- BECN1 (L152A)-Rev	CTCATTTTCAGTGACGTTCGCCTGAGTGTCCAGCTGGTC	Site-directed mutagenesis	4
16.	pCR3.1- BECN1 (E158A)-For	CTCAACGTCACTGAAAATGCGTGTCAGAACTACAAACGC	Site-directed mutagenesis	4
17.	pCR3.1- BECN1 (E158A)-Rev	GCGTTTGTAGTTCTGACACGCATTTTCAGTGACGTTGAG	Site-directed mutagenesis	4
18.	pCR3.1- BECN1 (Y162A)-For	GAAAATGAGTGTCAGAACGCGAAACGCTGTTTGGAGATCTTAGAG	Site-directed mutagenesis	4
19.	pCR3.1- BECN1 (Y162A)-Rev	CTCTAAGATCTCCAAACAGCGTTTCGCGTTCTGACACTCATTTTC	Site-directed mutagenesis	4
20.	pCR3.1- BECN1 (L166A)-For	CAGAACTACAAACGCTGTGCGGAGATCTTAGAGATCTTAGAG	Site-directed mutagenesis	4
21.	pCR3.1- BECN1 (L166A)-Rev	CTCTAAGATCTCTAAGATCTCCGCACAGCGTTTGTAGTTCTG	Site-directed mutagenesis	4

Primer Number	Primer Name	Sequence	Function	Chapter
22.	pCR3.1- BECN1 (L169A)-For	CGCTGTTTGGAGATCGCGGAGATCTTAGAGATCTTAGAG	Site-directed mutagenesis	4
23.	pCR3.1- BECN1 (L169A)-Rev	CTCTAAGATCTCTAAGATCTCCGCGATCTCCAAACAGCG	Site-directed mutagenesis	4
24.	pET29b-BECN1 (aa175)-For	AAGAAGGAGATATACATATGGATGACAGTGAACAGTTACAG	Cloning (Gibson)	5
25.	pET29b-BECN1 (aa265)-Rev	GTGGTGGTGGTGCTCGAGCTTCAGCTTATCCAGCTGCGT	Cloning (Gibson)	5
26.	pMBP-ATG14 (aa88)-For	GTGCCTGACTATGCCAGCCTGGGATCCATGGCGTCTCCCAGTGGGAAGGGAG	Cloning (Gibson)	5
27.	pMBP-ATG14 (aa178)-Rev	GGACCCTCACTCTAGAGTCGCGGCCGCTTAACGGTGTCCAGTGTAAGCTTTA	Cloning (Gibson)	5
28.	pCR3.1-BECN1 (L184A)-For	CAGTTACAGATGGAGGCAAAGGAGCTG GCACTAGAG	Site-directed mutagenesis	5
29.	pCR3.1-BECN1 (L184A)-Rev	CTCTAGTGCCAGCTCCTTTGCCTCCATCTGTAACTG	Site-directed mutagenesis	5
30.	pCR3.1-BECN1 (L212A)-For	GACGTGGCAGAAAATGCCGAGAAGGTCCAGGCTGAG	Site-directed mutagenesis	5
31.	pCR3.1-BECN1 (L212A)-Rev	CTCAGCCTGGACCTTCTCGGCATTTTCTGCCACGTC	Site-directed mutagenesis	5
32.	pCR3.1-BECN1 (Y233A)-For	GAAGCTCAGTATCAGAGAGAAGCCAGTGAATTTAACGACAG	Site-directed mutagenesis	5

Primer Number	Primer Name	Sequence	Function	Chapter
33.	pCR3.1-BECN1 (Y233A)-Rev	CTGTCGTTTAAATTCACTGGCTTCTCTCTGATACTGAGCTTC	Site-directed mutagenesis	5
34.	pEBB-ATG14 (L109A)-For	GGAAAATGGATAACAGATCAGGCGAGATGGAAAATAATGTCC	Site-directed mutagenesis	5
35.	pEBB-ATG14 (L109A)-Rev	GGACATTATTTTCCATCTCGCCTGATCTGTTATCCATTTTCC	Site-directed mutagenesis	5
36.	pEBB-ATG14 (I120A)-For	GTCCTGCAAGATGAGGGCTGAACAGTTAAAACAAACAATATG	Site-directed mutagenesis	5
37.	pEBB-ATG14 (I120A)-Rev	CATATTGTTTGTTTTAACTGTTCAGCCCTCATCTTGCAGGAC	Site-directed mutagenesis	5
38.	pEBB-ATG14 (L123A)-For	CCTGCAAGATGAGGATTGAACAGGCAAAACAAACAATATG	Site-directed mutagenesis	5
39.	pEBB-ATG14 (L123A)-Rev	CATATTGTTTGTTTTGCCTGTTCAATCCTCATCTTGCAGG	Site-directed mutagenesis	5
40.	pEBB-ATG14 (I127A)-For	GGATTGAACAGTTAAAACAAACAGCATGTAAAGGAAATGAAGAAATGG	Site-directed mutagenesis	5
41.	pEBB-ATG14 (I127A)-Rev	CCATTTCTTCATTTCCTTTACATGCTGTTTGTTTTAACTGTTCAATCC	Site-directed mutagenesis	5
42.	pEBB-ATG14 (L151A)-For	GGAAAAGAATCAGAAGGCTTACAGTCGAGCACAACGGC	Site-directed mutagenesis	5

Primer Number	Primer Name	Sequence	Function	Chapter
43.	pEBB-ATG14 (L151A)-Rev	GCCGTTGTGCTCG ACTGTAAGCCTTC TGATTCTTTTCC	Site-directed mutagenesis	5
44.	pEBB-ATG14 (I165A)-For	CCAAGAGAAAAA GGAGAAGGCTCA GAGGCATAATCGC	Site-directed mutagenesis	5
45.	pEBB-ATG14 (I165A)-Rev	GCGATTATGCCTC TGAGCCTTCTCCT TTTTCTCTTGG	Site-directed mutagenesis	5
46.	pCR3.1-BECN1 (N268AN271A)-Fwd	CTGGATAAGCTGA AGAAAACCGCCGT CTTTGCTGCAACC TTCCAC	Site-directed mutagenesis	6
47.	pCR3.1-BECN1 (N268AN271A)-Rev	GTGGAAGGTTGCA GCAAAGACGGCG GTTTTCTTCAGCTT ATCCAG	Site-directed mutagenesis	6
48.	pCR3.1-BECN1 (F274A)-Fwd	GTCTTTAATGCAA CCGCCCACATCTG GCACAG	Site-directed mutagenesis	6
49.	pCR3.1-BECN1 (F274A)-Rev	CTGTGCCAGATGT GGGCGGTTGCATT AAAGAC	Site-directed mutagenesis	6
50.	pCR3.1-BECN1 (I285AN286A)-Fwd	GGACAGTTTGGCA CAGCCGCTAACTT CAGGCTGGGTCGC	Site-directed mutagenesis	6
51.	pCR3.1-BECN1 (I285AN286A)-Rev	GCGACCCAGCCAG AAGTTAGCGGCTG TGCCAAACTGTCC	Site-directed mutagenesis	6
52	pCR3.1-BECN1 (R289AL290AG291V)-Fwd	GGCACAATCAATA ACTTCGCGGCGGT TCGCCTGCCCAGT	Site-directed mutagenesis	6
53.	pCR3.1-BECN1 (R289AL290AG291V)-Rev	CACTGGGCAGGCG AACCGCCGCGAAG CCATTGATTGTGC	Site-directed mutagenesis	6
54.	pCR3.1-BECN1 (E302AI303A)-Fwd	GTGGAATGAATGC GGCTAATGCTGCT TGGGGC	Site-directed mutagenesis	6

Primer Number	Primer Name	Sequence	Function	Chapter
55.	pCR3.1-BECN1 (E302AI303A)-Rev	GCCCCAAGCAGCATTAGCCGCATTCCATTCCAC	Site-directed mutagenesis	6
56.	pCR3.1-BECN1 (D366A)-Fwd	CACGTTTTTGTCTTGCCGCCAGGATGGATGTGGAG	Site-directed mutagenesis	6
57.	pCR3.1-BECN1 (D366A)-Rev	GCCACCATTGCATGGGCAAACTTGTTGTCCC	Site-directed mutagenesis	6
58.	pMBP-BECN1 (aa450)-Rev	GCGGCGGCGGCCGCTTCATTTGTTATAAAATTGTGAGGACACCCA	Cloning	7
59.	pCR3.1-BECN1 (C137AC140A)-For	GTGGATCACCCACTCGCTGAGGAAGCCACAGATACTC	Site-directed mutagenesis	7
60.	pCR3.1-BECN1 (C137AC140A)-Rev	GAGTATCTGTGGCTTCCTCAGCGAGTGGGTGATCCAC	Site-directed mutagenesis	7

APPENDIX B. PLASMIDS CONSTRUCTED IN EACH CHAPTER

Primer Number	Backbone	Plasmid name	Construction method	Chapter
1.	pMBP-Parallel-1	pMBP-Parallel-1-BECN1 (1-104)	Site-directed mutagenesis	3
2.	pMBP-Parallel-1	pMBP-Parallel-1-BECN1 (1-135)	Cloning	3
3.	pCR3.1	pCR3.1-Flag-BECN1 G120E+D121A	Site-directed mutagenesis	3
4.	pMBP-Parallel-1	pMBP-Parallel-1-(141-265)	Cloning	4, 7
5.	pMBP-Parallel-1	pMBP-Parallel-1-(175-265)	Cloning	4, 7
6.	pCR3.1	pCR3.1-Flag-BECN1 L144A	Site-directed mutagenesis	4
7.	pCR3.1	pCR3.1-Flag-BECN1 L148A	Site-directed mutagenesis	4
8.	pCR3.1	pCR3.1-Flag-BECN1 L152A	Site-direct mutagenesis	4
9.	pCR3.1	pCR3.1-Flag-BECN1 E158A	Site-direct mutagenesis	4
10.	pCR3.1	pCR3.1-Flag-BECN1 Y162A	Site-direct mutagenesis	4
11.	pCR3.1	pCR3.1-Flag-BECN1 L166A	Site-direct mutagenesis	4
12.	pCR3.1	pCR3.1-Flag-BECN1 L169A	Site-directed mutagenesis	4
13.	pCMV2	pCMV2-HA-AMBRA1 WT	Site-directed mutagenesis	4
14.	pET29b	pET29b-His_6-BECN (175-265)	Cloning (Gibson)	5
15.	pMBP-Parallel-1	pMBP-Parallel-1-ATG14 (88-178)	Cloning (Gibson)	5
16.	pCR3.1	pCR3.1-Flag-BECN1 L184A	Site-directed mutagenesis	5
17.	pCR3.1	pCR3.1-Flag-BECN1 L194A	Site-directed mutagenesis	5
18.	pCR3.1	pCR3.1-Flag-BECN1 V208A	Site-directed mutagenesis	5
19.	pCR3.1	pCR3.1-Flag-BECN1 L212A	Site-directed mutagenesis	5

Primer Number	Backbone	Plasmid name	Construction method	Chapter
20.	pCR3.1	pCR3.1-Flag-BECN1 L222A	Site-directed mutagenesis	5
21.	pCR3.1	pCR3.1-Flag-BECN1 Y233A	Site-directed mutagenesis	5
22.	pCR3.1	pCR3.1-Flag-BECN1 F236A	Site-directed mutagenesis	5
23.	pCR3.1	pCR3.1-Flag-BECN1 V250A	Site-directed mutagenesis	5
24.	pCR3.1	pCR3.1-Flag-BECN1 L222A	Site-directed mutagenesis	5
25.	pEBB	PEBB-HA-ATG14 L109A	Site-directed mutagenesis	5
26.	pEBB	PEBB-HA-ATG14 I120A	Site-directed mutagenesis	5
27.	pEBB	PEBB-HA-ATG14 L123A	Site-directed mutagenesis	5
28.	pEBB	PEBB-HA-ATG14 I127A	Site-directed mutagenesis	5
29.	pEBB	PEBB-HA-ATG14 L151A	Site-directed mutagenesis	5
30.	pEBB	PEBB-HA-ATG14 L165A	Site-directed mutagenesis	5
31.	pCR3.1	pCR3.1-Flag-BECN1 N268A+N271A	Site-directed mutagenesis	6
32.	pCR3.1	pCR3.1-Flag-BECN1 F274A	Site-directed mutagenesis	6
33.	pCR3.1	pCR3.1-Flag-BECN1 I285A+N286A	Site-directed mutagenesis	6
34.	pCR3.1	pCR3.1-Flag-BECN1 R289A+L290A+G291V	Site-directed mutagenesis	6
35.	pCR3.1	pCR3.1-Flag-BECN1 N268+N271A	Site-directed mutagenesis	6
36.	pCR3.1	pCR3.1-Flag-BECN1 E302A+I303A	Site-directed mutagenesis	6
37.	pCR3.1	pCR3.1-Flag-BECN1 D366A	Site-directed mutagenesis	6

Primer Number	Backbone	Plasmid name	Construction method	Chapter
38.	pMBP-Parallel-1	pMBP-Parallel-1-BECN1 (105-265)	Cloning	7
39	pMBP-Parallel-1	pMBP-Parallel-1-BECN1 (1-450)	Cloning	7
40.	pCR3.1	pCR3.1-Flag-BECN1 C137A+C140A	Site-directed mutagenesis	7